KK H

Composite Materials

Mechanical and physical behavior as influenced by phase geometry

Lauge Fuglsang Nielsen

DEPARTMENT OF CIVIL ENGINEERING

TECHNICAL UNIVERSITY OF DENMARK • DK-2800 LYNGBY • DENMARK

COMPOSITE MATERIALS

Mechanical and physical behavior as influenced by phase geometry

LAUGE FUGLSANG NIELSEN

DEPARTMENT OF CIVIL ENGINEERING

TECHNICAL UNIVERSITY OF DENMARK ● DK-2800 LYNGBY ● DENMARK

Overview

The subject dealt with in this monograph is the mechanical and physical behavior of composites as influenced by composite geometry. This subject has a high priority in the general study of composite materials. A better understanding of the behavior of natural composites, improvement of such materials, and design of new materials with prescribed properties are just three examples in modern materials research where more knowledge on geometry versus materials property is absolutely necessary.

An analysis of various composite properties versus composite geometries is presented in this monograph as the result of integrating the results of two sub-studies:

One study is made on composite properties as these can be related to composite geometry in general by so-called shape functions. The second study is made on shape functions as these are related to the geometry of specific composites, such as particulate composites, impregnated materials, laminated composites, and composites made by compaction of powders.

In other words, global solutions for composite properties are developed by the first study which apply for any composite. Final solutions for composites with specific geometries are then obtained from the global solutions introducing specific shape functions developed by the second study.

Special composite properties considered are stiffness, shrinkage, hygro-thermal behavior, viscoelastic behavior, and internal stress states. Other physical properties considered are thermal and electrical conductivities, diffusion coefficients, dielectric constants and magnetic permeability. Special attention is given to the effect of pore shape on the mechanical and physical behavior of porous materials.

The theories and methods developed are verified by results obtained from a FEM-analysis presented, and by experimental and theoretical data from the composite literature. A number of examples are presented which illustrate the very decisive influence of the internal geometry on the mechanical and physical properties of composites.

As a spin-off result the composite theory developed is re-organized to become a "diagnostic tool" with respect to quality control of empirical or semi-theoretical prediction methods suggested in the field of composite materials - and with respect to materials design.

Remark: It is emphasized that strength is not considered as a genuine materials property in this monograph. It is a phenomenon where discontinuities in the materials structure suddenly occur as the result of violating local potentials to carry stress and/or strain for example. As such strength is a 'materials property' which

can be calculated from stress/strain results obtained in this monograph. Examples of such strength predictions for composite materials are presented.

Readers guidance

Roughly speaking the monograph is divided into two parts. A theoretical part, and a more applicative part, starting at Chapter 10 where the theories developed are simplified, adapted, and generalized for most practice [1].

Lists of notations and references used are presented at the end of the monograph. The former list (Chapter 17) should be consulted frequently. Symbols and notations used in the monograph are generally explained only at their first appearance in the text.

The following superior concept of notations is emphasized: Whenever needed to distinguish single component properties from composite properties, subscripts P and S refer to property of component P and property of component S respectively while composite property is not subscripted. Usually the subscripts g and k are used to indicate quantities obtained from - or used in deviatoric analysis and in volumetric analysis respectively. Formally these analysis are very often identical. In such cases only the volumetric analysis is presented with deviatoric results referred to by analogy. Alternatively both subscripts k and g are dropped when the feature discussed applies in principles for both volumetric and deviatoric behavior.

A number of auxiliary expressions and data documentations are presented in appendix sections at the end of the monograph: Basic information are given on isotropic elasticity and cubical elasticity in Appendix A. A method is presented in Appendix B for the numerical determination of stresses in ellipsoidal particles in isotropic dilute suspensions. A generalized version of the so-called SCS-analysis of composite materials is presented in Appendix C (Self Consistency Scheme). A detailed description (with data documentation) of a FEM-analysis made on some composite materials is presented in Appendix D. Some detailed geometrical functions are presented in Appendix E. Some general viscoelastic models are presented in Appendix F. And finally, some re-interpretation of 'flat and long' geometries are considered in Appendix G.

---

1) Readers, who are interested primarily in applications may start at this chapter. Software (to be downloaded from *http://www.byg.dtu.dk/publicering/software_d.htm*) is developed to solve a number of problems considered in this monograph.

Content

1. Introduction

In the past four decades considerable attention has been devoted to composite materials. A number of expressions have been suggested by which macroscopic properties can be predicted when the properties, geometry, and volume concentrations of the constituent components are known. Many expressions are purely empirical or semi-theoretical. Others, however, are theoretically well founded such as the exact results from the the following classical boundary studies:

Bounds for the elastic moduli of composites made of perfectly coherent homogeneous isotropic linear elastic phases have been developed by Paul (1) and Hansen (2) for unrestricted phase geometry and by Hashin and Shtrikman (3) for phase geometries which cause macroscopic homogeneity and isotropy.

The composites dealt with in this monograph are of the latter type. For two specific situations (later referred to), Hashin (4) and Hill (5) derived exact solutions for the bulk modulus of such materials. Hashin considered the so-called Composite Spheres Assemblage (CSA) consisting of tightly packed congruent composite elements made of spherical particles embedded in concentric matrix shells. Hill considered materials in which both phases have identical shear moduli.

In the field of predicting the elastic moduli of homogeneous isotropic composite materials in general the exact Hashin and Hill solutions are of theoretical interest mainly. Only a few real composites have the geometry defined by Hashin or the stiffness distribution assumed by Hill. The enormous significance, however, of the Hashin/Hill solutions is that they represent bounds which must not be violated by stiffness predicted by any new theory claiming to consider geometries in general.

For a variety of other composites (than Hashin/Shtrikman/Hill) other theoretically well founded analytical methods have been developed for strictly defined specific phase geometries. Examples are as follows: Ellipsoidal particles in a continuous matrix are examined by Christoffersen (6) and Levin (7). Other particulate composites are considered in (8,9,10,11,12). A special particulate composite with compacted spherical particles is examined by Budiansky in (13). Special fibre reinforced materials are examined by Stang (14), and so-called graded composite materials are considered in (15,16).

Early composite theories based on statistically defined phase geometries are reviewed in (17). Such approach using statistical continuum theories has been further developed by Torquato in (18,19).

If real geometry and theoretically assumed geometry agree with each other excellent results can very often be obtained by the methods just mentioned. Many real composites, however, have geometries which are substantially different from any of the geometries considered in prediction methods known to day. Composites geometry will change - not only from type of composite to another type - but also in composites individually. First of all it is very likely that the geometry of material components will vary with phase concentration. This means, for example, that a method for stiffness prediction applying at one concentration is not necessarily the right one to use at another concentration.

This feature is illustrated in Figure 1.1 showing the influence of porosity on the stiffness of real porous systems such as tile and hardened cement paste. Very often a final critical porosity of 55 - 75% is approached where stiffness becomes zero. Obviously the critical porosity indicates the extreme state of a continuous process of geometry transformation where the solid phase is increasingly separated and surrounded by an increasing amount of pores. No model with fixed geometry can be used to predict stiffness of porous material. For this reason most relations to day between stiffness of porous materials and porosity are still the empirical expressions developed in (20,21,22) for example. Only empirical relations are qualified which do not violate the shaded area in Figure 1.1 bounded by the theory of Hashin (4) previously referred to.

Figure 1.1. Stiffness of an isotropic porous material as related to pore shapes. Dots are various exp-data reproduced from Chapter 11.

In itself the large number of completely different empirical stiffness expressions suggested for porous materials clearly indicates a need for a more rational research on composite properties versus composite geometry such as reported by the present author in a study (23) on porous materials and impregnated materials.

Change of geometry will influence any mechanical/physical behavior of composites. Stiffness and viscoelasticity (creep and relaxation) will change. Shrinkage and

12

eigenstress-strain (such as hygro-thermal) properties, and heat conductivity are other examples of materials behavior which will change with geometry.

In order to cope rationally with such changes in composite analysis we must increase our freedom to chose other analytical models than the specific, non-variable ones most often used to day. Valuable progress in materials science can then be achieved in areas, such as a better understanding of the behavior of natural composites, a more rational improvement of such composites, and a rational design of new materials.

Some ideas on how to obtain such freedom are presented by the author in (24) where it is shown that "global" property relations for composites can be established with geometry considered by independent variables, so-called shape functions, which can be studied separately with respect to specific geometries (discrete, continuous, etc).

Aspects of the same problem, how to construct a composite geometry such that prescribed properties can be obtained, have been studied by Milton (25) who introduced the term "inverse homogenization problem" for such composite analysis. Sigmund (26,27) approaches the problem of inverse homogenization numerically looking at basic porous material structures made by trusses and plates. Milton and Cherkaev (28) provide a basis for studying the problem through analytical studies and construction of so-called extreme materials.

Modern numerical solution techniques such as Finite Element Methods (FEM) have had a tremendous impact on the research on composite materials. These techniques introduced into composite analysis around 1970 (29,30) have proved themselves to be very efficient tools in handling composite problems of a complexity (e.g. 31,32,33,34,35,36) far beyond what can be treated by analytical means. Recently, numerical methods have also proved their potentials with respect to optimization between shape and properties of structures (37,38) and between geometry and properties of some special orthotropic composites (39). Such studies are very useful in the research of optimizing composite geometry in general with respect to composite properties. This feature has been recognized in the works of Sigmund (26,27) previously referred to.

1.1 Objectives of this work

In summary, the main objectives of this monograph is to increase our general understanding of the influence of composite geometry on composite behavior. Some good reasons for increasing our knowledge on geometry versus behavior of compo-

site materials have already been mentioned with respect to natural composites, improvement of such materials, and with respect to design of new materials with prescribed properties.

As can be noticed from the literature previously cited, other composite researchers agree that research is necessary on the significance of composite geometry. A number of ways have been applied to approach the problem. Important works have been reported which are based on very strict descriptions and studies (analytical or FEM) of composite geometries, statistically defined (as in 18), or arranged from basic microstructures (as in 26,28). Fine results can be expected from such studies using continuum mechanics on microstructures the geometries of which are basically fixed.

The author's approach presented in this monograph has another point of departure with respect to "real" composite geometry: It is recognized that varying phase geometries produced by nature or by man can not in general be described (or defined) very precisely. A description must reflect deductions made from experimental studies primarily, including such which consider technologies used to produce composites.

Basically the methods presented are further developments of the ideas presented in (23,24,40) of predicting the properties of any composite material from global expressions with specific composite geometries considered by so-called shape functions. Such functions are developed by which the author's view on real co mposite geometries previously explained is reflected by expressions with only a few parameters to be calibrated. Geometries described with shape functions are shown to be consistent with the overall composite assumptions previously made with respect to macroscopical homogeneity and isotropy.

Shape functions are developed for a variety of composites including specific co mposites previously considered in the composite literature. Also considered are the somewhat self-defining geometries which appear in so-called SCS-analysis of composites (Self-Consistency-Scheme).

Special composite problems/properties considered are stiffness, shrinkage, hygrothermal behavior, viscoelastic behavior, and internal stress states - as well as other physical properties of composites such as thermal and electrical conductivities, diffusion coefficients, dielectric constants and magnetic permeabilities.

The theoretical results obtained are verified by a FEM-analysis made by the author and by theoretical results obtained by other authors. The principal success criteria, however, for the methods developed are that the results predicted comply with data

14

obtained from experiments on real composites as these data are reproduced from the composite literature.

As a spin-off result the composite theory developed is re-organized to become a "diagnostic tool", useful in materials design and in quality control of empirical or semi-theoretical prediction methods suggested in the field of composite materials (are such methods consistent with "promises" made with respect to geometry and isotropy?).

1.1.1 A summary of composites considered

We re-call that the composites primarily considered in this monograph are perfectly coherent two-phase materials with phase geometries causing macroscopic homogeneity and isotropy. Both phases are isotropically linear-elastic (or -viscoelastic).

Flexible phase geometries primarily are considered which can adjust themselves to form a tight composite. The adjustment can be natural (as in suspensions) or organic (as in bone structures) or it can be the result of compaction (as in sintered powder composites).

As in most literature on composite materials the terms composite, composite material, and two-phase material are used synonymously - unless otherwise indicated as in minor sections of this monograph where composites in practice do not behave 'theoretically':

When phase geometries are not flexible (such as in composites made of stiff particles in a solidifying matrix as concrete for example) air voids are inevitable at certain concentrations. The two-phase material originally considered becomes a porous two-phase material. In practice such a material can be considered as a "normal" two-phase composite with a porous matrix. This feature is explained in further details in Chapter 11 together with some other composite "defects" (such as incomplete impregnation and incomplete phase contact) which can also be considered introducing some simple phase modifications.

2. Classification of composites

A systematic classification of composites is a necessity in any discussion and analysis of, how the mechanical and physical properties of composites are influenced by their internal geometries. A model is suggested in this monograph by which basic isotropic composite geometries can be classified continuously as stages in a process of geometry transformation where one phase changes from spheres to spherical shells ("anti-spheres") - while the other phase in a complementary way transforms from spherical shells to spheres.

Spherical shapes and spherical shell shapes are the most extreme geometries when isotropic composites are considered. Arguments for accepting this geometrical concept can be found in the work of Hashin and Shtrikman (3) on bulk stiffness bounds for isotropic composites. One H/S-bound is the exact solution to stiffness of a composite where one phase has the geometry of spheres. The other H/S-bound is the exact solution to stiffness of a composite where the other phase has the geometry of spheres.

2.1 Volume concentrations

The most elementary information needed to quantify a composite is its content of constituent phases. In the analysis of composites with respect to mechanical and physical behavior it is very appropriate to quantify the content of a certain phase by its volume fraction relative to the composite volume. It is implicitly understood in this monograph that concentration c means volume fraction of phase P as defined in Equation 2.1 where volumes are indicated by V. Phase S concentration is then 1 - c.

$$ c = \frac{V_P}{V_P + V_S} \quad (phase\ P) \quad ; \quad 1 - c = \frac{V_S}{V_P + V_S} \quad (phase\ S) \qquad (2.1) $$

On the basis of phase concentrations material property bounds can be developed assuming that phase geometries take their most extreme, opposite shapes: Parallel lamella for anisotropic composites - and sphere/shell geometries for isotropic composites. No more information can be achieved on the behavior of composites unless additional information is given on internal geometry.

Information on phase geometry is just as essential as concentration is. In some cases it is even more important. A very simple example will demonstrate this statement: A cracked material is a porous material with pores (phase P) having an extremely flat geometry of no volume, meaning c = 0. Stiffness (and streng

th) of this material is not at all equal to stiffness and strength of the original un cracked material which, of course, also has a porosity of c = 0. From an elastic point of view it is more appropriate to compare the cracked material with a material with spherical pores of diameters equal to crack diameters in the original material. Thus a real porous material can easily be a better material than a material which is thought to be non-porous.

2.1.2 Concrete and hardening cement paste.
At various occasions HCP and concrete are studied in this monograph. The volumetric models used for these materials are presented in Table 2.1 which is based on the basic paste concept developed by the author in (41). Water/cement and aggregate/cement ratios (by weights) are denoted by W/C and A/C respectively. Basic paste is that volume part of a hardening cement paste which will hydrate 100 % transforming to cement gel, including gel pores.

CONCRETE		
is HCP mixed with aggregates of volume concentration c	$C = \dfrac{38A/C}{100W/C + 38A/C + 32}$	$A = \dfrac{1 - c}{1 + c}$
HARDENING CEMENT PASTE (HCP)		
with **W/C > 0.38** is basic paste mixed with voids of vol-concentration c_{VOID}	$c_{VOID} = \dfrac{100W/C - 38}{100W/C + 32}$	$A_{VOID} = \dfrac{35}{100W/C - 3}$
with **W/C ≤ 0.38** is basic paste mixed with cem-grains of vol-concentration c_{CEM}	$c_{CEM} = \dfrac{32 - 84W/C}{100W/C + 32}$	$A_{CEM} = \dfrac{23W/C}{8 + 2W/C}$

Table 2.1. Composition of concrete and HCP as related to A/C, W/C, and basic paste. Any volume concentration is relative to total volume of components considered. Vol-parameter is $A_i = (1-c_i)/(1+c_i)$ with i=cem,void.

Basic paste has a constant volume. Its stiffness, however, is time dependent with E_{BAS} = 3.2e4*g(t) MPa where g(t) is the absolute degree of hydration (amount of cement hydrated at time t relative to total amount of cement.

Cement grains (subscript cem in Table 2.1) which will never hydrate act as particles in basic paste. Water which will never be used in the hydration process act as voids (subscript void in Table 2.1) in basic paste.

Densities assumed in Table 2.1 are 3.1 gr/cm³ and 2.6 gr/cm³ for cement and aggregates respectively. Hydration products (gel, including gel pores) occupy a volume 2.2 greater than the bulk volume of the cement involved in the hydration process. These specifications are consistent with the hydration studies of Powers and Brownyard (42,43).

The major advantage of using the concept of basic paste in concrete analysis is that hardening cement paste can always be modelled by a simple two-phase model.

2.1.3 Porosity of hardening cement paste.
Also the porosities of hardening cement paste are of interest in this monograph. The porosity expressions presented in Table

2.2 are reproduced from (44) where they have been determined on the basis of the principles developed by Powers and Brownyard in (42,43) previously referred to.

The time dependent change of porosities is controlled by the absolute degree of hydration, g(t) previously referred to. The description of g(t) presented in Table 2.2 is suggested by Freiesleben in (45) with characteristic hydration parameters τ and β. The relative degree of hydration q(t) is amount of cement hydrated relative to the amount of cement which can be hydrated in capillary space available. The two hydration degrees are related as shown in the Table 2.2.

W/C	c_{TOT}	c_{CAP}	q(t)
> 0.38	$\dfrac{100W/C-18q(t)}{100W/C+32}$	$\dfrac{100W/C-38q(t)}{100W/C+32}$	g(t)
≤ 0.38	$\dfrac{100W/C[1-0.47q(t)]}{100W/C+32}$	$\dfrac{100W/C[1-q(t)]}{100W/C+32}$	$\min\left[\dfrac{0.38}{W/C}g(t),1\right]$
HCP coheres only if $q \geq \max(0.5W/C, 0.19)$			
$g(t) = \exp\left[-(\tau/t)^{\beta}\right]$ *absolute degree of hydration*			

Table 2.2. Total porosity c_{TOT} and capillary porosity c_{CAP} in hardening cement paste. Absolute degree of hydration and relative degree of hydration are denoted by g(t) and q(t) respectively, see main text.
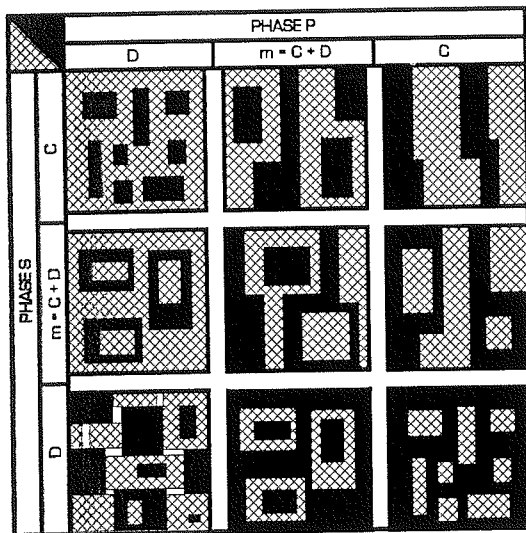
Figure 2.1. Phase geometries in two-phase materials. C, D and m (= C + D) denote continuous geometry, discrete geometry, and mixed geometry respectively.

2.2 Geometry at fixed phase concentrations

At fixed phase concentrations composites can be classified according to their internal geometry as stylized in Figure 2.1. A phase with continuous geometry (C) is a phase in which the total composite can be traversed without crossing the other

phase. This is not possible in a phase with discrete geometry (D). A mixed geometry (m) is a continuous geometry with some discrete elements. It is noticed that there are only eight possibilities of mixing phase P and phase S. A mixture where both phases are discrete is not possible.

2.2.1 Geometrical classification

Figure 2.2 is used in this work as a simplified classification scheme for composite geometries at fixed volume concentrations c. The former and the latter letter used in combinations indicate phase P and phase S geometry respectively.

- DC means that phase P appears as discrete elements in a continuous phase S.

- MM is a common descriptor for geometries mC, CC, mm, and Cm defined in Figure 2.1. Continuous elements are always present. Some times the signature CC will be used subsequently in stead of MM. Only, however, if MM in fact stands for a mixture of two fully continuous phases.

- CD means that phase P appears as continuous elements in a discrete phase S.

Combinations Dm and mD are not considered in this classification scheme. They are anticipated to appear in very narrow transition geometries which are very rare relative to other combinations found in practice (just think of a concrete made with aggregates which are both surrounded and filled with mortar).
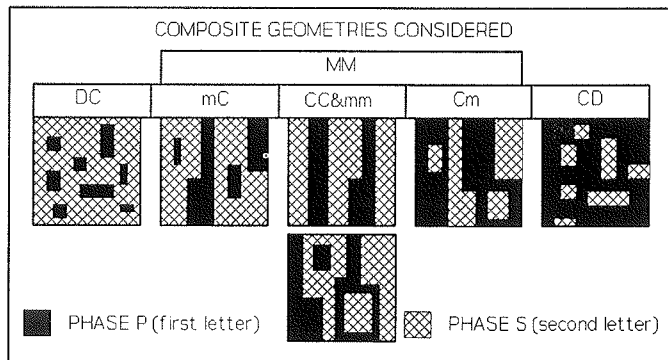
Figure 2.2. Simplified scheme of geometry classification.

2.3 Composites with variable geometry

Any of the geometry combinations considered in Section 2.2 can be thought of as stages in a process of geometry transformation where phase P transforms organically from having a compact discrete geometry to having a continuous geometry such that phase S simultaneously in a complementary way transforms from having a continuous geometry to having a compact discrete geometry.

The variable composite geometry just outlined can be illustrated as shown in Figure 2.3 where the critical concentrations c_p and c_s indicate geometrical transitions between MM geometries and the geometry of phase P being fully continuous

with fully discrete phase S particles (CD geometry) at c_P - and the geometry of phase S being fully continuous with fully discrete phase P particles (DC geometry) at c_S. The critical concentrations illustrated in Figure 2.3 are real (inside c = 0-1). Formally, however, they can also be non-real (outside c = 0-1). This feature is demonstrated shifting the movable geo-cylinders outlined in Figure 2.4. Examples: If c_S < 0 then a MM-composite is described at low concentrations. If c_P > 1 then a MM-composite is described at high concentrations. If c_S < 0 and c_P > 1 then a composite is described which has a MM-geometry at any concentration.
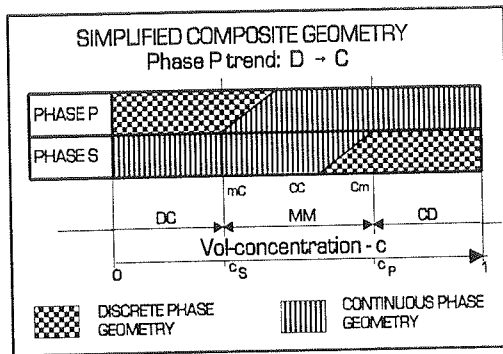
Figure 2.3. Composite geometry when phase P goes from D to C.
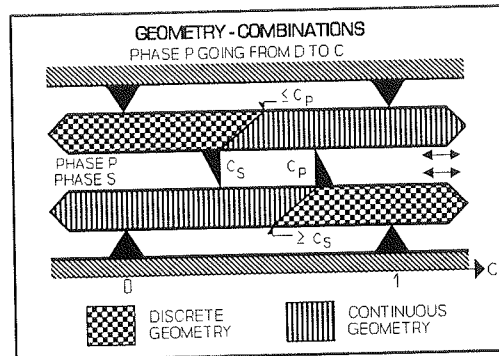
Figure 2.4. Change of geometry. Various composites are defined by different positions of the movable geo-cylinders.

2.3.1 Geometrical classification

Various geometrical compositions can be illustrated by the model illustrated in Figure 2.4 where the movable "geometry cylinders" help us to classify composites as shown in Equation 2.2.

$$\begin{matrix} DC\text{-}DC \\ DC\text{-}MM \\ DC\text{-}CD \end{matrix} \quad \begin{matrix} MM\text{-}MM \\ MM\text{-}CD \end{matrix} \quad CD\text{-}CD \quad \begin{matrix} first\ two\ letters:\ geometry\ at\ c = 0 \\ last\ two\ letters:\ geometry\ at\ c = 1 \end{matrix} \quad (2.2)$$

Equation 2.2 is the main scheme of composite classification used in this monog raph. It defines a composite by its geometries at c = 0 and c = 1. Critical concentrations required to 'realize' these geometries are explained in Figure 2.5.

In principles the process of geometry changes proceeds as previously indicated in this chapter. For both natural and man made composites, geometries change as the result of increasing the concentration of one phase on the expense of the other.

Remark: It is re-called at this point that it is assumed implicitly in this monograph that geometries change such that phase P varies on a path from discrete geometry to continuous geometry (as in Figures 2.3 and 2.4) unless otherwise indicated. The

choice of phase numbering (P,S) in practice can always be chosen to agree with this assumption involving critical concentrations $c_P \geq c_S$.

Critical concentrations

It is obvious that the critical concentrations previously defined are very important classification parameters. They are key-concentrations defining what concentrations are used to change phase P from discrete particles in a continuous S-matrix to the inverse of this geometry, namely discrete phase S particles in a continuous P-matrix. Critical concentrations are determined by technology (including appearance and size distribution of raw materials) used to produce composite materials.
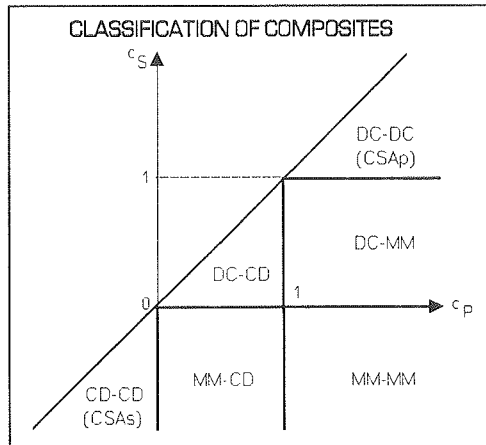
Figure 2.5. *Composite geometries as related to critical concentrations, (CSA-geometries are explained in Section 2.3.2).*

Example: To illustrate the latter statement: In a DC-CD composite such as a porous material the critical concentration c_S is that void concentration at which discrete voids start to interfere forming continuous geometries. Single sized voids will produce a lower c_S than will aggregates with a smooth and continuous size distribution. At increasing void concentration the interference becomes so pronounced that the porous material looses its coherence (no stiffness, no strength) at a critical void concentration of c_P. The original porous material has become a composite with solid particles dissolved in a "void matrix".

Remark: It has been mentioned that critical concentrations can be real (inside 0-1) or they can be non-real (outside 0-1). It is emphasized, however, that the latter concentrations have no physical meanings others than indicating directions of geometrical trends.

Percolation, permeability, impregnability

The discussion of composites geometry is closely related to the study of percolation in composites. Percolation theory considers the connectivity of a phase across a microstructure (46,47). A minor study on connectivity as related to the geometrical classification of composites has been made by the author in (48). Trans-

port properties of composite materials were considered such as permeability and impregnability of porous materials.
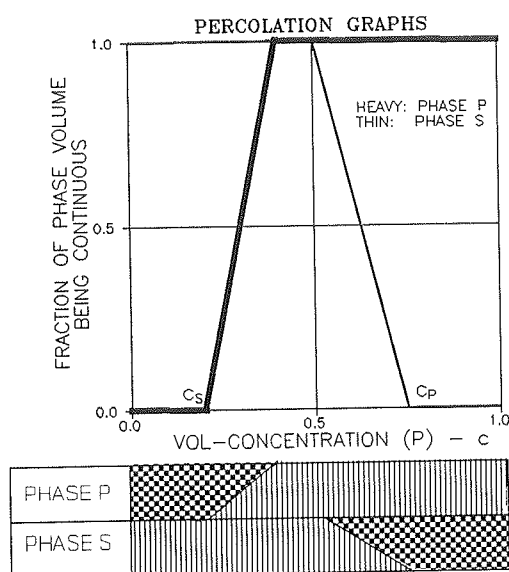
Figure 2.6. *Percolation graphs for phase P and phase S respectively.*
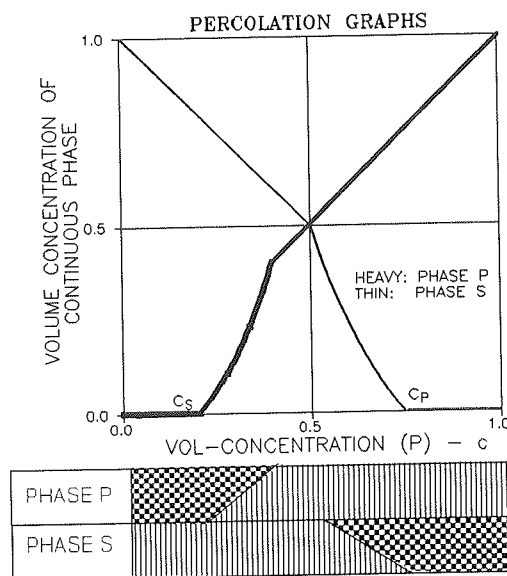
Figure 2.7. *Concentration of continuous parts of phase P and phase S respectively.*

The relation between geometrical classification and connectivity is outlined in Figure 2.6 with so-called percolation graphs. When the material considered in the figure has an empty phase P we notice that the material is not impregnable in c = 0 - c_s. It is partly impregnable in c = c_s - 0.4, and it is fully impregnable in c = 0.4 - 1. In c = c_p - 1, however, the porous material breaks down because of no coherence. As noticed from Figure 2.7 the percolation graphs can easily be converted to volume concentrations of continuous phases.

The concept of connectivity has recently been used by Bentz in (49) to relate the microstructure of cement paste to the amount of cement hydrated.

2.3.2 Some composite examples

Some composites may keep their geometrical type independently of volume concentrations. Normally, however, composites change their geometry with volume concentrations. Some examples of both types are considered in this section.

Composite Spheres Assemblage (CSA)

The Composite Spheres Assemblage shown in Figure 2.8 is a theoretical model of a two-phase material introduced by Hashin (4): Tightly packed congruent co mposite elements made of spherical particles embedded in concentric matrix shells.
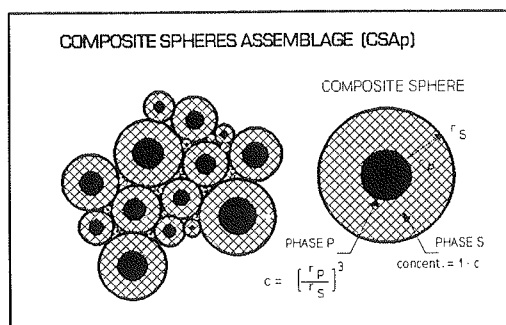
Figure 2.8. Composite Spheres Assemblage with phase P particles (CSAₚ).

Two types of CSA-materials are subsequently referred to: A CSA$_P$-material has phase P particles and a phase S matrix at any concentration which makes it a type DC-DC composite. A CSA$_S$-material, see subsequent Figure 4.1, has phase S particles and a phase P matrix at any concentration which makes it a type CD-CD composite.

Particulate composites

At low concentrations a particulate composite is a mixture of discrete phase P particles in a continuous phase S (so-called matrix). An ideal particulate composite has a DC geometry at any concentration. This does not necessarily mean that the geometry at c = 1 is exactly the same as at c = 0 (such as in the CSA-composites previously considered).

Shapes may change considerably within a certain type classification. New shapes may be formed, for example, by particle agglomeration. Ideal particulate composites are classified as DC-DC composites. Very often the term, particulate composite, is kept even if phase P particles grow together at higher concentrations such that MM and CD geometries are formed. Thus, the term particulate composite is frequently used as a somewhat inaccurate common descriptor for any DC-DC, DC-MM, and DC-CD composite.

Special particulate composites are fibre reinforced materials. The fibres can be straight or shaped like pearls on a string (rugged fibres). Other particulate composites considered in this monograph are disc reinforced materials. The discs can be plain (pennies) or shaped like a jelly fish (frayed discs), or shaped like fried eggs (rugged discs).

Lamella composites (incl. crumbled foils)

A lamella composite is the result of mixing two phases the geometries of which are continuous at any concentration. Lamella composites (ribbons, long fibres, sheets, and foils included) can be the results of mixing lamella shaped phase P elements into a continuous phase S. They can also be the results of compacting a mixture made of phase P lamella and phase S lamella. Lamella composites are type CC composites at any concentration, which make them of the CC-CC type.

When equal types of phase P and phase S geometries are used lamella composites are likely to become phase-symmetric as explained below.

Special lamella considered in this monograph are so-called "Pearls on a string" with geometries like interconnected compact particles. Pearls on a thin string and pearls on a thick string are considered. A special lamella composite, the crumbled foils composite, is considered where both phases have the shapes of crumbled foils (or sheets).

Powder composites

A powder composite is the result of compacting a mixture of two powders. At low concentrations (of phase P) such a composite appear as a type DC composite. At high concentrations it is a type CD composite. When equally shaped powders are used, powder composites are likely to become phase-symmetric as explained below. In general powder composites are of type DC-CD. In the terminology used in this monograph powder composites are special particulate composites.

Phase-symmetric composites

Phase-symmetric composites have geometries which are symmetric with respect to $c = 0.5$: The type of composite geometry at $c = 0.5-\Delta c$ (fx DC) equals the symmetric type of composite geometry at $c = 0.5+\Delta c$ (CD). Composites qualifying to be phase-symmetric are types DC-CD and MM-MM (including CC-CC).

Porous material and impregnable material

The geometry of pores in a porous material changes with porosity (c). Pores are not impregnable at $c < c_s$, see Figures 2.6 and 2.7. Pores start being impregnable at $c = c_s$ and become increasingly impregnable as $c = c_P$ is approached. A 100 % impregnability is guarantied beyond $c = c_P$. Then, however, the porous material is not coherent as in bricks which cannot in general be produced with porosities higher than $c = c_P \approx 70\%$ without loosing their strength and stiffness. A pore system with pearls on a string geometry is a transition system between a discrete pore system and a continuous pore system. The strings are so-called bottle necks.

3. Preliminaries on stress/strain

Some basic expressions are presented in this chapter which are subsequently used to predict composites behavior as influenced by variable geometry. A consistent composite analysis is ensured when these basic expressions are used properly. In the present context consistency means that predicted stiffness, for example, does not violate the Hashin/Shtrikman bounds (3) (H/S) presented in Equation 3.1 and illustrated by solid lines in Figures 3.1 and 3.2. Prediction methods are no good which involve violation of these bounds, even if they predict stiffness which do not violate the Poul/Hansen bounds (1,2) (P/H) presented in Equation 3.2 and illustrated by dashed lines in Figures 3.1 and 3.2. (In the presentation of bounds just made both Poisson's ratios $\nu_P = \nu_S = 0.2$ have been assumed).

$$\frac{n + 1 + c(n - 1)}{n + 1 - c(n - 1)} \leq e \leq n\frac{2 + c(n - 1)}{2n - c(n - 1)} \qquad \begin{array}{l} \textit{Isotropic bounds} \\ \textit{for } n \geq 1, \textit{ reverse} \\ \leq \textit{ when } n < 1 \end{array} \qquad (3.1)$$

$$1 + (n - 1)c \geq e \geq \frac{n}{n - (n - 1)c} \qquad \textit{Anisotropic bounds} \qquad (3.2)$$

Compare Appendix A, the symbols used have the following meanings: Stiffness ratio is n = E_P/E_S. Relative Young's modulus of composite is e = E/E_S. Young's moduli are denoted by E. Subscripts P and S indicate composite phase. No subscript means composite.
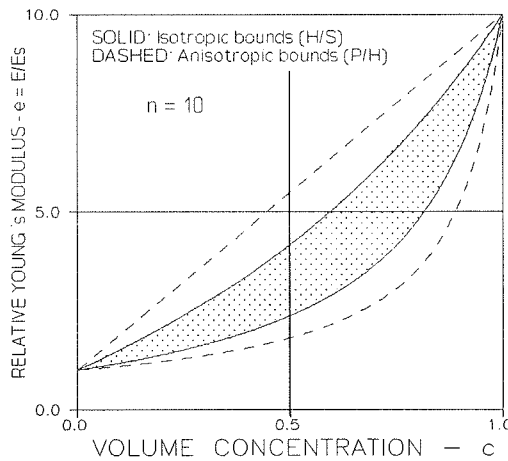
Figure 3.1. Shaded area is range of stiffness for isotropic composites.
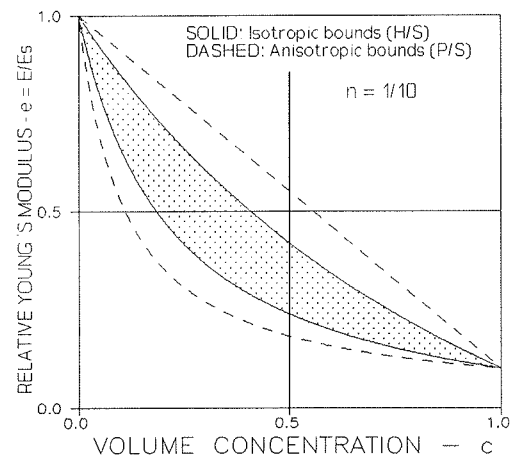
Figure 3.2. Shaded area is range of stiffness for isotropic composites.

3.1 Stiffness

Hill (5) has shown that the remarkably simple relations presented in Equations 3.3 exist between averages (by volume) of stresses, strains, and stiffness of homogene-

ous (not necessarily isotropic) composite materials consisting of homogeneous and isotropically elastic components.

$$
\begin{array}{ll}
\sigma_{kk} = (1 - c)\,\sigma_{Skk} + c\,\sigma_{Pkk} & \quad s_{ij} = (1 - c)\,s_{Sij} + c\,s_{Pij} \\
\varepsilon_{kk} = (1 - c)\,\varepsilon_{Skk} + c\,\varepsilon_{Pkk} & \quad e_{ij} = (1 - c)\,e_{Sij} + c\,e_{Pij} \\
\varepsilon_{Pkk} = \dfrac{\sigma_{Pkk}}{3K_P} \;\; ; \;\; \varepsilon_{Skk} = \dfrac{\sigma_{Skk}}{3K_S} & \quad e_{Pij} = \dfrac{s_{Pij}}{2G_P} \;\; ; \;\; e_{Sij} = \dfrac{s_{Sij}}{2G_S}
\end{array} \tag{3.3}
$$

The symbols used have the following meanings: σ_{kk} is volumetric stress, s_{ij} is deviatoric stress, ε_{kk} is volumetric strain, e_{ij} is deviatoric strain. K is bulk modulus, and G is shear modulus. As before, subscripts P and S indicate phase of composite. No subscripts P and S indicate overall (average) stresses and strains of composite.

The expressions in Equation 3.3 form the basis of the author's stiffness analysis of composites made in this monograph. They can be organized as follows,

$$
\varepsilon_{kk} = \frac{\sigma_{kk}}{3K_S} + c\sigma_{Pkk}\left[\frac{1}{3K_P} - \frac{1}{3K_S}\right] \;\; ; \;\; e_{ij} = \frac{s_{ij}}{2G_S} + cs_{Pij}\left[\frac{1}{2G_P} - \frac{1}{2G_S}\right] \tag{3.4}
$$

from which the stiffness of isotropic composites can be obtained introducing the overall isotropic stress-strain relations,

$$
\varepsilon_{kk} = \frac{\sigma_{kk}}{3K} \;\; ; \;\; e_{ij} = \frac{s_{ij}}{2G} \tag{3.5}
$$

where K and G are bulk modulus and shear modulus respectively of the composite.

The results are the following remarkably simple expressions which tell that composite stiffness can be predicted from knowing the average stress (or strain) in phase P.

$$
\begin{aligned}
k = \frac{K}{K_S} &= \left[1 + c\frac{1 - n_k}{n_k}\frac{\sigma_{Pkk}}{\sigma_{kk}}\right]^{-1} = 1 + c(n_k - 1)\frac{\varepsilon_{Pkk}}{\varepsilon_{kk}} \\
g = \frac{G}{G_S} &= \left[1 + c\frac{1 - n_g}{n_g}\frac{s_{Pij}}{s_{ij}}\right]^{-1} = 1 + c(n_g - 1)\frac{e_{Pij}}{e_{ij}}
\end{aligned} \tag{3.6}
$$

The symbols used, k $= K/K_S$ and g $= G/G_S$, are relative bulk modulus and relative shear modulus respectively. Bulk stiffness ratio is $n_k = K_P/K_S$. Shear stiffness ratio is $n_g = G_P/G_S$.

Remarks: It is emphasized that any expression mentioned above and subsequent expressions derived from them are exact, meaning for example, that exact stiffness are predicted if the exact phase P stresses are known. It is furthermore noticed that stiffness (K_C, G_C) of cubical composites, with stress strain planes coinciding with planes of elastic symmetry are also described by Equation 3.6. We only have to replace (k,g) with ($k_C = K_C/K_S$, $g_C = G_C/G_S$).

It is interesting to notice that the simple anisotropic P/H bounds, formally are described by Equation 3.6 introducing a homogeneous stress condition ($\sigma_P/\sigma = 1$) and a homogeneous strain condition ($\epsilon_P/\epsilon = 1$) respectively.

Curiosum: The following expression (to be used in Appendix B) can also be derived from Equation 3.3. It applies also for both isotropic composites and cubical composites.

$$e = \frac{E}{E_s} = \left[1 + c\frac{1 - n}{n}\frac{S_{Pii}}{\sigma_{ii}} \right]^{-1} \quad with \quad n = \frac{E_P}{E_s} \quad and$$

$$S_{Pii} = \frac{1 + \nu_P - n(1 + \nu_s)}{1 - n}\sigma_{Pii} - \frac{\nu_P - n\nu_s}{1 - n}\sigma_{Pkk} \quad (ii = 11,22,33) \tag{3.7}$$

3.1.1 Dilute suspension

At very low phase P concentration (dilute suspension) where there is no interaction between phase elements Equation 3.6 can be written as follows where supscript o indicates stress at vanishing concentration c.

$$\frac{1}{k} = 1 + c\frac{1 - n_k}{n_k}\frac{\sigma^o_{Pkk}}{\sigma_{kk}} \quad ; \quad \frac{1}{g} = 1 + c\frac{1 - n_g}{n_g}\frac{s^o_{Pij}}{s_{ij}} \tag{3.8}$$

Example: From the Goodier's and Dewey's analysis (50,51) of a spherical particle in an infinite matrix we have

$$\frac{\sigma^o_{Pkk}}{\sigma_{kk}} = \frac{n_k(1 + \kappa_s)}{n_k + \kappa_s} \quad \left(= f_k(E_P, E_s, \nu_p, \nu_s)\right)$$

$$\frac{s^o_{Pij}}{s_{ij}} = \frac{n_g(1 + \gamma_s)}{n_g + \gamma_s} \quad \left(= f_g(E_P, E_s, \nu_p, \nu_s)\right) \tag{3.9}$$

where κ_s, γ_s are Poisson parameters defined in Appendix A and f_k, f_g are so-called stress functions. The stiffness of a dilute suspension with spherical particles is now predicted as follows from Equation 3.8.

$$\frac{1}{k} = 1 + \frac{(1 + \kappa_s)(1 - n_k)}{n_k + \kappa_s}c \quad ; \quad \frac{1}{g} = 1 + \frac{(1 + \gamma_s)(1 - n_g)}{n_g + \gamma_s}c \qquad (3.10)$$

3.2 Stress

Equation 3.6 can be used as follows for stress prediction when stiffness are known.

$$\frac{\sigma_{Pkk}}{\sigma_{kk}} = \frac{1/k - 1}{c(1/n_k - 1)} \quad ; \quad \frac{\sigma_{Skk}}{\sigma_{kk}} = \frac{1/n_k - 1/k}{(1 - c)(1/n_k - 1)} \qquad (3.11)$$

$$\frac{s_{Pij}}{s_{ij}} = \frac{1/g - 1}{c(1/n_g - 1)} \quad ; \quad \frac{s_{Sij}}{s_{ij}} = \frac{1/n_g - 1/g}{(1 - c)(1/n_g - 1)} \qquad (3.12)$$

Stresses in general (σ_{ij}) are determined from Appendix A combining these expressions. Stress prediction is exact if exact stiffness properties are known.

3.3 Composite stiffness estimated by SCS
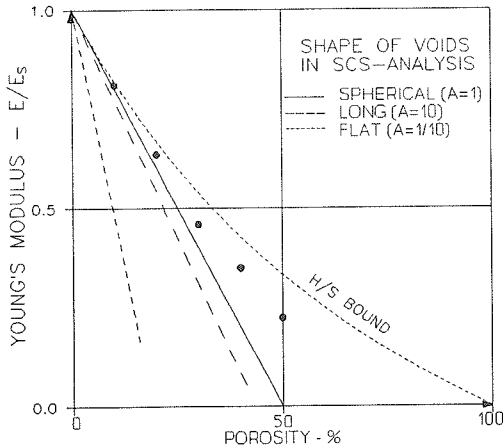
Figure 3.3. Stiffness of porous sintered Aluminum. SCS used with voids of various shapes. Aspect ratio A is length of particle relative to its diameter.

The stress functions, f_k and f_g, defined in Equation 3.9 can be used to estimate phase P stress in general if the phase S properties are replaced with the composite properties (not yet known). This method of generalizing a dilute suspension stress to apply at any phase P concentration is the basis of so-called SCS-estimates of the behavior of composite materials (Self Consistency Scheme).

A new numerical SCS-analysis is developed in Appendix C at the end of this monograph. It is based on Equation 3.6 with phase P stresses introduced by numerically determined SCS-estimates. Composites are considered with ellipsoidal particles of general shapes (including

28

mixtures). Results of applying the SCS-analysis on stiffness of porous materials with voids of various shapes are presented in Figure 3.3.

Closed analytical SCS-solutions for various aspects of the mechanical/physical behavior of composites with special uni-shaped particles have previously been presented in the literature: Spherical particles were considered by Landauer, Böttcher, and Budiansky in (52,53,13), extremely thin discs were considered by Bruggeman in (54), and extremely long fibres were considered by Van Beek in (55).

Obviously a SCS-solution is accurate at low phase P concentrations (dilute suspensions). In Figure 3.3 this feature is observed by noticing that the SCS-solution for a spherical pore system coincides with the H/S bound at low concentrations, (it is subsequently shown in this monograph that the stiffness of porous CSA_P composites is very well predicted with the upper H/S-bound).

The approximate nature of stiffness estimates by SCS at higher phase P concentrations must be emphasized. In general the SCS-analysis works on self-defined geometries the real shapes of which can, at the present time, only be guessed upon. It is demonstrated in Appendix C (as indicated in Figure 3.3) that any deviation from spherical pores will cause lower SCS stiffness predictions than the prediction obtained with spherical pores. Thus, the experimental data (22) in Figure 3.3 cannot be better described by SCS than by assuming that the pores are spherical voids.

Remarks: It is obvious that the success of the SCS-method to predict stiffness of composites in practice depends on how much the geometry in practice resembles the self-defined geometry made by the SCS-analysis. Obviously the real pore system of the porous aluminum considered in Figure 3.3 has a geometry which disagrees with the SCS-geometry at higher porosities. Thus, SCS-methods cannot in general be used as a "tool" in the research on composite materials behavior versus composite geometry. This statement applies also for modified SCS-methods where "new particles" are defined as the original ones surrounded by some matrix (eg. 56).

4. Composite stress and geometry

It has been shown in Chapter 3, Equation 3.6, that any stiffness modulus of isotropic composite materials can be predicted if stresses are known for one of the constituent phases. Therefore, the analysis of stiffness versus phase geometry is basically an analysis of internal stresses as a function of phase geometry.

In this chapter a method is developed by which consistent estimates can be given on stress versus geometry as classified in Chapter 2 for various types of composites. The term, consistent, means that the stress estimates presented agree with exact quantities whenever such are known from the literature on composite materials - and that the stiffness predictions subsequently made in Chapter 5 do not violate the H/S bounds previously referred to.

4.1 Volumetric stress
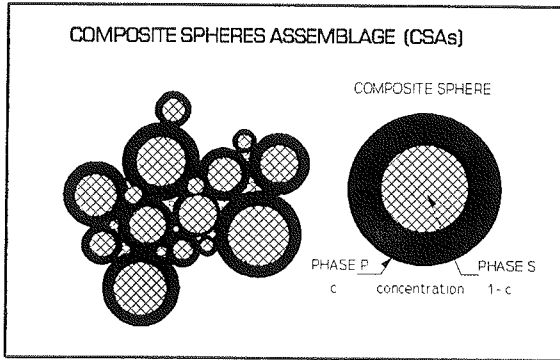
Figure 4.1. Composite Spheres Assemblage with phase S particles of concentration 1-c (CSAₛ).

As previously stated, the most extreme, opposite phase geometries to think of when isotropic composites are considered are defined by the CSA_P geometry illustrated in Figure 2.8 and the CSA_S geometry illustrated in Figure 4.1. In this chapter this statement forms the basis of establishing consistent stress solutions for any isotropic composite.

4.1.1 CSA-composites

The phase P stress in a CSA_P-material can easily be derived from Hashin (4), Goodier (50), or Sokolnikoff (57). The result can be written as shown in the first expression in Equation 4.1. The second expression is the phase S stress derived by the equilibrium expression in Equation 3.3. The Poisson parameter κ_S is a function of the Poisson's ratio ν_S as explained in Appendix A.

$$\frac{\sigma_{Pkk}}{\sigma_{kk}} = \frac{n_k(1 + \kappa_s)}{n_k + \kappa_s[1 + (n_k - 1)c]}$$
$$\frac{\sigma_{Skk}}{\sigma_{kk}} = \frac{n_k + \kappa_s}{n_k + \kappa_s[1 + (n_k - 1)c]} \qquad CSA_P \ geometry \qquad (4.1)$$

The stress state of a CSA$_S$ material can be obtained from the CSA$_P$ stresses in Equation 4.1 by subscript interchange, $(S,c,n_k,\kappa_S) \Leftrightarrow (P,1\text{-}c,1/n_k,\kappa_P)$. The results are presented in Equation 4.2.

$$
\begin{aligned}
\frac{\sigma_{Pkk}}{\sigma_{kk}} &= \frac{1 + n_k\kappa_P}{1 + \kappa_P[1 + (n_k - 1)c]} \\[2mm]
\frac{\sigma_{Skk}}{\sigma_{kk}} &= \frac{1 + \kappa_P}{1 + \kappa_P[1 + (n_k - 1)c]}
\end{aligned}
\qquad CSA_s \ \ geometry
\tag{4.2}
$$

It is observed, see (24), that Equations 4.1 and 4.2 can be given a common formulation as shown in Equation 4.3 where the parameter $\theta_k = \kappa_S$ when phase P has the geometry of spheres and where $\theta_k = N_k\kappa_S$ when the phase P geometry is that of spherical shells. The modified stiffness ratio N_k introduced has the meaning given in Equation 4.4 with Poisson parameters (κ) introduced from Appendix A.

$$
\frac{\sigma_{Pkk}}{\sigma_{kk}} = \frac{n_k(1 + \theta_k)}{n_k + \theta_k[1 + c(n_k - 1)]} \quad ; \quad \frac{\sigma_{Skk}}{\sigma_{kk}} = \frac{n_k + \theta_k}{n_k + \theta_k[1 + c(n_k - 1)]}
\tag{4.3}
$$

$$
N_k = n_k\frac{\kappa_P}{\kappa_S} = n_g \qquad Modified\ \ stiffness\ \ ratio
\tag{4.4}
$$

4.1.2 Any composite - geometry function
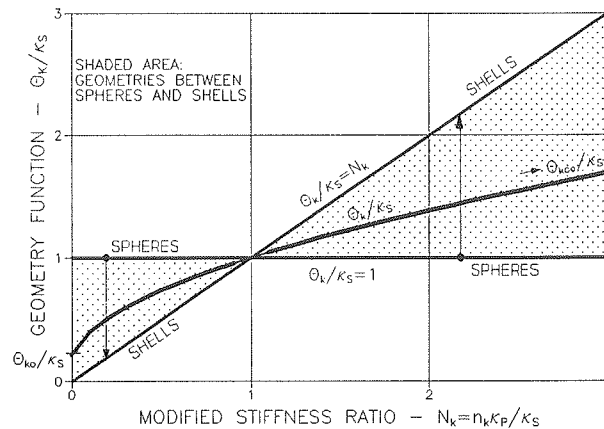
Figure 4.2. Influence of phase P geometry on geometry function.

The quantities $\theta_k = \kappa_S$ and $\theta_k = N_k\kappa_S$ express the boundaries of an area, described in Equation 4.5 and illustrated in Figure 4.2, where general geometry functions θ_k are found which generalize Equation 4.3 to predict stresses in composites with any isotropic geometry following the arrows in Figure 4.2 between the geometries of CSA$_P$ and CSA$_S$.

$$
N_k \le \frac{\theta_k}{\kappa_S} \le 1 \quad when\ N_k \le 1 \quad and \quad N_k \ge \frac{\theta_k}{\kappa_S} \ge 1 \quad when\ N_k > 1
\tag{4.5}
$$

31

Each isotropic composite geometry is represented in Figure 4.2 by its own geometry function θ_k. Because composites in general change geometry with volume concentrations, this statement is similar to saying that any volume concentration will have its own geo-function. Exceptions are geometry types which are independent of concentrations such as in CSA composites. In these cases all volume concentrations have the same geo-function.

Remark: It follows from Equation 4.3 and Figure 4.2 that the volumetric stresses are independent of geometry when $n_k = 1$ and when $N_k = 1$ respectively. The latter observation is of special interest: It tells (because $N_k = n_s$) that volumetric stresses are independent of geometry when shear moduli of the constituent phases are the same. The consequence on bulk stiffness of this observation is discussed in Section 5.3.2.

4.1.3 Geometry function and shape function

The stress solutions predicted by Equation 4.3 with θ_k from Equation 4.5 and Figure 4.2 are consistent with the concept of composite materials being isotropic. At this time we do not know more about stress. Stress prediction still has to be related to type of composite as classified in Chapter 2.

As a first step to establish such relationship we observe that θ_k obviously is a function of not only n_k, ν_P, ν_S, but also of the more detailed geometry of phase P and phase S. We consider these geometries by so-called shape functions $\mu_{Pk} = \mu_{Pk}(c)$ and $\mu_{Sk} = \mu_{Sk}(c)$ respectively such that a geometry function (geo-function) can be described by the former expression in Equation 4.6.

$$\theta_k = \theta_k(n_k, \nu_P, \nu_S, \mu_{Pk}, \mu_{Sk}) = n_k\theta_k(1/n_k, \nu_S, \nu_P, \mu_{Sk}, \mu_{Pk}) \qquad (4.6)$$

Invariance with respect to phase numbering is ensured by the latter expression in Equation 4.6 which is obtained from Equation 4.3 claiming that the first expression (σ_P) must equal the latter expression (σ_S) when subscripts P and S are interchanged (including c $\leftrightarrow$ 1-c).

The geometry function just defined is further restricted when specific composites are considered as they are classified in Chapter 2 according to their critical concentrations c_P and c_S. The influence of composite type on the geometry function is subsequently determined by looking at a composite where phase P can be extremely stiff ($n_k = \infty$) or it can be extremely soft ($n_k = 0$). The following expressions, derived from Equation 4.3 (with some help from Equation 3.3 with $K_P = n_kK_s$), tell about stress and strain in these two cases. θ_{ko} and $\theta_{k\infty}$ are limiting values of θ_k

for $n_k \to 0$ and $n_k \to \infty$ respectively. $M = \lim(\theta_k/n_k)$ for $n_k \to \infty$ has a finite value between 0 and κ_P, see Equation 4.5 with N_k from Equation 4.4.

$$
\begin{array}{ll}
\textit{Very soft P: } n_k = 0 & \Rightarrow \quad \varepsilon_{Pkk} = \dfrac{\sigma_{kk}}{3K_S} \dfrac{1 + \theta_{ko}}{\theta_{ko}(1 - c)} \\[3mm]
\textit{Very stiff P: } n_k = \infty & \Rightarrow \quad \sigma_{Skk} = \sigma_{kk} \dfrac{1 + M}{1 + M(1-c) + c\theta_{k\infty}}
\end{array}
\qquad (4.7)
$$
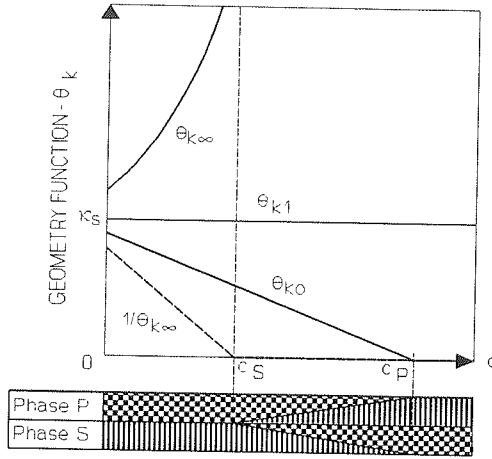
Figure 4.3. The variation in principles of θ for two-phase materials with gradually changing phase geometry.
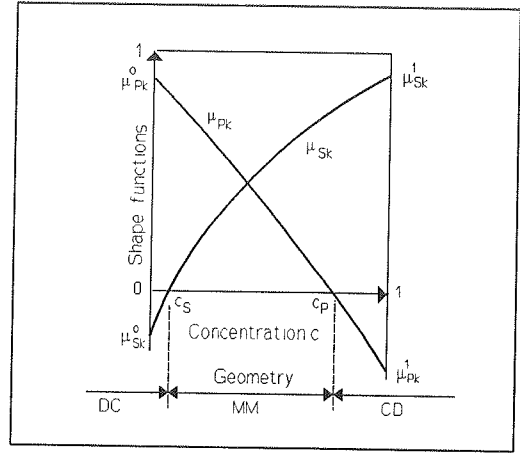
Figure 4.4. Shape functions μ_{Pk} and μ_{Sk}, both ≤ 1.

Equation 4.7 can be used as follows to 'calibrate' the geometry function to become consistent with the classification of composites made in Chapter 2. We simply compare this expression with the following general deductions which can be made from considering the two types of composites considered ($n_k \to 0$ and $n_k \to \infty$):

- Phase S is completely dissolved by phase P in $c \geq c_P$. This means that strain of a very soft phase P becomes infinite in $c \geq c_P$. The strain is finite in $c < c_P$.

- Phase P starts becoming continuous at $c = c_S$. This means that phase S stress becomes 0 in $c \geq c_S$ where phase P has become an extremely stiff skeleton. Stress is finite in $c < c_S$.

Equation 4.7 complies with these deductions only if θ_{ko} and $\theta_{k\infty}$ vary in principles as described in Equation 4.8 and illustrated in Figure 4.3. Also shown in Figure 4.3 is $\theta_{k1} \equiv \kappa_S$ which is θ_k from Figure 4.2 at $N_k = 1$.

$$
\theta_{ko} = \left[\begin{array}{ll} \textit{finite} & ; \ c < c_P \\ \equiv 0 & ; \ c \geq c_P \end{array} \right. ; \quad \frac{1}{\theta_{k\infty}} = \left[\begin{array}{ll} \textit{finite} & ; \ c < c_S \\ \equiv 0 & ; \ c \geq c_S \end{array} \right.
\qquad (4.8)
$$

A number of θ_k-expressions yield the conditions required in Equations 4.5, 4.6, and 4.8. The relatively simple expression presented in Equation 4.9 is a slightly modified version of an expression suggested in (24),

$$\theta_k = \frac{\kappa_S}{2}\left[\mu_{Pk} + \mu_{Sk}N_k + \sqrt{(\mu_{Pk} + \mu_{Sk}N_k)^2 + 4N_k(1 - \mu_{Pk} - \mu_{Sk})}\right] \qquad (4.9)$$

where the influence of geometry is decided by the shape functions $\mu_{Pk}(c)$ and $\mu_{Sk}(c)$ varying with phase geometry as outlined in Equation 4.10a and Figure 4.4.

$$\begin{array}{llll}
1 \geq \mu_{Pk} \geq 0 & at\ c \leq c_P & ; \quad \mu_{Pk} < 0 & at\ c > c_P \\
1 \geq \mu_{Sk} \geq 0 & at\ c \geq c_S & ; \quad \mu_{Sk} < 0 & at\ c < c_S
\end{array} \qquad (4.10a)$$

4.1.4 Shape functions - a closer look

It is noticed from Equation 4.10a and Figure 4.4 that DC, MM, and CD composite geometries are described by shape functions of magnitudes $(\mu_{Pk}, \mu_{Sk}) = (+,-)$, $(\mu_{Pk}, \mu_{Sk}) = (+,+)$, and $(\mu_{Pk}, \mu_{Sk}) = (-,+)$ respectively. These properties of shape functions represent the basic geometrical "signals" sent to Equation 4.3, through Equation 4.9, that a special composite is considered.

Shape factors

Shape function values of special interest are the so-called shape factors, $\mu_{Pk}^{\,o}, \mu_{Sk}^{\,o} = \mu_{Pk}(0), \mu_{Sk}(0)$ quantifying the composite geometry of a P-S mixture with a dilute (vanishing) amount of phase P. In the subsequent text the term 'shape factor' is also used for $\mu_{Pk}^{\,1}, \mu_{Sk}^{\,1} = \mu_{Pk}(1), \mu_{Sk}(1)$. An important principal difference between the two set of shape factors is emphasized by sharpening (re-phrasing) the terms of definition: A composite geometry is quantified by $\mu_{Pk}^{\,o}, \mu_{Sk}^{\,o}$ at vanishing amounts of phase P, while it is quantified by $\mu_{Pk}^{\,1}, \mu_{Sk}^{\,1}$ at overwhelming amounts of phase P.

Special shape functions

CSA-geometries: It is immediately observed that the special DC and CD shape functions presented in Equation 4.10b apply for the CSA_P and CSA_S composites.

$$\begin{array}{lll}
\mu_{Pk} \equiv 1\ and\ \mu_{Sk} \leq 0\ with\ c_S \to \infty & \Rightarrow & \theta_k = \kappa_S \quad (CSA_P\ geometry) \\
\mu_{Sk} \equiv 1\ and\ \mu_{Pk} \leq 0\ with\ c_P \to -\infty & \Rightarrow & \theta_k = \kappa_S N_S \quad (CSA_S\ geometry)
\end{array} \qquad (4.10b)$$

Crumbled foils: Let us think of a P-element transforming its shape from being a sphere to being the opposite, namely a spherical shell (see Figures 2.8 and 4.1).

34
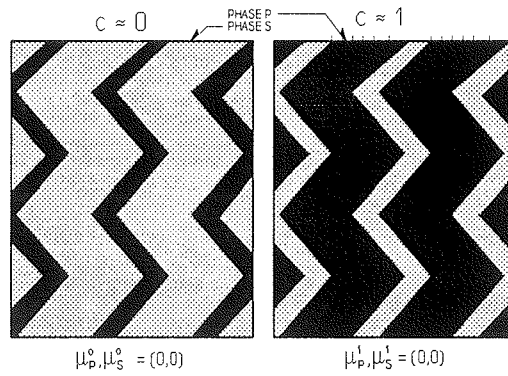
Figure 4.5. Crude model of crumbled foils composite. $\mu_P = \mu_S \equiv 0$ at any c.

It is very plausible that the 'mean geometry' in this transformation is a 'three dimensional Ply-wood' structure with both phases (P and S) having the geometry of crumbled foils, see Figure 4.5.

The following hypothesis is suggested for crumbled foils composites: Such materials will have shape functions as presented in Equation 4.10c with geo-functions being 'means' of geo-functions applying for the CSA composites presented in Equation 4.10b.

$$\mu_{Pk} = 0 \ and \ \mu_{Sk} = 0 \ \Rightarrow \ \theta_k = \kappa_s\sqrt{N_k} \quad \left[\begin{array}{l} Crumbled \ foils \ geometry \\ = \sqrt{CSA_p * CSA_s} \end{array} \right. \quad (4.10c)$$

At several occasions the hypothetical crumbled foils geometry is discussed in more details in subsequent sections of this monograph.

Outline of shape function graphs

In Chapter 2 it has been explained that composites considered in this monograph are such where geometries change along 'stations' between the composite being
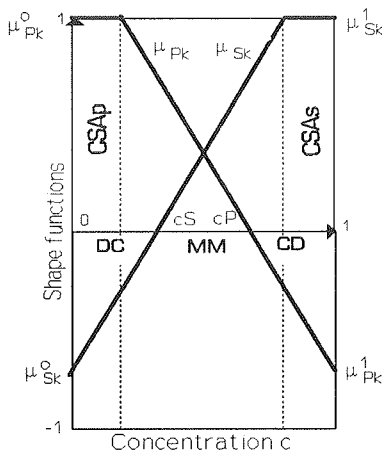
Figure 4.6. Shape functions for an ideal DC-CD composite.

a CSA_P material and a CSA_S material. Possible shape functions are outlined in Figure 4.6 for a composite which starts up as a CSA_P material at low concentrations and ends as a CSA_S material at high concentrations. A processing technique has been used which can keep a CSA_P structure up to the first 'dashed concentration' and then a less ideal DC structure up to the critical concentration c_S. In a similar way the technique used can keep a CSA_S structure after the second 'dashed concentration' with a less ideal CD structure from the critical concentration c_P. In the concentration area between the critical concentrations c_S and c_P both phases P and S appear with mixed geometries.

The principles of the above description of shape functions are the ones subsequently used in Chapter 7 to describe composite geometries in general.

Remark: Theoretically the simplified scheme of geometry classification used in this monograph (Figure 2.2) requires that the concentration at which μ_s becomes 1 is greater than c_p - and that the concentration at which μ_p becomes 1 is smaller than c_s. When approximate shape functions are subsequently constructed in this monograph we do not consider these conditions very seriously. We will just think of shape functions which are slightly less than 1 until the requirements mentioned are fulfilled. Numerical calculations show that the consequences of doing so are insignificant.

Interaction

In composite theory the term "no interaction between phase elements" means that a stress-strain analysis of a phase element can be made disregarding the presence of "neighbouring" elements. The CSA_p material subjected to volumetric load is a well-known example of composites with no interaction between particles.

Geometries involving no interaction between phase elements are described by constant shape functions in the geo-function, Equation 4.9. The geometrical influence on stress is absent when shape functions are constants.

The presence of interaction (variable shape functions) cannot be clearly demonstrated as its effect is mixed up with the effects of geometrical changes. It can, however, be shown by FEM-analysis that interaction also depends on loading mode, see Figure 9.2 in Chapter 9. A volumetric analysis and a deviatoric analysis was made on exactly the same particulate composite (TROC). The first analysis was clearly not influenced very much by interaction. The second analysis was.

In the present study the term "interaction" is used quite practically. The influence of geometry in general is considered as the joint influence of load induced interaction and geometrically induced interaction. Complete interaction is obtained at real critical concentrations (in c = 0-1) where geometries change from particulate to mixed. Geometrically induced interaction is anticipated to be overriding when critical concentrations are real. Load induced interaction is overriding when critical concentrations are non-real (outside c = 0-1).

4.1.5 Summary

A geo-function is presented in Equation 4.9 by which volumetric stresses for any composite geometry can be consistently predicted by Equation 4.3. Specific composite geometries and the variations of such with respect to volume concentration

c are considered by so-called shape functions outlined in Figure 4.4 and quantified in the subsequent Chapter 7.

Geo-functions depend on phase geometry and stiffness properties (as in N_k). Volume concentrations are involved only to tell about geometry at these concentrations. In a composite with variable geometry this means that each volume concentration has its own geometry function. When the class of composite geometry considered (DC, MM, or CD) does not change with c, then geo-functions are expected to keep relatively close in Figure 4.2. They are extremely close (coinciding) when composites with no interaction between phase elements are considered such as CSA_P and CSA_S materials with $\theta_k \equiv 1$ and $\theta_k \equiv n$ respectively ($\nu_P = \nu_S = 0.2$).

Finally, a crumbled foils geometry (3-dimensional Ply-wood structure) is suggested which represents a plausible transition (average) geometry of phase P changing organically from being spheres in CSA_P to being spherical shells in CSA_S.

4.2 Deviatoric stress

The phase P deviatoric stress in a CSA_P composite is postulated to be the following modified copy of Equation 4.1.

$$\frac{S_{Pij}}{S_{ij}} = \frac{n_g(1 + \gamma_s)}{n_g + \gamma_s[1 + (n_g - 1)c]} \tag{4.11}$$

Equation 4.1 is exact. Equation 4.11, however, is an approximation. No such simple, exact, and closed form relation is known from the literature. The approximation, however, is very good. This has been justified by a FEM stiffness analysis of particulate composites presented in (24). The approximation becomes exact at low phase P concentrations (c → 0) where the following solution has been presented (50,51,58).

$$\frac{S_{Pij}}{S_{ij}} = \frac{n_g(1 + \gamma_s)}{n_g + \gamma_s} \tag{4.12}$$

Remark: We emphasize that Equation 4.11 is considered exact in subsequent deductions with respect to the behavior of composite materials. Such procedure is strongly supported by some results obtained by Christoffersen (6) and Levin (7) in their analysis of materials reinforced with randomly distributed spherical particles. Predicted shear moduli in these references are the same as can be predicted by the present theory (Chapter 5) with Equation 4.11 considered exact.

4.2.1 Stress and geometry

Thanks to Equation 4.11 the deviatoric stresses in an isotropic composite can be considered just as volumetric stresses were considered in Section 4.1. In fact, the results subsequently presented in the following summary, Section 4.3, are complete duplicates of results obtained in Section 4.1 with bulk properties replaced with shear properties. This means that bulk stiffness ratio n_k is replaced by shear stiffness ratio $n_g = G_P/G_S$, bulk Poisson parameters κ_S, κ_P are replaced by shear Poisson parameters γ_S, γ_P (see Appendix A), and bulk geo-function θ_k is replaced by shear geo-function θ_g. The modified bulk stiffness ratio N_k is at the same time replaced with the modified shear stiffness ratio $N_g = n_g \gamma_P/\gamma_S$.

Deviatoric shape functions

Shape functions μ_{Pk} and μ_{Sk} are replaced with their deviatoric counterparts μ_{Pg} and μ_{Sg} determined in a similar way as μ_{Pk}, μ_{Sk} are determined in Chapter 7. Deviatoric shape factors are $\mu_{Pg}{}^{\circ} = \mu_{Pg}(0)$, $\mu_{Pg}{}^{1} = \mu_{Pg}(1)$, $\mu_{Sg}{}^{\circ} = \mu_{Sg}(0)$, and $\mu_{Sg}{}^{1} = \mu_{Sg}(1)$.

Real critical concentrations c_P and c_S are invariable with respect to loading mode. Deviatoric interaction is considered in a similar way as volumetric interaction has been considered in Section 4.1.4.

4.3 Summary

A summary of the results obtained in this chapter is presented below. Expressions are added which apply especially for porous materials (n = 0) and for composites with extremely stiff pore systems (n = ∞). We emphasize, once again, that the stress expressions are global. They apply for any geometry encountered. Geometrical information on specific composites are "hidden" in the shape functions μ_{Pk}, μ_{Sk}, μ_{Pg}, and μ_{Sg} considered in details in Chapter 7.

4.3.1 Stress

$$\frac{\sigma_{Pkk}}{\sigma_{kk}} = \frac{n_k(1 + \theta_k)}{n_k + \theta_k[1 + c(n_k - 1)]} \quad ; \quad \frac{\sigma_{Skk}}{\sigma_{kk}} = \frac{n_k + \theta_k}{n_k + \theta_k[1 + c(n_k - 1)]}$$

$$\frac{s_{Pij}}{s_{ij}} = \frac{n_g(1 + \theta_g)}{n_g + \theta_g[1 + c(n_g - 1)]} \quad ; \quad \frac{s_{Sij}}{s_{ij}} = \frac{n_g + \theta_g}{n_g + \theta_g[1 + c(n_g - 1)]} \qquad (4.13)$$

4.3.2 Geo-function

$$\theta_k = \frac{\kappa_S}{2}\left[\mu_{Pk}+\mu_{Sk}N_k+\sqrt{(\mu_{Pk}+\mu_{Sk}N_k)^2+4N_k(1-\mu_{Pk}-\mu_{Sk})}\right] \quad ; \quad N_K = n_k\frac{\kappa_P}{\kappa_S} = n_g$$

$$\theta_g = \frac{\gamma_S}{2}\left[\mu_{Pg}+\mu_{Sg}N_g+\sqrt{(\mu_{Pg}+\mu_{Sg}N_g)^2+4N_g(1-\mu_{Pg}-\mu_{Sg})}\right] \quad ; \quad N_g = n_g\frac{\gamma_P}{\gamma_S}$$

$$(4.14)$$

Porous materials and stiff pore systems

The geo-functions have the values presented in Table 4.1 when porous materials (n = 0) and stiff pore systems (n = ∞) are considered. Also presented in this table are the geo-functions for such systems if they are dilute (c « 1).

Porous material		Stiff pore system		
$\theta_{ko} = \kappa_S\mu_{Pk}$	$c \leq c_P$	$\theta_{k\infty} = \kappa_S\dfrac{\mu_{Pk} + \mu_{Sk} - 1}{\mu_{Sk}}$	$c < c_S$	
$\theta_{ko} \equiv 0$	$c > c_P$	$\theta_{k\infty} \equiv \infty$	$c > c_S$	
$\theta_{go} = \gamma_S\mu_{Pg}$	$c \leq c_P$	$\theta_{g\infty} = \gamma_S\dfrac{\mu_{Pg} + \mu_{Sg} - 1}{\mu_{Sg}}$	$c < c_S$	
$\theta_{go} \equiv 0$	$c > c_P$	$\theta_{g\infty} \equiv \infty$	$c > c_S$	
Dilute porous		Dilute stiff		
$\theta_{ko}^o = \kappa_S\mu_{Pk}^o$	$c \ll 1$	$\theta_{k\infty}^o = \kappa_S\dfrac{\mu_{Pk}^o + \mu_{Sk}^o - 1}{\mu_{Sk}^o}$	$c \ll 1$	
$\theta_{go}^o = \gamma_S\mu_{Pg}^o$		$\theta_{g\infty}^o = \gamma_S\dfrac{\mu_{Pg}^o + \mu_{Sg}^o - 1}{\mu_{Sg}^o}$		

Table 4.1. Geo-functions for porous materials and stiff pore systems.

5. Composite stiffness and geometry

The statement previously made in Chapter 4, that the analysis of stiffness versus phase geometry is basically an analysis of internal stresses versus phase geometry, is made very concrete in this chapter: Composite stiffness is predicted by Equation 3.6 introducing stresses as they have just been summarized in Section 4.3. The results of this straight forward procedure are subsequently presented with only a few comments.

The stiffness expressions presented are global just as are the stress expressions introduced. Specific geometrical information are hidden in the shape functions μ to be considered in more details in Chapter 7.

5.1 Bulk modulus and shear modulus

In general bulk modulus and shear modulus are predicted as follows with geo-functions introduced from Equation 4.14.

$$k = \frac{n_k + \theta_k[1 + c(n_k - 1)]}{n_k + \theta_k - c(n_k - 1)} \quad ; \quad g = \frac{n_g + \theta_g[1 + c(n_g - 1)]}{n_g + \theta_g - c(n_g - 1)} \tag{5.1}$$

5.1.1 Porous materials and stiff pore systems

When porous materials (n = 0) and very stiff pore systems (n = ∞) are considered Equation 5.1 reduces as follows with geo-functions introduced from Table 4.1. It is noticed that $k_o = g_o \equiv 0$ are predicted at $c > c_P$ and that $1/k_\infty = 1/g_\infty \equiv 0$ are predicted at $c > c_S$.

$$\left.\begin{array}{ll} k_o = \dfrac{1 - c}{1 + c/\theta_{ko}} & ; \quad \dfrac{1}{k_\infty} = \dfrac{1 - c}{1 + c\theta_{k\infty}} \\[3mm] g_o = \dfrac{1 - c}{1 + c/\theta_{go}} & ; \quad \dfrac{1}{g_\infty} = \dfrac{1 - c}{1 + c\theta_{g\infty}} \end{array}\right\} \quad \begin{array}{l} porous\ material\ and \\ stiff\ pore\ system \end{array} \tag{5.2}$$

$$\left.\begin{array}{ll} k_o = 1 - \left[1 + \dfrac{1}{\theta^o_{ko}}\right]c & ; \quad \dfrac{1}{k_\infty} = 1 - \left(1 + \theta^o_{k\infty}\right)c \\[5mm] g_o = 1 - \left[1 + \dfrac{1}{\theta^o_{go}}\right]c & ; \quad \dfrac{1}{g_\infty} = 1 - \left(1 + \theta^o_{g\infty}\right)c \end{array}\right\} \quad \begin{array}{l} dilute\ porous \\ material\ and \\ dilute\ stiff \\ pore\ system \end{array} \tag{5.3}$$

5.2 Young's modulus and Poisson's ratio

The Young's modulus and Poisson's ratio are determined as follows (Appendix A) with bulk modulus and shear modulus introduced as just predicted.

$$e = \frac{3kg}{2(1 + \nu_s)k + (1 - 2\nu_s)g} \quad ; \quad \nu = \frac{(1 + \nu_s)k - (1 - 2\nu_s)g}{2(1 + \nu_s)k + (1 - 2\nu_s)g} \qquad (5.4)$$

5.3 Special composites and observations

We re-call that Equations 5.1 and 5.4 apply in general for composite stiffness. As previously mentioned, specific composites are considered introducing shape functions which specify and quantify the special type of composite geometry considered. At this point of the analysis our knowledge to shape functions versus type of composite is limited to what is outlined in Figure 5.1 which is a summary of information presented in Section 2.3 and Chapter 4 (Figure 4.4). Conclusive information on shape functions in general are presented in Chapter 7 for various types of composites. Important observations, however, on some special composites can be made already now.
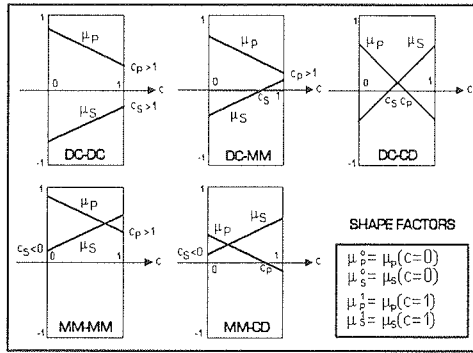
Figure 5.1. Composite types as related to critical concentrations. First two letters denote geometry at c = 0. Latter two letters denote geometry at c = 1.

5.3.1 CSA-composites

For two special composites we do not have to calculate the geo-functions. The CSA_P-composite and the CSA_S-composite have $\theta_k = \kappa_S$, $\theta_g = \gamma_S$ and $\theta_k = N_k\kappa_S$, $\theta_g = N_g\gamma_S$ respectively (see Figure 4.2). The stiffness moduli of the CSA-composites are then immediately obtained from Equation 5.1. We get

$$k = \frac{n_k + \kappa_S[1 + c(n_k - 1)]}{n_k + \kappa_S - c(n_k - 1)} \quad ; \quad g = \frac{n_g + \gamma_S[1 + c(n_g - 1)]}{n_g + \gamma_S - c(n_g - 1)} \quad CSA_P \qquad (5.5)$$

$$k = n_k\frac{1 + \kappa_P[1 + c(n_k - 1)]}{n_k(1 + \kappa_P) - c(n_k - 1)} \quad ; \quad g = n_g\frac{1 + \gamma_P[1 + c(n_g - 1)]}{n_g(1 + \gamma_P) - c(n_g - 1)} \quad CSA_S \qquad (5.6)$$

Hashin/Shtrikman's bounds

We re-call that these relations express the Hashin/Shtrikman's lower and upper bounds (3) respectively for isotropic composites with $n_{k,g} \geq 1$. When $n_{k,g} < 1$ the stiffness of CSA_P and CSA_S change their roles with respect to bounds.

5.3.2 Composites with special shear moduli

Geo-independent bulk moduli

It has previously been observed in Section 4.1.1 that the volumetric stress in a composite is independent of geometry when $n_g = 1$. With Equation 3.6 in mind this observation leads directly to the finding of Hill (5) previously referred to that the volumetric stiffness of a composite does not depend on geometry when shear moduli of the constituent phases are the same. This exact result can also be deduced from (59,60) where exact solutions are studied in the theory of composite materials.

Geo-independent shear moduli

It comes from the particles deviatoric stress in Equation 4.13 and the deviatoric counterpart to Figure 4.2 that deviatoric stresses are independent of geometry when $n_g \equiv 1$ and $N_g = (n_g \gamma_P / \gamma_S) \equiv 1$ respectively. Referring to Equation 3.6 the latter identity means that shear moduli of composite materials are independent of geometry when $n_g \equiv (4-5\nu_P)*(7-5\nu_S)/((4-5\nu_S)*(7-5\nu_P))$.

5.3.3 Paul/Hansen versus geo-functions

It is interesting to note that the homogeneous stress analysis made by Paul (1) and Hansen (2) to determine lower stiffness bounds for anisotropic composites is exactly reflected by the present theory introducing $\theta_k = \theta_g \equiv 0$ into the stiffness expression 5.1. In a similar way the homogeneous strain analysis made by Paul and Hansen to determine upper stiffness bounds for anisotropic composites is exactly reflected by the present theory introducing $\theta_k = \theta_g \equiv \infty$.

It might be worthwhile exploring the possibility of generalizing the concept of geo-functions to more general geometries. Apparently θ is, in a way, proportional to a "phase aspect ratio", $\underline{\theta}$, defined by phase "length" parallel to "load" divided by phase "thickness" perpendicular to load. The material models (parallel laminates) such defined by $\underline{\theta} = 0$ and $\underline{\theta} = \infty$ are exactly those used by Hansen (2) to establish the lower and upper bound respectively for stiffness of composites with unrestricted (un-known) phase geometries.

6. Composite eigenstrain/stress

An analysis is made in this chapter on composites subjected to eigenstress (self-equilibrated residual stresses) caused by different eigenstrains of the constituent components. Typical eigenstrains are hygro-thermal strains like shrinkage, swelling and thermal expansion which develop in solids without external forces and surface restraint. Another example of eigenstrain is strain developed during phase transformation such as in solidification of a liquid impregnant. The analysis is a modified version of similar analysis made by the author in (61,62,63).

6.1 Basics

The following expressions describe the volumetric stress-strain state in an isotropic composite subjected to eigenstrains just as Equation 3.3 describes the stress-strain state in a composite subjected to external load. Stresses and strains are volume averages (leaving no averages of deviatoric stress and deviatoric strain). Volumetric eigenstrains are denoted by $\lambda_{kk} = 3\lambda$ where λ are linear eigenstrains. Additional subscripts P, S, indicate phase P and phase S respectively. No additional subscript indicates composite.

$$
\begin{aligned}
0 &= c\sigma_{Pkk} + (1 - c)\sigma_{Skk} & \text{Equilibrium condition} \\
\lambda_{kk} &= c\varepsilon_{Pkk} + (1 - c)\varepsilon_{Skk} & \text{Compatibility condition} \\
\sigma_{Pkk} &= 3K_P(\varepsilon_{Pkk} - \lambda_{Pkk}) \\
\sigma_{Skk} &= 3K_S(\varepsilon_{Skk} - \lambda_{Skk})
\end{aligned} \Biggr\} \quad \text{Physical conditions}
\tag{6.1}
$$

The expressions in Equation 6.1 can be arranged as shown in Equation 6.2 to predict composite strain from a known phase P stress,

$$
\lambda_{kk} = \lambda_{Skk} + c\left[\Delta\lambda_{kk} + \frac{\sigma_{Pkk}}{3K_P}(1 - n_k)\right] \quad ; \quad \Delta\lambda_{kk} = \lambda_{Pkk} - \lambda_{Skk}
\tag{6.2}
$$

6.1.1 Simple composites

The eigenstrain of a CSA_P composite is predicted by Equation 6.2 introducing the phase P stress presented in Equation 6.3 which is a re-written version of an expression obtained by the author (64) in a stress analysis of CSA_P composites subjected to eigenstrain. The phase S stress also presented in Equation 6.3 is obtained from the equilibrium expression in Equation 6.1.

$$\left.\begin{array}{l} \dfrac{\sigma_{Pkk}}{3K_P} = -\Delta\lambda_{kk}\dfrac{\kappa_S(1-c)}{n_k + \kappa_S[1 + (n_k - 1)c]} \\[4mm] \dfrac{\sigma_{Skk}}{3K_P} = \Delta\lambda_{kk}\dfrac{\kappa_S c}{n_k + \kappa_S[1 + (n_k - 1)c]} \end{array}\right\} \quad (CSA_P \ geometry) \qquad (6.3)$$

The eigenstrain of a CSA_S composite is predicted by Equation 6.2 introducing the phase P stress as it develops in a CSA_S composite. With constant volume concentration this stress is expressed by Equation 6.4 obtained from Equation 6.3 interchanging the subscripts and replacing c with 1 - c.

$$\left.\begin{array}{l} \dfrac{\sigma_{Pkk}}{3K_P} = -\Delta\lambda_{kk}\dfrac{\kappa_P(1-c)}{1 + \kappa_P[1 + (n_k - 1)c]} \\[4mm] \dfrac{\sigma_{Skk}}{3K_P} = \Delta\lambda_{kk}\dfrac{\kappa_P c}{1 + \kappa_P[1 + (n_k - 1)c]} \end{array}\right\} \quad (CSA_S \ geometry) \qquad (6.4)$$

6.2 General geometry

It is noticed that Equations 6.3 and 6.4 can be given a common description as shown in the following Equation 6.5 where the parameter $\theta_k = \kappa_S$ when CSA_P composites are considered and where $\theta_k = N_k\kappa_S$ when CSA_S composites are considered. The quantities $\theta_k = \kappa_S$ and $\theta_k = N_k\kappa_S$ introduced express the boundaries of the area illustrated in Figure 4.2, where general geometry functions θ_k can be defined which generalize Equation 6.5 to predict eigenstresses in composites with any geometry (following the arrows in Figure 4.2 between the geometries of CSA_P and CSA_S). Consistency with other volumetric stress predictions presented in this monograph is obtained introducing the geo-function as it is expressed by former expression in Equation 4.14.

$$\left.\begin{array}{l} \dfrac{\sigma_{Pkk}}{3K_P} = -\Delta\lambda_{kk}\dfrac{\theta_k(1-c)}{n_k + \theta_k[1 + (n_k - 1)c]} \\[4mm] \dfrac{\sigma_{Skk}}{3K_P} = \Delta\lambda_{kk}\dfrac{\theta_k c}{n_k + \theta_k[1 + (n_k - 1)c]} \end{array}\right\} \quad general \ geometry \qquad (6.5)$$

6.2.1 Eigenstrain and eigenstress

Now, the eigenstrain/stress problem of a composite can be predicted in general by Equation 6.2 with phase P stress introduced from Equation 6.5. Doing so, and

eliminating the geo-function by the former expression in Equation 5.1, the remarkably simple results presented in Equations 6.6 and 6.7 are obtained between *linear eigenstrain* ($\lambda = \lambda_{kk}/3$) *and hydrostatic stress* ($\rho = \sigma_{kk}/3$).

$$\lambda = \lambda_S + \Delta\lambda \, \frac{1/k - 1}{1/n_k - 1} \quad ; \quad (\Delta\lambda = \lambda_P - \lambda_S) \qquad (6.6)$$

$$\rho_P = -3K_S\Delta\lambda \, \frac{c(1/n_k - 1) - (1/k - 1)}{c(1/n_k - 1)^2} \quad ; \quad \rho_S = -\frac{c}{1-c}\rho_P \qquad (6.7)$$

Equation 6.6 reduces as follows when eigenstrain is only experienced by phase S,

$$\frac{\lambda}{\lambda_S} = \frac{1/n_k - 1/k}{1/n_k - 1} \quad ; \quad (\lambda_P = 0) \qquad (6.8)$$

Remark: The eigenstress-strain phenomenon of composites has also been considered by other authors (9,65,66,67,68). Relative to these works the present study of the eigenstrain-stress problem has the advantage of reflecting the influence of any phase geometry and at the same time predict the internal composite stresses.

6.2.2 Pore pressure in porous materials

The linear composite strain ϵ ($= \epsilon_{kk}/3$) of a porous material with a hydrostatic pore pressure p ($= -\sigma_{Pkk}$) is developed as shown in Equation 6.9, first line, expressing that composite strain can be considered as the difference between strains obtained by considering the composite loaded 1) both externally and internally, and 2) only externally with the pore pressure p. (K and K_S denote bulk moduli of porous material and solid phase respectively).

The linear pore strain (ϵ_P) relation presented in Equation 6.9 is obtained combining the composite strain just developed with the compatibility condition also shown in Equation 6.9 of the problem considered.

$$\left.\begin{matrix} \varepsilon_{kk} = \dfrac{\sigma_{kk}}{3}\left[\dfrac{1}{K_S} - \dfrac{1}{K}\right] \\[2ex] \varepsilon_{kk} = c\varepsilon_{Pkk} + (1 - c)\varepsilon_{Skk} \end{matrix}\right\} \Rightarrow \left\{\begin{matrix} \varepsilon = \dfrac{p}{3}\left[\dfrac{1}{K} - \dfrac{1}{K_S}\right] & composit\ strain \\[2ex] \varepsilon_P = \dfrac{p}{3c}\left[\dfrac{1}{K} - \dfrac{1 + c}{K_S}\right] & pore\ strain \end{matrix}\right. \qquad (6.9)$$

These expressions have been used by the present author in (62) and in (69) to study the frost resistance and the phenomenon of drying shrinkage respectively

45

in porous materials. Quite recently the drying shrinkage phenomenon in porous glass has been studied in (70) using a method similar to the one used by the present author in (69).

7. Quantification of geometry

We re-call from Section 5.3 that phase P and phase S shape functions $\mu_{Pj} = \mu_{Pj}(c)$ and $\mu_{Sj} = \mu_{Sj}(c)$ (j = k,g) as outlined in Figure 7.1 consider the influence of phase geometries on internal composite stresses - and therefor also on composite stiffness. Thus, shape functions are the prime information needed in any analysis of composites. The behavior of natural composites can not be explained - and design of new materials can not be made without knowing these functions.
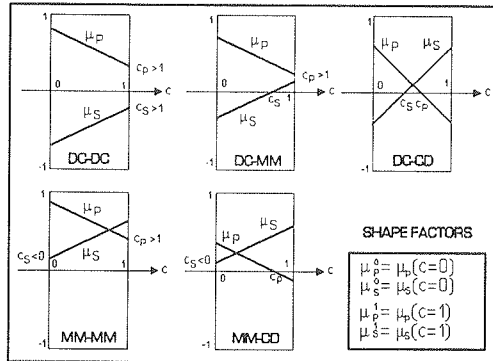
Figure 7.1. Composite types as related to critical concentrations. First two letters denote geometry at c = 0. Latter two letters denote geometry at c = 1.

In general it is not possible to determine shape functions analytically. The complexity of most real composite geometries is much too high and too un-predictable to think of 'accurately' determined shape functions. As demonstrated in this chapter it is, however, possible to estimate, in a relative simple way, shape functions of relevance for studies of the composites considered in this monograph.

The concepts used have already been touched upon in Section 4.1.3. We will construct shape functions from knowing about shape factors, which can be calculated or accurately estimated, and knowing (from processing technology) about critical concentrations at which, shape function values are zero. The basic geometrical models used for shape factor determination are outlined in the following. The final determination of shape functions is considered in Section 7.2

DC (and CD) composite: The basic materials model to be used extensively in the shape function analysis of DC and CD composites is the following: A dilute particulate composite with isotropically distributed particles of regular shapes as defined in Figure 7.2. Fibre length is l, cross-section is d*d, and aspect ratio is A = l/d. With particles of compact shapes, flat shapes (disc path), and long shapes (fibre path) this model can be considered as a reasonable working model with A = 1, A < 1, and A > 1 respectively.

MM composite: The particulate composites model presented above cannot be used for the analysis of shape factors of MM composites. Results from FEM analysis have to be used. One of the FEM models applied for this purpose is an isotropic mixture of cubic grid-composites as illustrated in Figure 7.3.

Cylindrical inclusison with
Aspect ratio: A = ℓ/d

Fibres have   A > 1
Compacts have A = 1
Discs have   A < 1
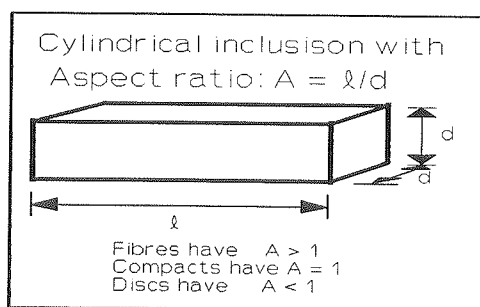
Figure 7.2. Cylindrical inclusions are fibres, compacts, and discs of ellipsoidal shapes enveloped as shown.

CROSS-COMPOSITE
illustrated at c = 0.5

P as agglomerated long fibres
in S-matrix at c = 0:
$\mu_p^0, \mu_s^0 = (0.75, 0.25)$

P as matrix for agglomerated
long S-fibres at c = 1:
$\mu_p^1, \mu_s^1 = (0.25, 0.75)$
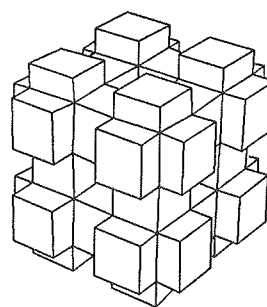
Figure 7.3. FEM-model used for shape factor analysis of MM-composites.

In principles, a third model is needed to describe the transition between DC and MM geometries. The strict cylindrical inclusions model is unable to describe the 'organic' shapes considered in this monograph. According to Appendix G, however, this discrepancy is effectively compensated for by the geo-function, θ, only by re-interpreting aspect ratios according to the following:

Long shapes (A > 4) represent fibre particles preparing to serve as an enveloping matrix phase. Flat shapes (A < 1/4) represent disc particles preparing to serve as an enveloping matrix phase. For intermediate particle shapes ($\approx 1/4 < A < \approx 4$), no reinterpretations of particles have to be introduced. The rate of 'preparing to become continuous' is such that the results of an analysis of a composite with organic particles approach the results of a counterpart analysis of a composite with strict particles - when extreme stiffness ratios are approached (n → 0 or n → ∞).

Thus, the determination of shape factors and shape functions proceeds on the basis of the two geometrical models explained above. The transition model is automatically taken care of just by shape re-interpretation as just explained.

Remark: We notice that "preparing to become continuous" shapes are probably more relevant in practice than strict shapes. It is very likely that interference between long and thin particles will form these particles to appear organically.

7.1 Shape factors[2]

7.1.1 DC-composites

The stiffness expression in Equations 3.8 for dilute suspensions is the basis of the present analysis. At extreme stiffness ratios (n = 0 and ∞) this equation can be written as follows,

$$
\left. \begin{array}{l} k_o = 1 - \left\{ 1 + \dfrac{1}{m_{ko}} \right\} c \\[3mm] g_o = 1 - \left\{ 1 + \dfrac{1}{m_{go}} \right\} c \end{array} \right\} n = 0 \quad ; \quad \left. \begin{array}{l} \dfrac{1}{k_\infty} = 1 - \left\{ 1 + \dfrac{1}{m_{k\infty}} \right\} c \\[3mm] \dfrac{1}{g_\infty} = 1 - \left\{ 1 + \dfrac{1}{m_{g\infty}} \right\} c \end{array} \right\} n = \infty \qquad (7.1)
$$

with so-called *shape parameters* expressed by

$$
\begin{array}{ll} \dfrac{1}{m_{ko}} = \lim_{n_r \to 0} \left[\dfrac{1 - n_k}{n_k} \dfrac{\sigma^o_{Pkk}}{\sigma_{kk}} - 1 \right] & ; \quad \dfrac{1}{m_{k\infty}} = -\lim_{n_r \to \infty} \left[\dfrac{1 - n_k}{n_k} \dfrac{\sigma^o_{Pkk}}{\sigma_{kk}} + 1 \right] \\[5mm] \dfrac{1}{m_{go}} = \lim_{n_r \to 0} \left[\dfrac{1 - n_g}{n_g} \dfrac{S^o_{Pij}}{S_{ij}} - 1 \right] & ; \quad \dfrac{1}{m_{g\infty}} = -\lim_{n_r \to \infty} \left[\dfrac{1 - n_g}{n_g} \dfrac{S^o_{Pij}}{S_{ij}} + 1 \right] \end{array} \qquad (7.2)
$$

Accurate shape parameters, $(m_{ko}, m_{go}) = (\kappa_S, \gamma_S)$ and $(m_{k\infty}, m_{g\infty}) = (1/\kappa_S, 1/\gamma_S)$, for spherical particles (A = 1) are easily obtained from Equation 7.2 introducing the exact phase P stress solutions presented in Equation 3.9. In general, however, numerical methods have to be used to calculate shape parameters for arbitrary fibre aspect ratios A.
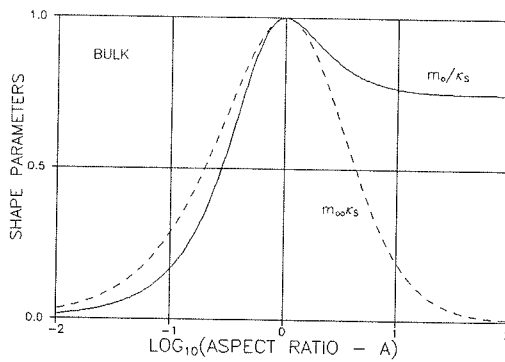

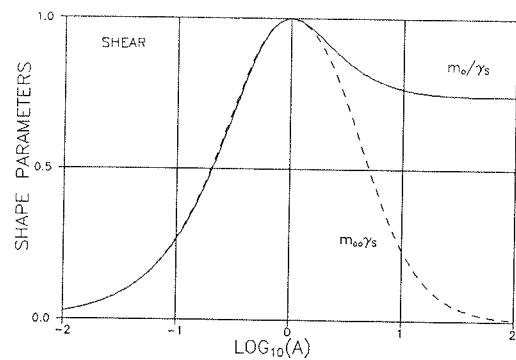**Figure 7.4.** Bulk shape parameters for isotropic composite, $v_s = 0.2$.

Figure 7.5. Shear shape parameters for isotropic composite with $v_s = 0.2$.

2) It is noticed that the shape factor analysis in this section resulting in Equation 7.6 can be approximated very well by method described in Appendix Bb.

49

For this purpose such a method has been developed in Appendix B by which particles stress in isotropic dilute composites (with ellipsoidal inclusions) can be calculated for any stiffness ratio (n). Shape parameters for any aspect ratio can then be determined numerically with stiffness ratios n approaching 0 and ∞ in Equation 7.2 simulated by n $= 10^{-30}$ and 10^{30} respectively. Examples of shape parameters determined in this way are shown in Figures 7.4 and 7.5. Shape parameters do not depend very much on the phase P Poisson's ratio ν_P. When spherical inclusions (A $= 1$) are considered they do not depend at all.

For the sake of curiosity: Young's modulus related shape parameters defined in Equation 7.3 are obtained from their bulk and shear counterparts by Equation 7.4 which is developed from Equation 7.1 and Equation A2 in Appendix A with c $\rightarrow$ 0. Examples of shape parameters related to Young's modulus are illustrated in Figure 7.6.

$$e_o = 1 - \left[1 + \frac{1}{m_{eo}}\right] c \quad ; \quad \frac{1}{e_\infty} = 1 - \left[1 + \frac{1}{m_{e\infty}}\right] c \qquad (7.3)$$

$$\frac{1}{m_{ei}} = \frac{1}{3}\left[\frac{1 - 2\nu_s}{m_{ki}} + \frac{2(1 + \nu_s)}{m_{gi}}\right] \qquad (i = o, \infty) \qquad (7.4)$$

Shape factors
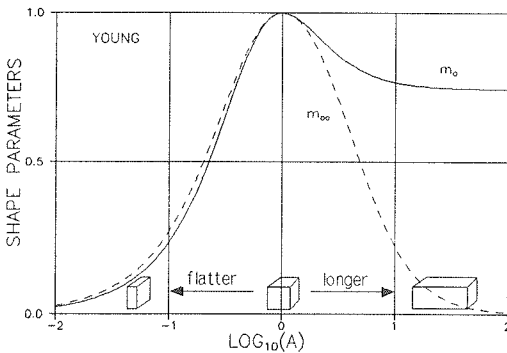
Figure 7.6. Uniaxial shape parameters for isotropic composite with $\nu_s = 0.2$.

Shape parameters are related to 'dilute' geo-functions comparing Equation 7.1 with Equation 5.3. We get $(m_o, 1/m_\infty)_{k,g} = (\theta_o{}^o, \theta_\infty{}^o)_{k,g}$ which, by using Table 4.1, can be re-written as shown in Equation 7.5 to relate shape parameters and shape factors. Over-lined m means shape parameter normalized as indicated in Equation 7.5. This equation can be solved explicitly with respect to shape factors as shown in Equation 7.6. Like shape parameters, shape factors can be considered practically independent of ν_P.

So-called shape factor graphs can now be established as shown in Figures 7.7-7.9 which relate shape factors $\mu_P{}^o$ of a discrete phase P to the complementary shape factors $\mu_S{}^o$ of the continuous phase S.

50

$$\overline{m}_{ko} = \frac{m_{ko}}{\kappa_S} = \mu^o_{Pk} \quad ; \quad \overline{m}_{k\infty} = m_{k\infty}\kappa_S = \frac{\mu^o_{Sk}}{\mu^o_{Pk} + \mu^o_{Sk} - 1}$$

$$\overline{m}_{go} = \frac{m_{go}}{\gamma_S} = \mu^o_{Pg} \quad ; \quad \overline{m}_{g\infty} = m_{g\infty}\gamma_S = \frac{\mu^o_{Sg}}{\mu^o_{Pg} + \mu^o_{Sg} - 1}$$

(7.5)

$$\mu^o_{Pj} = \overline{m}_{jo} \quad ; \quad \mu^o_{Sj} = -\overline{m}_{j\infty}\frac{1 - \overline{m}_{jo}}{1 - \overline{m}_{j\infty}} \quad ; \quad (j = k,g)$$

(7.6)

Notice: We notice that the shape factors for a CSA$_P$ composite are $\mu_P{}^o = 1$ and $\mu_S{}^o \approx -1$ at any Poisson's ratio around 0.2. As the exact quantities are not needed very often we keep $(\mu_P{}^o, \mu_S{}^o) = (1,-1)$ as reference quantities for CSA$_P$ composites whenever shape factors in general are subsequently discussed in this monograph.
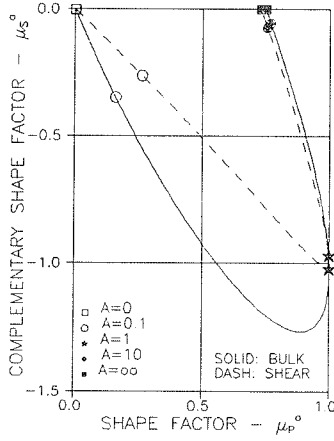
Figure 7.7. Shape factor graphs. $v_S = 0.15$.
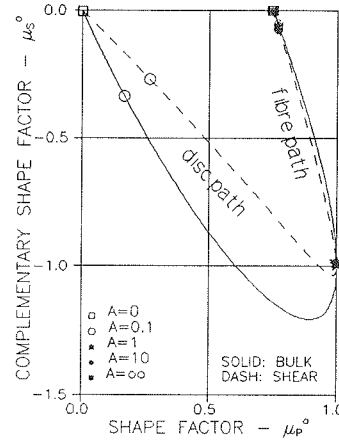
Figure 7.8. Shape factor graphs. $v_S = 0.2$.
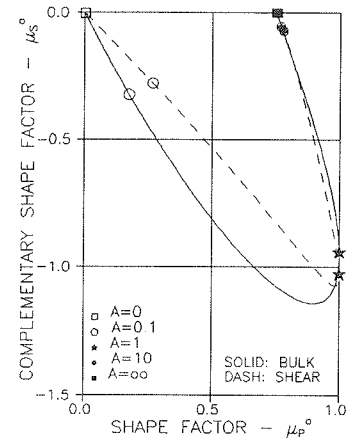
Figure 7.9. Shape factor graphs. $v_S = 0.25$.

Multi-shaped particles

Composite geometries hitherto considered in this chapter are based on uni-shaped regular fibres and discs. More realistic models of composite geometries can be made introducing shape distributed particles as shown in this section.

The average volumetric stress $<\sigma_{Pkk}{}^o>$ in particles of mixed shapes in a dilute suspension is expressed by Equation 7.7 where $\sigma_{Pkk,i}{}^o$ is volumetric stress in a vol-fraction α_i of phase P.

$$\frac{<\sigma^o_{Pkk}>}{\sigma_{kk}} = \sum_{i=1}^{\infty} \alpha_i \frac{\sigma^o_{Pkk,i}}{\sigma_{kk}} \quad is \ average \ stress \ in \ phase \ P \quad ; \quad \left[\sum_{i=1}^{\infty} \alpha_i = 1\right]$$

(7.7)

51

Average deviatoric particle stress is expressed in a similar way. It comes from Equation 7.2 and Appendix B that the average shape parameters of the mixture considered with discrete shape distributions can now be determined by Equation 7.8. The resulting average shape factors are presented in Equation 7.9 which is a modified copy of Equation 7.6.

$$\frac{1}{<\overline{m}_{mj}>} = \sum_{i=1}^{\infty} \frac{\alpha_i}{\overline{m}_{mj,i}} \quad ; \quad (m = k,g, \quad j = o,\infty) \tag{7.8}$$

$$<\mu^o_{Pm}> = <\overline{m}_{mo}> \quad ; \quad <\mu^o_{Sm}> = -<\overline{m}_{m\infty}> \frac{1-<\overline{m}_{mo}>}{1-<\overline{m}_{m\infty}>} \quad ; \quad (m = k,g) \tag{7.9}$$

Continuous shape distributions $\Phi = \Phi(A)$ can be used as shown in Equation 7.10. An example is outlined in Equation 7.11 with a linear log-A distribution with average aspect ratio A_{AV} and standard deviation s.

$$\frac{1}{<\overline{m}_{mj}>} = \int_0^{\infty} \frac{1}{\overline{m}_{mj}(A)} \, d\Phi(A) \quad ; \quad (subscipts \; m = k,g \; , \, j = o,\infty) \tag{7.10}$$

$$\Phi = \frac{1}{2}\left[1 + \frac{\log_{10}(A/A_{AV})}{s}\right] \equiv \begin{cases} 0 & when \; \log_{10}(A/A_{AV}) < -s \\ 1 & when \; \log_{10}(A/A_{AV}) > s \end{cases} \Rightarrow$$
$$\frac{1}{<\overline{m}_{mj}>} = \frac{1}{2s}\int_{X-s}^{X+s} \frac{dX}{\overline{m}_{mj}(X)} \quad ; \quad (X, \; \overline{X} = \log_{10}A, \; \log_{10}A_{AV}) \tag{7.11}$$

Rugged fibres, Frayed discs, and Rugged discs

Three examples of special dilute suspensions made with double shaped particles are shown in Figure 7.10:

DISC (A≤1)

FRAYED DISCS: discs + fibres
RUGGED DISCS: discs + spheres
RUGGED FIBRES: fibres + spheres

FRAYED DISC (FD)

FIBRE (A>1)

RUGGED DISC (RD)
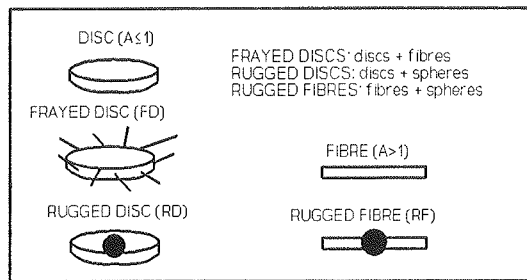
RUGGED FIBRE (RF)

Figure 7.10. Special multi-shaped particles. Stylized.

Rugged fibres (RF) are fibres (A > 1) mixed with spheres (A = 1). Rugged fibres are subsequently also referred to as "Pearls on a string" fibres, thinking of spheres interconnected by fibres (strings). Pearls on a thick/thin string is referred to when the volume fraction of fibres is

larger/smaller than the volume fraction of spheres.

Frayed discs (jelly-fish) (FD) are discs (A < 1) mixed with fibres (A > 1).

Rugged discs (fried eggs) (RD), are discs (A < 1) mixed with spheres (A = 1).

Examples of shear shape factor determination by Equation 7.9 of suspensions made with these special two-shape particles are presented in Figures 7.11 - 7.13. All examples assume $\nu_S = 0.2$.
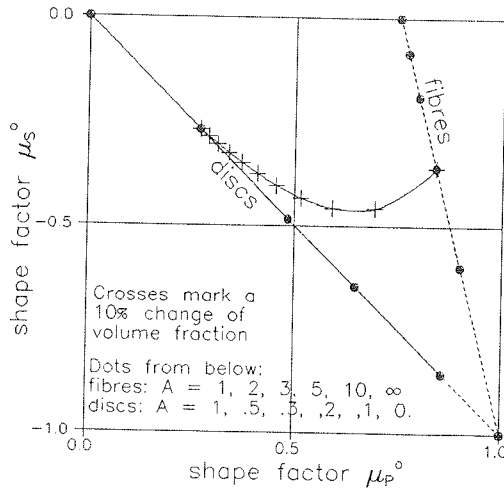
Figure 7.11. *Frayed discs (FD) Jelly-fish: Mixture of A = 0.1 and A = 3.*
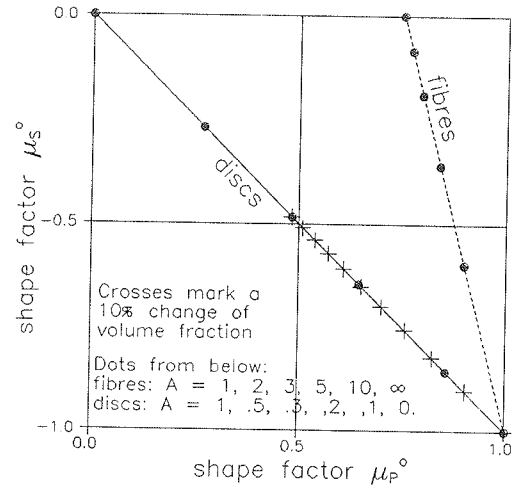
Figure 7.12. *Rugged discs (RD), Fried eggs: Mixture of A = 0.2 and spheres (A = 1).*

Remark: We notice that frayed discs (FD), at small aspect ratios, keep behaving as discs almost independently of the fibre volume fraction.

Also noticed is that rugged discs (RD) keep behaving as discs independently of spheres volume fraction.

Of interest is also that $\mu_P{}^\circ = 1$ is approached for any rugged fibre (RF) increasing the spheres volume fraction.

7.1.2 CD-composites

The shape factors hitherto considered ($\mu_P{}^\circ, \mu_S{}^\circ$) are those which quantify the geometry of a DC-composite with a very small amount of phase P (c ≈ 0). A similar quantification can be made with respect to the shape factors ($\mu_P{}^1, \mu_S{}^1$) which quantify the geometry of a CD-composite with a very small amount of phase S (c ≈ 1).

CD shape factors can be determined copying the DC-analysis with phase properties interchanged: Let us say that the DC shape factors are calculated by the algorithm
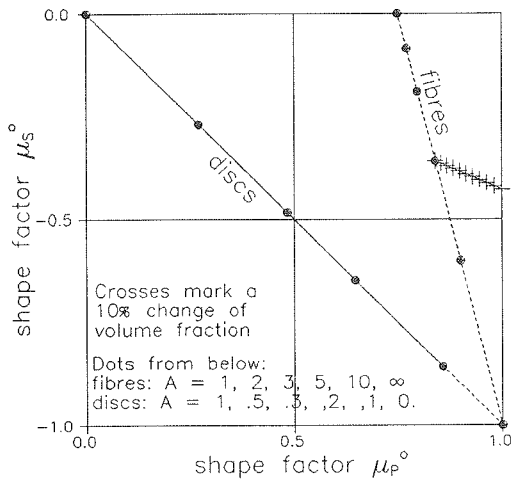
Figure 7.13. Rugged fibres (RF), Pearls on a string: Mixture of A = 3 and spheres (A = 1).

FAC. Then CD shape factors are determined as explained in Equation 7.12. An example of using this expression is shown in Figure 7.14.

If   DC-shape factors are obtained by $FAC(v_P,v_S,A_P, _P,$
then   CD-shape factors are (obtained) by $FAC(v_S,v_P,A_S,\mu_S^1,$

Remark: We re-call from Section 4.1.4 that $\mu_P{}^1, \mu_S{}^1$ in Figure 7.14 quantify the geometry of a composite material where phase P is the enveloping phase for a small concentration of discrete S particles of aspect ratios as indicated in the figure.

Theoretically, the above observations agree with Figure 7.15 where results are shown from deductions of various theoretical/experimental data subsequently considered in this monograph.
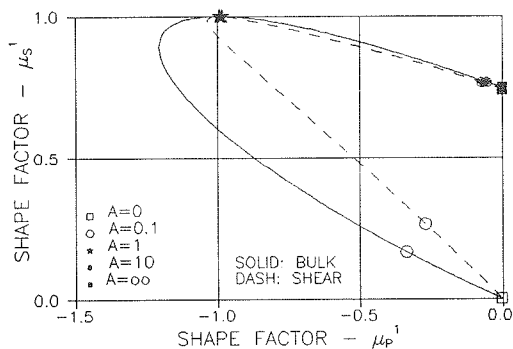
Figure 7.14. Shape factors in CD-composite. $v_P = 0.2$. Aspect ratios indicated apply for phase S fibres.

Figure 7.15. Bulk shape factors for CSA composites. $v_P = v_S$ (= 0.2)

54

7.1.3 MM-composites

To get a full picture of how shape factors vary with phase geometries we need information with respect to MM-composites which are transition materials where geometries change from being DC to CD. For two MM-geometries shape factors can be deduced/estimated from the stiffness results obtained in a FEM-analysis presented in Chapter 9: The CROSS composite is a phase-symmetric material reinforced by three dimensional grids. The pearls on a string composite is a material reinforced by continuous fibres grown together with compacts (rugged fibres). The shape factor results for these composites are presented in Figures 7.16 and 7.17 with data reproduced from Table 9.1.

The geometry of a dilute CROSS-system is that of a matrix reinforced with a 3-D fibrework of very long agglomerated fibres. It is therefor not surprising that the magnitudes of shape factors for this system are close to the theoretical result $(\mu_P{}^\circ, \mu_S{}^\circ = 0.75, 0)$ previously obtained (Figure 7.8) for particulate composites with very long cylindrical inclusions (A → ∞). The geometrical symmetry of the CROSS-system is reflected by $(\mu_P{}^1, \mu_S{}^1 = \mu_S{}^\circ, \mu_P{}^\circ)$. We will use these observations to suggest that shape factors for agglomerated fibres will develops with $\mu_P{}^\circ + \mu_S{}^\circ \approx 0.75$.
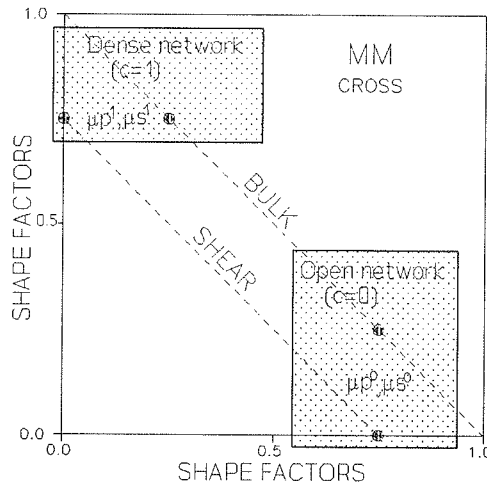
Figure 7.16. Shape factors for 3-D grid reinforced material (CROSS) $(v_P = v_S = 0.2)$. Deduced from FEM-analysis.
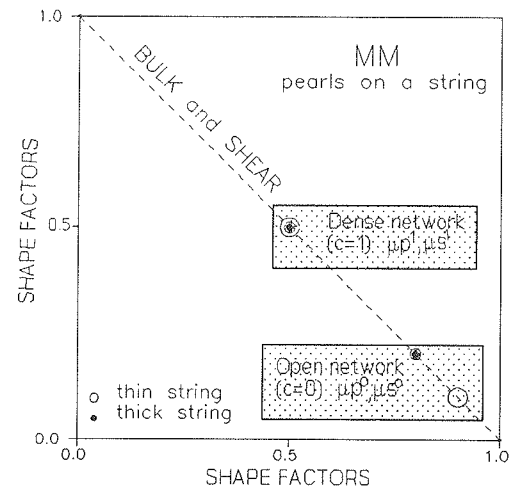
Figure 7.17. Shape factors for Rugged fibre reinforced (Pearls on a string) material $(v_P = v_S = 0.2)$. Deduced from FEM-analysis.

The pearls on a string path previously considered (see Figure 7.13, rugged fibres with many spheres) has $\mu_P \equiv 1$ in the DC-section. From this observation and Figure 7.17 is suggested that the shape factors for pearls on a string geometry proceed in MM such that $\mu_P{}^\circ + \mu_S{}^\circ \approx 1$.

Summarizing the observations made above we suggest that shape factors for MM-composites can be roughly estimated as suggested in Equation 7.13.

$$\mu_P^{o(1)} = a(1 - \gamma) \quad ; \quad \mu_S^{o(1)} = a\gamma$$

P-geometries getting continuous   Degree of transforming DC–CD

$$a \approx \begin{cases} 1 & \textit{fibre/sphere mix} \\ \approx 0.75 & \textit{fibres} \\ \approx 0.5 & \textit{fibre/disc mix} \\ 0 & \textit{discs and plates} \end{cases} \qquad \gamma \approx \begin{cases} 0 & \textit{starting} \\ 0.5 & \textit{medium} \\ 1 & \textit{complete} \end{cases}$$

(7.13)

Remark: The crumbled foils composite previously defined is considered in Equation 7.13 with $(a,\gamma) = (0,1)$: At an average, discs are assumed to pass the MM area agglomerating along $\mu_P^o + \mu_S^o \approx 0$ which is approximately the trend already prepared in the DC area, see Figure 7.8, and suggested in Section 4.1.4.

7.2 Shape functions and geo-path

As already indicated in the introductory section to this chapter we will now construct shape functions by straight line interpolations between known shape function data sets: At c = 0 and c = 1 where shape factors are as determined in previous sections of this chapter, and at critical concentrations c_P and c_S (known from processing technique) where shape function values are zero.

Such construction means that shape functions are represented by simple broken line with 'knees' at the critical concentrations (e.g. Figure 7.18a) - and that unknown geometries are approximated to vary 'linearly'.

The shape function construction technique considered above is outlined (exercised) in the following Figure 7.18a where a DC-CD composite is considered. In principles the construction of shape functions for other composite proceeds along the same scheme. Some additional estimated/calibrated geo-parameters, however, have to be introduced. This is illustrated in Figures 7.18b-7.18d where DC-MM, DC-DC, and MM-MM composites respectively are considered.

Appropriate mathematical descriptions of the shape functions obtained are summarized in Equations 7.14 and 7.15.

In principles shape functions for both bulk and deviatoric behavior are established in the same way. Subscripts, k and g, are therefor omitted.

56

7.2.1 DC-CD and DC-MM composites

- Determine $\mu_P{}^o,\mu_S{}^o,\mu_P{}^1,\mu_S{}^1$ as explained in Section 7.1 with known specific shape distributions of particles at c $\approx$ 0 and c $\approx$ 1.

- Mark these data as $(0,\mu_P{}^o)$, $(0,\mu_S{}^o)$ and $(1,\mu_P{}^1)$, $(1,\mu_S{}^1)$ in a shape function coordinate system (c,μ) together with the critical concentration data $(c_P,0)$ and $(c_S,0)$. Also mark $(\mu_P{}^o,\mu_S{}^o)$ and $(\mu_P{}^1,\mu_S{}^1)$ into a (μ_P,μ_S) coordinate system (a so-called shape-function graph).

- In the shape function system, connect with straight lines $(0,\mu_P{}^o)$ to $(c_P,0)$ to $(1,\mu_P{}^1)$, and $(0,\mu_S{}^o)$ to $(c_S,0)$ to $(1,\mu_S{}^1)$. The shape functions are now described.

- Read a $= \mu_P(c_S)$ and b $= \mu_S(c_P)$ in the shape function system and mark these data as $(a,0)$ and $(0,b)$ into the shape function system - and connect $(\mu_P{}^o,\mu_S{}^o)$ to $(a,0)$ to $(0,b)$ to $(\mu_P{}^1,\mu_S{}^1)$. The graph such obtained is the so-called *geo-path* which describes type of composite geometry traversed as c proceeds from 0 to 1.
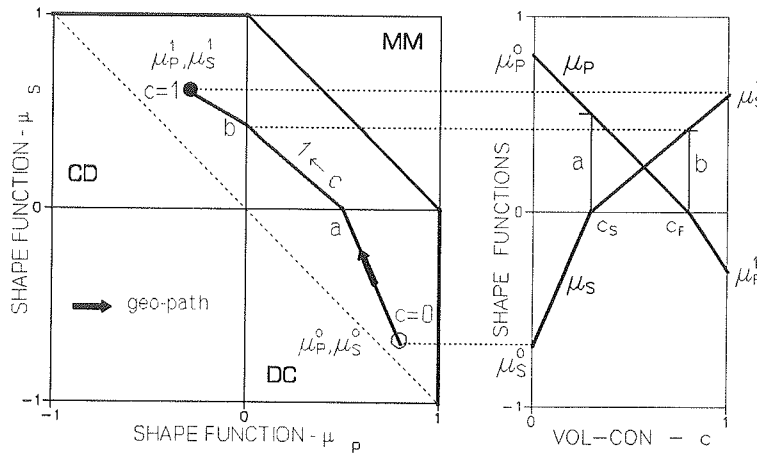
Figure 7.18a. DC-CD: Shape function graph, geo-path, and shape functions for DC-CD composite. Geo-properties: Known $(\mu_P{}^o,\mu_S{}^o,\mu_P{}^1,\mu_S{}^1)$ and real critical concentrations (c_P,c_S).
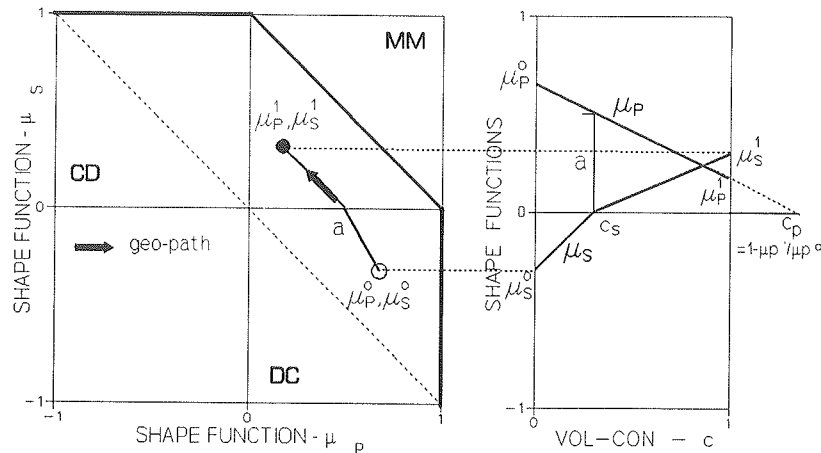
Figure 7.18b. DC-MM: Geo-properties: Known $(\mu_P{}^o,\mu_S{}^o)$ and c_S. Estimated $(\mu_P{}^1,\mu_S{}^1)$ by Equation 7.13. Calculated $c_P > 1$.

Remark: To facilitate the identification of composite geometries traversed by the geo-path at increasing phase P concentrations the 'profiles' $\mu_P + \mu_S = 0$ and $\mu_P + \mu_S = 1$, are 'standards' in a shape function graph. See subsequent Figure 7.19.

Mathematically the construction of shape functions for DC-CD and DC-MM composites can be put into the 6-parameter representations shown in Equation 7.14.

$$\underline{DC\text{-}CD \ \ and \ \ DC\text{-}MM}$$

$$\mu_P = \begin{cases} \mu_P^o \dfrac{c_P - c}{c_P} & at \ c \le c_P \\[2mm] \mu_P^1 \dfrac{c - c_P}{1 - c_P} & at \ c > c_P \end{cases} \quad ; \quad \mu_S = \begin{cases} \mu_S^o \dfrac{c_S - c}{c_S} & at \ c \le c_S \\[2mm] \mu_S^1 \dfrac{c - c_S}{1 - c_S} & at \ c > c_S \end{cases} \quad (7.14)$$

7.2.2 DC-DC and MM-MM composites
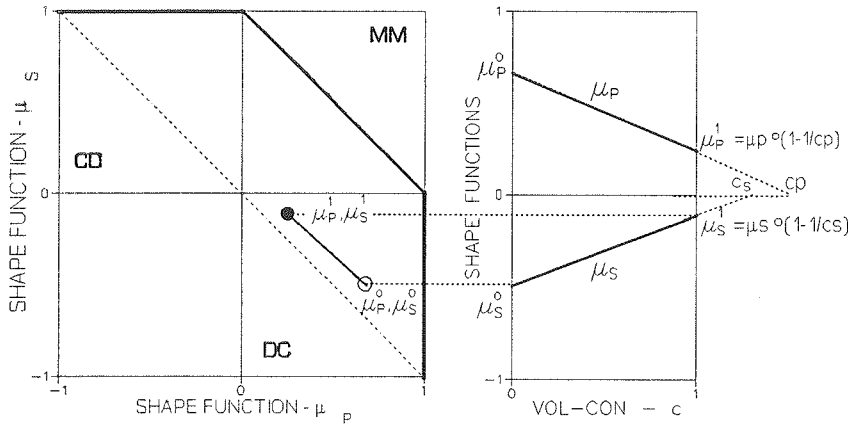
Figure 7.18c. DC-DC: Known μ_P^o, μ_S^o and estimated/calibrated $c_P \ge c_S > 1$.
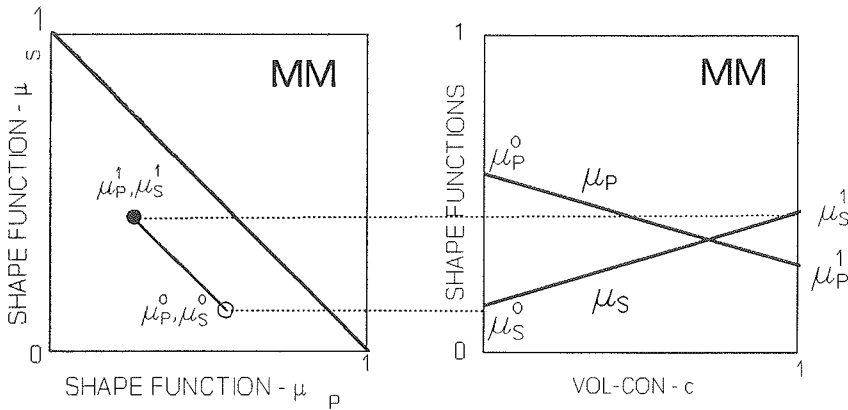
Figure 7.18d. MM-MM: Estimated $(\mu_P^o, \mu_S^o, \mu_P^1, \mu_S^1)$ from Equation 7.13.

58

Mathematically the construction of shape functions for DC-DC and MM-MM composites can be put into the representation shown in Equation 7.15 which is simple modified version of Equation 7.14.

$$\begin{aligned} \mu_P &= (1 - c)\mu_P^o + c\mu_P^1 \\ \mu_S &= (1 - c)\mu_S^o + c\mu_S^1 \end{aligned} \right\} \quad \underline{DC\text{-}DC \ and \ MM\text{-}MM} \qquad (7.15)$$

7.2.3 Composite geometry - a 'stylized summary'

The principles of the geometry quantification just made are outlined in Figure 7.19 representing both deviatoric and volumetric quantification.
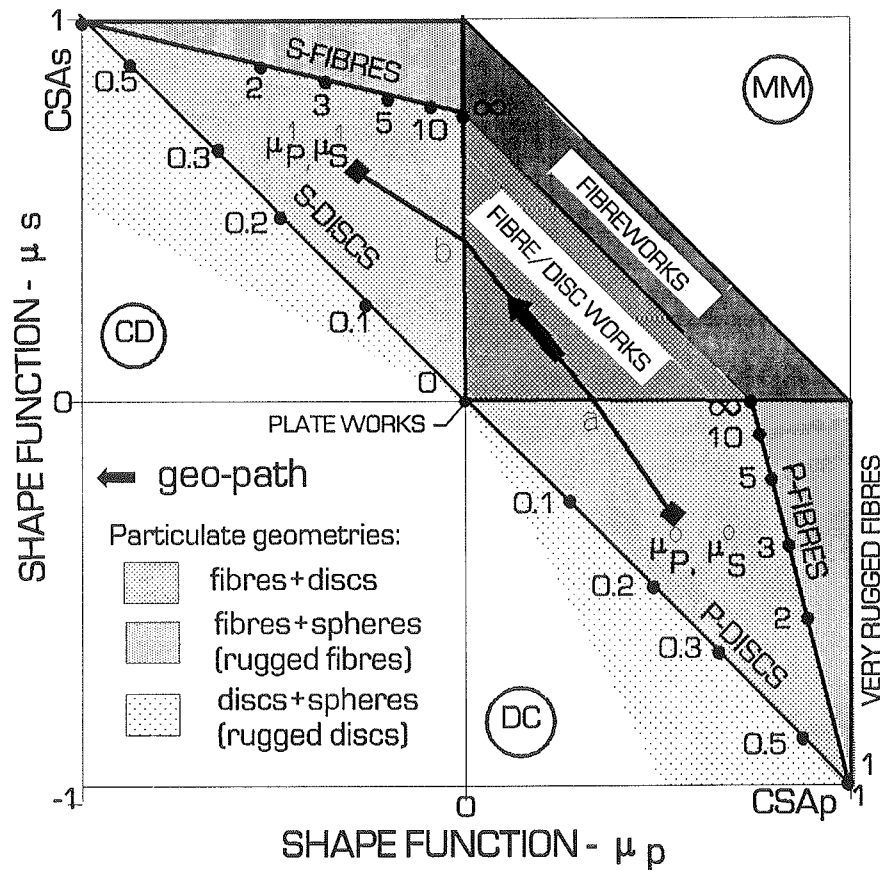
Figure 7.19 Stylized shape function graph and geo-path. Numbers are aspect ratios, A, of strict discs/fibres. A shape function value in DC quantifies the geometry of discrete phase P in a continuous phase S. A shape function value in CD quantifies the geometry of phase P envelopes for discrete S fibres. Very rugged fibres are fibres mixed with a large amount of spheres. Fibreworks are agglomerating crumbled fibres. Fibre/disc works are agglomerating crumbled fibres and discs. Plateworks are agglomerating crumbled discs.

We re-call that the areas around the axis $\mu_P \equiv 0$ and $\mu_S \equiv 0$ of Figure 7.19 define geometries where strict fibre/disc shapes are reinterpreted as 'preparing to become continuous shapes', see introduction to this chapter.

Remarks: As an approximation for practice Figure 7.19 can be used in general for first estimate analysis (including shape factor estimations) of composites for which geometrical and stiffness information are still somewhat uncertain, (assuming both Poisson's ratios to be around 0.2 and approximating deviatoric and volumetric shape functions to be similar).

As previously mentioned, the 'profiles' $\mu_P + \mu_S = 0$ and $\mu_P + \mu_S = 1$, are 'standards' in a shape function graph. They facilitate the identification of composite geometries (approximate) traversed by the geo-path at increasing phase P concentrations.

7.2.4 Examples

It is anticipated that modern technologies (in the near future) can produce any composite geometry, meaning that the geo-path/geometry concept discussed in this chapter is realistic enough to pursue experimentally - and to be used as a tool in the analysis of real composite geometries.

We will put this statement into perspective by looking at two examples with geometries produced by presently wellknown techniques. The shape functions and the shape function graphs are constructed as previously explained in this chapter.

DC-CD composite
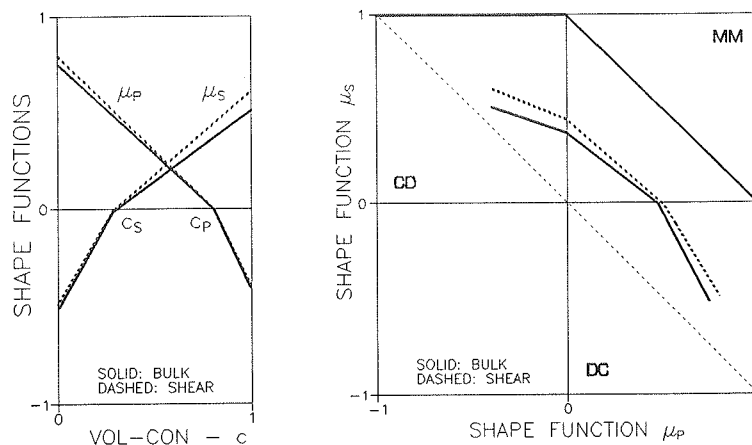
Figure 7.20. Shape function graph, geo-path, and shape functions for DC-CD composite, $(v_P, v_S) = (0.3, 0.1)$. Critical concentrations $(c_P, c_S) = (0.8, 0.3)$. Particulate mixture at c = 0: P-particles: 80% A = 3 + 20% A = 0.3. At c = 1: S-particles 50% A = 5 + 50% A = 0.2.

60

The DC-CD composite geometry presented in Figure 7.20 can be thought of as produced by the following process: Phase P and phase S powders are made as indicated in the capture of Figure 7.20. The powders are mixed and compacted (voids squeezed out) such that the phase P concentration is c - and such that the first sign of P-continuity appears at c $=$ c_S $=$ 0.3 - and the first sign of S-discontinuity appears at c $=$ c_P $=$ 0.8.
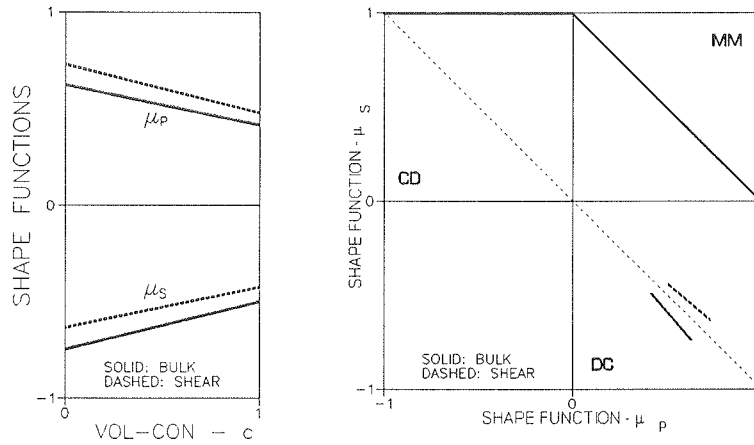
Figure 7.21. Shape function graph, geo-path, and shape functions for DC-DC composite (v_P, v_S) $=$ $(0.2, 0.2)$: Non-real critical concentrations: (c_P, c_S) $=$ $(3,3)$. Particulate mixture at c $=$ 0: P-particles: 60% A $=$ 0.3 $+$ 40% A $=$ 3.

DC-DC composite

The DC-DC geometry presented in Figure 7.21 can be thought of as being the result of mixing extremely well graded phase P particles into a solidifying phase S. An estimate of critical concentrations c_P $=$ c_S $>$ 1 is used as suggested in (24) for particulate composites.

For the two composites considered average geometries met at increasing concentrations of phase P can be estimated by placing the shape function graphs in Figures 7.20 and 7.21 on top of Figure 7.19.

The influence on the composite stiffness and other composite properties of the geometry described in Figure 7.20 is demonstrated in the following Chapter 8.

7.3 Comment on the level of geometrical knowledge

We recognize that the 'broken line' shape functions established in this chapter are approximate descriptions. Most often, however, we cannot do better than that. Probably, more realistic functions are curved such as parabolas. More geometrical knowledge is required to establish more accurate functions. Examples: A shape

61

function of $\mu_P \approx \mu_P^{\circ}(1-c/c_P)^{0.42}$ for $c \leq c_P$, was determined theoretically by the present author in (40) for a porous material with uni-sized pores. A DC-CD composite with CSA_P geometries at low concentrations will have a shape function μ_P which starts up at $c = 0$ with a horizontal tangent of $\mu_P \equiv 1$.

In the present monograph it is assumed that three levels of geometrical knowledge are obtained from studies on the production technology used:

- *Fairly high level (in present chapter):* The critical concentrations composite geometry at $c = 0$ and at $c = 1$ are known/estimated as described in the preceding Section 7.2. This level of geometrical knowledge is assumed in any example presented in the general parts of this monograph.

- *High level:* The geometry is known at any volume concentration (or a number of concentrations). Complex representations of shape functions (as suggested in Appendix E) are needed to consider this level of geometrical knowledge in composite analysis. This feature is further discussed in a subsequent example considering a plane-isotropic composite with cylindrical inclusions.

- *Modest level:* One critical concentration is known together with the geometry at $c = 0$. As a default level of geometrical knowledge, this level is assumed in chapters of this monograph which are based on the simplified version (Chapter 10) of the general theory presented. At modest levels of geometrical knowledge composite analysis can be made with simple straight line representations of shape functions (e.g. Figure 10.6). In most practice the level of geometrical knowledge is modest which means that only simple straight line presentations of shape functions are justified. This feature is further discussed in Chapter 10.

8. Theory - summarized

A composite analysis proceeds as follows for any type of composite considered with shape functions determined from Chapter 7:

- Geo-functions are determined as shown in Equation 4.14 (Chapter 4).
- Composite stresses are calculated by Equation 4.13 (Chapter 4).
- Bulk modulus, shear modulus, Young's modulus, and Poisson's ratio are calculated by Equations 5.1 and 5.4 (Chapter 5) respectively.
- Eigenstrain/stress behavior and pore-pressure/strain relations are determined by Equations 6.6 - 6.9 (Chapter 6).

For a rational computer programming it is worth recognizing that the general stress/stiffness analysis is in fact a combination of two almost identical analysis. A volumetric analysis where geometry is considered by volumetric shape functions and a deviatoric analysis where geometry is considered by deviatoric shape functions. Formally the eigenstrain/stress analysis is a volumetric analysis.

8.1 Examples

8.1.1 DC-CD composite

Results from a composite analysis are presented in Figures 8.1 - 8.4. The composite geometry considered is the one defined in Figure 7.20.
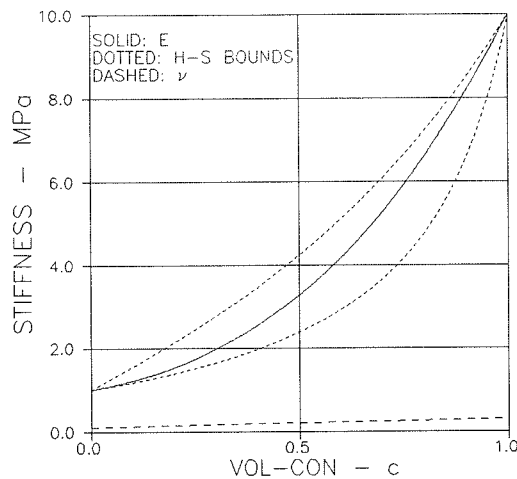
Figure 8.1. Stiffness and Poisson's ratio of composite with geometry and Poisson ratios defined in Figure 7.20. $(E_P, E_S) = (10,1)$ MPa.
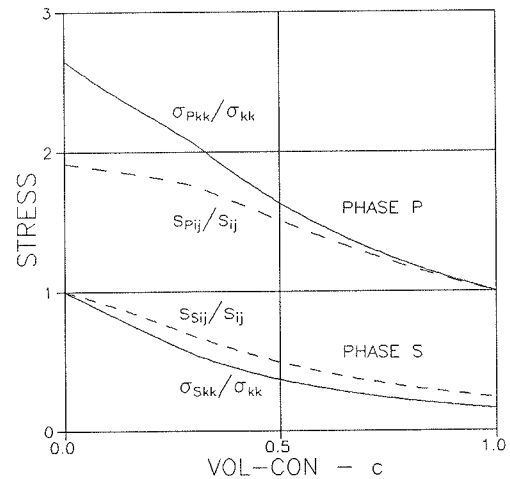
Figure 8.2. Stresses in composite with geometry and Poisson ratios defined in Figure 7.20. $(E_P, E_S) = (10,1)$ MPa.
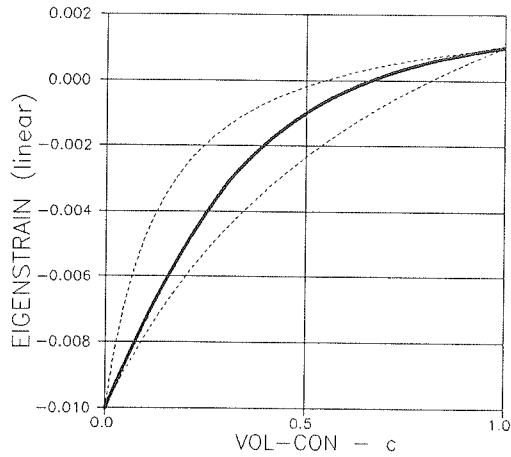
Figure 8.3. Eigenstrain of composite with geometry defined in Figure 7.20. $(\lambda_P, \lambda_S) = (0.001, -0.010)$. $(E_P, E_S) = (10, 1)$ MPa.
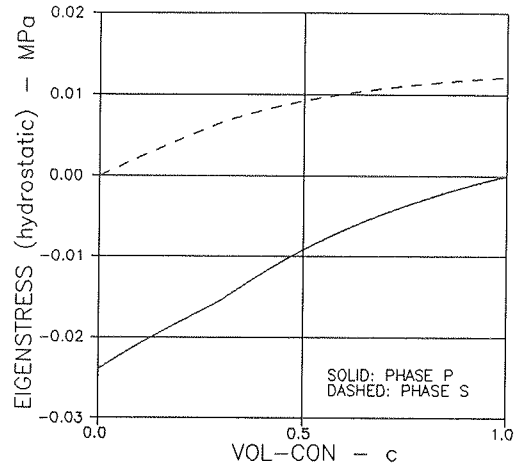
Figure 8.4. Eigenstresses in composite with geometry defined in Figure 7.20. $(\lambda_P, \lambda_S) = (0.001, -0.010)$. $(E_P, E_S) = (10, 1)$ MPa.

8.1.2 Crumbled foils composite

The results presented in Equation 8.1, Figure 8.5, and Figure 8.6 are from a composite bulk analysis of a crumbled foils composite with $(E_P, E_S) = (10, 1)$ and $\nu_P = \nu_S = 0.2$. We re-call from Section 4.1.4 that the composite considered is made of crumbled P-foils mixed with crumbled S-foils, producing a 3-dimensional Plywood geometry, with geo-functions determined from Equation 4.10c.
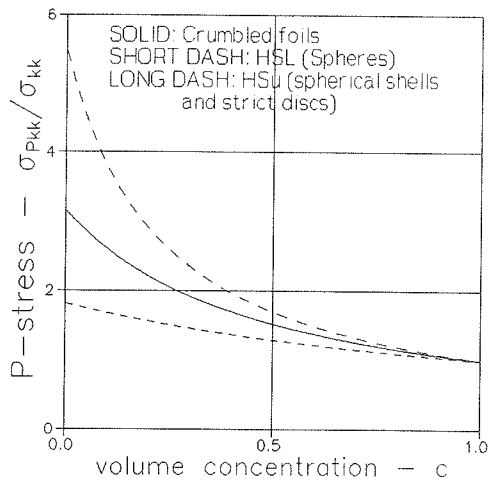
Figure 8.5. Phase P stress in a crumbled foils composite.
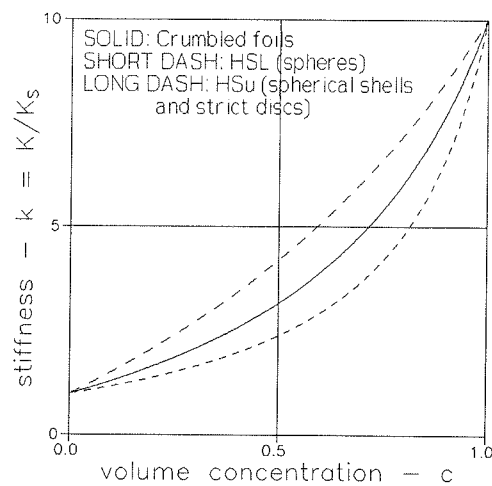
Figure 8.6. Bulk modulus of a crumbled foils composite.

$$\frac{\sigma_{Pkk}}{\sigma_{kk}} = \frac{\sqrt{n}}{1 + c(\sqrt{n} - 1)} \quad ; \quad \frac{\sigma_{Skk}}{\sigma_{kk}} = \frac{1}{1 + c(\sqrt{n} - 1)}$$

$$k = \frac{n + \sqrt{n}\,[1 + c(n - 1)]}{n + \sqrt{n} - c(n - 1)} \qquad (\theta_k \equiv \sqrt{n}) \tag{8.1}$$

8.1.3 Porous MM-MM composite
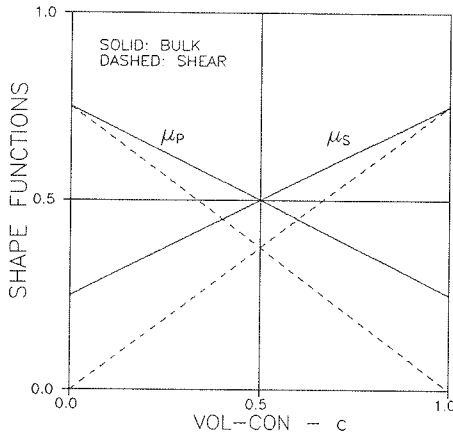
Figure 8.7. Shape functions for porous 'grid composite'.

A special phase symmetric MM-MM composite is considered in this section which consists of 3-D phase P grids (pores) mixed with 3-D phase S grids. This composite (CROSS composite) is further explained in Chapter 9.

The shape functions for a CROSS composite are presented in Figure 8.7 reproduced from Figure 9.24. A composite analysis reveal Young's moduli and Poisson's ratios as illustrated in Figures 8.8 and 8.9 respectively.

Remark: It is noticed that the composite Poisson's ratio approaches its maximum of $\nu = 0.5$ at increasing porosity.
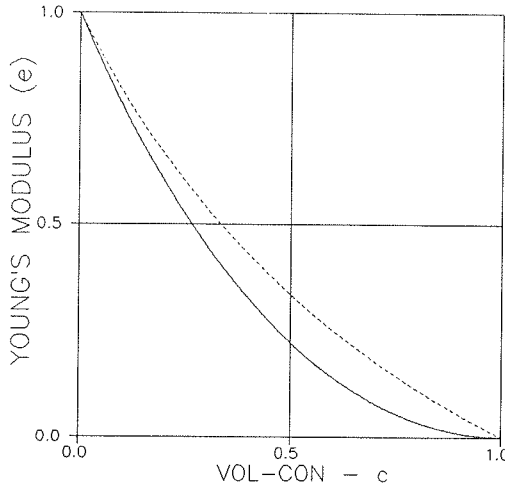
Figure 8.8. Young's modulus of porous 'grid composite' with $\nu_s = 0.2$.
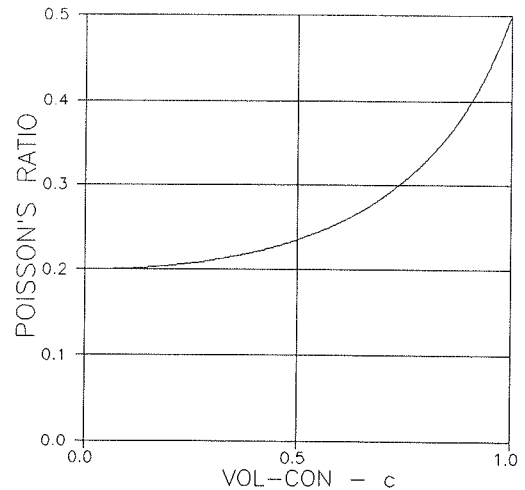
Figure 8.9. Poisson's ratio of porous 'grid composite' with $\nu_s = 0.2$.

9. Justification of theory

Results obtained by the composite theory just presented in Chapter 8 are compared in this chapter with results obtained by FEM-analysis (the author's) and results reported by other authors in the fields of theoretical and numerical analysis of cracked materials and phase-symmetric particulate composites.

Only stiffness data are considered. As indicated in Chapter 3 these data can be considered as representatives also for composite stresses (predicted composite stiffness is exact if composite stress introduced is exact - and vice versa). This means that, if the theory developed is verified with respect to stiffness prediction, it is at the same time verified with respect to stress prediction.

9.1 FEM-analysis

The theory presented in Chapter 8 on stiffness prediction of composites is based on the concept introduced in Chapter 2 and quantified in Chapter 7 that the geometry of any isotropic composite can be thought of as stages in a process of one phase transforming its geometry from spherical to anti-spherical (spherical shell), while the geometry of the other phase in a complementary way transforms from spherical shells to spheres.

The following three composites have been chosen to test the stiffness prediction presented and the underlying geometrical concepts by finite element methods (FEM). The four-letter classification used refers to path of geometrical changes as explained in Chapter 2.

- DC-DC composite: Compact particles in continuous matrix at any volume concentration ("*Particulate composite*").
- CC-CC composite: Interconnected compact particles in continuous matrix ("*pearls on a string composite*").
- CC-CC composite: Three-dimensional grids of one phase in complementary grids of the other phase ("*Grid composite*"). The composite considered is phase symmetric.

A special analysis of the influence of *defective phase-contacts* on composite stiffness has been made as part of the analysis of particulate composites.

Parts of the FEM-analysis has previously been reported in (24,71). A full report with data compilation is presented in Appendix C at the end of this monograph. All FEM-results obtained are presented graphically in this chapter and discussed together with results predicted by the method presented in Chapter 8.

66

Data presentation

The FEM-results presented apply to isotropic composites as converted from isotropic mixtures of cubic composites. This means that shear moduli, Young's moduli, and Poisson's ratios are calculated as simple averages of bounds presented in Appendix D. This procedure is well justified as these bounds are very close. FEM-data are shown by symbols in the figures. Theoretical (predicted) data are shown by graphs. The two data sets are very close. Whenever there might be any doubt which FEM-result "belongs" to which theoretical graph it is always the closest graph.

Shape factors

For any of the composites considered predicted data are calculated with shape functions described by Equation 7.15. The shape factors (μ°, μ^1) associated are calibrated as summarized in Table 9.1.

COMPOSITE TYPE	MODE	μ_P°	μ_S°	μ_P^1	μ_S^1
TROC-PARTICULATE (DC-DC)	bulk (k)	1.0	-1.0	0.95	-0.95
	shear (g)			0.5	-0.5
PEARLS ON A THIN STRING (α = 76%) (CC-CC)	bulk (k)	0.9	0.1	0.5	0.5
	shear (g)				
PEARLS ON A THICK STRING (α = 60%) (CC-CC)	bulk (k)	0.8	0.2	0.5	0.5
	shear (g)				
CROSS-GRID (CC-CC)	bulk (k)	0.75	0.25	0.25	0.75
	shear (g)	0.75	0.0	0.0	0.75

Table 9.1. Summary of shape factors for DC-DC composites (shaded area) and CC-CC composites deduced from the FEM-analysis presented in this chapter with $\nu_P = \nu_S = 0.2$.

9.1.1 Particulate composite

The TROC-composite shown in Figure 9.1 is the material model used in the FEM-analysis of particulate composites (DC-DC) with compact particles. It is a tight composition of identical composite elements each of which has the shape of a TRuncated OCtahedron with edges of equal lengths. The composite element is reinforced by a centrally placed particle the shape and orientation of which are similar to the composite element itself. Basically the TROC-material is cubic. From
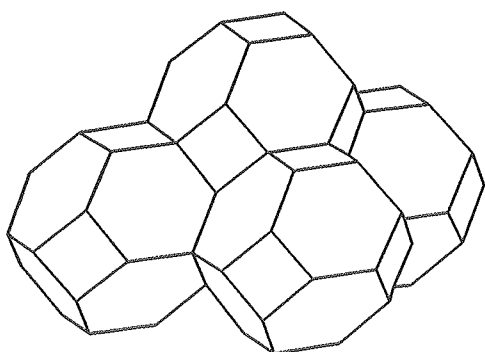
Figure 9.1. TROC-composite. Stacked TROC composite elements.

a modelling point of view this is no problem. Isotropic composites can be considered as isotropic mixtures of parts from cubic model sources. These sources may have different sizes of composite elements such that the final composite modelled by TROC elements can be thought of as one made by filling smaller and smaller composite elements into holes left in a stack of larger composite elements.

The FEM-data presented in Figures 9.4 - 9.13 are reproduced from Appendix D, Table D3 (with shear-data at (n,ν_s,ν_p,c) = $(10^5,0.4,0.2,0.73)$ declared false for reasons explained in Appendix D). The theoretical stiffness data presented are predicted with shape functions and geo-paths as illustrated in Figures 9.2 and 9.3.
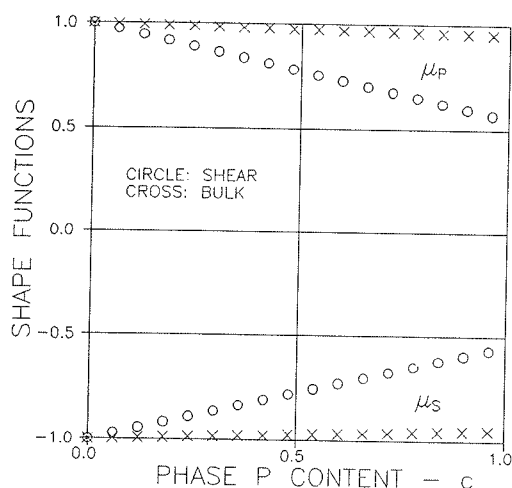
Figure 9.2. Shape functions of DC-DC composite considered (TROC).
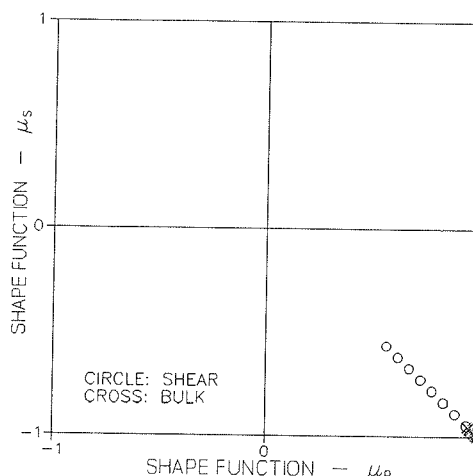
Figure 9.3. Geo-paths for DC-DC composite considered (TROC).

Discussion

An excellent agreement is observed between FEM-results and results predicted theoretically with the shape functions illustrated in Figure 9.2 which look just as expected from Chapter 7 for DC-DC composites. The bulk modulus shape functions are close to $(\mu_p,\mu_s)_k \equiv (1,-1)$ which indicate that the TROC-composite behaves almost like the theoretical CSA_p-composite in volumetric compression with no interaction between phase P elements. In shear the TROC-composite behaves strictly as a CSA_p-composite only at low phase P concentrations where there is no inter-

action. Increasing deviations of $(\mu_P, \mu_S)_g$ from $(1,-1)$ indicate increasing interaction between phase elements.

We recall that any TROC-analysis made in this section are based on shape factors (Table 9.1) calibrated from FEM-tests where $\nu_S = 0.2$. Thus, the results with ν_S different from 0.2, presented in Figures 9.4, 9.5, and 9.10-9.13 indicate that shape factors are not very sensitive to ν_S variations in the area 0-0.4. It has previously been indicated that the influence of ν_P on DC-DC shape factors is insignificant. Thus, DC-DC shape functions can practically be considered to be independent of Poisson's ratios.
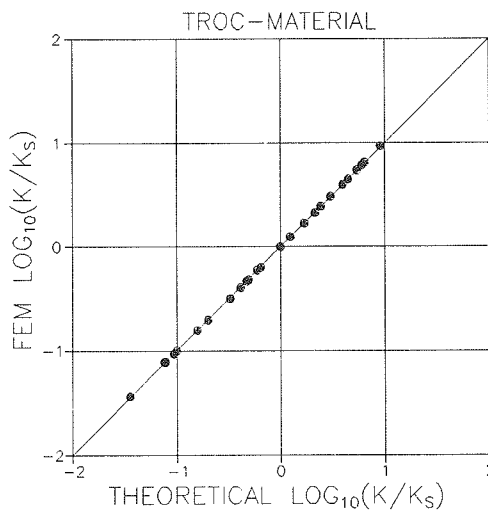
Figure 9.4. TROC-composite with various ν-combinations: All bulk modulus data.
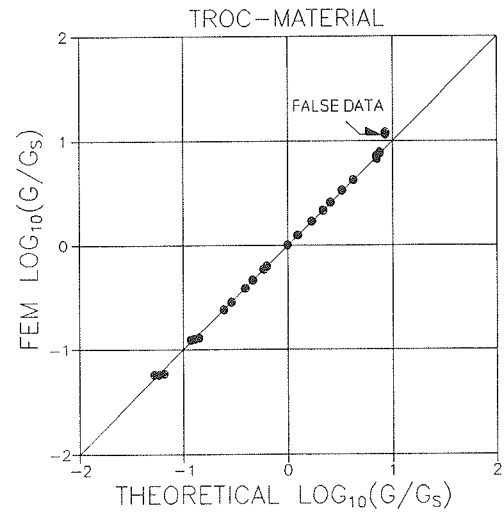
Figure 9.5. TROC-composite with various ν-combinations). All shear modulus data represented by upper and lower bounds.
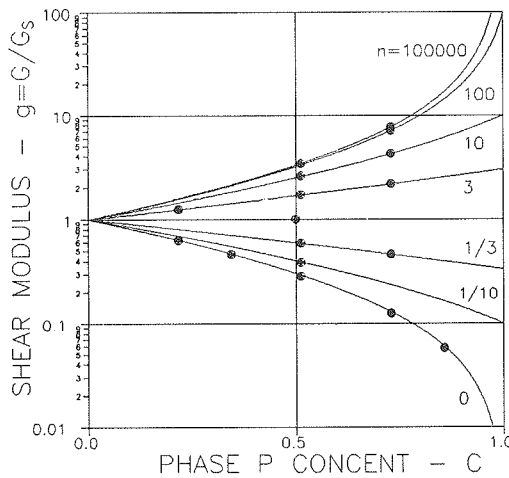
Figure 9.6. TROC-composite with $\nu_S = \nu_P = 0.2$. Shear modulus.
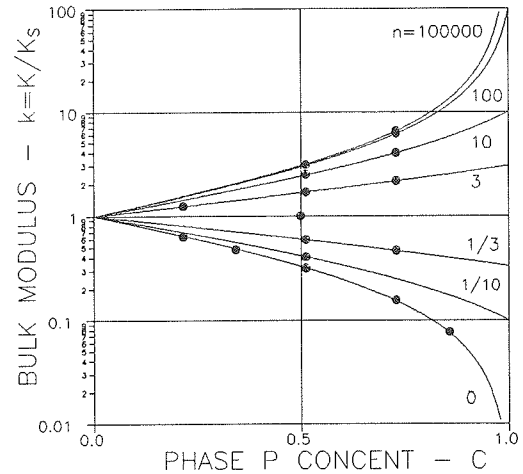
Figure 9.7. TROC-composite with $\nu_S = \nu_P = 0.2$. Bulk modulus.
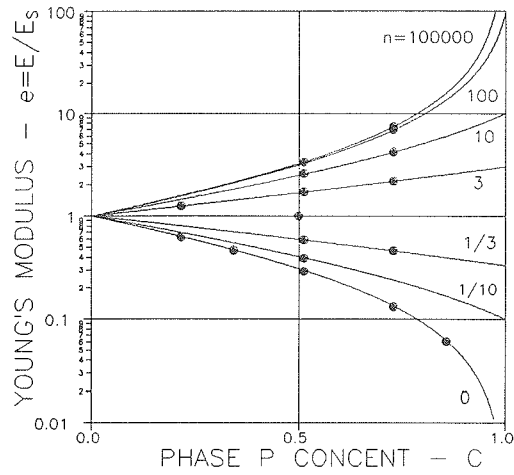
Figure 9.8. TROC-composite with $v_s = v_p = 0.2$. Young's modulus.
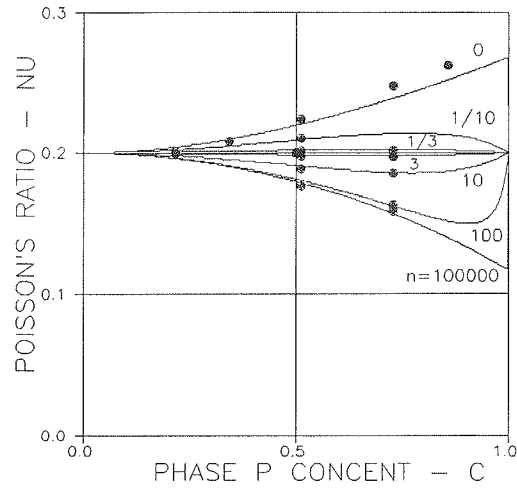
Figure 9.9. TROC-composite with $v_s = v_p = 0.2$. Poisson's ratio.
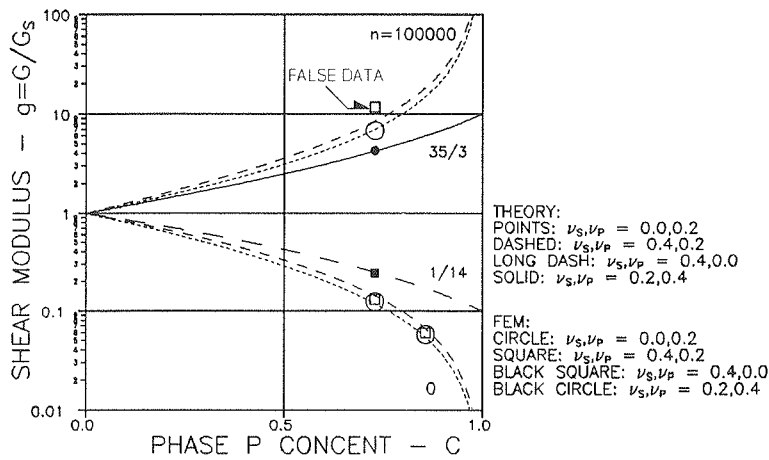
Figure 9.10. TROC-composite with $v_s \neq v_p$. Shear modulus.
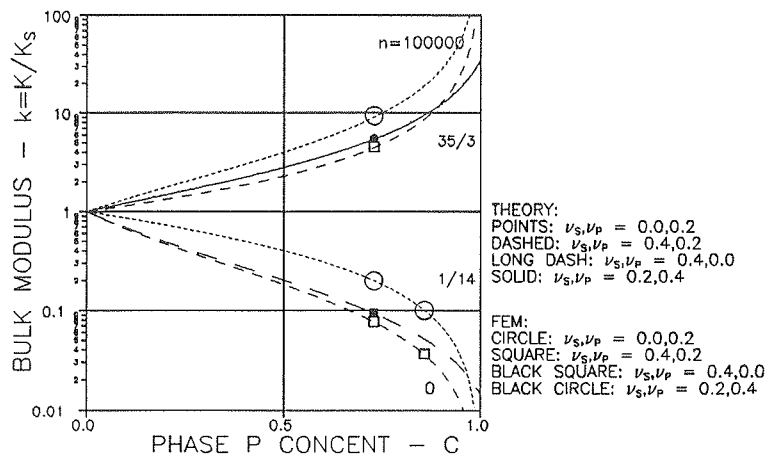
Figure 9.11. TROC-composite with $v_s \neq v_p$. Bulk modulus.
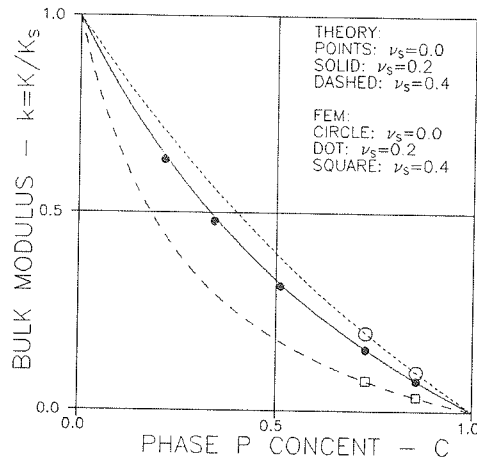
Figure 9.12. Porous TROC-composite with different Poisson's ratios v_S. Bulk modulus.
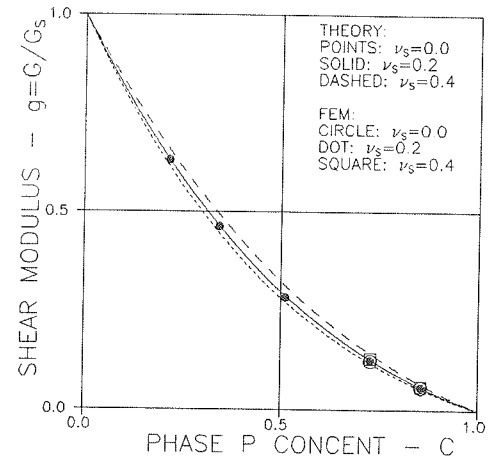
Figure 9.13. Porous TROC-composite with different Poisson's ratios v_S. Shear modulus.
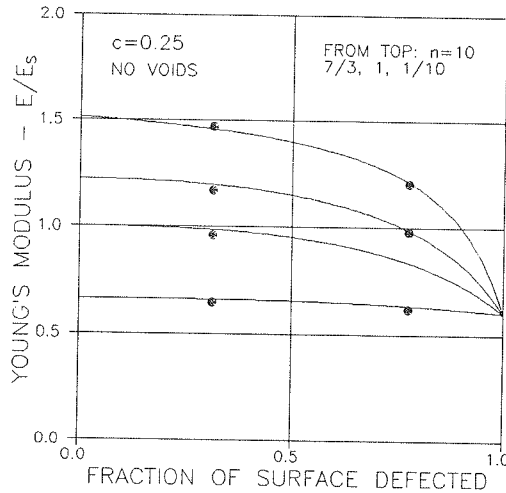
Figure 9.14. Defective TROC with both v = 0.2. Prediction with b = 15.
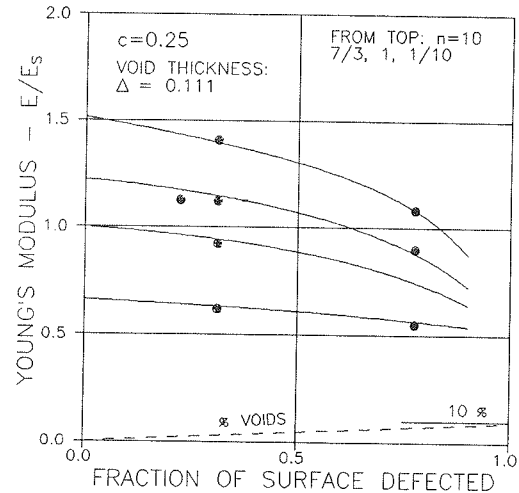
Figure 9.15. Defective TROC with $v_P = v_S$ = 0.2. (b = 15 and z = 1.5).

9.1.2 Defective particulate composite

A special FEM-analysis was made on TROC-composites with thin layers of "voids" (or zones of missing phase contact) spread over the surface of the particle phase. Such zones were introduced by simple joint-cutting and by finite elements of no stiffness. Sufficient openings are assumed between opposite zone faces such that load does not produce closure effects. The degree of missing phase contact χ is defined in Equation 9.1 together with concentration c_a of associated void volume, relative to composite volume. Particle surface is denoted by S. Thickness of void, relative to mean radius vector of particle, is denoted by Δ.

71

$$\chi = S_{inactive}/S_{total} \quad degree \ of \ missing \ phase \ contact$$

$$c_a = \chi c[(1 + \Delta)^3 - 1] \quad associated \ void \ volume \tag{9.1}$$
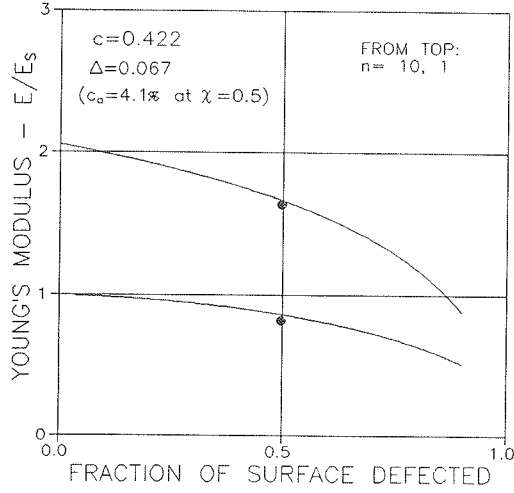
Figure 9.16. *Defective TROC with $v_P = v_S$ = 0.2. (b = 15 and z = 1.5).*

The FEM-data presented in Figures 9.14 - 9.16 are reproduced from Appendix D, Table D6. These data cannot be used for verification of the theory presented in this monograph where perfect phase contact is assumed in general. They can, however, be used to suggest an approximate method by which the Young's modulus of defective particulate composites with compact particles can be predicted. This feature is discussed just below.

Discussion

The hypothesis is suggested that Young's modulus of particulate composites with compact particles can be predicted approximately by the Young's modulus of a CSA_P-composite with an effective phase P stiffness ($n_{EFF} = E_{P,EFF}/E_S$) which depends on particle surfaces not effective. Voids associated with missing phase contact can be considered approximately by a simple reduction factor (f). Following this hypothesis, the "defective" stiffness of the composite considered is now predicted by Equation 9.2, developed from Equations 5.4 and 5.5 with $v_P = v_S = 0.2 \Rightarrow \kappa_S = \gamma_S = 1$,

The effective stiffness ratio and the reduction factor are determined by Equation 9.3 calibrating the hypothesis to the FEM-results obtained. Few larger defective areas are considered with the lower distribution parameter b. Many smaller defective areas are considered with a higher b.

$$e \approx \frac{n_{EFF} + 1 + c(n_{EFF} - 1)}{n_{EFF} + 1 - c(n_{EFF} - 1)} * f \quad ; \quad (v_P = v_S = 0.2) \tag{9.2}$$

$$n_{EFF} \approx n(1 - \chi^a) \quad with \quad a = \max\left[1, \frac{b}{5 + n}\right] \quad ; \quad b = 7\text{-}15$$
$$f = 1 - zc_a \qquad with \quad z = 1.5 - 2 \tag{9.3}$$

72

"Theoretical" data calculated by Equation 9.2 are presented in Figures 9.14 - 9.16 with solid lines. The hypothesis considered seems well justified by these figures. This conclusion is consistent with results obtained in a work reported in (71) o n particulate composites with defective phase contacts. Only Young's moduli h ave been considered in this section. The FEM-results in Table D6, Appendix D, indicate, however, that the influence of defective phase contacts on Young's moduli, bulk moduli, and shear moduli can be estimated in similar ways.

9.1.3 Pearls on a string composite

A special FEM-analysis was made on TROC-materials where particles grow together changing phase P from being discrete to being continuous like pearls on a string - or in other words, from being a *closed "pore" system* to being an *open "pore" system*. The growing together zones were introduced by letting phase S FEM-elements between TROC-particles take the phase P elastic properties. The term "open" is used because the composite may be thought of as an impregnated porous material with a fully continuous pore systems.

The phase P volume occupied by TROC-particles is quantified by the volume fraction α of the total phase P volume. α is large for *pearls on a thin string* geometry. α is small for *pearls on a thick string* geometry.
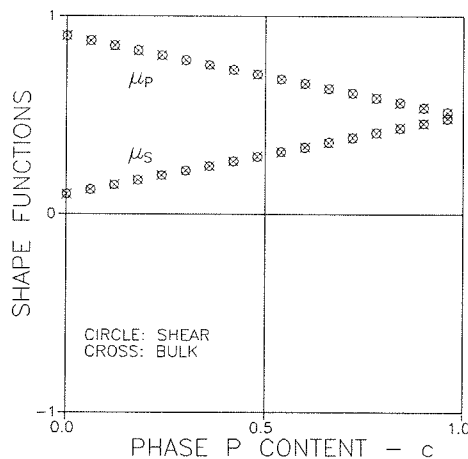
Figure 9.17. Shape functions for a pearls on a thin string composite (α = 76%).
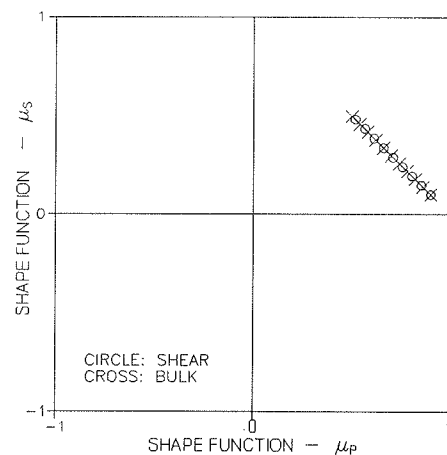
Figure 9.18. Geo-paths for a pearls on a thin string composite (α = 76%).

The FEM-data presented in Figures 9.21 and 9.22 are reproduced from Appendix D, Table D9. The theoretical data presented are predicted with CC-CC shape functions as presented in Figures 9.17 and 9.18 for α = 0.76 and in Figures 9.19 and 9.20 for α = 0.60 with shape factors as summarized in Table 9.1. "Closed system" data presented in Figures 9.21 and 9.22 are added from the analysis of TROC-composites in Section 9.1.1.
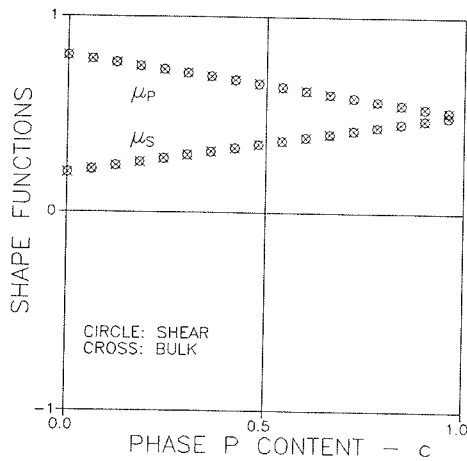
Figure 9.19. Shape functions for a pearls on a thick string composite, (α = 60%).
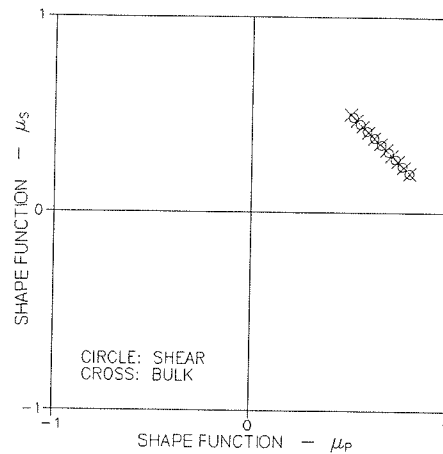
Figure 9.20. Geo-paths for a pearls on a thick string composite, (α = 60%).
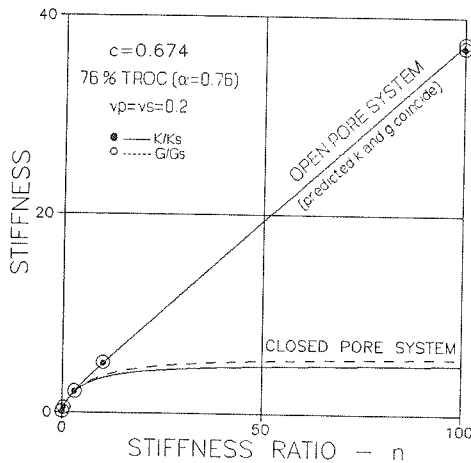
Figure 9.21. Pearls on a thin string, $\nu_s = \nu_P = 0.2$, 76 % of phase P is TROC.
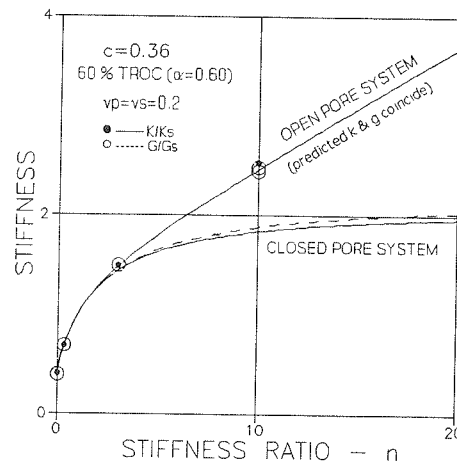
Figure 9.22. Pearls on a thick string, $\nu_s = \nu_P = 0.2$, 60% of phase P is TROC.

Discussion

A very fine agreement is observed between FEM-results and results predicted theoretically with the shape functions illustrated in Figures 9.17 - 9.20. It is noticed that $\mu_P + \mu_S = 1$ applies for both the bulk modulus shape functions and the shear modulus shape functions independently of thickness (α) of strings.

Shape factors $\mu_P^\circ > 0.75$ are expected because the phase P geometry at low phase P concentrations can be considered as a frame work formed by an agglomeration of long rugged fibres, see Figure 7.13. Individually such fibres have shape factors > 0.75 increasing with increasing degree of ruggedness (increasing fraction of spherical shapes). This can be observed from Figure 7.13. In the present context

74

of pearls on a string this means that the higher shape factors, $\mu_P{}^\circ$, should apply at $\alpha = 76\%$, which is also the case, see Figure 9.18 versus Figure 9.20.

The influence of pore geometry on the stiffness of porous materials impregnated with a stiff impregnant (n > 1) is clearly demonstrated in Figure 9.21 and 9.22: Composite stiffness increases considerably when pores transform from discrete (closed) pores to continuous (open) pores.

9.1.4 Grid composite

The CROSS-composite shown in Figure 9.23 is the material model used in the FEM-analysis of grid composites (CC-CC). It is a phase symmetric cubic frame work of phase P embedded in a complementary cubic frame work of phase S.

Basically the CROSS-material is cubic. From a modelling point of view this is no problem as previously indicated. Isotropic composites can be considered as isotropic mixtures of parts from cubic model sources. These sources may have different sizes of composite elements.

The FEM-data presented in Figures 9.26-9.33 are reproduced from Appendix D, Table D12. The theoretical data presented are based on the phase symmetric CC-CC shape functions illustrated in Figures 9.24 and 9.25 with shape factors as summarized in Table 9.1.

Figure 9.23. CROSS-composite. As illustrated, c = 0.5.

Discussion

A very fine agreement is observed between FEM-results and predicted results. It is observed that $(\mu_P + \mu_S)_g = 0.75$ and $(\mu_P + \mu_S)_k = 1$. Shape factors $\mu_{Pk}{}^\circ \approx \mu_{Pg}{}^\circ \approx 0.75$ were expected because the CROSS-model at low phase P concentrations can be considered as a frame work formed by agglomeration of long fibres, see Figure 7.13. The shape function μ_{Pg} decreases more rapidly than μ_{Pk}, indicating that shear interaction is greater than bulk interaction - just as was observed in the TROC analysis.
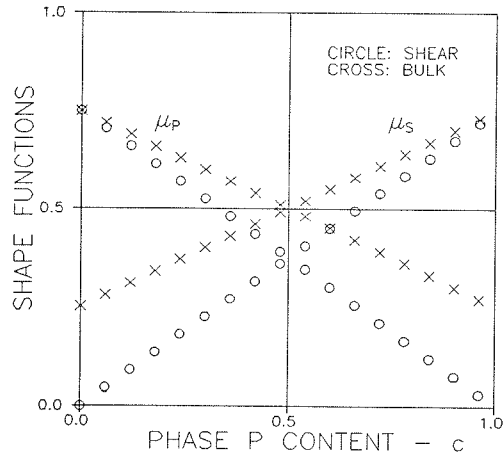
Figure 9.24. *CROSS-composite: Shape functions.*
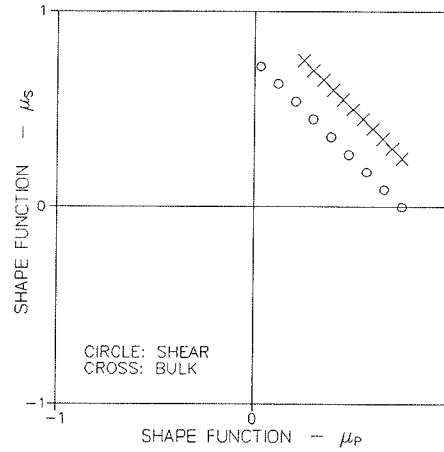
Figure 9.25. *CROSS-composite: Shape function graph.*
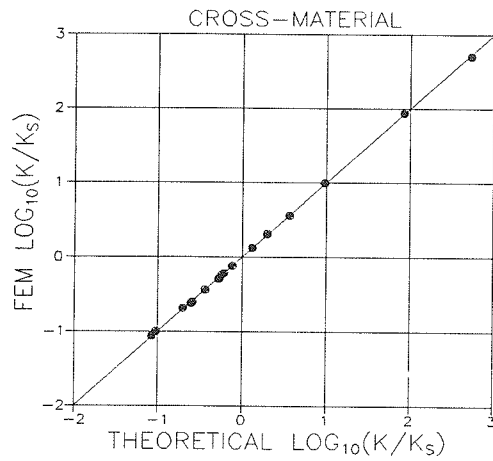
Figure 9.26. *CROSS-composite with* $v_s = v_p = 0.2$: *All bulk modulus data.*
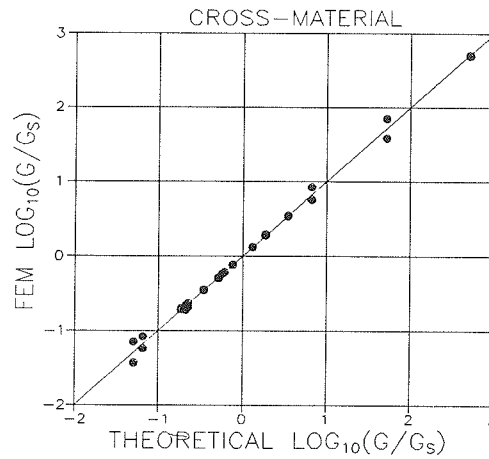
Figure 9.27. *CROSS-composite with* $v_s = v_p = 0.2$: *All shear data (bounds).*
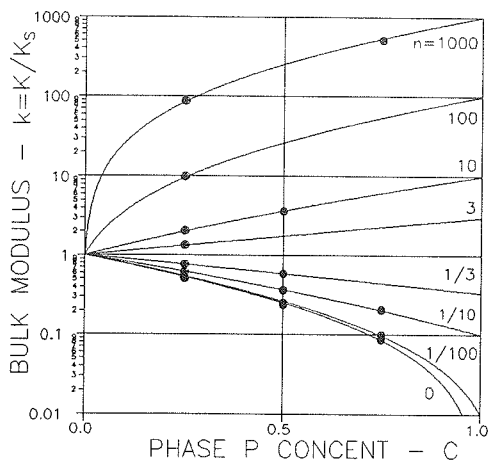
Figure 9.28. *CROSS-composite with* $v_s = v_p = 0.2$: *Bulk modulus.*
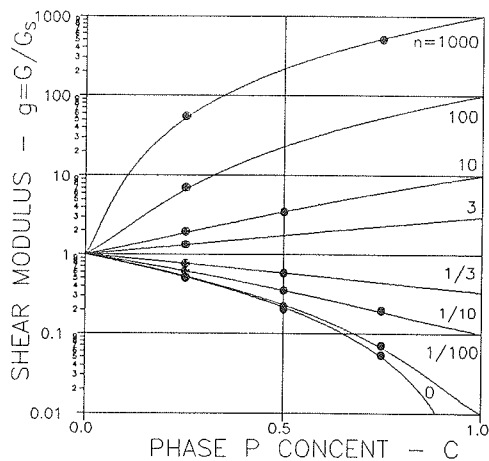
Figure 9.29. *CROSS-composite with* $v_s = v_p = 0.2$: *Shear modulus.*

76
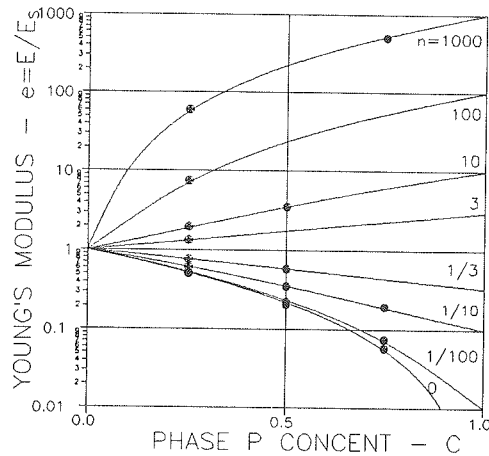
Figure 9.30. *CROSS-composite with* $\nu_s = \nu_P = 0.2$: *Young's modulus.*
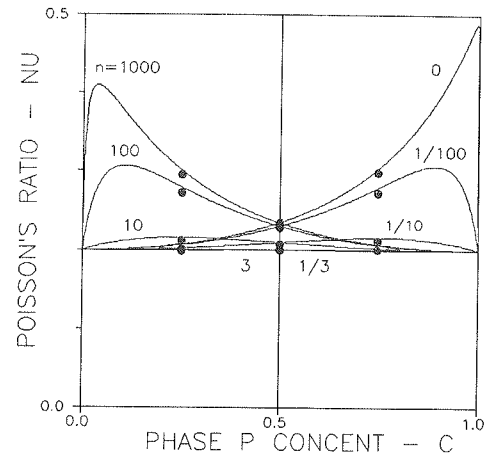
Figure 9.31. *CROSS-composite with* $\nu_s = \nu_P = 0.2$: *Poisson's ratio.*
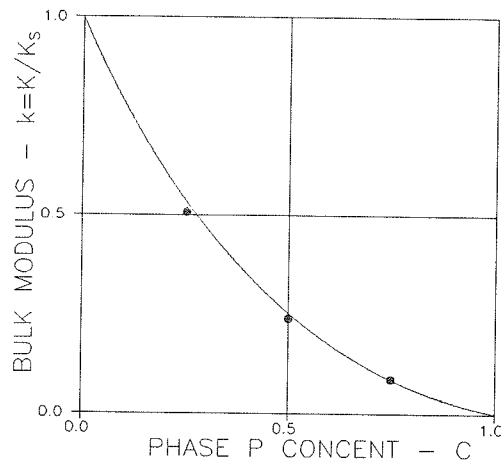
Figure 9.32. *Porous CROSS-composite with* $\nu_s = 0.2$: *Bulk modulus.*
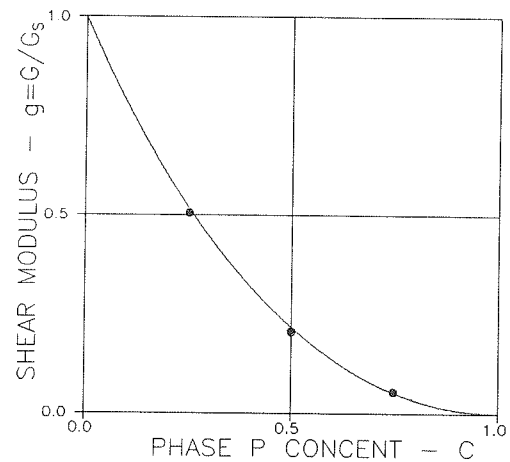
Figure 9.33. *Porous CROSS-composite with* $\nu_s = 0.2$: *Shear modulus.*

9.1.5 Discussion of FEM-analysis

The influence on composite stiffness of two very different types of composite geometries have been FEM-analyzed in this chapter: The TROC-composite with a DC geometry at any concentration - and the CROSS-composite with a CC geometry at any concentration.

A very satisfying agreement is observed between stiffness results obtained by FEM-analysis of these composites and results obtained by the theory developed in this monograph. Shape functions used in theory are fully compatible with such expected from the analysis in Chapter 7 on shape quantification.

The composite geometries considered represent important "stations" on the path of geometrical changes, DC → CC → CD. The TROC geometry is the start of this

77

path. The CROSS geometry is the middle of the path - and a TROC$_S$ geometry (phase S particles) is the end of the path. It is expected that other composites along the path just indicated can also be considered by the theory developed. For example DC-MM and DC-CD composites. Support to this expectation is obtained from the very salifying agreement observed in Section 9.1.3 between stiffness results of "Pearls on a string" composites obtained by FEM-analysis and by theoretical predictions. The phase P geometry of this composite can be seen as a frame work made of long rugged fibres, see Figure 7.13.

An important conclusion can be made from the analysis of Pearls on a string composites: Stiffness of porous materials impregnated with a stiff impregnant will increase considerably when pores transform from discrete (closed) pores to continuous (open) pores.

Finally, from the FEM-analysis of TROC-composites: A semi-theoretical method is suggested in Section 9.1.2 on, how defective phase contacts can be considered in stiffness predictions of particulate composites. The method is subsequently justified by experimental results presented in Section 11.6.

9.2 Crack analysis

In this section results from a crack analysis based on the present theory are compared with results analytically determined by Levin (7). Also considered are results which can be deduced from the FEM-analysis of defective particulate composites presented in Section 9.1.2. Any crack considered is strict as defined by the cylinder model in the introduction to Chapter 7 with an aspect ratio of A $\approx$ 0. Also from the introduction to Chapter 7: As extremely low (or high) stiffness ratios are considered no re-definition of flat shapes is required. This means that a composite analysis with organic particle shapes in the present theory produce the same results as a composite analysis with strict particle shapes.

9.2.1 Soft cracks

Stiffness of dilute porous materials with isotropically distributed fibre shaped voids can be written as presented in Equations 9.4 and 9.5 derived from Equations 5.3 and 5.4 with geo-functions from Table 4.1, and porosity of ellipsoidal voids c = $(\pi/6)pAd^3$ where p is void density (number of voids per vol-unit). As usual d and A denote diameter and aspect ratio respectively of a fibre.

$$k_o = 1 - h_k pd^3 = 1 - \frac{6h_k}{\pi A}c \quad ; \quad h_k = \frac{\pi}{6}A\left[1 + \frac{1}{\kappa_s \mu_{Pk}^o}\right]$$

$$g_o = 1 - h_g pd^3 = 1 - \frac{6h_g}{\pi A}c \quad ; \quad h_g = \frac{\pi}{6}A\left[1 + \frac{1}{\gamma_s \mu_{Pg}^o}\right] \Rightarrow \qquad (9.4)$$

$$e_o = 1 - h_e pd^3 = 1 - \frac{6h_e}{\pi A}c \quad ; \quad h_e = \frac{h_k + 4h_g}{5} \qquad (9.5)$$

Examples of the h_k and h_g factors from Equation 9.4 are shown in Figures 9.34 and 9.35 with shape factors (μ_P^o) calculated as explained Chapter 7. The situation of a cracked material is approached with aspect ratio $A \to 0$.
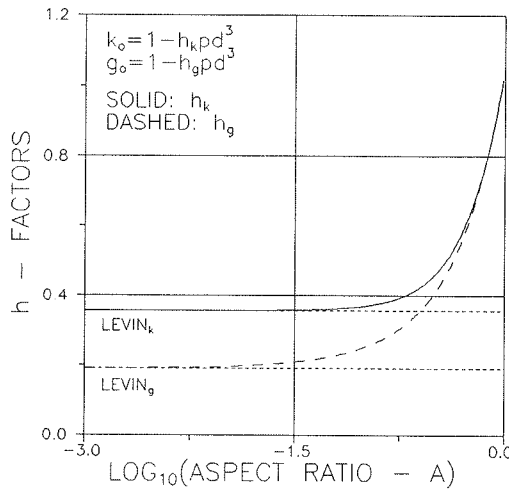
Figure 9.34. *h-factors for soft disc mixture.* $v_s = 0.2$. *Dotted lines, see text.*
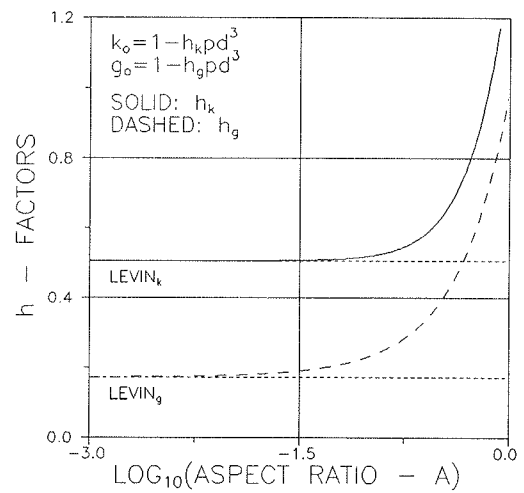
Figure 9.35. *h-factors for soft disc mixture.* $v_s = 0.3$. *Dotted lines, see text.*
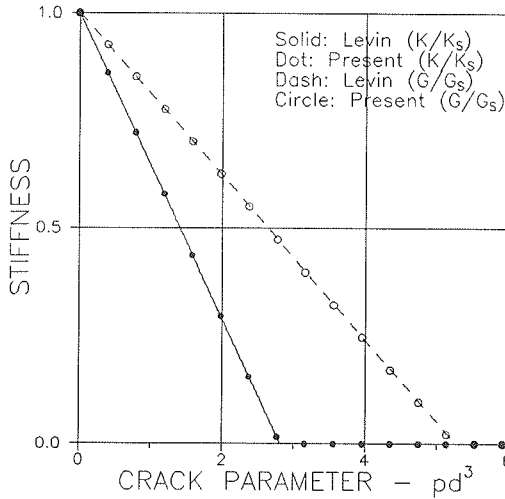
Figure 9.36. *Stiffness of material with thick "cracks".* $(A, v_s) = (0.001, 0.2)$.
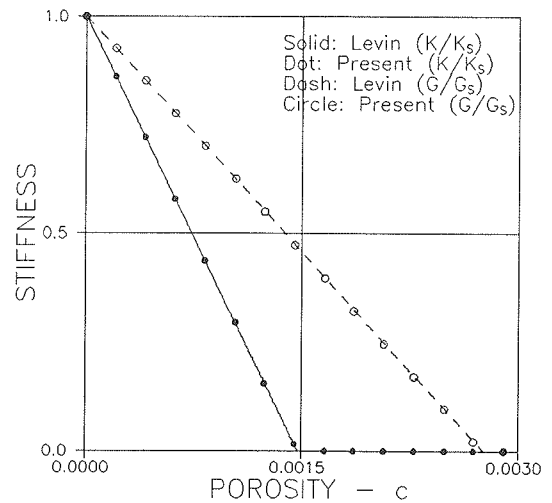
Figure 9.37. *Stiffness of material with thick "cracks".* $(A, v_s) = (0.001, 0.2)$.

It is noticed from Figures 9.34 and 9.35 that the crack results (A = 0) of the present analysis agree with results presented in Equation 9.6 which are deduced from Levin's theoretical work (7) on materials with isotropically distributed cracks. Similar expressions can also be obtained from other works (14,23,72) in the field of cracked materials.

$$h_k = \frac{2}{9}\frac{1 - \nu_s^2}{1 - 2\nu_s} \quad ; \quad h_g = \frac{4}{45}\frac{(1 - \nu_s)(5 - \nu_s)}{2 - \nu_s} \quad ; \quad Levin \ (A = 0) \qquad (9.6)$$

Remarks: It is noticed from comparing the results from the present analysis with the Levin results that "thick" cracks can be considered as real cracks as long as A < 0.01. This feature is illustrated in Figures 9.36 and 9.37 (with a porosity of c = $(\pi/6)pAd^3$).

It is worth noticing that the results in Figure 9.36 (and 9.37) are accurately predicted also by the SCS-method presented in Appendix C with (E_p,E_s) = $(0^+,1)$, (ν_p,ν_s) = (-,0.2), A < 0.01, and pd^3 = $6c/(\pi A)$. The statement previously made that SCS-solutions can be considered accurate when composites considered are dilute is clearly supported by this observation where very small crack "volumes" are involved.

FEM-analysis

Some results were presented in Section 9.1.2 from a FEM-analysis on defective "composites" with $(n,\nu_p = \nu_s)$ = (1,0.2). This composite is in fact a cracked

material with cracks placed on hypothetical TROC particles. These cracks, however, are not isotropically distributed. They form a certain pattern by which the original material in the end will transform to a porous material of finite stiffness with TROC-shaped pores. We do not, therefor, expect the results of the FEM-analysis to be accurately predicted by Equations 9.4 and 9.5.
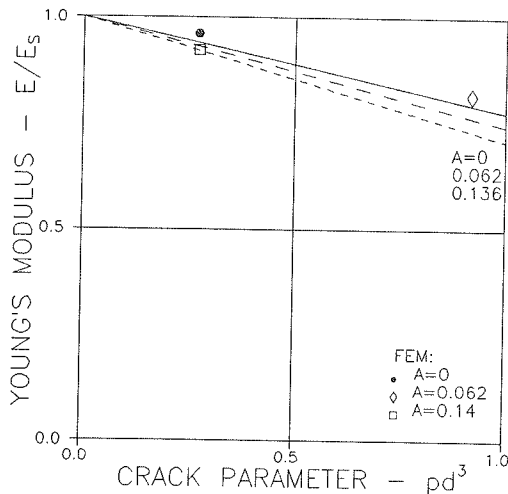
Figure 9.38. Lines: Isotropically cracked material. FEM-data: Cracks placed on hypothetical TROC-particles. ν = 0.2 all over.

It is, however, of some interest to compare the two data sets. This is done in Figure 9.38 with crack para-

meters (pd³) and aspect ratios (A) calculated in Section "Defective particulate composite" in Appendix D.

9.2.2 Stiff "cracks"

The problem of very stiff discs in a material can be solved in a very similar way the 'soft crack' problem was solved in Section 9.2.1. The results are presented in Equation 9.7 with the h-factors illustrated in Figure 9.39. As for soft cracks the stiff crack solutions apply also for thick cracks of finite thickness $A < 0.01$.

$$\frac{1}{k_\infty} = 1 - h_k pd^3 = 1 - \frac{6h_k}{\pi A}c \quad ; \quad h_k = \frac{\pi}{6}A\left[1 + \kappa_s\frac{\mu_{Pk}^o + \mu_{Sk}^o - 1}{\mu_{Sk}^o}\right]$$

$$\frac{1}{g_\infty} = 1 - h_g pd^3 = 1 - \frac{6h_g}{\pi A}c \quad ; \quad h_g = \frac{\pi}{6}A\left[1 + \gamma_s\frac{\mu_{Pg}^o + \mu_{Sg}^o - 1}{\mu_{Sg}^o}\right] \tag{9.7}$$

9.2.3 Discussion

A very satisfying agreement is observed in this section between stiffness of materials with isotropically distributed cracks predicted by the present theory and results
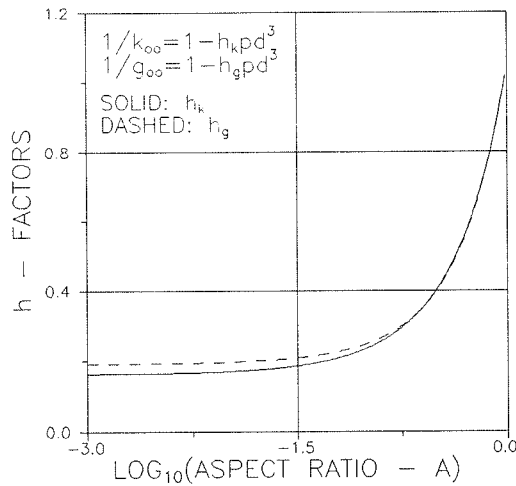
Figure 9.39. h-factors for stiff disc mixture.
$v_s = 0.2.$

presented in (7). It is furthermore concluded that "thick" cracks with $A < 0.01$ can be considered as real cracks. FEM-results reported in Section 9.1.2 from an analysis of a special cracked material have been compared with results predicted by the present theory. The comparison is satisfying. As can be seen from Figure 9.38, the FEM-results are somewhat underestimated by the theory because the cracks are defined to follow paths on imaginary TROC-particles (n = 1), creating, at the end, a porous material of finite stiffness.

9.3 Special DC-CD composite

The results presented in Figures 9.40 and 9.41 are from an analysis of a composite with the special DC-CD geometry described in Appendix E. In the example consi-

dered phase P is Silicon carbide (SiC) with E_P = 320 GPa and ν_p = 0.3. Phase S is Carbon (C) with E_s = 28 GPa and ν_s = 0.3. These phase properties are adopted from (15,16) where a FEM-analysis, further discussed in Section 9.3.1, was made on a layered SiC-C composite.
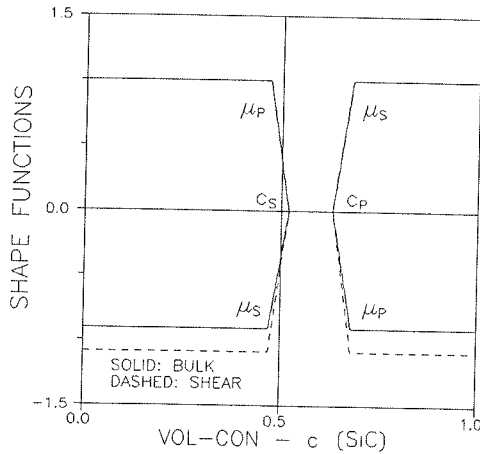
Figure 9.40. Shape functions for a special isotropic SiC/C composite.
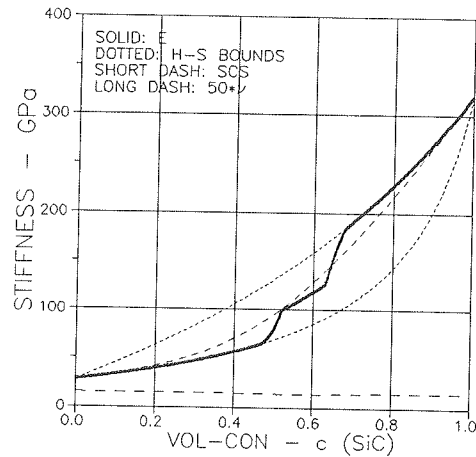
Figure 9.41. Stiffness of a special isotropic DC-CD SiC/C composite.

Remark: It is noticed that predicted stiffness and SCS-determined stiffness are very close in the geometrical transition area. It is obvious, however, that such simple procedure for stiffness estimation can only be used when the transition area is small with a "centre" around c = 0.5.

The author is aware of no results from experimental analysis or FEM-analysis of isotropic particulate DC-CD composites to which the results predicted in this section can be compared. Implicitly, however, justifications of the theory can be found studying the results from the following FEM-analysis.

9.3.1 Plane-isotropic fiber composite with long parallel fibres

A FEM-analysis was made in (15,16) on various mechanical/physical properties of a parallel-layered composite. With gradually increasing amount of phase P each layer can be considered as a plane-isotropic version of the isotropic composite just considered in Section 9.3 (and Appendix E): Up to a volume concentration of c = 0.47 the composite geometry is FEM-modelled by discrete phase P fibres of hexagonal cross-sections in a continuous phase S. From a concentration of c = 0.68 the geometry is modelled by discrete phase S fibres with hexagonal cross-sections in a continuous phase P. The agglomeration of P-fibres starts creating continuous phase P elements at c = 0.52. "De-agglomeration" of phase S into discrete fibres starts at c = 0.63.

It is observed in (16) that the numerical FEM-results obtained are very close to
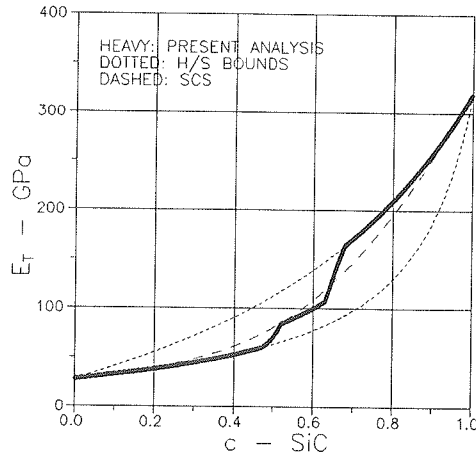
Figure 9.42. Stiffness of plane-isotropic composite with parallel circular fibres. (E_P, E_S) = (320,28) GPa, $\nu_P = \nu_S = 0.25$.

results which can be obtained in an analysis of the layered composite considered with each layer homogenized as follows with properties predicted by known analytical plane-isotropic composite expressions: By the Mori-Tanaka theory (11) at lower and higher concentrations (discrete cylinders in a continuum), and by the Davies SCS-expression (73) at medium concentrations (skeletal microstructure). The "gaps" between the two estimates (at c $\approx$ 0.49 and c $\approx$ 0.65) were considered in (16) by some empirical 'transition functions'.

The observation made in (15,16) with respect to plane-isotropic, transverse composite Young's moduli versus phase P concentrations are presented graphically in Figure 5 of the latter reference which is extremely well reproduced by Figure 9.42 presenting the results of a composite analysis made using the plane-isotropic version of the isotropic theory presented in this monograph, see Appendix C in (24).

With Poisson's ratios $\nu_P = \nu_S = 0.25$ the plane-isotropic analysis simplifies as summarized in Equation 9.8. The difference between the actual (0.3) and Poisson's ratios of 0.25 is considered small enough to use this expression as a reliable basis for numerical evaluations. Shape functions are assumed to be similar to those used in the isotropic counterpart analysis, see Appendix E.

Plane-isotropic stiffness: For DC-CD composites with fibres of circular cross-sections and $\nu_P = \nu_S = 0.25$ the plane-isotropic theory referred to can be summarized as presented in Equation 9.8 where $k_t = K_t/K_s$, $g_t = G_t/G_s$, and $e_t = E_t/E_s$, are transverse plane strain bulk modulus, transverse shear modulus, and transverse Young's modulus normalized with respect to their respective phase S moduli. The transverse Poissons's ratio is denoted by ν_t. The stiffness ratio is n = E_P/E_S.

$$k_t = g_t = \frac{n + \theta[1 + c(n - 1)]}{n + \theta - c(n - 1)} = x$$

$$e_t = \frac{16x}{15 + x/[1 + c(n - 1)]} \quad ; \quad \nu_t = 1.25\frac{e_t}{g_t} - 1 \tag{9.8}$$

$$\theta = \frac{1}{4}\left[\mu_P + n\mu_S + \sqrt{(\mu_P + n\mu_S)^2 + 4n(1 - \mu_P - \mu_S)}\right] \quad ; \quad H/S: \theta \equiv \begin{cases} 1/2 \\ n/2 \end{cases}$$

SCS-solutions are very close to solutions obtained by Equation 9.8 with shape functions $\mu_P = -\mu_S = 1 - 2c$.

9.3.2 Discussion

We may conclude from this section that theoretically predicted Young's moduli of a DC-CD composite agree well with results obtained by FEM-analysis.

The suggestion made in (15,16) of estimating stiffness by SCS and 'transition functions' in areas of geometrical transition is acceptable only in small transition areas around $c = 0.5$. The present theoretical approach of considering the transition geometry as a platework (crumbled foils) geometry is better, and more logical. This approach also provides a more continuous analysis, well qualified for computer analysis.

9.4 Conclusion

A general analysis of stiffness and eigenstrain/stress behavior has been presented in Chapter 8. Important aspects of this analysis, including the underlying geometrical concepts, have been checked successfully in this Chapter 9:

- Stiffness predictions of various composites, DC-DC, CC-CC, and DC-CD, compare positively with results obtained by FEM-analysis.

- Stiffness predictions of cracked materials compare positively with results obtained by FEM-analysis and theoretical results obtained by other authors.

- From the CROSS analysis presented in Section 9.1.4 is noticed that shape functions reverse from $(\mu_P,\mu_S) = (\mu_P^o,\mu_S^o)$ at $c = 0$ to $(\mu_P,\mu_S) = (\mu_P^1,\mu_S^1) = (\mu_S^o,\mu_P^o)$ at $c = 1$ when composite geometries reverse. The same observation can be made from looking at the special DC-CD composite analysis presented in Section 9.3.

  From the latter analysis is also observed that composite geometry changes from DC to CD through a transition area with shape functions $(\mu_P,\mu_S) = (0,0)$. These observations speak in favour of the concept, introduced in Chapter 7, of considering transition geometries as the result of discrete shapes agglomerating into crumbled continuous shapes.

It seems now justified to suggest that the theory developed in this monograph can be used, as summarized in Chapter 8, in a complete analysis of isotropic composite materials with arbitrary geometry. Results from real experiments reported in subsequent chapters support this statement. We re-call that positive conclusions with respect to stiffness predictions automatically imply positive conclusions with respect to stress and eigenstrain/stress predictions.

10. Simplified theory

It has been justified in Chapter 9 that a complete analysis of composites with arbitrary phase geometries can be made by the method developed in this monograph and summarized in Chapter 8. It is recognized, however, that the great many geometrical parameters (up to 10) and stiffness coefficients needed for such analysis are by far not present in most normal practice.

The purpose of this chapter is to show how the theory can be simplified to reflect more realistically the somewhat limited knowledge available in most practice on geometry and elasticity (Poisson's ratios especially). An implicit consequence of the simplifications introduced, is that a 'modest level' of geometrical knowledge is assumed, see Section 7.3.

A number of comparative studies have been made between results obtained by various simplified versions of the theory and results obtained by the accurate version as it is presented in Chapter 8. It has been found that very acceptable results are obtained introducing the following basic simplifications:

- Both Poisson's ratios are 0.2 (in most practice Poissons's ratios varies in 0.1 - 0.3).
- Both shape functions (μ_P, μ_S) can be approximated by their shear versions. They are quantified by two shape factors, μ_P°, μ_S°, and one critical concentration, for example c_s. They vary linearly all the way in c = 0 - 1 such that $\mu_P + \mu_S$ = a where the constant $0 \le a \le 1$ is the so-called geo-path factor a = $\mu_P^\circ + \mu_S^\circ$.

Immediate consequences of these assumptions are the following reductions: Poisson's parameters become $\kappa_S = \gamma_S = 1$, Stiffness ratios become $N_k = N_g = n_k = n_g = n$, Geo-functions become identical, $\theta_k = \theta_g = \theta$. Any internal stress component (σ_{Pij} and σ_{Sij}) relative to its external stress counterpart becomes predicted as σ_P/σ and σ_S/σ. Average normalized stiffness k = g = e are predicted. For typographical reasons this triviality is not always expressed. Thus, whenever e is mentioned subsequently k and g may as well be thought of - or vice versa.

A consequence of introducing the simplified description of shape functions is that the other shape factors μ_P^1, μ_S^1, and the other critical concentration appearing in the accurate analysis become dependent variables. For practice, however, this discrepancy can be counteracted by simple averaging measures explained in Section 10.1.3.

The subsequent presentation of the simplified theory and applications will follow the same disposition as used for the general theory: Description of geometry, quantification of geometry, preparation of analysis, and the analysis itself. The text is rather brief. As the 'translation' of accurate analysis to simplified analysis is rather obvious, no further explanations are really necessary. The presentation can be adapted and used immediately as a 'users manual' with operational introductions

to computer programs which can be downloaded from *http://www.byg.dtu.dk/pub-licering/software_d.htm*.

10.1 Basis of analysis

The composites considered in this analysis are isotropic mixtures of two linear elastic components: phase P and phase S. The amount of phase P is quantified by the so-called volume concentration defined by $c = V_P/(V_P + V_S)$ where volume is denoted by V. The volume concentration of phase S then becomes 1-c.

The specific composite properties considered are stiffness and eigenstrain phenomenons (such as shrinkage and thermal expansion) as related to volume concentration, composite geometry, and phase properties: Young's moduli E_P and E_S with stiffness ratio n = E_P/E_S and linear eigenstrains λ_P and λ_S. (Further notations used in the text are explained in the list of notations at the end of the paper).

The strength of the composite analysis presented, relative to other prediction methods (with fixed, not variable type of composite geometry such as spheres and fibres in a matrix), is that global (standard) solutions are presented which apply for any composite geometry. Specific composites are considered in these global solutions by so-called 'geo-functions' (θ, Equation 10.2) where specific geometries are quantified by so-called 'shape functions' (μ_P, μ_S, Equation 10.1). Thus, properties can be predicted where geometry can be respected as it really develops in natural or man-made composite materials.

10.1.1 Geometry

As demonstrated in Figure 10.1 composite geometry can be described by so-called shape functions which are determined by so-called shape factors (μ_P°, μ_S°) and critical concentrations, c_P and $c_S \leq c_P$: Shape factors tell about the shapes of phase components at dilute concentrations. Critical concentrations are concentrations where the composite geometry changes from one type to another type.

At fixed concentrations we operate with the following types of composite geometries[3]: DC means a discrete phase P in a continuous phase S. MM means a mixed phase P geometry in a mixed phase S geometry, while CD means a continuous

---

3) A phase with continuous geometry (C) is a phase in which the total composite can be traversed without crossing the other phase. This is not possible in a phase with discrete geometry (D). A mixed geometry (M) is a continuous geometry with some discrete elements.

phase P mixed with a discrete phase S. We notice that MM-geometries (if porous) are partly impregnable. In modern terminology this means that phase P percolation exists in composites with c > c_S. Percolation is complete for c $\geq$ c_P. Porous materials have lost any coherence in this concentration area with no stiffness and strength left.
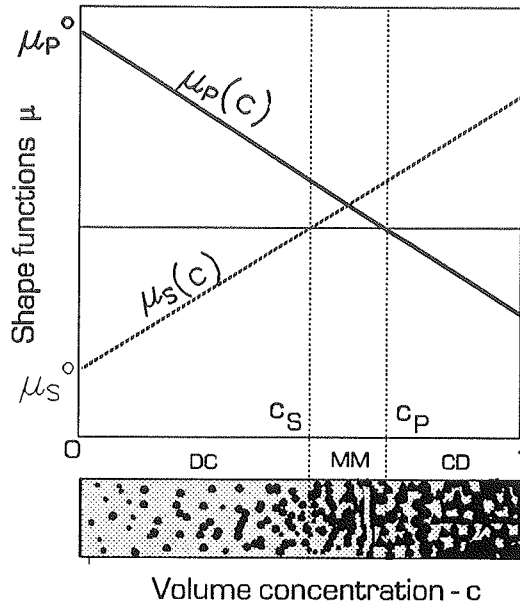
Figure 10.1. Geometrical significance of shape functions. (μ_P, μ_S) = $(+,-)$ means discrete P in continuous S. (μ_P, μ_S) = $(+, +)$ means mixed P in mixed S. (μ_P, μ_S) = $(-, +)$ means continuous P with discrete S. Black and white signatures denote phase P and phase S respectively.

Composite geometries may change as the result of volume transformations associated with increasing phase P concentration. We will think of changes as they are stylized in Figure 10.1: At increasing concentration, from c = 0, discrete P elements agglomerate and change their shapes approaching a state at c = c_S where they start forming continuous geometries. Phase P grows fully continuous between c = c_S and c = c_P such that the composite geometry is a mixture of a continuous phase P with discrete de-agglomerating phase S particles from the concentration of c = c_P.

In a complementary way the geometry history of phase S follows the history of phase P and vice versa. The geometries just explained can be shifted along the concentration axis. A composite may develop from having a DC geometry at c = 0 to having a MM geometry at c = 1. Such composite geometries, with c_P > 1 and 0 < c_S < 1, are named DC-MM geometries. Other composites may keep their DC type of geometry all the way up to c = 1 in which case the composite geometry is denoted as a DC-DC geometry, with both critical concentrations > 1. The geometry outlined in Figure 10.1 changes from DC to CD geometry which makes it a DC-CD geometry with both critical concentrations in c = 0-1.
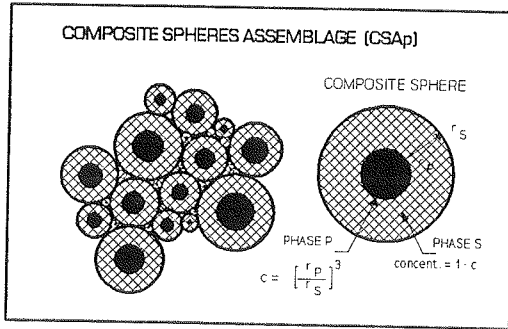
Figure 10.2. Composite spherical assemblage with phase P particles, CSA_P.
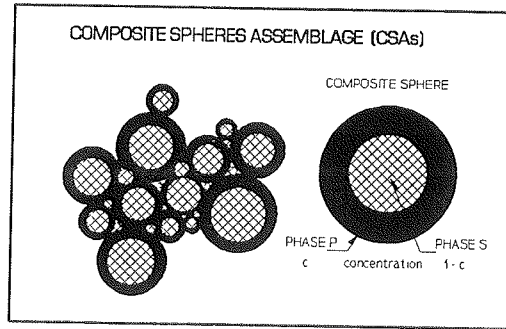
Figure 10.3. Composite Spheres Assemblage with phase S particles (CSA_S).

Ideal geometries at c = 0 and at c = 1 of a DC-CD composite are illustrated in Figures 10.2 and 10.3 respectively. We notice in this context that the composite theory developed in the present monograph is based on the concept that any isotropic composite geometry is a station on a geo-path going from the CSA_P geometry shown in Figure 10.2 to the CSA_S geometry shown in Figure 10.3. CSA is an abbreviation of Composite Spheres Assemblage introduced by Hashin in (4). It is noticed that the four letter symbols for composite geometries are subsequently also used in the meaning, a 'DC-CD type of composite' or just a 'DC-CD composite'.
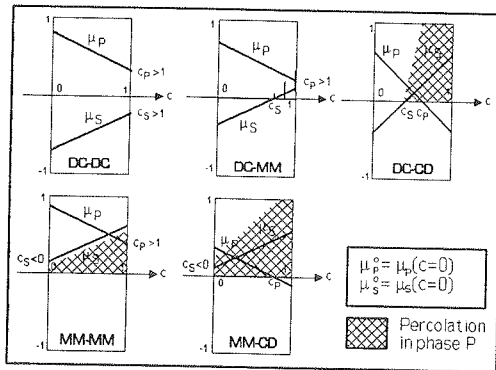
Figure 10.4. Composite types versus critical concentrations. Former and latter two letters denote composite geometry at c = 0 and at c = 1 respectively.

10.1.2 Quantification of composite geometry

The various types of geometries considered are listed in Figure 10.4 which defines the following two composite classes considered in this chapter: *Particulate composites* are defined by the former row. They have a 'particles in a matrix' geometry (DC) at small concentrations. *Lamella composites* are defined by the latter row. They have a mixed phase P geometry in a mixed phase S geometry (MM) at low concentrations. The phenomenon of percolation previously considered is noticed to appear in Figure 10.4 in concentrations areas indicated by grey shadings (c > c_s).

We emphasize that the terms 'particulate composites' and 'lamella composites' are 'working' terms telling about composite geometry at small concentrations only. A number of other geometries may develop as the result of increasing volume concentrations.

Particle shapes - Aspect ratio

Particle shapes are subsequently referred by their aspect ratios A = length/diameter of particles. Spherical particles have A = 1. Long particles (fibres) have A > 1. Flat particles (discs) have A < 1.

SHAPE FACTORS
Particulate composite with uni-shaped particles (DC)
$$\mu_P^o = \begin{cases} \dfrac{3A}{A^2 + A + 1} & ; \ A \le 1 \\ 3\dfrac{A^2 - A + 1}{4A^2 - 5A + 4} & ; \ A > 1 \end{cases} \quad ; \quad \mu_S^o = -\begin{cases} \mu_P^o & ; \ A \le 1 \\ 4\mu_P^o - 3 & ; \ A > 1 \end{cases}$$
Particulate composite with multi-shaped particles (DC) [4]
$$\mu_P^o = <m_o> \quad ; \quad \mu_S^o = -<m_\infty> \frac{1 - <m_o>}{1 - <m_\infty>} \quad with$$ $$<m_j> = \left[\sum_{i=1}^{\infty} \frac{\alpha_i}{m_{j,i}} \right]^{-1} \quad ; \quad j = o, \infty \quad ; \quad \sum_{i=1}^{\infty} \alpha_i = 1$$ where α_i is volume fraction of joining aspect ratio A_i and $$m_\infty = \frac{3A}{A^2 + A + 1} \qquad for \ any \ A$$ $$m_o = \begin{cases} m_\infty & for \ A \le 1 \\ \dfrac{3 - 2m_\infty}{4 - 3m_\infty} = 3\dfrac{A^2 - A + 1}{4A^2 - 5A + 4} & for \ A > 1 \end{cases}$$
Composite with transition geometry (MM)
$$\mu_P^o = a(1 - \gamma) \quad ; \quad \mu_S^o = a\gamma$$ P-geometries getting continuous   Degree of transforming DC to CD $$a \approx \begin{cases} 1-0.75 & fibres \\ 0.5 & fibre/disc \ mix \\ 0 & discs \ and \ plates \end{cases} \qquad \gamma \approx \begin{cases} 0 & starting \\ 0.5 & medium \\ 1 & complete \end{cases}$$

Table 10.1. Shape factors to be used in simplified theory. The so-called geo-path factor is determined as $a = \mu_P^o + \mu_S^o$.

---

4) For first estimate determination of shape factors for particulate composites with multi shaped particles a very easy formula is presented in Appendix B, Equation B8.

Shape factors and geo-paths

Shape functions μ_P and μ_s are related as illustrated in Figure 10.5 which is a modified reproduction of Figure 7.19 in the present monograph. The geometries passed when the phase P concentration increases from c = 0 to c = 1 are indicated in this figure by the geo-path.

Shape factors can be calculated from Table 10.1 which represents a summary of the accurate shape factor determination in Section 7.1 - except that the shape factors for particulate composites with uni-shaped particles, Equation 7.6, have been introduced by their approximations presented in Appendix B, assuming shear and $\nu_S = 0.2$.
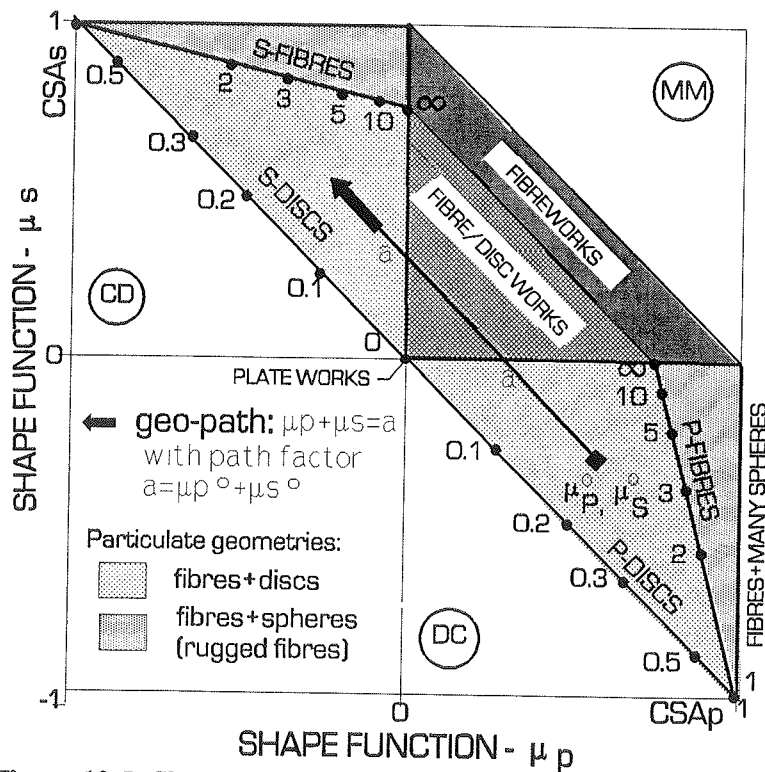
Figure 10.5. Shape function graph with geo-path. Numbers indicate fibre aspect ratio A of particles. Fibreworks are agglomerating crumbled fibres. Fibre/discworks are agglomerating crumbled fibres + discs. Plateworks are crumbled discs (sheets, foils).

Critical concentrations

It is emphasized that the critical concentrations depend very much on the processing technique used to produce composites. We notice that particle size distribution is part of the processing. For particulate composites, for example, the critical concentration c_s can be thought of as the concentration at first interference of phase P

particles. Improved quality of size distribution (smoothness and density) is considered by increasing c_S. At this concentration porous materials become very stiff when impregnated with a very stiff material. At the other critical concentration, $c = c_P$, the composite becomes a mixture of phase S elements completely wrapped in a matrix of phase P. As previously mentioned porous materials loose their stiffness and strength at c_P because phase P has become a continuous void system.

It is noticed that critical concentrations can be fictitious (outside $c = 0 - 1$). In such cases they do not, of course, have the immediate physical meanings just explained. Theoretically, however, we may keep the explanation given in order to describe in an easy way how the rate of changing the composite geometry is influenced by the processing technique used. In such fictitious cases critical concentrations will have to be estimated from experience, or detected from calibration experiments.

TYPE		Crit-con c_S	EXAMPLES
DC	DC	$c_S > 1$	Particulate composite (concrete, mortar). Extremely high quality of grading (approaching CSA_P composites). *Pore system:* Not impregnable. Finite stiffness at any porosity
	MM	$1 > c_S > -\mu_S{}^\circ/\mu_P{}^\circ$	Particulate composite (concrete, mortar) with particle interference at $c = c_S$. Increasing quality of grading is quantified by larger concentration c_S at first interference. *Pore system:* Only impregnable for porosities $c > c_S$. Finite stiffness at any porosity.
	CD	$-\mu_S{}^\circ/\mu_P{}^\circ > c_S > 0$	Mixed powders (ceramics). *Pore system:* Only impregnable for porosities $c > c_S$. No stiffness for porosities $c > c_P$.
MM	MM	$-\mu_S{}^\circ/\mu_P{}^\circ > c_S$	Mixed lamella/foils ("3D-plywood"). *Pore system:* Fully open at any porosity. Finite stiffness at any porosity.
	CD	$0 > c_S > -\mu_S{}^\circ/\mu_P{}^\circ$	Mixed lamella/foils ("3D-plywood"). *Pore system:* Fully open at any porosity. No stiffness for porosities $c > c_P$.

Table 10.2. Range of critical concentrations applying for various composites.

10.1.3 Preparation of composite analysis

The preparation of a composite analysis is as follows:

- Calculate shape factors $(\mu_P{}^\circ, \mu_S{}^\circ)$ from Table 10.1. (Or for first estimate analysis: read directly from Figure 10.5).
- Then decide the critical concentration c_S (or c_P) from knowing about mixing technology and observations made on geometrical formation.

91

- These information quantify the composite geometry by the so-called shape functions expressed by Equation 10.1.

We recall from the introductory section to this chapter: Shape functions are expressed by simple mathematical expressions (in order not to predict properties with an 'accuracy' out of proportions to what is actually know about composite geometry). A consequence of such simplification is that the quantities of $(\mu_P{}^o, \mu_S{}^o)$ and $(c_s$ or $c_p)$ chosen above must be adapted to each other such that the critical concentration not chosen is predicted realistically by Equation 10.1. Figure 10.4 and Table 10.2 are useful when deciding on realistic shape functions for a practical composite analysis. An example of shape quantification is shown in Figure 10.6.

$$\mu_S = MIN\left[\mu_S^o\left[1 - \frac{c}{c_S}\right], 1\right] \quad ; \quad \mu_P = \mu_P^o\left[1 - \frac{c}{c_P}\right] \quad with \quad c_P = -\frac{\mu_P^o}{\mu_S^o}c_S$$

$$Geo\text{-}path: \quad \mu_S = \begin{cases} a - \mu_P & for \quad \mu_P > a - 1 \\ 1 & for \quad \mu_P \leq a - 1 \end{cases} \quad where \quad a = \mu_P^o + \mu_S^o \qquad (10.1)$$
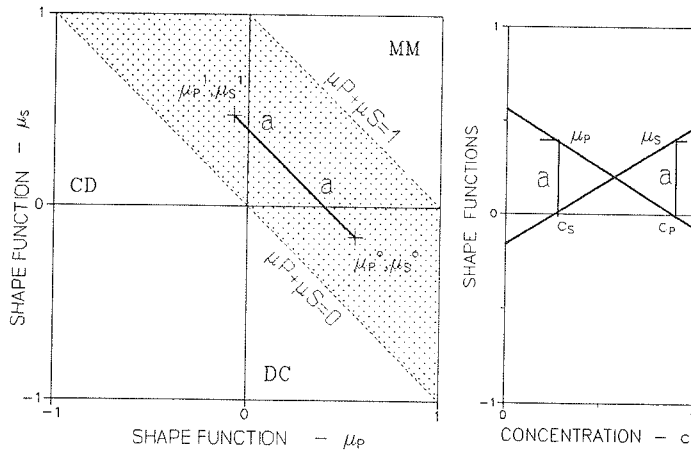
Figure 10.6. *Geo-path and shape functions for a DC-CD composite with multi shaped particles at c = 0 (20% A = 0.1 + 80% A = 10) and a critical concentration of c_s = 0.26.*

- The last step of preparing a composite analysis with the global solutions (valid for any geometry) presented in Table 10.3 is to calculate the so-called geo-function expressed by Equation 10.2.

$$\theta = \frac{1}{2}\left[\mu_P + n\mu_S + \sqrt{(\mu_P + n\mu_S)^2 + 4n(1 - \mu_P - \mu_S)}\right] \quad ; \quad n = \frac{E_P}{E_S} \qquad (10.2)$$

10.2 Composite analysis

With composite geometry described by the geo-function presented in Equation 10.2 a property analysis can now be made using the following global predictions with symbols explained in the list of notations presented at the end of the paper.

STIFFNESS
$$e = g = k = \dfrac{n + \theta[1 + c(n - 1)]}{n + \theta - c(n - 1)}$$

STRESS CAUSED BY EXTERNAL LOAD
$$\dfrac{\sigma_P}{\sigma} = \dfrac{n(1 + \theta)}{n + \theta[1 + c(n - 1)]} \quad ; \quad \dfrac{\sigma_S}{\sigma} = \dfrac{n + \theta}{n + \theta[1 + c(n - 1)]}$$ $or \quad \dfrac{\sigma_P}{\sigma} = \dfrac{1/e - 1}{c(1/n - 1)} \quad ; \quad \dfrac{\sigma_S}{\sigma} = \dfrac{1/n - 1/e}{(1 - c)(1/n - 1)}$

EIGENSTRAIN
$$\lambda = \lambda_s + \Delta\lambda \dfrac{1/k - 1}{1/n - 1} \quad ; \quad (\Delta\lambda = \lambda_P - \lambda_s)$$
$$\dfrac{\lambda}{\lambda_s} = \dfrac{1/n - 1/k}{1/n - 1} \quad ; \quad (\lambda_P = 0)$$

EIGENSTRESS ($K_S \approx E_S/1.8$)
$$\rho_P = -3K_S\Delta\lambda\dfrac{c(1/n - 1) - (1/k - 1)}{c(1/n - 1)^2} \quad ; \quad \rho_S = -\dfrac{c}{1 - c}\rho_P$$

Table 10.3. Stiffness, stress, and eigenstrain/stress of composite material calculated by simplified method of analysis. (λ_P, λ_S) and (ρ_P, ρ_S) are eigenstrain (linear) and eigenstress (hydrostatic) of phase P and phase S respectively. K_S is bulk modulus of phase S.

10.2.1 Bounds and other accurate stiffness expressions

It comes from (24,48) and the present monograph that the above stiffness predictions are bounded as follows between the exact solutions for the CSA composites illustrated in Figures 10.2 and 10.3.

$$\frac{n + 1 + c(n - 1)}{n + 1 - c(n - 1)} \leq e \leq n\frac{2 + c(n - 1)}{2n - c(n - 1)} \quad (n \geq 1)$$
$$reverse \ signs \ when \ n < 1 \tag{10.3}$$
$$e(n,c) * e(1/n,c) = 1 \quad ; \quad e(n,c) = n * e(1/n,1-c)$$
$$CSA_P \qquad\qquad\qquad Phase-symmetric$$

The stiffness bounds are obtained introducing $\theta \equiv 1$ and $\theta \equiv n$ respectively into the stiffness expression of Table 10.3. The bounds such determined are the same

as can be obtained from the studies made by Hashin and Shtrikman in (3) on composite stiffness. The bounds are subsequently referred to by H/S. The latter two relations in Equation 10.3 are reproduced from (24). They express some interesting relations between e, c, and n for CSA_P- and phase-symmetric composites respectively. In the present context: TROC (approximately) and CROSS composites.

10.2.2 Test of simplified theory

To test the accuracy of the simplified theory a composite analysis has been made on the TROC material and the phase symmetric CROSS material previously considered with $\nu_P = \nu_S = 0.2$. The geo-parameters used, see Figures 10.7 and 10.8, are calibrated from the FEM-results reported in Sections 9.1.1 and 9.1.4 respectively. The results of the analysis are shown by solid lines in Figures 10.9 - 10.12. Dots are FEM-data.
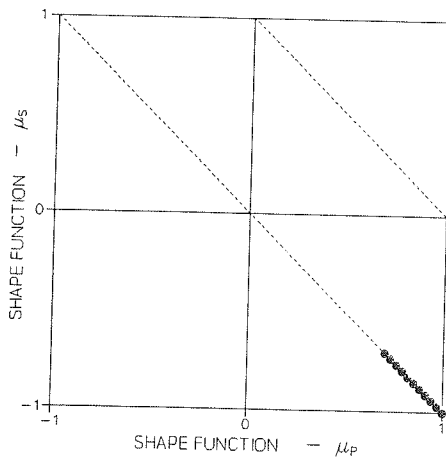
Figure 10.7. TROC: DC-DC composite with $(\mu_P{}^o, \mu_S{}^o, c_s) = (1,-1,3.33)$, $(c_P = 3.33)$.
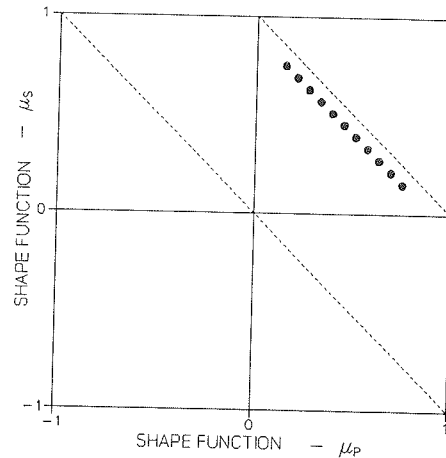
Figure 10.8. CROSS: Phase-symmetric MM-MM: $(\mu_P{}^o, \mu_S{}^o, c_s) = (0.75, 0.15, -0.25)$, $(c_P = 1.25)$.
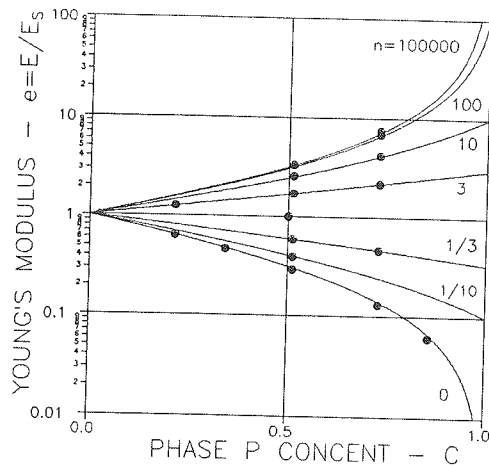
Figure 10.9. TROC: Young's modulus predicted by simplified theory.
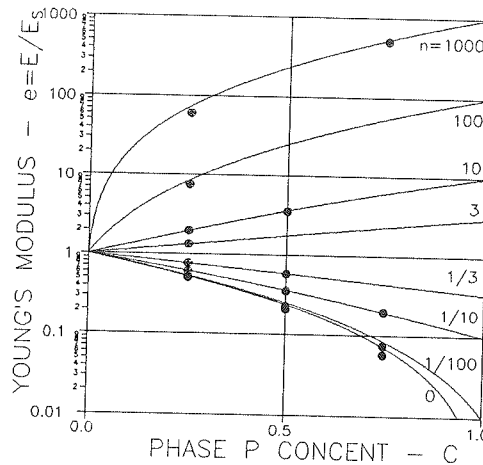
Figure 10.10. CROSS: Young's modulus predicted by simplified theory.

94
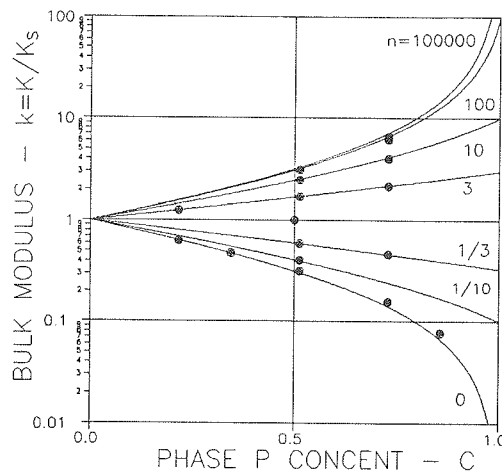
Figure 10.11. TROC: Bulk modulus predicted by simplified theory.
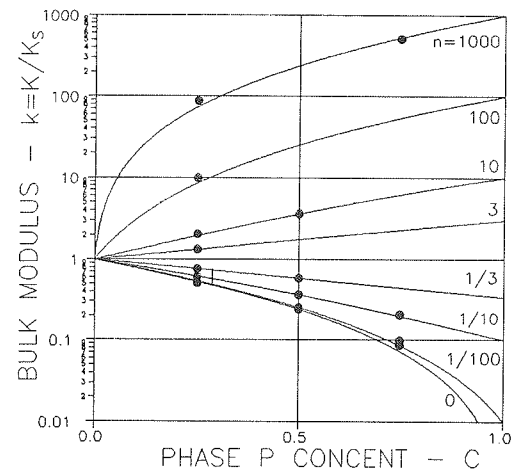
Figure 10.12. CROSS: Bulk modulus predicted by simplified theory.

10.2.3 Intermediate conclusion

We notice from Figures 10.7 and 10.8 that the calibrated geo-parameters are consistent with values suggested in Section 10.1.2 for a simplified analysis. It is furthermore observed from Figures 10.9 - 10.12 that results predicted by the simplified theory are very close to the more accurately predicted results presented in Chapter 9.

It seems then justified to proceed the analysis of composite materials using the simplified theory. First by looking at the theoretical potentials of the theory in Section 10.3 and then by looking at practical applications in Chapter 11.

10.3 Illustrative examples

Theoretical examples are considered in this section which illustrate how the simplified theory works in the analysis of various composite materials such as particulate composites, phase-symmetric composites and porous materials. Numerically the analysis is made by Table 10.3 with geo-functions (and shape functions) from Equation 10.2 (and Equation 10.1). Whenever possible, however, full analytical solutions are presented in order to illustrate most clearly the basic influence of geometry on the behavior of composite materials. Practical examples are presented in Chapter 11 where the theory is tested against real experimental data.

10.3.1 Composites with spherical particles (CSA$_p$)

As previously mentioned a CSA$_p$ composite has a geo-function of $\theta = 1$. A complete composite analysis can easily be made by Table 10.3. The results are presented in Table 10.4. The additional solutions of the matrix stresses at spheres are

95

developed in (61,62) from the Sokolnikoff stress solutions (57) of a hollow sphere subjected to internal pressure (equal to pressure in phase P). We re-call that the stiffness of a CSA_P composite represents the lower H/S bound solution for $n > 1$, and the lower H/S bound solution for $n < 1$.

Some results of an eigenstrain/stress analysis are graphically presented in Figures 10.13 and 10.14.

PROBLEM	CSA_P-SOLUTIONS
Young's modulus	$e = \dfrac{E}{E_S} = \dfrac{A + n}{1 + An}$ with $A = \dfrac{1 - c}{1 + c}$ and $n = \dfrac{E_P}{E_S}$
Internal stress caused by external stress σ	$\sigma_P = \sigma \dfrac{(1 + A)n}{A + n}$; $\sigma_S = \dfrac{\sigma - c\sigma_P}{1 - c}$
Eigenstrain/stress caused by particle eigenstrain λ_P and matrix eigenstrain λ_S	$\lambda = \lambda_S + \Delta\lambda \dfrac{n(1 - A)}{A + n}$; $\Delta\lambda = \lambda_P - \lambda_S$ $\rho_P = -3K_P\Delta\lambda \dfrac{A}{A + n}$; $\rho_S = -\dfrac{c}{1 - c}\rho_P$; $K_P = \dfrac{E_P}{1.8}$
Matrix-stress at spheres	$\sigma_{S,RAD} = \rho_P$; $\sigma_{S,TAN} = -\dfrac{3 - A}{4A}\rho_P$

Table 10.4. Composite analysis of CSA_P-material. In eigenstrain/stress analysis: (λ_P, λ_S) and (ρ_P, ρ_S) are eigenstrain (linear) and eigenstress (hydrostatic) of phase P and phase S respectively. $\sigma_{S,RAD}$ is radial phase S stress at sphere, $\sigma_{S,TAN}$ is tangential phase S stress at sphere.
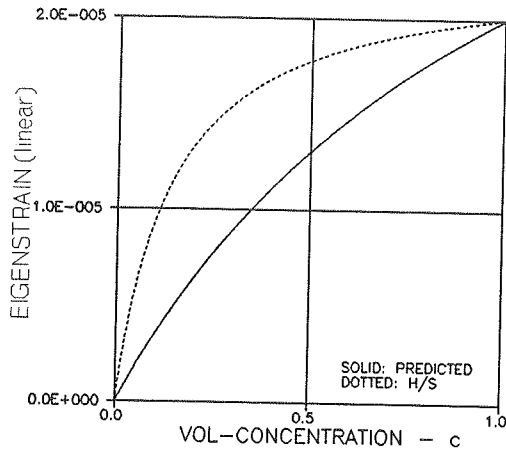
Figure 10.13. Thermal eigenstrain/°C of CSA_P composite $(E_P, E_S) = (15,1)*10^2$ MPa. $(\lambda_P, \lambda_S) = (2*10^5, 0)/°C$.
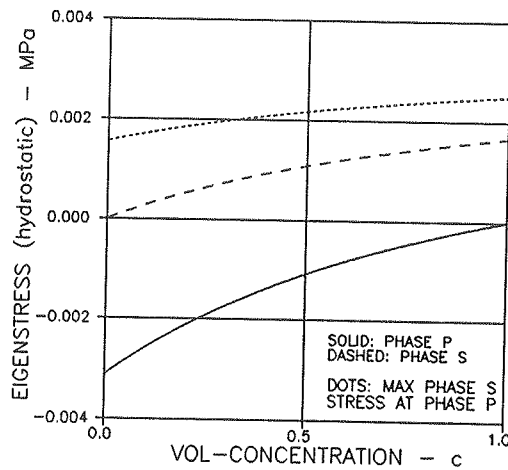
Figure 10.14. Thermal eigenstress/°C in CSA_P composite $(E_P, E_S) = (15,1)*10^2$ MPa. $(\lambda_P, \lambda_S) = (2*10^5, 0)/°C$.

96

Nearly CSA_P composites

We look at particulate DC-DC composites with spherical particles (aspect ratio $A = 1$). According to the simplified composite theory, shape factors for such composites are $\mu_P^\circ = -\mu_S^\circ = 1$ with critical concentrations $c_P = c_S > 1$. A composite analysis proceeds with the following geo-function introduced in Table 10.3.

$$\theta = \frac{1}{2}\left[D + \sqrt{D^2 + 4n)}\right] \quad \text{with} \quad D = \mu_P^\circ(1 - n)\left[1 - \frac{c}{c_S}\right] \ ; \ n = \frac{E_P}{E_S} \quad (10.4)$$
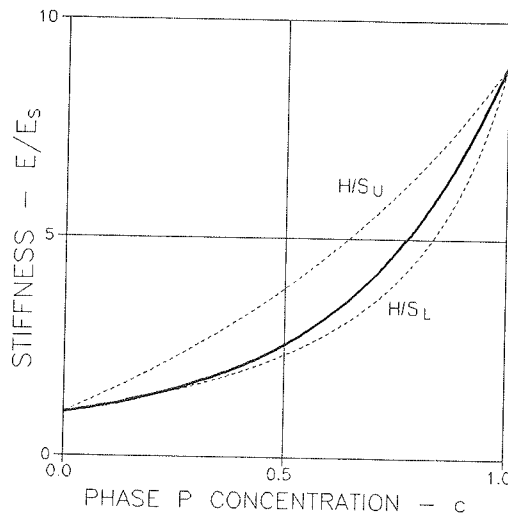
Figure 10.15. Stiffness of a nearly CSA_P composite with $c_P = 1$ and $n = 9$.
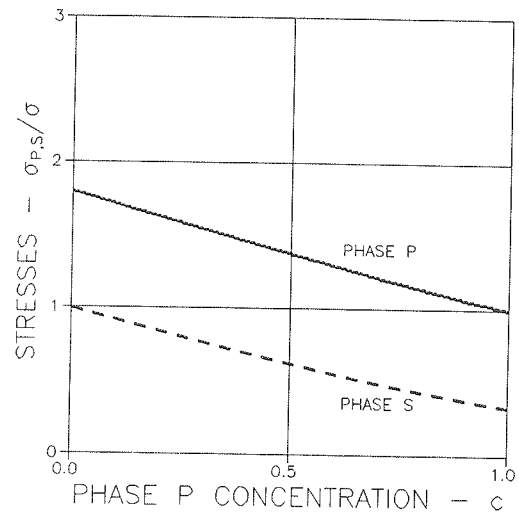
Figure 10.16. Stresses in a nearly CSA_P composite with $c_P = 1$ and $n = 9$.

Comment: As previously mentioned, the critical concentration c_S tells about quality of the phase P size distribution (smoothness and density). Increasing quality is associated with increasing c_S. CSA_P composites have an extremely high quality of size distribution, $c_S = \infty$. Some results from a composite analysis of a nearly CSA_P composite with a less ideal size P distribution ($c_S = 1$) are shown in Figures 10.15 and 10.16.

10.3.2 Phase symmetric composites

Looking at composites which change geometry along a disc path with $\mu_P = -\mu_S$ (see Figure 10.5) we get coinciding critical concentrations, $c_P = c_S = 0.5$, from Equation 10.1 which produces the geo-function presented in Equation 10.5, forming the basis for the analysis of so-called phase-symmetric compacted powder composites (DC-CD) and phase-symmetric compacted lamella composites (MM-MM).

$$\theta = \frac{1}{2}\left[D + \sqrt{D^2 + 4n}\right]$$
$$D = \mu_P^o(1 - 2c)(1 - n)$$
$$; \quad c_P = c_S = 0.5 \qquad\qquad (10.5)$$
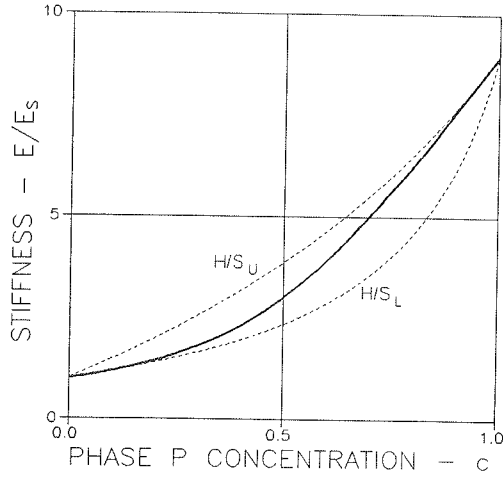
Figure 10.17. Stiffness of spherical-powder composite with n = 9.
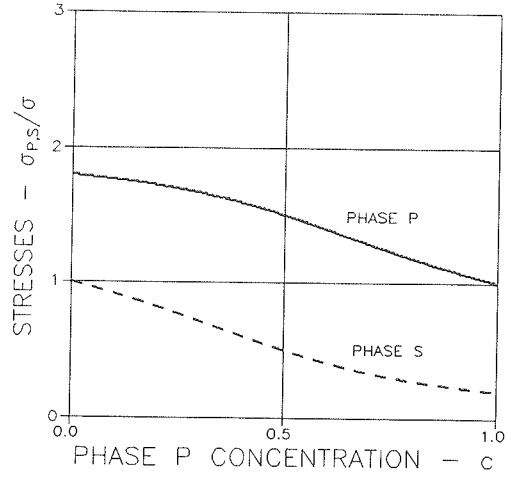
Figure 10.18. Stresses in spherical-powder composite with n = 9.

Example 1: Compacted spheres composite

A special phase-symmetric composite is the one made with compacted spherical-powders ($\mu_P^o = 1$). The geo-function for this composite becomes as expressed by Equation 10.6 by which the stiffness solution presented in Equation 10.7 is predicted from Table 10.4. Stiffness and other results of a composite analysis by Table 10.4 are demonstrated in Figures 10.17 - 10.20.

$$\theta = \frac{1}{2}\left[D + \sqrt{D^2 + 4n}\right]$$
$$D = (1 - n)(1 - 2c)$$
$$; \quad \begin{cases} Spheres: \\ c_S = c_P = 0.5 \end{cases} \qquad (10.6)$$

$$e = \frac{1}{2}\left[(1 - n)(1 - 2c) + \sqrt{(1 - n)^2(1 - 2c)^2 + 4n}\right] \qquad (10.7)$$

Remarks: It is observed that Equation 10.7 is exactly the same expression as can be deduced from the analysis of Budiansky (13) on phase-symmetric composites made of compacted spheres.

It is of some interest to notice that Equation 10.7 relates to the simple P/H-bounds as illustrated in Figure 10.21. It is also interesting to notice that Equation 10.7

98

can be obtained implicitly from the general stiffness expression in Table 10.3 by introducing $\theta = e$.
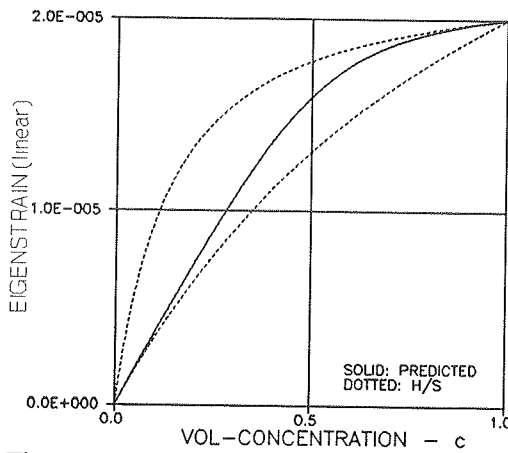
Figure 10.19. Thermal eigenstrain/°C of spherical powder composite. (E_P, E_S) = $(15,1)*10^2$ MPa. (λ_P, λ_S) = $(2*10^5, 0)/°C$.
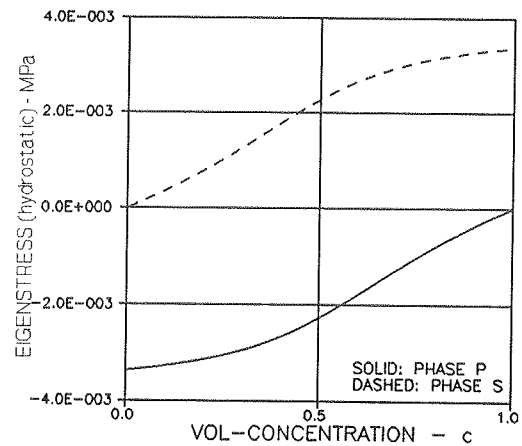
Figure 10.20. Thermal eigenstress/°C in spherical powder composite. (E_P, E_S) = $(15, 1)*10^2$ MPa. (λ_P, λ_S) = $(2*10^5, 0)/°C$.
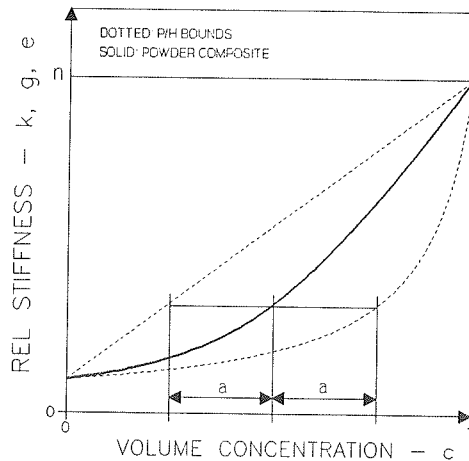
Figure 10.21. Stiffness of spherical powder composite is "horizontal mean" of P/H bounds.

Example 2: Compacted lamella composite

A compaction of a mixture of crumbled P-plates and S-plates with $\mu_P{}^\circ = 0$ can be thought of as the plate counterpart to the compacted spheres composite just considered. A geo-function of $\theta = \sqrt{n}$ is obtained from Equation 10.5 which is the same geo-function applying for the crumbled foils composite previously considered in Section 4.1.4. The composite stiffness obtained from Table 10.3 is presented

in Equation 10.8 with examples shown in Figure 10.22. The results of a subsequent stress analysis are illustrated in Figure 10.23.

$$e = \frac{n + \sqrt{n}\,[1 + c(n - 1)]}{n + \sqrt{n} - c(n - 1)} \qquad\qquad (10.8)$$
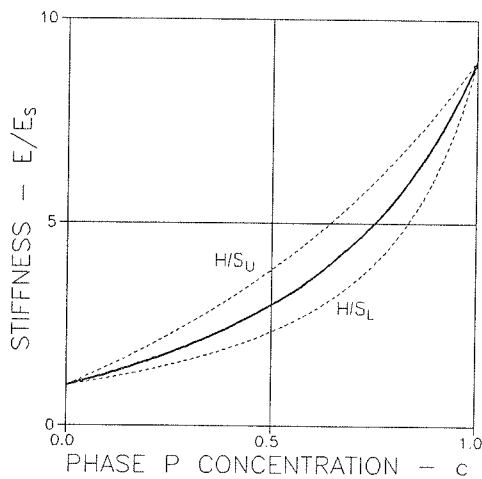
Figure 10.22. *Stiffness of crumbled foils composite with n = 9.*
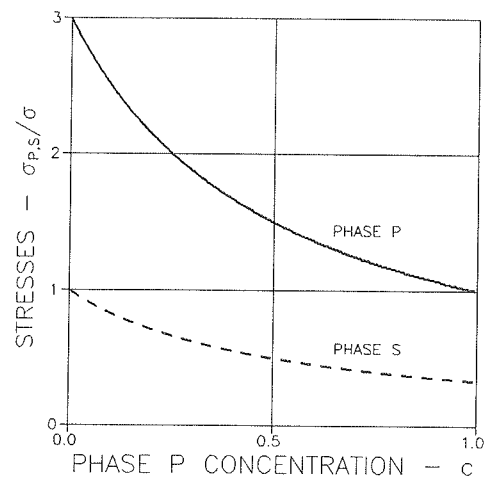
Figure 10.23. *Stresses in crumbled foils composite with n = 9.*

10.3.3 Eigenstrain/stress versus geometry

The influence of phase geometry on composite shrinkage and stresses is demonstrated in this section. We proceed using the simplified composite analysis as summarized in Table 10.3.
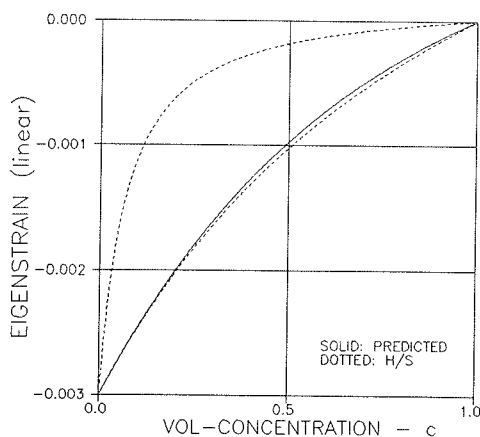
Figure 10.24. *Eigenstrain (shrinkage) of TROC composite with shrinking phase S.*
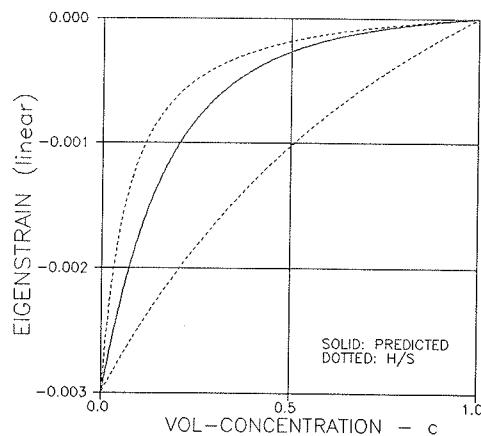
Figure 10.25. *Eigenstrain (shrinkage) of CROSS composite with shrinking phase S.*

100

The TROC (DC-DC) and CROSS (CC-CC) composites previously defined are considered with geo-parameters, phase properties, and eigenstrains assumed as follows.

TROC	$(\mu_P^o, \mu_S^o, c_S) = (1, -1, 3.33), (c_P = 3.33)$
CROSS	$(\mu_P^o, \mu_S^o, c_S) = (0.75, 0.15, -0.25), (c_P = 1.25)$
Phase S:	$E_S = 1000$ MPa, Shrinkage, $\lambda_S = -3\%o$
Phase P:	$E_P = 30000$ MPa, Shrinkage, $\lambda_P = 0$

The results of an eigenstrain/stress analysis are presented in Figures 10.24 - 10.27.
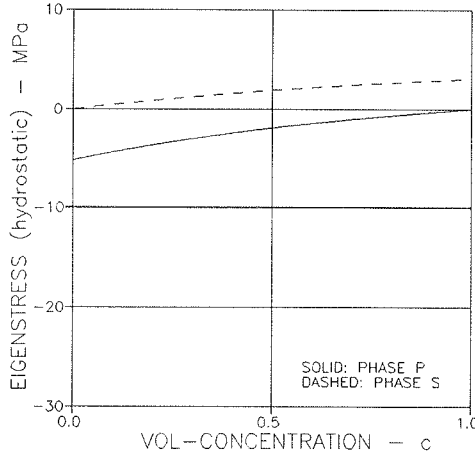
Figure 10.26. Eigenstress in TROC composite with shrinking phase S.
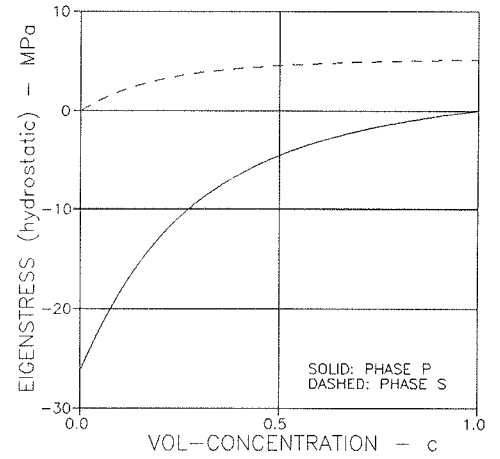
Figure 10.27. Eigenstress in CROSS composite with shrinking phase S.

10.3.4 Porous materials

Porous materials are composites where one phase is an empty pore system. In the present context we consider phase P to be pores. Porosity and stiffness ratio are then given by c and n = 0 respectively from which the following stiffness expression is easily obtained by the simplified analysis with a geo-function of $\theta = \mu_P$. Stiffness is identical 0 whenever negative values are predicted.

$$e = \frac{1 - c}{1 + c/\theta_o} \quad with \quad \theta_o = \begin{cases} \mu_P = \mu_P^o(1 - c/c_p) & when \ c < c_p \\ 0 & when \ c > c_p \end{cases} \quad (10.9)$$

$$e \rightarrow 1 - \left[1 + \frac{1}{\mu_P^o}\right] c \qquad as \quad c \rightarrow 0$$

Examples of stiffness predictions by Equation 10.9 are presented graphically in Figures 10.28 and 10.29. An easy approximation of Equation 10.9 is presented

in Equation 10.10 with e $\equiv$ 0 for c > c_P. Qualitatively Equation 10.10 applies at any c_P < 1. Quantitatively, however, it is best when c_P and $\mu_P{}^\circ$ are related as indicated.

$$e \approx \left[1 - \frac{c}{c_P}\right]^D \; ; \; D = c_P\left[1 + \frac{1}{\mu_P^o}\right] \; for \; c_P \leq \begin{cases} 1 & if \; \mu_P^o > 0.5 \\ \mu_P^o & if \; \mu_P^o < 0.5 \end{cases} \quad (10.10)$$

Remark: This equation tells us that stiffness of porous materials can be predicted approximately by a very simple porosity relation raised to a power reflecting only the pore geometry. In general (with a fixed c_P) this power will increase with increasing complexity of the pore geometry (decreasing $\mu_P{}^\circ$).
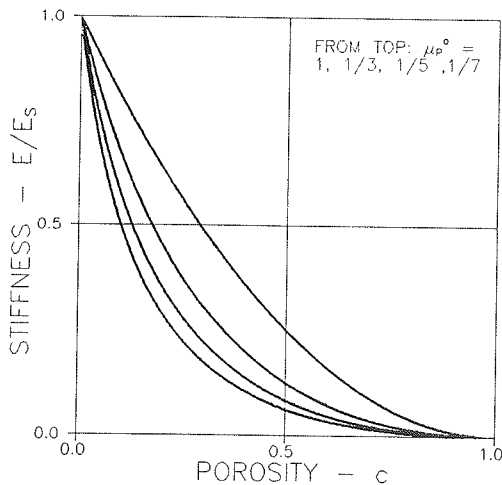
Figure 10.28. Porous material with shape factors as indicated, and c_P = 1.
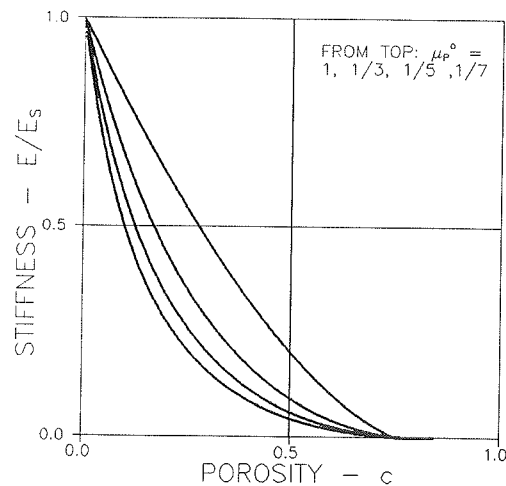
Figure 10.29. Porous material with shape factors as indicated, and c_P = 0.75.

Theory versus empirical expressions

A variety of empirical stiffness-porosity expressions, critically reviewed by Fager-lund in (20), are presented in the literature on porous materials. It is of some interest to discuss briefly Equations 10.9 and 10.10 in relation to the two expressions presented in Equation 10.11 which are among the most frequently used to fit data obtained from tests on porous media - the former in (74,75) and the latter in (76,77) for example. F and H are constants to be determined experimentally.

$$\left. \begin{array}{l} e = (1 - c)^F \\ e = \exp(-Hc) \end{array} \right\} \rightarrow \begin{cases} 1 - Fc \\ 1 - Hc \end{cases} \; as \; c \rightarrow 0 \quad (10.11)$$

102

Excellent fits are often observed by these expressions at low and moderately low porosities. At higher porosities, however, difficulties may be encountered. The former expression cannot be used when DC-CD and MM-CD composites are considered with $c_P < 1$. The latter expression always predicts a finite stiffness at $c = 1$. Non of these disadvantages apply to Equations 10.9 and 10.10.

Remark: Mathematically the expressions presented in Equations 10.10 and 10.11 are of similar types. It is concluded that the factors F and H of the empirical expressions are related to composite geometry just as is the factor M of Equation 10.10.

Deduction of shape parameters from experiments

At low porosities both fit expressions in Equation 10.11 and the results obtained by the present method in Equations 10.9 and 10.10 approach identical stiffness when Equation 10.12 applies.

$$F = H = \frac{1}{\mu_P^o} + 1 \qquad \left[i.e., \ \mu_P^o = \frac{1}{F - 1} = \frac{1}{H - 1} \right] \qquad (10.12)$$

Obviously this observation can be used to deduce shape factors from experimental data - or it can be used to give some geometrical explanation to the empirical factors F and H used in the literature. More general information, however, on the geometry and stiffness of porous materials can be retrieved from experimental data. We linearize Equation 10.9 (with $e = E/E_s$) as shown in Equation 10.13. Then μ_P^o, c_P, and E_s are easily deduced by linear regression of the manipulated experimental data (X,Y), optimizing the fit quality with respect to c_P.

$$Y = Y_o + \alpha X \quad with \quad X = \frac{c}{1 - c/c_P} \quad and \quad Y = \frac{1 - c}{E} \quad \Rightarrow$$
$$E_s = 1/Y_o \ ; \quad \mu_P^o = Y_o/\alpha \quad from \ intersection \ Y_o \ and \ slope \ \alpha \qquad (10.13)$$

Remark: It is noticed that no other information on composite geometry than μ_P and c_P can be obtained directly from mechanical tests on porous materials. To get information on μ_S and c_S the pore system considered has to be impregnated - or supplementary studies on percolation and diffusivity have to be made.

10.3.5 Stiff pore systems

Stiff pore systems are composites where one phase (P) is extremely stiff relative to the other phase (S). The stiffness relation presented in Equation 10.14 is easily

obtained by the simplified analysis letting n → ∞ and utilizing that the geo-function θ reduces as shown in Table 4.1. Infinite stiffness is predicted for c ≥ c_s. A graphical representation of Equation 10.14 is shown in Figure 10.30. The composite considered is particulate with an aspect ratio of A = 2 and a critical concentration of c_s = 0.6. Equation 10.14 is also developed in (78,79).

$$ e = \frac{1 + \theta_\infty c}{1 - c} \quad ; \quad \theta_\infty = \begin{cases} \dfrac{\mu_P + \mu_s - 1}{\mu_s} & c < c_s \\ \infty & c > c_s \end{cases} \qquad (10.14) $$

10.4 Conclusion

The general composite analysis presented in Chapter 8 has been successfully simplified in this Chapter to reflect realistically the somewhat limited knowledge available in most practice on composite geometry. Standard stiffness-, stress-, and eigenstrain/stress solutions for various types of composites have been developed. The CSA composite especially has been considered - and special attention has been given to the mechanical behavior of porous materials. Reliable empirical evidence compares positively with predictions made by the simplified theory. It is demonstrated, how experiments on porous materials can be used to detect important composite geometrical information.
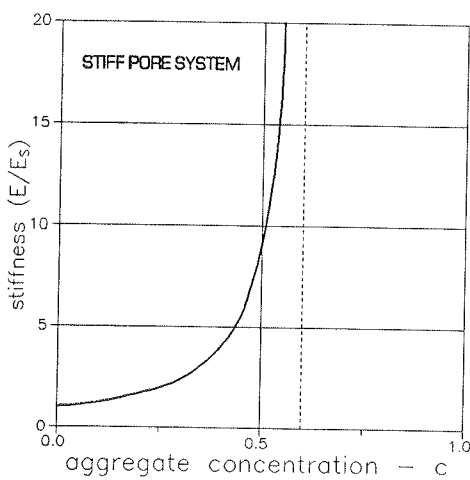
Figure 10.30. Particulate composite with shape functions defined by particles of aspect ratios A = 2 and a critical concentration of c_s = 0.6

The overall positive expectations build up in this chapter to the simplified theory are further justified in the subsequent Chapter 11 where theoretical results and experimental data are compared directly.

$$ CSA_p: \qquad e(n,c) * e\left[\frac{1}{n},c\right] = 1 \qquad (TROC) $$

$$ Phase\text{-}symmetric: \quad e(n,c) = n * e\left[\frac{1}{n},1-c\right] \quad (CROSS) \qquad (10.15) $$

11. Theory and experiments

A number of examples are presented in this chapter where experimentally obtained data for various mechanical composite properties are compared with data predicted by the simplified method presented in Chapter 10. Predictions of internal stresses are included whenever such information might be of interest.

Some times the analysis has to be slightly modified in order to consider special features which apply to composites in practice. Examples are modifications with respect to interference phenomena, modifications with respect to incompletely impregnated pore systems, and modifications with respect to defective phase contacts. These topics are considered in the following introductory section.

11.1 Introduction

11.1.1 Non-flexible geometry - interference

We recall from the introductory section of Chapter 2 that flexible phase geometries are considered primarily in this monograph which can adjust themselves (naturally, by compaction, or otherwise) to form a tight composite. When phase geometries are not flexible, air voids are inevitable at certain concentrations. For example, in a material reinforced by non-flexible particles (phase P) voids will turn up at concentrations $c > c_{PACK}$ where the latter concentration is the packing concentration of particles (as packed in the composite) where a stable phase P structure is formed.

FLAT PARTICLES, $A \ll 1$ LONG PARTICLES, $A \gg 1$

$c_s \approx \ell d^2/d^3 = A$ $c_s \approx \ell d^2/\ell^3 = 1/A^2$
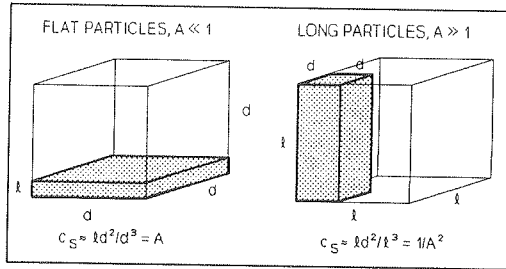
A number of theories (ex 80,81) have been developed by which the packing concentration can be estimated. For uni-sized discs and fibres very rough estimates can be made from Equation 11.1 based on the figure presented close to this paragraph. In practice considerably higher packing concentrations can be obtained by modern grading and vibration techniques.

$$c_{PACK} > 0.5 \begin{bmatrix} 1/A^2 & ; & A > 1 \\ A & ; & A < 1 \end{bmatrix} \quad \textit{rough estimate} \tag{11.1}$$

The amount of voids, $c_{VOID} = V_{VOID}/(V_s + V_{VOID})$, relative to the original phase S volume can be expressed as follows,

$$c_{VOID} = \begin{cases} \dfrac{c - c_{PACK}}{c(1 - c_{PACK})} & ; \quad c > c_{PACK} \\ 0 & ; \quad c \leq c_{PACK} \end{cases} \qquad (11.2)$$

There is some resemblance between c_{PACK} and the critical concentration c_s where phase P leaves the state of being 100 % discrete. In the present context we may put $c_s \approx c_{PACK}$ assuming that the state of interference is considered to be a so-called stable interference where large areas of contact between neighbouring particles are "glued" together by a very thin layer of a sufficiently strong phase S.
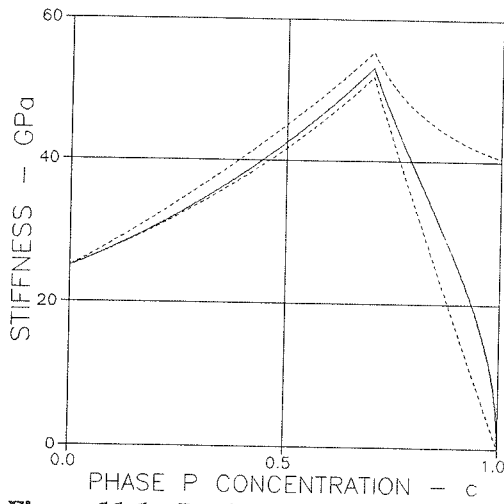
Figure 11.1. Particulate composite with non-flexible particles. $(\mu_P{}^o, \mu_s o) = (1,-0.5)$, $c_{PACK} = 0.7$. $(E_s, E_P) = (25,75)$ MPa.
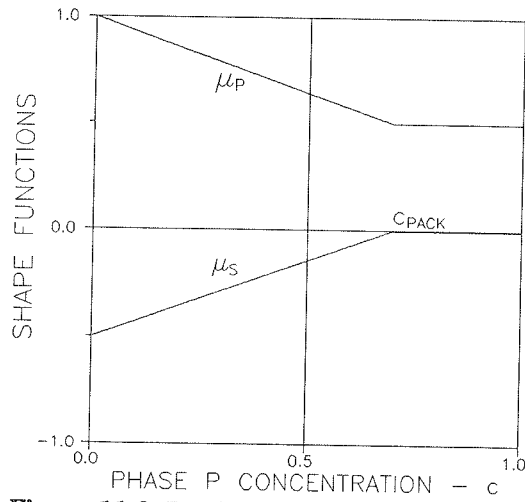
Figure 11.2. Particulate composite with non-flexible particles. $(\mu_P{}^o, \mu_s{}^o) = (1,-0.5)$, $c_{PACK} = 0.7$.

The analysis of composites with non-flexible phase P is not different from the analysis of composites hitherto considered when $c \leq c_s$ (= c_{PACK}). When $c > c_{PACK}$ phase geometry is frozen to stay as it is at $c = c_{PACK}$ where the MM-geometry is just about to be encountered. The volume concentration of phase P (relative to phase S) can only increase by replacing some phase S material with voids. Obviously the stiffness of phase S now becomes that of a porous phase S. We introduce effective stiffness geometric properties as presented in Equation 11.3 assuming that pores are spherical (other void shapes can easily be considered; to do so, however, is too speculative). We recall that composite geometry stays at the geometry defined at $c = c_{PACK}$. Then the analysis proceeds as explained in Equation 11.4 following the general principles presented in this monograph. As a consequence of the frozen MM-geometry of the composite stiffness approaches 0 as c approaches 1.

106

An example of a stiffness analysis of particulate composites with non-flexible multi shaped particles is demonstrated in Figures 11.1 and 11.2, 10% short fibres (A = 2.5) + 90% spheres (A = 1).

$$
\left.
\begin{array}{l}
E_{S,EFF} = E_S \dfrac{1 - c_{VOID}}{1 + c_{VOID}} \quad ; \qquad n_{EFF} = n \dfrac{1 + c_{VOID}}{1 - c_{VOID}} \\[2mm]
\mu_{P,EFF} \equiv \mu_P(c_{PACK}) \quad ; \quad \mu_{S,EFF} \equiv \mu_S(c_{PACK}) \equiv 0 \\[2mm]
\theta_{EFF} = 0.5\left[\mu_{P,EFF} + \sqrt{\mu_{P,EFF}^2 + 4n_{EFF}(1 - \mu_{P,EFF})} \ \right]
\end{array}
\right\}
\quad c > c_{PACK}
\qquad (11.3)
$$

$$
E = E_{S,EFF} \frac{n_{EFF} + \theta_{EFF}[1 + c_{PACK}(n_{EFF} - 1)]}{n_{EFF} + \theta_{EFF} - c_{PACK}(n_{EFF} - 1)} \quad ; \quad c > c_{PACK}
\qquad (11.4)
$$

In most practice the interference phenomenon is of theoretical interest mainly. For a number of reason we do not want composites with self-inflicted voids. Much efforts are made to produce particle size distributions such that voids can be avoided. In some special cases, however, where weight and heat insulation are principal design parameters such voids may be desirable. This feature is discussed in Section 11.5.

11.1.2 Incomplete impregnation

If a composite is made by impregnation of a porous material, then the impregnant (phase P) may be porous itself for a number of reasons. Shrinkage of the impregnant, for example, may cause this phenomenon. In this case phase P appears as a porous material the effective stiffness property of which can be approximated as shown in Equation 11.6 with void ratio and degree of impregnation defined in Equation 11.5. Spherical void shapes are assumed. Other shapes can easily be considered. However, to assume void shapes others than spherical might be too speculative.

$$
\begin{array}{ll}
\beta = \dfrac{volume \ of \ impregnant}{pore \ volume} & is \quad degree \ of \ impregnation \\[3mm]
c_{VOID} = 1 - \beta & is \quad void \ ratio \ in \ impregnant
\end{array}
\qquad (11.5)
$$

$$
E_{P,EFF} \approx E_P \frac{1 - c_{VOID}}{1 + c_{VOID}} = E_P \frac{\beta}{2 - \beta} \quad \Rightarrow \quad n_{EFF} = n \frac{\beta}{2 - \beta}
\qquad (11.6)
$$

11.1.3 Incomplete phase contact

For several reasons perfect contact between phases in a composite material may be destroyed. Impurities on aggregate, bleeding, early age volume changes, and particles interference in concrete, for example, may cause this problem. It is justified in Section 9.1.2 that missing phase contact in particulate composites with compact particles can be considered approximately in a stiffness analysis by replacing the stiffness ratio, n, with an effective stiffness ratio, n_{EFF}. In a slightly modified version the procedure is demonstrated in Equation 11.7 determining the stiffness of a CSA_P composite with a degree of defective particle surfaces (S) defined as $\chi = S_{DEFECT}/S$. Defective areas are considered with no voids associated.

$$e = \frac{A + n_{EFF}}{1 + An_{EFF}} \quad with \quad \begin{cases} A = (1 - c)/(1 + c) \\ n_{EFF} = n(1 - \chi^a) \\ a = \max[1, 9/(5 + n)] \end{cases} \quad (11.7)$$

11.2 Various porous materials
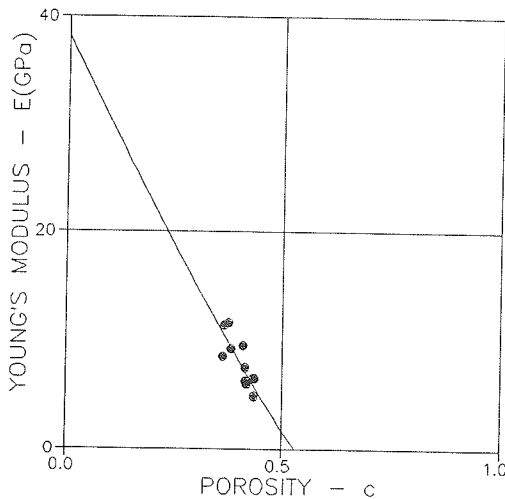
Figure 11.3. Stiffness of tile: $(\mu_P^{\circ}, c_P) = (0.9, 0.53)$.

Experimentally determined stiffness data of porous materials are compared in this section with data described by Equation 10.9 in Section 10.3.4. Geo-parameters (μ_P°, c_P) and solid phase stiffness (E_S) are deduced from the experimental stiffness data using the regression technique also explained in Section 10.3.4. In the following figures experimental data and theoretical data are presented by dots and lines respectively.

11.2.1 Tile

Young's modulus of tile has been determined experimentally in (82) as shown by dots in Figure 11.3. The theoretical stiffness presented is based on $E_s = 38000$ MPa, $\mu_P^{\circ} = 0.9$, and $c_P = 0.53$.

108

11.2.2 Porous magnesium oxide

Experimental data on Young's modulus of porous magnesium oxide (MgO) were collected in (77) from six sources representing a variety of processing techniques. Porosities considered were c < 30%. It was shown that all these data were fitted very well by the exponential expression presented in Equation 10.11 with H = 4.74 and E_S = 3.2*10^5 MPa. The data such described are digitalized as presented in Figure 11.4 with dots. The theoretical data are based on the geometrical information $(\mu_P°,c_P)$ = (0.24,0.88). It is noticed that the shape factor obtained complies well with $\mu_P°$ ≈ 0.26 deduced by Equation 10.12.

11.2.3 Porous aluminum oxide

In a similar experimental analysis of the elasticity of porous aluminum oxide (Al_2O_3) it was shown in (83) that experimental data from 11 sources with porosities c < 40 % were very well fitted by the exponential expression in Equation 10.11 introducing H = 3.95 and E_S = 4.1*10^5 MPa. The data such described are digitalized as presented in Figure 11.4 with dots. The theoretical data are based on the geometrical information $(\mu_P°,c_P)$ = (0.35, ≈1). It is noticed that the shape factor obtained complies well with $\mu_P°$ ≈ 0.34 deduced by Equation 10.12.
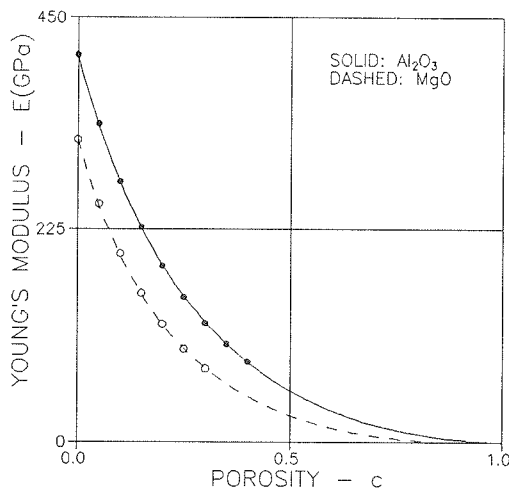
Figure 11.4. Stiffness of porous materials made of polycrystalline oxides.
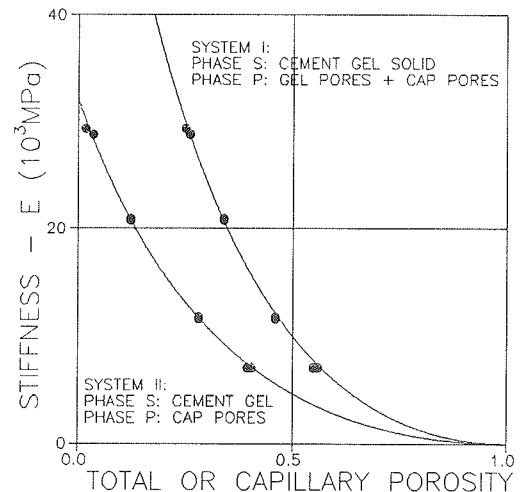
Figure 11.5. Young's modulus of hardened Portland cement paste.

11.2.4 Hardened cement paste

The data presented in Figure 11.5 illustrate the influence of porosity (evaporable water measurement) on elasticity of nearly fully hydrated hardened portland cement paste (HCP). The experimental data presented in the figure are from (75, cement

109

15366). They are related to two pore systems defined in (24). *System I:* Solid phase (S) is made of cement gel solids, the pore phase is the total of cement gel pores and capillary pores. *System II:* Solid phase is cement gel, the pore phase is capillary pores. The theoretical data are based on the following information.

Composite: System I: $(\mu_P^o, c_P) = (0.33, \approx 1)$

System II: $(\mu_P^o, c_P) = (0.4, \approx 1)$

Phase S: System I: $E_s = 80000$ MPa (gel solid)

System II: $E_s = 32000$ MPa (gel including gel pores)

11.2.5 Lime mortar

An examination of lime mortars with porosities of approximately c = 0.3 was reported in (84). Various material properties (such as stiffness, frost resistance, and capillary suction) were measured and related qualitatively to the microstructure of material tested. Different microscopical techniques were used to characterize the microstructure for homogeneity and coherence on a scale from H = 1 (bad) to H = 5 (high quality). The stiffness data are presented in Figure 11.6.
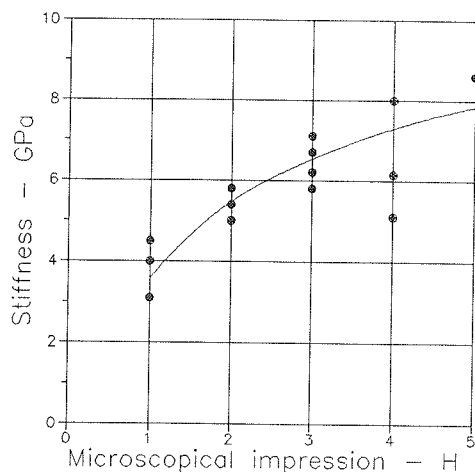
Figure 11.6. Young's modulus of lime mortars as related to structure (microscopical impression H).

The idea was suggested by Nielsen (85,86) that the qualitative evaluation made in (84) can be quantified by Equation 10.9 with $c_P = 1$ and shape factors μ_P^o = H/5 introduced. This means that high quality mortars are assumed to have spherical voids, while bad mortars have flat voids. Nielsen's description of structure versus stiffness made in this way with $E_s = 16$ GPa is illustrated in Figure 11.6 reproduced from (85). The ideas of Nielsen were evaluated positively in an image analysis (87) on planar sections made on some of the mortars considered in (84). This analysis seems to indicate that it might be worthwhile pursuing the possibilities of using image analysis in quality control of porous materials.

11.2.6 Summary - porous materials

Stiffness data obtained from tests on porous materials have been shown in this section to be very well described by the theoretical Equation 10.9. The geometrical information used indicate that the pore systems become finer and more complex

110

(decreasing μ_P^o) as we go from tile (μ_P^o = 0.9), to HCP(cap-por) (0.4), to HCP(tot-por), to Al_2O_3 (0.33), to MgO (0.24). For comparison the theoretical descriptions made in Sections 11.2.1-11.2.4. The results are presented in Equation Equation 11.8. The lime mortar results from Section 11.2.5 are not presented in Equation 11.8 because only one porosity was considered. At an average, however, one may expect that lime mortar behaves approximately as HCP.

$$\begin{array}{llll} e \approx (1 - 1.9c)^{1.12} & ; & Tile & (\mu_P^o, c_p) = (0.9, 0.53) \\ e \approx (1 - c)^{3.5} & ; & HCP(cap\text{-}pore) & (\mu_P^o, c_p) = (0.4, 1) \\ e \approx (1 - c)^{4.0} & ; & HCP(tot\text{-}pore), Al_2O_3 & (\mu_P^o, c_p) = (0.33, 1) \\ e \approx (1 - 1.14c)^{4.55} & ; & MgO & (\mu_P^o, c_p) = (0.24, 0.88) \end{array} \quad (11.8)$$

The expressions in Equation 11.8 are ranked with respect to increasing powers of the stiffness descriptions. It is observed that this ranking is the same as a ranking with respect to decreasing shape factors. This feature can be taken as an experimental justification of the theoretical statement made in Section 10.3.4 that stiffness of porous materials can be expressed by simple porosity relations raised to a power which increases with increasing complexity (away from spherical) of pore geometry.

It is interesting to note that the third expression in Equation 11.8 is numerically identical to an empirical expression suggested in (88) to predict the elasticity of pore systems created by incomplete compaction of cement concrete. Thus, it seems that pores created by incomplete compaction of concretes have a geometry the complexity of which is similar to the geometry of the total pore system in HCP.

11.3 Sulphur impregnated cement/silicate system

Figure 11.7 illustrates the influence of pores (measured by Helium comparison pycnometry) on the elasticity of autoclaved ("empty") systems made of water and equal amounts of portland cement and silica powders (SiO_2, max diameter 0.15 mm) - and such systems impregnated by sulphur. The experimental data are from (89) and (90) respectively. The theoretical data shown are predictions by the simplified composite theory previously presented with the geo-parameters μ_P^o, c_p, and solid phase stiffness E_s obtained by regression of experimental stiffness data from the empty system. The additional information on type of composite (phase symmetry) is estimated as no further geometrical information can be obtained from (89,90).

Composite: Phase-symmetric CC-CC with $(\mu_P{}^\circ, c_P) = (0.45, 1)$

Phase S: $E_S = 36000$ MPa

Phase P: $E_P = 16000$ MPa, $ß = 0.82$ $(E_{P,EFF} = 11000$ MPa)

The stiffness of Sulphur is calculated from information presented in (91) for Young's moduli of polycrystalline sulphur. An inspection of the test results in (90)
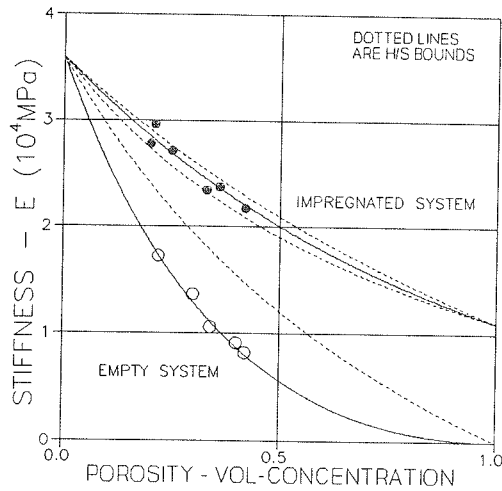
Figure 11.7. Young's moduli of porous and sulphur impregnated autoclaved Portland cement/silicate systems.

reveals that the degree of impregnation varies non-systematically between 0.75 and 0.87 with an average of $ß = 0.82$ from which the effective stiffness of Sulphur is calculated by Equation 11.6. (The incomplete impregnation was due to shrinkage of sulphur when solidifying).

Remarks: It is noticed that similar orders of magnitudes apply for the shape factor $\mu_P{}^\circ$ and stiffness for the pore system considered in this example and for the HCP pore system II in Section 11.2.4. This observation agrees with the expectation one might have that pores defined by Helium comparison pycnometry will not include gel pores. These pores are included in the "solid phase" of the system considered which has a stiffness of similar magnitude as cement gel in Figure 11.5.

The assumed composite geometry (phase-symmetric CC-CC) of the system considered is justified implicitly by the excellent simultaneously agreement between experimental data and theoretical data demonstrated in Figure 11.7 for both empty and impregnated pore systems.

11.4 Salt infected bricks

The thermal expansion of salt infected (impregnated) bricks shown in Figure 11.9 has been determined experimentally in (92) as related to porosity and weight amount of salt (NaCl). The theoretical data shown are based on the following information:

Composite: CC-CD with $(\mu_P{}^\circ, \mu_S{}^\circ, c_P) = (0.9, 0, 0.53)$, $(c_S = 0)$

Phase S (Tile): $E_S = 38000$ MPa, $\lambda_S = 6.0 * 10^{-6}/°C$

Phase P (Salt): $E_P = 20000$ MPa, $\lambda_P = 3.8 * 10^{-5}/°C$, $ß = 0.15$-0.25

112
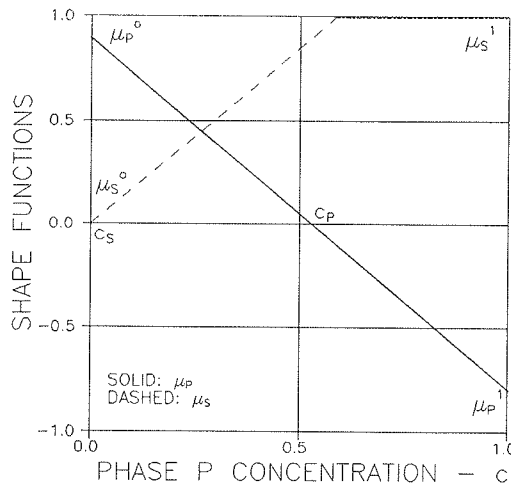
Figure 11.8. Shape functions for tile: $(\mu_P^o, \mu_S^o, c_P) = (0.9, 0.0, 0.53)$.

The thermal expansion coefficients (λ) of plain rock salt and plain tile were determined in (92). The Young's modulus of salt is estimated from the literature (93). The geometrical data (μ_P^o, c_P) and the Young's modulus for tile are reproduced from Section 11.2.1. The additional information of shape factor $\mu_S^o = 0$ is estimated from knowing that the major part of pores in tile are continuous. We may think of a pearls on a string pore system with $\mu_S^o = 0$. It is noticed that μ_S in Figure 11.8 has been truncated to have $\max(\mu_S) = 1$ as required in Equation 10.1.

An inspection of the test results in (92) reveals that the degree of impregnation varies non-systematically as indicated with an average of ß = 0.20 from which an effective stiffness $E_{P,EFF} = 2200$ MPa of the pore system can be calculated from Equation 11.6.
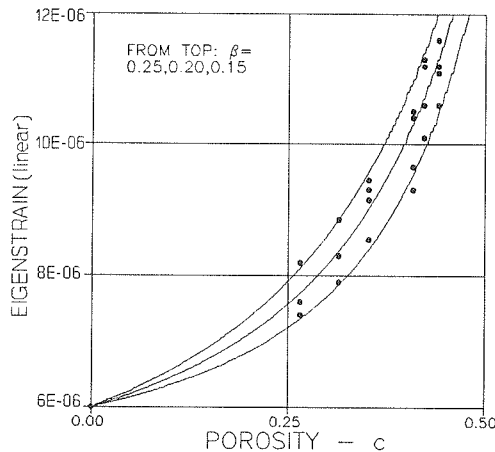
Figure 11.9. Thermal eigenstrain (/C°) of salt infected tile.
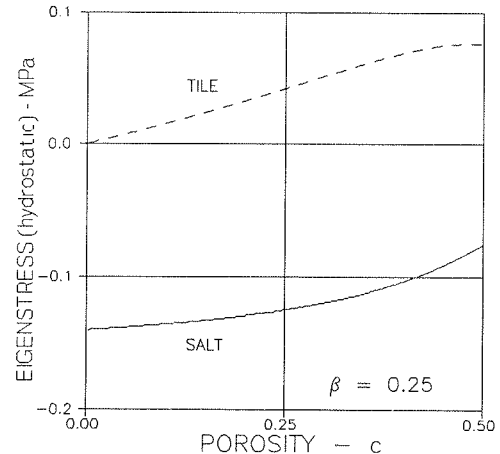
Figure 11.10. Predicted thermal eigenstresses (/°C) in salt infected brick.

Remark: The assumed geometry of considering tile as a CC-CD composite with shape functions from Figure 11.8 is justified implicitly by the excellent agreement between experimental data and theoretical data demonstrated in Figure 11.9. The internal stress state calculated for a degree of impregnation, ß = 0.25, is shown in Figure 11.10.

11.5 Non-flexible particles in particulate composite

The experimental data shown in Figure 11.11 are from tests reported in (94) on cement mortars made of cement paste mixed with compact, nearly uni-sized coarse quartz particles, which interfere at $c_{PACK} = 0.55$. It is assumed that the composite considered is basically a CSA_P material with $(\mu_P{}^o, \mu_S{}^o) = (1,-1)$. The method of analysis used to predict stiffness (solid lines) is the one outlined in Section 11.1.1 where particulate composites with non-flexible geometries are considered.
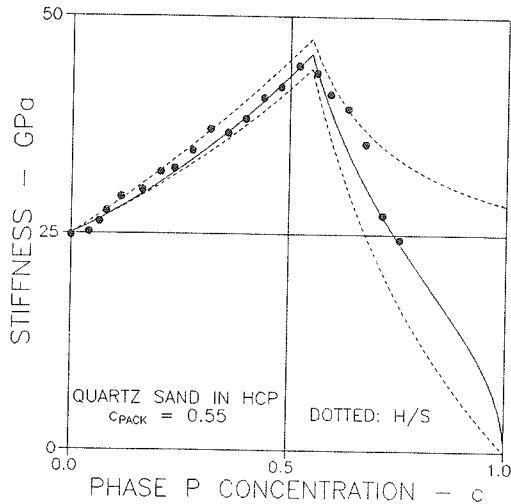
Figure 11.11. Sand in HCP. $(E_P, E_S) = (75, 25)$ GPa. $(\mu_P{}^o, \mu_S{}^o) = (1,-1)$.
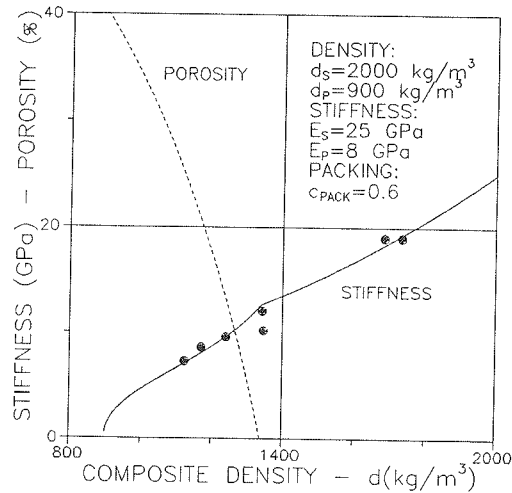
Figure 11.12. Ligth clinker concrete. Material properties as indicated. $(\mu_P{}^o, \mu_S{}^o) = (1,-1)$.

The experimental data shown in Figure 11.12 are from (95) where the phenomenon of interference has been used deliberately (weight, economy, heat insulation) in design of light weight concrete. The method of analysis used for stiffness prediction (solid lines) is the same as used in the previous example. It is assumed that the concrete considered starts up at $c = 0$ being a CSA_P composite with $(\mu_P{}^o, \mu_S{}^o) = (1,-1)$. A packing concentration of $c_{PACK} = 0.6 \ (= c_S)$ is a realistic estimate for the packing of light clinker. Density of composite is $d = c*d_P + (1-c)*d_S$. Porosity indicated in the figure is relative to composite volume, meaning porosity $= V_{VOID}/(V_S+V_P+V_{VOID}) = (c-c_{PACK})/c$.

11.6 Defective phase contact in concrete

Hansen suggests in (96,97) that stiffness of concrete (with stiffness ratio n > 1) can be predicted by the lower P/H bound as indicated by dots in Figure 11.13. Hansen's suggestion is strongly justified by experimental data. Implicitly Hansen's observations seem to indicate that concrete is an anisotropically layered composite. Concrete, however, *is* a macroscopically isotropic composite similar to a CSA_P material (spheres in a continuous matrix). Stiffness should therefor be predicted close to the lower H/S-bound also indicated in Figure 11.13.

One might state that this discrepancy in observations can be explained as a consequence of defective phase contacts between aggregates and mortar. The theoretical data shown in Figure 11.13 indicated by a solid line are calculated by Equation 11.7 assuming that the concrete considered behaves as a CSA_P material with defective phase contacts. Further information used are:

Defective phase contact: $\chi = 20\%$
Phase S (Mortar): $E_s = 30000$ MPa
Phase P (Coarse aggregate): $E_P = 70000$ MPa

Stiffness such estimated are order of magnitudes usually met in concrete technology. The degree of defective phase contact assumed between coarse aggregate and mortar agrees with observations made by Nielsen in (98) on normal concrete.

It seems then justified by Figure 11.13 that the "Hansen's paradox" can very well be explained as the result of defective phase contacts.
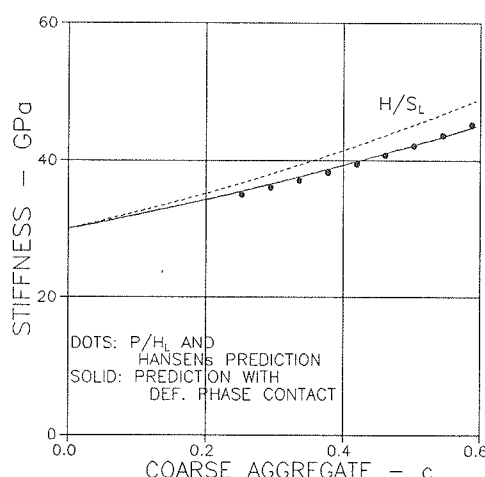
Figure 11.13. Stiffness of concrete with defective contact between coarse aggregate and mortar.
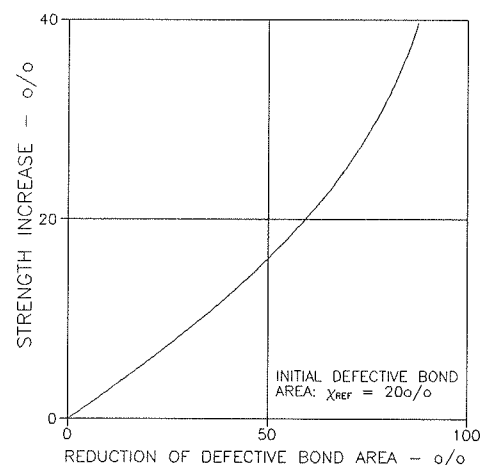
Figure 11.14. Gain of concrete strength obtained by reducing defective bond areas on coarse aggregates.

115

11.6.1 A strength mechanism for concrete. When stiffness reduction is known as a function of increasing defective bond areas then strength reduction can be estimated as follows using some ideas, suggested in (71) on the basis of the well-known 'Compliance calibration equation', see (99) for example. The ideas are subsequently demonstrated on a CSA_p composite subjected to tensile stress σ. Defective bond areas are considered as a crack system expanding along the bond area. For such a crack system the energy involved in crack expansion can be expressed by the 'Compliance calibration equation' formulated as shown in Equation 11.9a with E, from Equation 10.7, and Γ denoting Young's modulus and the so-called strain energy release rate.

Equation 11.9a can be organized as shown in Equation 11.9b performing the differentiation of E with respect to crack area. Strength (σ_{CR}) can then be predicted introducing a failure criterion which tells that failure will occur when Γ becomes critical ($\Gamma = \Gamma_{CR}$). Relative strength, $\sigma_{CR}/\sigma_{CR,REF}$ is given by the latter expression in Equation 11.9b where Γ_{CR} has been eliminated introducing the reference strength ($\sigma_{CR,REF}$) at a reference degree of defective aggregate surface (χ_{REF}).

$$\Gamma \propto \sigma^2 \frac{d(1/E)}{dB} \quad where \quad \begin{cases} \Gamma = Strain\ energy\ release\ rate \\ B = \dfrac{3\chi c}{R} = Crack\ area\ per\ vol-unit \\ R = Radius\ of\ particle \end{cases} \quad (11.9a)$$

$$\frac{\Gamma E_s}{\sigma^2} \propto \frac{Rna\chi^{a-1}}{3c} \frac{1 - A^2}{(A + n_{EFF})^2} \implies \frac{\sigma_{CR}}{\sigma_{CR,REF}} = \frac{A + n_{EFF}}{A + n_{EFF,REF}} \left[\frac{\chi}{\chi_{REF}}\right]^{(1-a)/2} \quad (11.9b)$$

An example is presented in Figure 11.14 where Equation 11.9b has been used to estimate which strength gain can be expected by reducing the defective bond areas on coarse aggregates in a concrete with $(c,n) = (0.5,2.5)$ where c and n are volume concentration and stiffness ratio respectively of coarse aggregates.

It is emphasized that predicted strength must be truncated at a certain level determined by the theoretical (un-cracked) bond strength. It should also be noted that strength in the present context refers to bond failure. Other failure mechanisms may act simultaneously.

11.7 Hydrating cement paste and concrete

The stiffness of a hardening cement paste and concrete can be calculated from Table 11.1 which combines the volumetric models of these materials presented in Section 2.1.2 with the geometry of CSA_p composites. The exponent Q introduced to describe the stiffness of HCP with W/C > 0.38 considers empirically that the geometrical complexity of basic paste voids decreases with increasing degree of hydration.

Theoretically predicted Young's moduli by Table 11.1 and experimentally determined moduli from (100) are compared in Figure 11.16. The degree of hydration

shown in Figure 11.15 is fitted by the g(t)-expression presented in Table 2.2 from experimental data reported in (100).

Recently the influence of hydration on the stiffness of HCP has also been studied by Bentz in (101) using a special computer simulation technique, and by Lok-horst & Breugel (102) considering HCP as part of concrete modelled as a layered composite.

CONCRETE	
$E = E_{HCP}\dfrac{A + n}{1 + An}$ with $n = \dfrac{E_P}{E_{HCP}}$	
HCP	
W/C > 0.38	$E_{HCP} = E_{BAS} * A_{VOID}^Q$ with $Q = 7 - 5g(t)$
W/C ≤ 0.38	$E_{HCP} = E_{BAS} * \dfrac{A_{CEM} + n_{BAS}}{1 + A_{CEM}n_{BAS}}$ with $n_{BAS} = \dfrac{E_{CEM}}{E_{BAS}} = \dfrac{1.7}{g(t)}$
Basic paste	$E_{BAS} = 32000*g(t)$ MPa

Table 11.1. Stiffness of concrete and HCP as related to volume parameters from Table 2.1 and stiffness of basic paste. It is assumed that un-hydrated cement has a Young's modulus of 55000 MPa.
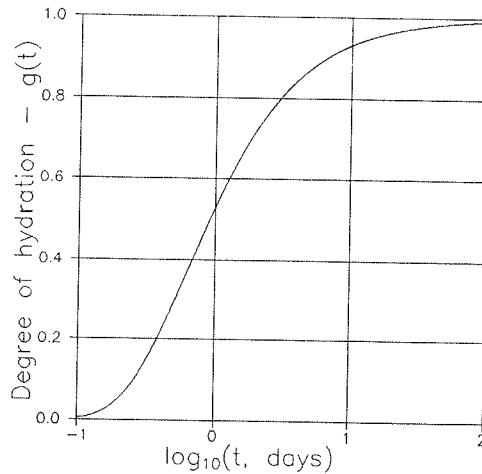
Figure 11.15. Degree of hydration, g(t), defined by $(\tau,\beta) = (0.625$ days,0.95).
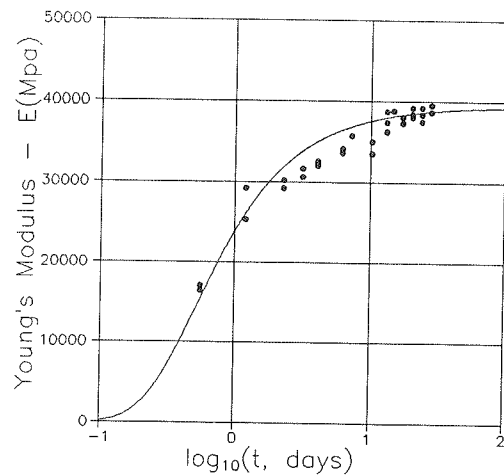
Figure 11.16. Concrete with (W/C, A/C) = (0.45,5.21), $E_P = 50000$ MPa, and degree of hydration from Figure 11.15.

11.7.1 A strength mechanism: Just for the sake of curiosity, a crack mechanical theory has been presented in (40,44) by which compressive strength σ_{CR} of HCP can be related to total porosity (c_{TOT}) and relative degree of hydration (q), see Table 2.2. The result is presented in Equation 11.10 and illustrated in Figure 11.17.

117

$$S = \begin{cases} 450(1 - c_{TOT})^B \ MPa & at \ q > (W/C)/2 \\ 0 & at \ q < (W/C)/2 \end{cases} \ with \ B = \frac{2.35}{[q(t) - 0.19]^{0.45}} \quad (11.10)$$

11.8 Conclusion

In this chapter results of the simplified composite theory presented in Chapter 10 have been successfully compared with experimental results reported from the literature. Composites of different geometries have been considered such as hardened cement paste, salt infected tile materials, impregnated silicate systems, concrete, and cement mortars made with sand of discontinuous size grading. Stiffness was considered together with other composite properties such as thermal expansion and internal stresses. Also the effect of defective phase contact as well as interference between non-flexible particles on stiffness properties of composites have been studied. Special topics considered are stiffness of porous materials relative to pore geometry.

Summary: All together it can be concluded that the simplified prediction method presented qualifies as an efficient tool in the analysis of various practical problems with respect to the mechanical behavior of composite materials. Combining this statement with the positive indications made in Chapter 10 on the many types of composite classes the theory can handle, is seems that the simplified composite theory presented in Chapter 10 is well qualified as the basic instrument in further studies of the behavior of composite materials. Examples, such as rheology and other physical properties are considered in the subsequent Chapters 13 - 15.

Figure 11.17. Compressive strength of a HCP with W/C = 0.45 and degree of hydration from Figure 11.15.

Two further arguments for this statement is presented in the subsequent Chapter 12: 1) The theory qualifies as a reliable diagnostic instrument for evaluating experimentally, semi-theoretically, and theoretically (SCS) obtained prediction methods with respect to reliability and underlying geometry, and 2) The theory has potentials with respect to design of composites.

118

12. Diagnostic aspects of theory

The principles of the present theory to work with global descriptions (θ) of composite geometries have been successfully justified in previous chapters. Potentially these principles qualify the theory also to be used as a "diagnostic tool" in two areas of importance in modern composite theory: 1) Examination with respect to isotropy and geometry of empirical or seme-theoretical composite expressions - and 2) Design of composite materials. These two features are considered in this chapter.
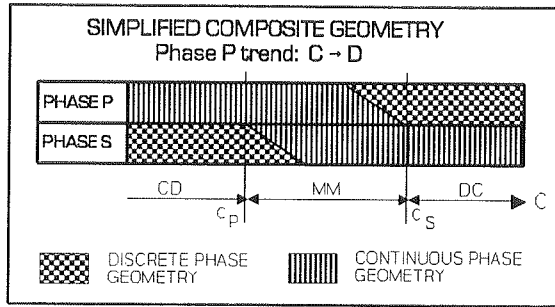
Figure 12.1. *Stylized illustration of a composite with reversed geo-path. Phase P geometry changes from C at c = 0 to D at c = 1.*

Remark: The composites hitherto considered in this monograph have geo-paths going from CSA_P to CSA_S geometries, which is the default path considered. The phase numbering P,S have been chosen consistent with this concept.

In this chapter where diagnostic aspects of the theory are considered we must be prepared to meet reversed geo-paths where composite geometries change along paths going from CSA_S geometries to CSA_P geometries, see Figure 12.1. There are no difficulties in using the theory hitherto developed on composites with reversed geo-paths. Some obvious changes of signs for shape functions turn up - and the critical concentrations change their relative orders of magnitudes, meaning that the default $c_P \geq c_S$ becomes $c_P \leq c_S$.

12.1 Examination of stiffness expressions

A number of semi-empirical and semi-theoretical expressions are suggested in the literature for stiffness prediction of composites. Very often these expressions are not well documented with respect to isotropy and consistency of underlying geometries. In other words:

- They are not guarantied, not to violate the bounds of Hashin/Shtrikman's, meaning that isotropy is not guarantied.
- They are not guarantied to have underlying geometries which are invariable with respect to stiffness ratios, n.

Methods are developed in this chapter by which prediction methods can be checked with respect to isotropy and geometry. The frame of geometrical reference used is the concept of organic geometries used throughout this monograph. This means

that geometries, successfully checked are those by which the present analysis and the analysis being investigated will predict the same stiffness. Implicitly this statement means that each stiffness expression which passes the checks can be taken as a justification of the composite analysis developed in this monograph.

Remark: For SCS-expressions being tested, a special remark should be made: We re-call that strict cylindrical particles (as used in SCS-analysis) do not comply with the organic geometry considered in this monograph. Therefor, we cannot expect composite geometries to be fully independent of stiffness ratios unless the SCS-expressions considered are based on particles defined as explained in the introductory remarks to Chapter 7, meaning aspect ratios $\approx 1/4 < A < \approx 4$ or extreme stiffness ratios, $n \to 0$ and $n \to \infty$.

We can expect, however, that reliable composite types (DC-CD, MM-CD, a.s.o.) are revealed - together with accurate shape factors, namely those applying to the particle shape used to establish the SCS-expression.

It is demonstrated in Chapter 15 that the methods developed in this chapter can also be used to evaluate expressions suggested to describe other physical properties of materials such as conductivity and dielectricity.

12.1.1 Isotropy check

Stiffness expressions can be tested for consistency with respect to isotropy by the following expression,

$$\theta = \frac{[n - c(n - 1)]e_{EST} - n}{1 + c(n - 1) - e_{EST}} \quad ; \quad isotropy \ check \qquad (12.1)$$

which comes from Table 10.3 solving the stiffness expression (e) with respect t o the geo-function (θ). The consistency considered requires that the geo-function obtained respects $n \leq \theta \leq 1$ when $n \leq 1$ and $n \geq \theta \geq 1$ when $n > 1$, see Figure 4.2 simplified with $\kappa_P = \kappa_S = 1$.

Examples

Re-written versions of three of the more well-known semi-theoretical stiffness prediction methods are presented below. Hirsch (103)/Dougill (104) and Popovicz/Erdey (105) suggested that composite stiffness can be determined from the Paul/Hansen's lower bound e_L and Paul/Hansen's upper bound e_U (Equation 12.2) as shown in Equation 12.3. The expression in Equations 12.4 was suggested by Counto (106) and by Lokhorst & Breugel (102). These three methods have

recently been reviewed in (107) with respect to their quality to predict stiffness of fired clay-perlite composites. The theoretical expression added in Equation 12.5 is deduced from the SCS-analysis of Budiansky (13) on a compacted spheres composite. The results of isotropy checks on these four expressions are presented in Figures 12.2 - 12.6 where admissible θ-variations are indicated by shaded areas.

$$e_U = 1 + (n - 1)c \quad ; \quad e_L = \frac{n}{n - (n - 1)c} \quad (Paul/Hansen) \qquad (12.2)$$

$$\frac{1}{e_{EST}} = \frac{\alpha}{e_U} + \frac{1 - \alpha}{e_L} \quad ; \quad (0 \le \alpha \le 1) \qquad (Hirsch/Dougill)$$

$$e_{EST} = \frac{1}{2}(e_u + e_L) \qquad (Popovics/Erdey) \qquad (12.3)$$

$$\frac{1}{e_{EST}} = 1 - \sqrt{c} + \frac{\sqrt{c}}{1 + (n - 1)\sqrt{c}} \qquad (Counto/Lokhorst-Breugel) \qquad (12.4)$$

$$e_{EST} = \frac{1}{2}\left[(1 - n)(1 - 2c) + \sqrt{(1 - n)^2(1 - 2c)^2 + 4n}\right] \qquad (Budiansky) \qquad (12.5)$$
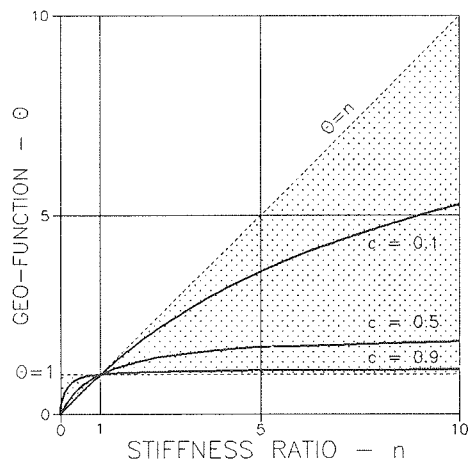
Figure 12.2. Hirsch/Dougill with $\alpha = 0.5$. (For other α the geo-functions fall outside the shaded area).
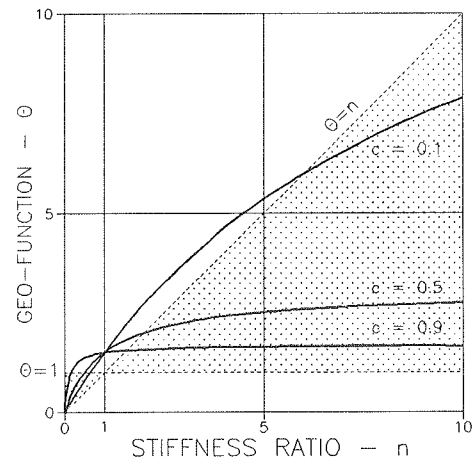
Figure 12.3. Hirsch/Dougill with $\alpha = 0.6$.

It is obvious that only the Hirsch/Dougill expression with $\alpha = 0.5$, the Popovicz/Erdey expression, and the Budiansky expression qualify as reliable for stiffness prediction of isotropic composites. The expression suggested by Counto and Lokhorst/Breugel is clearly influenced by some sort of anisotropic sub-modelling, see Section 5.3.3.
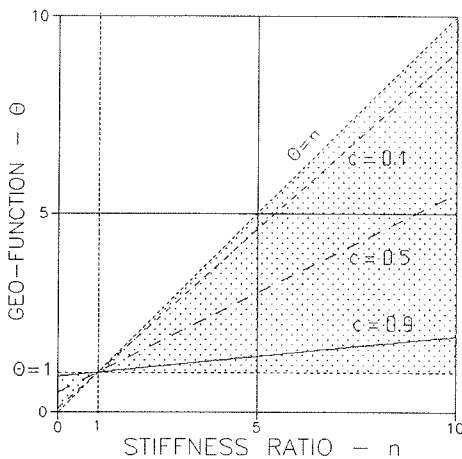
Figure 12.4. Popovics/Erdey.
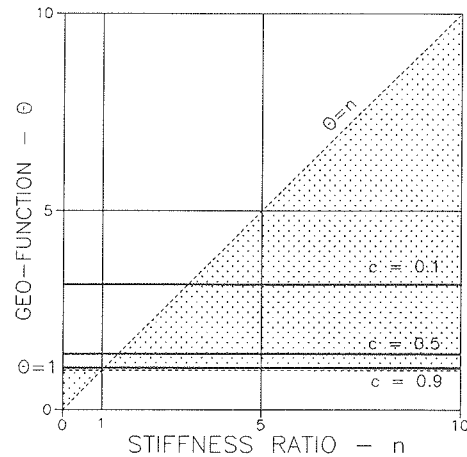
Figure 12.5. Counto and Lokhorst-Breugel
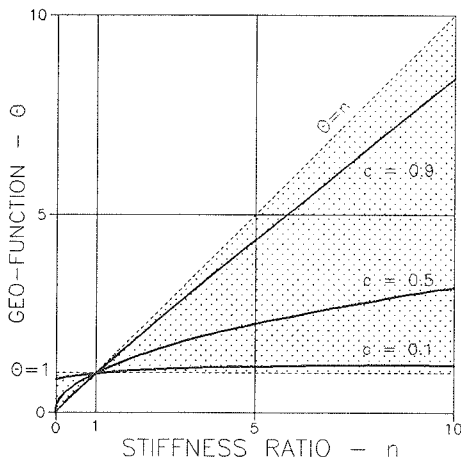
Figure 12.6. Budiansky

Remark: The review (107) of stiffness expressions previously referred to includes the Maxwell model (108) for particulate composite with spheres. This model applies for diffusion properties, not for stiffness. In the present isotropic check of composites the Maxwell model comes out with a geo-function of $\theta \equiv 2$ which is exactly the value expected for an expression predicting diffusion properties of the composites considered by Maxwell, see Chapter 15.

12.1.2 Geometry check

Stiffness expressions can be checked as follows with respect to geometries. The geo-function applied in this monograph is examined in details as shown in Equation 12.6. Specific shape functions (μ_P and μ_S) can be derived from this expression if geo-functions (θ_1, θ_2) are introduced as they are determined by Equation 12.1, at two stiffness ratios (n_1, n_2). The results are presented in Equation 12.7 from which the composite geometry can be evaluated.

As previously indicated, shape functions determined must show invariance with respect to stiffness ratios chosen if the stiffness expression investigated can be considered fully consistent with respect to geometry. For numerical reasons the well-known solutions (μ_P, μ_S) $\equiv$ (1,-1) for the CSA$_P$ composite with $\theta \equiv 1$ - and

122

$(\mu_P, \mu_S) \equiv (-1,1)$ for the CSA_S composite with $\theta \equiv n$ cannot be predicted by Equation 12.7.

$$\theta = \frac{1}{2}\left[\mu_P + n\mu_S + \sqrt{(\mu_P + n\mu_S)^2 + 4n(1 - \mu_P - \mu_S)}\right] \quad \Rightarrow$$

$$\theta^2 - \theta(\mu_P + n\mu_S) - n(1 - \mu_P - \mu_S) = 0 \quad \Rightarrow \qquad (12.6)$$

$$\mu_S = \frac{n(1 - \mu_P) - \theta(\theta - \mu_P)}{n(1 - \theta)} \quad ; \quad \mu_P = \frac{n(1 - \mu_S) - \theta(\theta - n\mu_S)}{n - \theta}$$

$$\mu_P = \frac{n_1 n_2(\theta_2 - \theta_1) + \theta_1^2 n_2(1 - \theta_2) - \theta_2^2 n_1(1 - \theta_1)}{n_1 n_2(\theta_2 - \theta_1) + \theta_1 n_2(1 - \theta_2) - \theta_2 n_1(1 - \theta_1)} \quad ; \; geometry \;\; check \quad (12.7)$$

$$\mu_S = \frac{n_1(1 - \mu_P) - \theta_1(\theta_1 - \mu_P)}{n_1(1 - \theta_1)}$$

Examples

The following checks are the results of running Equation 12.7 with various combinations of stiffness ratios. The geometry check of the Budiansky's expression presented in Figure 12.7 shows that the composite considered by this expression is a phase-symmetric DC-CD composite changing its geometry along a disc path - with P spheres in a continuous phase S at c = 0 to discrete phase S spheres in a continuous phase P at c = 1.
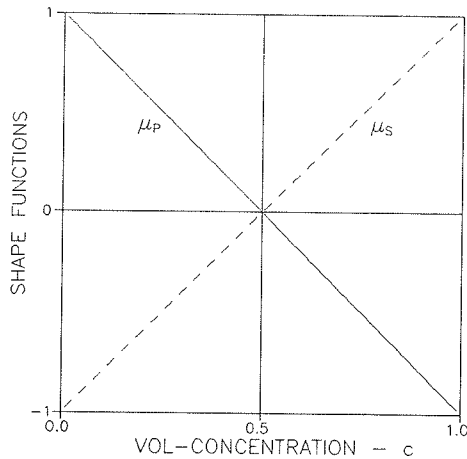
Figure 12.7. Budiansky: Geometry check.
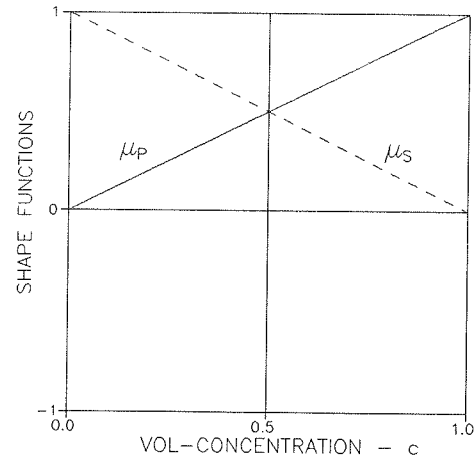
Figure 12.8. Popovics/Erdey: Geometry check.

The geometry check of the Popovics/Erdey expression presented in Figure 12.8 shows that the composite considered by this expression is a phase-symmetric MM-MM composite changing its geometry along the path of PS-frameworks - with continuous phase S fibres in a continuous phase P at c = 0 to continuous phase P fib-

res in a continuous phase S at c = 1. (We notice that the geo-path associated with Figure 12.8 is reversed describing geometries on a path going from CSA_S to CSA_P).

A geometry check of the Hirsch/Dougill expression shows a strong n-dependency on shape functions, (the results of a geometry check become completely un-reasonable). The following examples illustrated in Figure 12.9a and 12.9b illustrate the influence of the stiffness ratio: At n = 50 the Hirsch/Dougill model corresponds to a nearly CSA_P composite. At n = 1/50 the model corresponds to the "opposite" of this material, namely a nearly CSA_S composite. It is obvious that such geometrical modelling is no good.
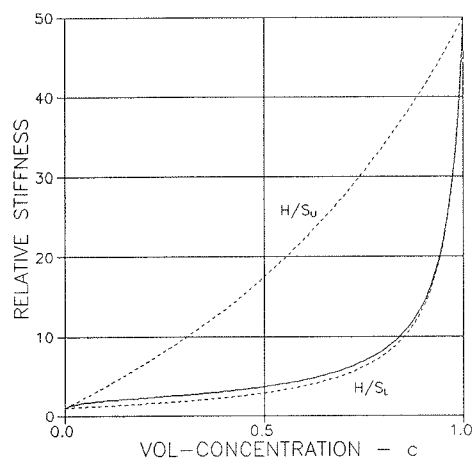
Figure 12.9a. Hirsch/Dougill stiffness prediction with stiffness ratio, n = 50.
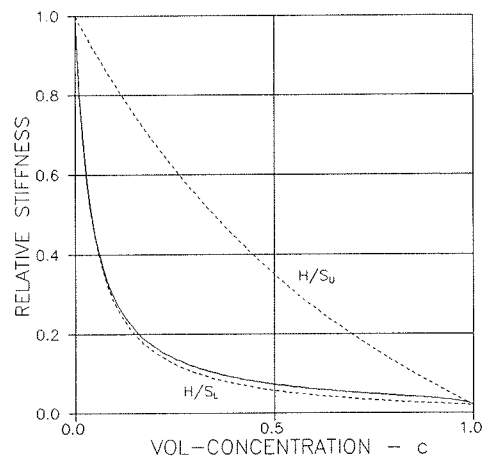
Figure 12.9b. Hirsch/Dougill stiffness prediction with stiffness ratio, n = 0.02.

12.1.3 Summary

The stiffness estimates considered in this section are checked with the results summarized in Table 12.1.

METHOD → ↓ CHECK	Hirsch/Dougill ($\alpha = 0.5$)	Popovics/Erdey	Counto/Lok- hurst/Breugel	Budiansky
Isotropy	+	+	-	+
Geometry	-	+ (rev)	-	+

Table 12.1 Summary of check results for methods considered. Good results and less good results are denoted by '+' and '-' respectively. Reversed geo-path is denoted by 'rev'.

12.2 Aspects of materials design

Equations 12.1 and 12.6 can be used to suggest types of composite geometries which will produce pre-described composite Young's moduli. The procedure to follow is summarized in the algorithm presented in Equation 12.8 with pre-described quantities indicated by *. As usually two materials, phase P and phase S, are considered with Young's moduli E_P and E_S respectively with stiffness ratio n = E_P/E_S. The first term of the algorithm is the geo-function value at c^* determined by Equation 12.1. The second term is shape function value μ_S^* at c^* determined by the third expression of Equation 12.6. The simplified shape functions have been used with function values related by $\mu_P^* = a - \mu_S^*$ where the geo-path factor a = $\mu_P^o + \mu_S^o$, see introduction to Chapter 10.

$$Pre\text{-}described\ Young\ modulus\ is\ e^* = E^*/E_s\ at\ c = c^*$$

$$\theta^* = \frac{[n - c^*(n - 1)]e^* - n}{1 + c^*(n - 1) - e^*}$$

$$\mu_S^* = \frac{n(1 - a) + \theta^*(a - \theta^*)}{\theta^*(1 - n)} \quad : \quad \mu_P^* = a - \mu_S^* \tag{12.8}$$

Remark: We notice that a number of composite geometries are suggested by Equation 12.8. For the simple geometries considered in Section 10.1 geo-paths are defined for any $0 \le a \le 1$. The number of geometrical possibilities is reduced for each additional pre-described composite property. Potential processing technique must also be considered in this context. For example, composites produced by impregnation of porous materials exclude DC-DC geometries.
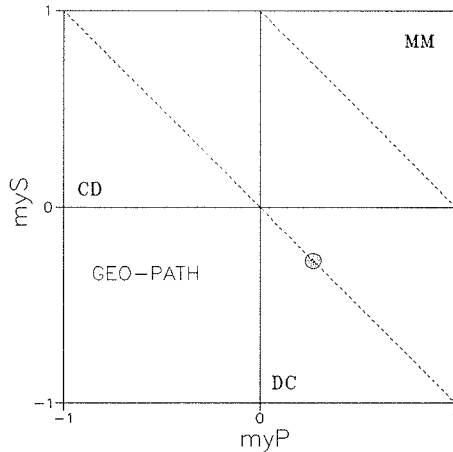
Figure 12.10.   Example 1: Geometry of composite for which pre-described Young's modulus can be obtained using a geo-path with a = 0.
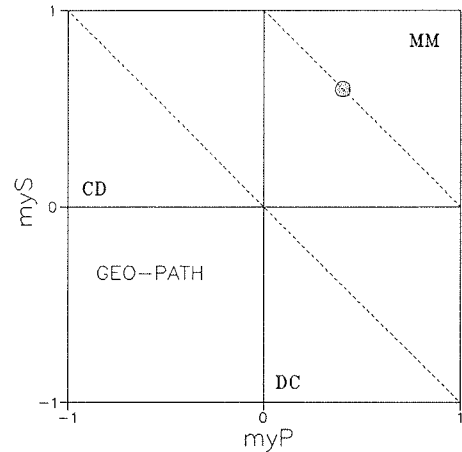
Figure 12.11.   Example 1: Geometry of composite for which pre-described Young's modulus can be obtained using a geo-path with a = 1.

12.2.1 Examples

Two examples are subsequently presented where Equation 12.8 is used to identify which type of geometry a composite must be given in order to obtain pre-described composite stiffness properties (Young's moduli) which, of course must not violate the H/S bounds presented in Equation 10.3.
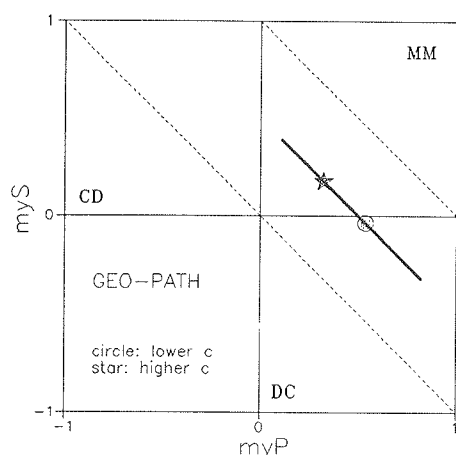
Figure 12.12. Example 2: Geometry of composite for which pre-described Young's moduli can be obtained using a geo-path with a = 0.5.

Example 1: Stiffness ratio: n = 0.1. Pre-described property: Composite Young's modulus: $e^* = 0.5$ at $c^* = 0.5$. Some results of an analysis with Equation 12.8 are illustrated in Figures 12.10 and 12.11.

It is noticed that the pre-described Young's modulus can be obtained forming the composite with a DC geometry (a = 0), and forming it with a MM geometry (a = 1). The latter geometry is to prefer if an additional design criterion is that the composite geometry must be produced by impregnation technique.

Figure 12.13. Example 2: Shape functions consistent with geo-path in Figure 12.12.
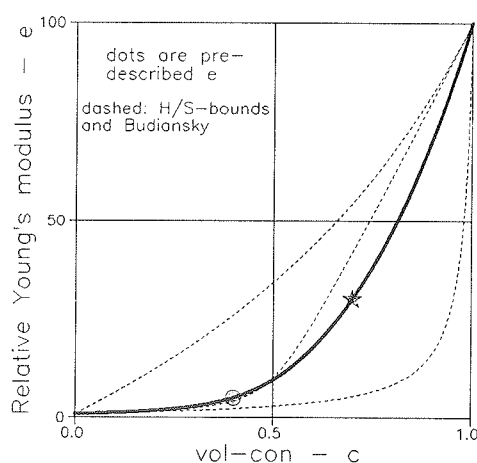
Figure 12.14. Example 2: Young's moduli of designed composite.

Example 2: Stiffness ratio: n = 100. Pre-described moduli: $e^* = 5$ at $c^* = 0.4$ and $e^* = 30$ at $c^* = 0.7$. Each pre-described property can be considered individually as in Example 1. We will, however, add the following pre-description that the two pre-described Young's moduli must be based on the same geo-path (the same processing technique!). It is then tempting to predict stiffness for any P-concentra-

126

tion along this particular geo-path. The results of such an analysis, with a geo-path parameter of a $= 0.5$, are shown in Figures 12.12 - 12.14 showing that the pre-described Young's moduli, for example, can be obtained producing a compacted particulate composite with P fibres of aspect ratios A ≈ 3 (see Figure 10.5) which start growing together at a packing concentration of $c_s \approx 0.45$. (The compaction ensures a tight composite when $c > c_s$).

12.2.2 More refined materials design

Theoretically the method suggested above for a simple materials design process can easily be generalized also to apply for composites not restricted by the simplified theory introduced in Chapter 10. Implicitly, shape function values can be determined from Equation 12.6 for any geo-path ($\mu_s = f(\mu_P)$) - and the analysis can be split into a deviatoric and a volumetric part from which we can determine a number of qualified deviatoric and volumetric shape function values (various geometry suggestions).

The difficult part, however, is left. How can we attach these values to specific composite geometries. More geometrical knowledge is required than what is sufficient for the simplified theory. The following future research is suggested in this area:

- FEM tests on a number of standard composites should be made - from which shape function values can be deduced at various concentrations - in principles as made in this monograph for the CROSS composite considered in Section 9.1.4 (and Appendix D).
- This step, of course, has to be made parallel with technology studies on, how to produce such standard composites in practice.

As an example of more refined design, look at Section 8.1.3 which can be read as the result of a design process to suggest porous materials with Poisson's ratios higher than 0.2 (being the matrix Poisson's ratio).

12.3 Conclusion

Justifications have been presented in Chapter 11 that the theory developed in Chapter 10 is a qualified basic instrument in further studies of the behavior of composite materials - such as with respect to rheology and other physical properties of composites. Further qualifications of the theory have been presented in this Chapter 12: The theory can be used also to evaluate semi-theoretical and empirical prediction methods, and it has potentials with respect to design of materials.

13. Viscoelasticity

Any relation previously developed on geometry, stiffness, stress, strain, and eigen-stress/strain are further developed in Chapter 14 also to apply when composites are considered with linear viscoelastic components. The analytical basics for doing so are certain powerful analogies which exist between the theory of viscoelasticity and the theory of elasticity. To keep this monograph self-contained with respect to viscoelastic analysis, including analogies, it has been found appropriate to summarize very briefly the theory of viscoelasticity as it has been adapted by the author in (e.g. 64,109,110) for the analysis of viscoelastic composites.

Viscoelastic materials are considered which comply with the elastic materials considered in Chapter 10, meaning that bulk creep and shear creep develops proportionally with Poisson's ratios keeping the orders of magnitudes ≈ 0.2. Theoretically it is not difficult to perform a more general analysis (111,112). The mathematics, however, will increase to a level which cannot be justified by our present knowledge on the rheological properties of most materials, especially when composite geometrical aspects are also considered as they are in Chapter 14. The relevance of assuming an approximately constant Poisson's ratio in concrete analysis has been further discussed in (113).

Unless otherwise indicated viscoelastic materials are considered with constant material properties meaning, for example, that Young's modulus does not change with time. Most materials behave in this way. One very important group of materials, however, does not. Portland cement paste and related materials are so-called aging viscoelatic materials with properties which change considerably, especially at young ages ($<$ ≈ 3 weeks). At more mature ages hardened cement paste (HCP) and concrete can be considered by easy approximate methods presented in this chapter together with methods developed for the analysis of non-aging viscoelastic materials. These methods suffice for most practice. At early age loading, however, cement paste and concrete have to be considered by the more complex theory of aging viscoelasticity presented by the author in (109,113,114).

13.1 Stress-strain relations

The stress-strain relation of a viscoelastic material can be expressed in three different ways as shown in Equation 13.1, see (115) for example. The integral expressions relate strain and stress through the creep function, C(t) defined in Figure 13.1, or the relaxation function, R(t) defined in Figure 13.2. The creep function and the relaxation function are related as shown in Equation 13.2.

$$\sum_{k=0}^{N} p_k \frac{d^k \sigma}{dt^k} = \sum_{k=0}^{N} q_k \frac{d^k \varepsilon}{dt^k} \qquad \textit{differential representation}$$

$$\varepsilon = \int_{t=-\infty}^{t} C(t - \theta) \frac{d\sigma}{d\theta} d\theta \qquad \textit{creep integral representation} \qquad (13.1)$$

$$\sigma = \int_{t=-\infty}^{t} R(t - \theta) \frac{d\varepsilon}{d\theta} d\theta \qquad \textit{relaxation integral representation}$$

$$\int_{t=-\infty}^{t} C(t - \theta) \frac{dR(\theta)}{d\theta} d\theta = \int_{t=-\infty}^{t} R(t - \theta) \frac{dC(\theta)}{d\theta} d\theta \equiv 1 \qquad (13.2)$$
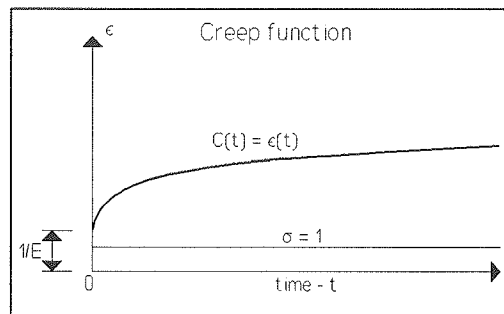
Figure 13.1. Creep function is strain of material subjected to a constant stress of magnitude 1 applied at $t = 0$.
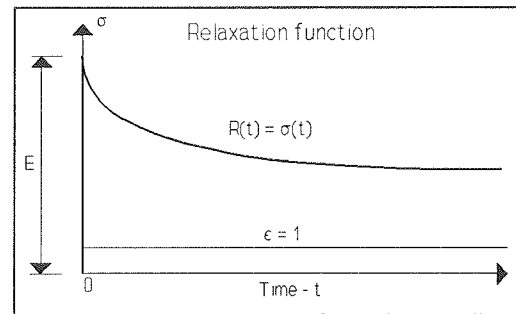
Figure 13.2. Relaxation function is stress in material subjected to a constant strain of magnitude 1 applied at $t = 0$.

13.1.1 Analogy Young's modulus

Very compact and efficient versions of the stress-strain relations for viscoelastic materials can be obtained by Laplace transformation of Equation 13.1, see (115,116). This feature has been used by the author in (110) to introduce the concept of "analogy Young's modulus" into the theory of viscoelasticity: Laplace transformed stress and laplace transformed strain are related by the viscoelastic "Hooke's law" in Equation 13.3 where the analogy Young's modulus E^A relates to laplace transformed creep- and relaxation functions as presented in Equation 13.4.

The advantage of introducing the analogy Young's modulus is that statements or expressions subsequently presented can be given a very rational and short formulation, especially when viscoelastic composites are considered.

$$\overline{\varepsilon} = \frac{\overline{\sigma}}{E^A} \quad \textit{"Hooke's law"with laplace transformed stress and strain} \qquad (13.3)$$

$$E^A = E^A(s) = \frac{\sum\limits_{k=0}^{N} q_k s^k}{\sum\limits_{k=0}^{N} p_k s^k} = \frac{1}{s\overline{C}(s)} = s\overline{R}(s) \quad \textit{Analogy Young's modulus} \qquad (13.4)$$

Laplace transformation: In laplace transformation the image function, overlined f(s), and the object function f(t) are related as shown in Equation 13.5. The symbols $\mathscr{L}$ and $\mathscr{L}^{-1}$ mean laplace transformed and inversion of laplace transformed respectively. The complex variable is denoted by s. α and β are real numbers. The imaginary unit is denoted by i.

$$\overline{f}(s) = \mathscr{L}\{f(t)\} = \int\limits_{0-}^{\infty} f(t)e^{-st}dt \quad ; \quad f(t) = \mathscr{L}^{-1}\{\overline{f}(s)\} = \frac{1}{2\pi i}\lim_{\beta\to\infty}\int\limits_{\alpha-i\beta}^{\alpha+i\beta} \overline{f}(s)e^{st}ds \qquad (13.5)$$

Information on laplace transformation, laplace transformed, and their inverse can be found in a number of mathematical handbooks, for example (117,118, 119). Numerical methods are found in (120,121,122). Some general properties of Laplace transforms and some special Laplace transforms are shown in Table 13.1.

Elastic-viscoelastic analogy (e-v-analogy)

A number of analogies have been presented (e.g. 123,124,116) which formulate the relationship between *quasi-static* stress analysis of viscoelastic structures and similar stress analysis of elastic counterpart structures. The basic version of these analogies (elastic-viscoelastic analogies, e-v-analogies) can be expressed as follows: Viscoelastic solutions are obtained from their corresponding elastic solutions replacing flexibility (1/E) or stiffness (E) in these solutions with the corresponding viscoelastic integral operators expressed in Equation 13.6.

$$\frac{1}{E} \Rightarrow \int\limits_{-\infty}^{t} C(t - \theta)\frac{d[\ ]}{d\theta}d\theta \quad ; \quad E \Rightarrow \int\limits_{-\infty}^{t} R(t - \theta)\frac{d[\ ]}{d\theta}d\theta \qquad (13.6)$$

The author's version of the e-v-analogy is the following formulated and applied in (109,110):

130

The Laplace transformed solution to a linear-viscoelastic structural problem is obtained from the corresponding linear-elastic solution by replacing Young's modulus with the analogy Young's modulus presented in Equation 13.4 - and time dependent terms, such as load/stress and displacement/strain, with their respective Laplace transformed quantities.

OBJECT - $f(t)$	IMAGE - $\bar{f}(s)$	OBJECT - $f(t)$	IMAGE - $\bar{f}(s)$
$c * g(t)$	$c * \bar{g}(s)$	$H(t)$ (Heaviside)	$\dfrac{1}{s}$
$g(t) + h(t)$	$\bar{g}(s) + \bar{h}(s)$	$\delta(t) = \dfrac{dH(t)}{dt}$ (Dirac)	1
$g(t) * \exp(c * t)$	$\bar{g}(s - c)$	t^n $(n \geq 0)$	$\dfrac{\Gamma(n+1)}{s^{n+1}} = \dfrac{n!}{s^{n+1}}$
$g(t/c)$	$c * \bar{g}(cs)$	e^{-ct}	$\dfrac{1}{s + c}$
$g(t - \tau)$	$e^{-\tau s} * \bar{g}(s)$	$t^n e^{-ct}$	$\dfrac{n!}{(s + c)^{n+1}}$
$\displaystyle\int_0^t g(\tau) * h(t - \tau)d\tau$	$\bar{g}(s) * \bar{h}(s)$	$\cos(\omega t)$	$\dfrac{s}{s^2 + \omega^2}$
$\displaystyle\int_0^t g(\tau)d\tau$	$\bar{g}(s)/s$	$\sin(\omega t)$	$\dfrac{\omega}{s^2 + \omega^2}$
$\dfrac{d^n g(t)}{dt^n}$; $g(t<0) \equiv 0$	$s^n \bar{g}(s)$	$\dfrac{1}{c}(1 - e^{-ct})$	$\dfrac{1}{s(s + c)}$
$f(0) = \lim_{s \to \infty}[s * \bar{f}(s)]$; $f(\infty) = \lim_{s \to 0}[s * \bar{f}(s)]$		$\dfrac{1}{c}\left[t - \dfrac{1}{c}(1 - e^{-ct})\right]$	$\dfrac{1}{s^2(s + c)}$
		$\dfrac{e^{-at} - e^{-bt}}{b - a}$	$\dfrac{1}{(s + a)(s + b)}$

Table 13.1. Some general properties of Laplace transforms and some special Laplace transforms. Gamma function $\Gamma(a+1) = faculty\ a\ (a!)$.

Unless otherwise indicated this (quasi-static) version of the e-v-analogy is always used in the following sections of this monograph. Formally the e-v-analogy works as outlined in Equation 13.7 where Δ is the solution to a viscoelastic problem in the analysis of a viscoelastic body. Time dependent actions are symbolized by $P = P(t)$. Usually the inversion of the second expression in Equation 13.7 must be made by handbook tables or by numerical means as previously referred to.

$$\left.\begin{array}{rcl} \Delta_{ELAS}(t) & = & F[E,\ P(t)] \\[4pt] \overline{\Delta}_{VISC}(s) & = & F[E^{A}(s),\ \overline{P}(s)] \\[4pt] \Delta_{VISC}(t) & = & \mathcal{L}^{-1}\{\overline{\Delta}_{VISC}(s)\} \end{array}\right] \qquad E\text{-}v\text{-}analogy \qquad (13.7)$$

13.1.2 Vibrations

We re-call that the analogy just considered applies strictly only for quasi-static analysis with any forces of inertia neglected. A general analogy, however, can be established which considers such forces also (dynamic problems). Keeping the concept of analogy Young's modulus in mind it can be concluded from (125,126) that:

> The Laplace transformed solution to a viscoelastic structural problem is obtained by Laplace transforming its elastic counterpart solution, and replace Young's modulus with its analogy Young's modulus.

Obviously the quasi-static e-v-analogy previously considered is included in this general analogy. Usually the Laplace transforms obtained are rather complicated. Numerical inversion procedures have to be used. One special dynamic problem, however, can be solved in a more easy way. As shall subsequently be seen the important harmonic vibration problem can be solved analytically introducing the so-called complex Young's modulus.

Complex Young's modulus

The special stress-strain relation presented in Equation 13.8 applies to viscoelastic materials subjected to harmonic stress $\sigma_H = \sigma_o e^{i\omega t}$ where σ_o is stress amplitude, ω is angular frequency [5], and i is complex unity. The so-called complex Young's modulus E_C is related to the analogy Young's modulus as shown in Equation 13.9. The stress-strain relation is graphically presented in Figures 13.3 and 13.4 with complex Young's modulus in algebraic notation as explained in Equation 13.10.

$$\begin{array}{l} \varepsilon_H = \dfrac{\sigma_H}{E_C} \quad \text{with harmonic stress/strain} \quad \left[\begin{array}{l} \sigma_H = \sigma_o \exp(i\omega t) \\[4pt] \varepsilon_H = \varepsilon_o \exp(i(\omega t - \delta)) \end{array}\right. \\[20pt] \varepsilon_o = \dfrac{\sigma_o}{|\,E_C\,|} \quad \text{is strain amplitude and } \delta \text{ is loss angle} \end{array} \qquad (13.8)$$

$$E_C = E_C(\omega) = E^A(i\omega) \qquad \text{Complex Young's modulus} \qquad (13.9)$$

---

5) Angular frequency $\omega = 2\pi/T$ where T is cyclic (or oscillation) time. It relates to tradional frequency, f (cycles/time unit) by $\omega = 2\pi f$. If time unit is second then f is in Hz.

$$E_c = E_R + iE_I \qquad ; \quad E_R, \ E_I \ \text{are real, imag. Young's moduli}$$

$$|E_c| = \sqrt{E_R^2 + E_I^2} \qquad ; \quad \text{is absolute stiffness}$$

$$\tan(\delta) = E_I/E_R \qquad ; \quad \text{is loss tangent} \qquad (13.10)$$

Equations 13.8 and 13.9 are easily verified by the first expression in Equation 13.1 introducing stress and strain from Equation 13.8 and then comparing the results obtained with Equation 13.4. An example of complex Young's modulus determined by Equation 13.9 is presented in Section 13.3.
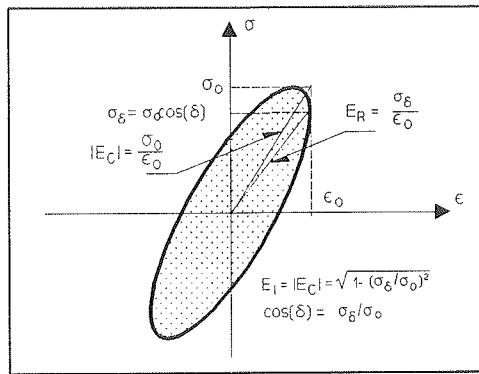
Figure 13.3. Stress-strain test of viscoelastic material subjected to harmonic vibration.
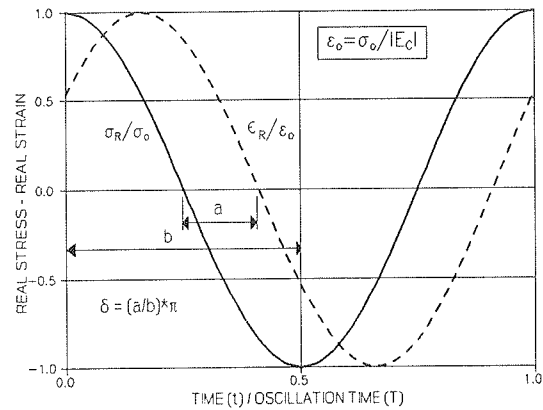
Figure 13.4. Oscillation time T, $\Rightarrow$ frequency $f = 1/T$, (angular frequency $\omega = 2\pi f$).

Creep functions and relaxation functions are related to the complex Young's modulus by Equation 13.12 adapted from (127,128,129). Examples of creep and relaxation determined from the complex Young's modulus are presented in the subsequent Section 13.3.

$$R(t) = E - \frac{2}{\pi} \int_0^\infty E_I(\omega) \ \frac{1 - \cos(\omega t)}{\omega} \ d\omega \quad (E \text{ is } R \text{ at very high } \omega)$$

$$C(t) = \frac{1}{E} + \frac{2}{\pi} \int_0^\infty J_I(\omega) \ \frac{1 - \cos(\omega t)}{\omega} \ d\omega \quad ; \quad \left[J_I = \frac{E_I}{|E_c|^2} \right] \qquad (13.11)$$

Remark: We re-call that one of the functions considered in Equation 13.11 (usually the relaxation function) can be determined from the other one (creep function) by Equation 13.2.

133

Vibration analogy

From (125,126) can be concluded that the general e-v-analogy previously presented can be continued as follows when harmonic vibration problems specifically are considered (keeping in mind the concept of analogy Young's modulus):

> The analysis of a viscoelastic structure with sine (or cosine) varying load can be made by the theory of elasticity with Young's modulus replaced by its viscoelastic counterpart, namely the complex Youngs modulus expressed by $E_c = E^\wedge(i\omega)$ from Equation 13.4.

Formally the analogy works as outlined in Equation 13.12 where the vibration deflection Δ of a viscoelastic body is considered subjected to the harmonically varying load P_H.

$$\begin{aligned} \Delta_{H,EL} &= F[E, \ P_H] \\ \Delta_{H,VISC} &= F[E_c, \ P_H] \end{aligned} \qquad \text{Vibration-analogy} \qquad (13.12)$$

Experimental vibration analysis

The vibration analogy has been used by the author in (130,131,132, 133) to develops a method by which the complex Young's modulus of a material can be determined experimentally by modern vibration analysis equipment like the Brüel & Kjær type 3550 apparatus (134). Creep and relaxation are subsequently determined by Equation 13.11. This new experimental method of determining materials viscoelasticity is a promising supplement (135) to the more traditional ways of material testing by direct measurements of creep and relaxation, see Figures 13.1 and 13.2.

13.2 Models of viscoelastic materials

A complete analogy exist between viscoelastic stress-strain relations and force-deflection relations for mechanical systems composed of springs (Hooke elements) and dash pots (Newton elements). For practical convenience we subdivide viscoelastic materials into two groups: Simple viscoelastic materials, and less simple viscoelastic materials. The former group can be modelled as shown in Table 13.2 with up to 4 basic elements (Hooke, Newton). More than 4 basic elements are needed to model the latter group of materials.

13.2.1 Simple models

Closed analytical expressions for stress-strain relations, analogy Young's moduli, creep- and relaxation functions apply for simple viscoelastic materials. They are summarized in Tables 13.3 and 13.4 reproduced from (110). Complex stiffness of the simple material models are easily obtained by replacing s with $i\omega$ as explained in Equation 13.9.

The so-called Burgers model is the most general of the simple models of a viscoelastic material. All basic strain modes observed in practice are considered: Elastic strain (Hooke), delayed elastic strain (Kelvin), and flow strain (Newton). The latter two strain components are also named reversible creep and irreversible creep respectively. The viscoelasticity of a number of building materials can be modelled by the Burgers model.
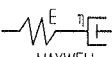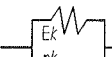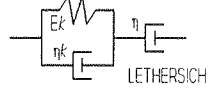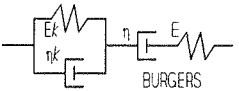
MODELS	MATERIAL PARAMETERS
HOOKE, NEWTON, MAXWELL, KELVIN, THOMSON, LETHERSICH, BURGERS	$\tau = \dfrac{\eta}{E}$; $\tau_K = \dfrac{\eta_K}{E_K}$ Relaxation times $\alpha = \dfrac{E}{E_K}$; $m_T = 1 + \alpha$; $m_L = \dfrac{1}{1 + \eta/\eta_K}$ $\begin{aligned} m_{B1} \\ m_{B2} \end{aligned} = \dfrac{1}{2}\left[1 + \alpha + \dfrac{\tau_K}{\tau} \pm \sqrt{\left(1 + \alpha + \dfrac{\tau_K}{\tau}\right)^2 - 4\dfrac{\tau_K}{\tau}} \right]$ $\left[Control:\ m_{B1}m_{B2} = \dfrac{\tau_K}{\tau} \ ;\quad m_{B1} + m_{B2} = 1 + \alpha + \dfrac{\tau_K}{\tau} \right]$

Table 13.2. Simple models of viscoelastic materials. Hooke and Newton are the basic models. Reproduced from (110).

MODEL	STRESS-STRAIN RELATION	E^A (ANALOGY-E)
Hooke	$\sigma = E\varepsilon$	E
Newton	$\sigma = \eta \dfrac{d\varepsilon}{dt}$	ηs
Maxwell	$\dfrac{d\sigma}{dt} + \dfrac{\sigma}{\tau} = E\dfrac{d\varepsilon}{dt}$	$E\,\dfrac{s}{s + 1/\tau}$
Kelvin	$\sigma = E_K\left[\tau_K\dfrac{d\varepsilon}{dt} + \varepsilon\right]$	$E_K\tau_K(s + 1/\tau_K)$
Thomson	$\tau_K\dfrac{d\sigma}{dt} + m_T\sigma = E\left[\tau_K\dfrac{d\varepsilon}{dt} + \varepsilon\right]$	$E\,\dfrac{s + 1/\tau_K}{s + m_T/\tau_K}$
Lethersich	$\tau_K\dfrac{d\sigma}{dt} + m_L\sigma = m_L\eta\left[\tau_K\dfrac{d^2\varepsilon}{dt^2} + \dfrac{d\varepsilon}{dt}\right]$	$m_L\eta\dfrac{s(s + 1/\tau_K)}{s + m_L/\tau_K}$
Burgers	$\tau_K^2\dfrac{d^2\sigma}{dt^2} + (m_{B1} + m_{B2})\tau_K\dfrac{d\sigma}{dt} + m_{B1}m_{B2}\sigma =$ $= E\left[\tau_K^2\dfrac{d^2\varepsilon}{dt^2} + \tau_K\dfrac{d\varepsilon}{dt}\right]$	$E\dfrac{s(s + 1/\tau_K)}{(s + m_{B1}/\tau_K)(s + m_{B2}/\tau_K)}$

Table 13.3. Simple viscoelastic models: Stress-strain relations and analogy Young's moduli. Abbreviations from Table 13.2. Reproduced from (110).

MODEL	CREEP FUNCTION	RELAXATION FUNCTION
Hooke	$1/E$	E
Newton	t/η	$\eta\delta(t)$; Dirac's delta function $\delta(t)$
Maxwell	$\dfrac{1}{E}\left[1 + \dfrac{t}{\tau}\right]$	$E\exp\left[-\dfrac{t}{\tau}\right]$
Kelvin	$\dfrac{1}{E_K}\left[1 - \exp\left[-\dfrac{t}{\tau_K}\right]\right]$	$E_K\left(1 + \tau_K\delta(t)\right)$
Thomson	$\dfrac{1}{E}\left[1 + \alpha\left[1 - \exp\left[-\dfrac{t}{\tau_K}\right]\right]\right]$	$E\left[1 - \dfrac{\alpha}{1 + \alpha}\left[1 - \exp\left[-m_T\dfrac{t}{\tau_K}\right]\right]\right]$
Lethersich	$\dfrac{t}{\eta} + \dfrac{1}{E_K}\left[1 - \exp\left[-\dfrac{t}{\tau_K}\right]\right]$	$m_L\eta\left[\delta(t) + \dfrac{1 + m_L}{\tau_K}\exp\left[-m_L\dfrac{t}{\tau_K}\right]\right]$
Burgers	$\dfrac{1}{E}\left[1 + \dfrac{t}{\tau} + \alpha\left[1 - \exp\left[-\dfrac{t}{\tau_K}\right]\right]\right]$	$\dfrac{E}{m_{B1} - m_{B2}}\left[(m_{B1} - 1)\exp\left[-m_{B1}\dfrac{t}{\tau_K}\right] - (m_{B2} - 1)\exp\left[-m_{B2}\dfrac{t}{\tau_K}\right]\right]$

Table 13.4. Simple viscoelastic models: Creep functions and relaxation functions. Abbreviations from Table 13.2. Reproduced from (110).

136

13.2.2 Less simple models

It can be shown that general mechanical models for viscoelastic materials can be established in two ways. One general model is a Maxwell model connected in series with a chain of several Kelvin models in series. The other general model is a Hooke model connected in parallel with a chain of several Maxwell models in parallel. Both these models are discussed in further details in Appendix F.

Power Law model (Wood, Polymers, Ceramics)

A very special and important "less simple model" is the so-called Power Law model presented in Table 13.5. This model cannot be composed by a finite number of elementary mechanisms. An infinite number of elements have to be used.

The Power Law model is the result of a complete analysis made in (129) of an expression, $C(t) = (1 + at^b)/E$ with constants a and b, which has very often been used successfully in the literature (e.g. 136) to fit experimental data from creep tests on a variety of building materials such as wood, polymers, and ceramic materials. Physically the fit expression is very unfortunate (one material constant "a" has the dimension of time raised to minus the other material constant "b").

POWER LAW CREEP	
CREEP FUNCTION C(t)	**RELAXATION FUNCTION R(t)**
$\dfrac{1}{E}\left[1 + \left[\dfrac{t}{\tau}\right]^b\right]$	$E\sum\limits_{k=0}^{\infty}\dfrac{(-Z(t))^k}{\Gamma(1 + kb)} \approx \dfrac{1}{C(t)}\ \ if\ b < \dfrac{1}{3}$
ANALOGY YOUNG'S MODULUS $E^A(s)$	
$E\ \dfrac{(\tau s)^b}{\Gamma(1 + b) + (\tau s)^b}$	

Table 13.5. Power law creep. $Z(x) = \Gamma(1+b)(x/\tau)^b$ where Γ means gamma function. Reproduced from (129). τ is relaxation time. b is creep power.

Re-formulated, however, as it is in in Table 13.5 the expression becomes viscoelastically sound, characterizing the materials rheology by independent material properties, namely the relaxation time τ (or creep doubling time $(C(\tau) = 2C(0))$, and the dimensionless creep power, b.

The Power Law model is a very efficient tool in viscoelastic stress-strain analysis. A number of material problems for a number of different materials can be solved in one approach, by developing standard solutions ('master solutions') from which solutions for specific materials can be picked introducing specific material parameters, τ and b.

Remark: The efficiency of the Power Law model in viscoelastic stress-strain analysis of materials can be generalized to include the influence of curing conditions with respect to moisture and temperature: The relaxation time is the obvious materials parameter to be influenced by climatic conditions. For wood, for example, τ is known to be very sensitive to moisture content (137). This observation has been utilized in (137) to produce 'master graphs' from which fatigue-life of wood can be predicted as a function of moisture content.

Complex stiffness of a material with Power-law creep is obtained by replacing s with $i\omega$ in $E^A(s)$ as explained in Equation 13.9. The results are presented in Equation 13.13 and 13.14 reproduced from (129). The Power law creep model degenerates with $b = 1$ to the so-called Maxwell model defined in Table 13.2. The complex stiffness quantities become very simple as demonstrated in Equation 13.15.

$$|E_c| = \frac{E}{\sqrt{1 + Y^2 + 2Y\cos(b\pi/2)}} \quad ; \quad \tan\delta = \frac{Y\sin(b\pi/2)}{1 + Y\cos(b\pi/2)}$$

$$with \quad Y = \frac{\Gamma(1 + b)}{(\tau\omega)^b} = \frac{b!}{(\tau\omega)^b} = \frac{\tan(\delta)}{\sin(b\pi/2) - \tan(\delta)\cos(b\pi/2)} \qquad (13.13)$$

$$E_R = E\frac{1 + Y\cos(b\pi/2)}{1 + Y^2 + 2Y\cos(b\pi/2)} \quad ; \quad E_I = E\frac{Y\sin(b\pi/2)}{1 + Y^2 + 2Y\cos(b\pi/2)}$$

$$|E_c| \rightarrow \left\{\begin{array}{ll} E & \text{if } \omega \rightarrow \infty \\ 0 & \text{if } \omega \rightarrow 0 \end{array}\right. \quad ; \quad \tan(\delta) \rightarrow \left\{\begin{array}{ll} 0 & \text{if } \omega \rightarrow \infty \\ \tan(b\pi/2) & \text{if } \omega \rightarrow 0 \end{array}\right. \qquad (13.14)$$

$$|E_c| = E\frac{\tau\omega}{\sqrt{1 + (\tau\omega)^2}} = E\cos(\delta) \quad ; \quad \tan(\delta) = \frac{1}{\tau\omega} \quad ; \quad (Maxwell) \qquad (13.15)$$

Time modified models - aging viscosity

Some viscoelastic materials like Portland cement paste and concrete are so-called aging viscoelastic materials (109) with time dependent material properties meaning that the creep functions, relaxation functions, and the material parameters p and q in Equation 13.1 become dependent of time. Some aging materials, however, can be analyzed by the theory of non-aging materials hitherto considered if we assume that the "spring constants" (E) in the mechanical models are constants (in practice almost constants) and that viscosities (η) change in the same way with age. Then the aging phenomenon can be removed by introducing a modified time as subsequently demonstrated in Equation 13.16 on a Maxwell material with age dependent viscosity or time dependent relaxation time.

138

Aging Maxwell:

$$\frac{d\sigma}{dt} + \frac{\sigma}{\tau(t)} = E\frac{d\varepsilon}{dt} \qquad \Rightarrow$$

differentiation through ϕ:

$$\frac{d\sigma}{d\phi}\frac{d\phi}{dt} + \frac{\sigma}{\tau(t)} = E\frac{d\varepsilon}{d\phi}\frac{d\phi}{dt} \qquad \Rightarrow \qquad (13.16)$$

$$\frac{d\sigma}{d\phi} + \frac{\sigma}{\tau(t)d\phi/dt} = E\frac{d\varepsilon}{d\phi} \qquad \Rightarrow$$

Maxwell with modified
time ϕ and $"\tau" = 1$

$$\frac{d\sigma}{d\phi} + \sigma = E\frac{d\varepsilon}{d\phi} \qquad (13.17)$$

where modified time is related to real time by $\tau(t)d\phi/dt = 1$, meaning

$$\phi = \phi(t) = \int_{t_o}^{t+t_o} \frac{1}{\tau(\theta)}d\theta \qquad with \quad \begin{cases} time \ t \ measured \ from \\ age \ at \ first \ loading \ t_o \end{cases} \qquad (13.18)$$

Thus, a Maxwell material with aging viscosity can be considered as a non-aging Maxwell material when time t is replaced with modified time ϕ (also named "creep parameter"), and relaxation time τ is replaced with modified relaxation time $\tau = 1$. Then from Table 13.4 creep functions and relaxation functions become as presented in the first row of Table 13.6.

Remarks: The e-v-analogy applies for time-modified models if stress and strain are formulated in modified time before laplace transformation. The vibration analogy, however, does not apply. The analogy becomes meaningless introducing "harmonic" variations in stress and strain with time in modified time.

Hardened cement paste (HCP)

Based on the classical papers of Dischinger's (138,139) on creep of concrete the modified time concept was suggested by the author in (109,140) and subsequently further developed and generalized in a number of papers (110,41, 141,147,142) on the rheology of hardened portland cement paste and portland cement based materials. The concept was introduced into international concrete codes in (143).

For hardened HCP, cured at (T,RH) $\approx$ (20°C,60%), the creep parameter can be estimated by the expression presented in Table 13.6 which is developed from Equation 13.18 assuming a relaxation time (or viscosity) which develops proportional with time. The expressions presented in Table 13.6 are consistent with general rheological observations made in (109,114,113) on cement paste and concrete.

MATURE HCP (age > 3 weeks)	
CREEP FUNCTION	RELAXATION FUNCTION
$C(t)_{HCP} = \dfrac{1}{E_{HCP}}(1 + \phi)$	$R(t)_{HCP} = E_{HCP} * \exp(-\phi)$
STIFFNESS (MPa)	CREEP PARAMETER (t in days)
E_{HCP} (Table 11.1, $g(t) \equiv 1$)	$\phi = \phi^* * \log_E \left[\dfrac{t + t_o}{t_o} \right]$; $\phi^* \approx \begin{cases} 1.4 & ; \ W/C \geq 0.4 \\ 3.5 W/C & ; \ W/C < 0.4 \end{cases}$

Table 13.6. Creep of hardened cement paste at t days after loading at the age of t_o days. Creep factor is denoted by ϕ^*.

The creep parameter for hardened HCP is independent of W/C > 0.4. Very soft aggregates (voids) in a particulate composite do not influence the type of viscosity relative to the one applying to the matrix (here, basic paste) (110,78,79).

DRYING SHRINKAGE OF HCP AT RH ≈ 0.6
$\lambda = k * \phi$ with $k \approx -0.5 \, o/oo$

Table 13.7. Drying shrinkage of hardened cement paste. Shrinkage factor is denoted by k.

Shrinkage: A composite analysis of concrete will subsequently be demonstrated in Chapter 14 where concrete is modelled as aggregates mixed into a matrix of cement paste. In this context, it is of great interest to evaluate the influence of cement paste shrinkage on the shrinkage of concrete. For this purpose cement paste shrinkage can be estimated by Table 13.7, adopting an idea from (147).

Remark: When early age cement pastes are considered where stiffness and viscosity properties change very much with age the concept of time modified Maxwell behavior is not applicable. More refined models have to be used such as referred to in Section 14.2.4.

13.3 Summary, analysis, and approximate analysis

A number of material models have been demonstrated in this chapter some of which are of immediate relevance for the analysis of viscoelastic materials often met in practice. Examples are cement- and wood based materials, asphalt, and polymers.

Various tools have been presented which can be used to predict the stress-strain behavior of viscoelastic materials subjected to static or dynamic loads. Methods

are presented which convert material properties (creep function, relaxation function, and complex elastic moduli) of relevance for such analysis. An illustrative example of property conversion between creep/relaxation functions and complex elastic moduli are demonstrated in Figures 13.5 and 13.6.

The material considered is a Burgers material with E = 30000 MPa, α = 1, and (τ,τ_K) = (1000,10) days. The complex Young's modulus is determined from the analogy Young's modulus presented in Table 13.3 replacing s with $i\omega$ as previously explained. The results (calculated on a computer with complex number facilities) are presented in Figure 13.5.

The creep function and relaxation function presented in Figure 13.6 are calculated in two ways: The solid line data are exact as determined directly from Table 13.4. The dotted data are predicted by Equation 13.11 with complex stiffness introduced as previously calculated (Figure 13.5). The two data set agree very positively (as they should) which tells about the quality of Equation 13.11 to act as a materials property 'converter'.

Remark: The latter observation is emphasized: With modern technology, the data in Figure 13.5 could have been detected experimentally, meaning that Equation 13.11 opens a new way of property determination for viscoelastic materials, see Section 13.1.2.
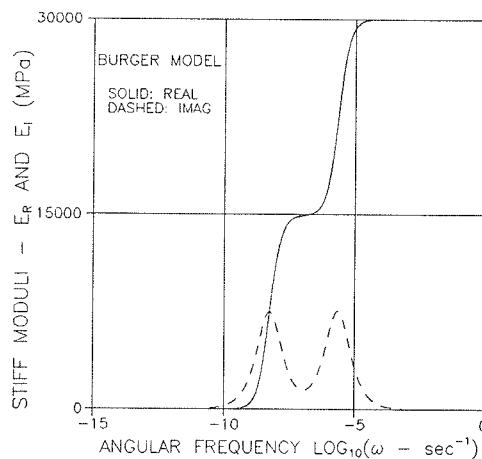
Figure 13.5. Complex stiffness of Burgers: E = 30000 MPa, α = 1, and (τ,τ_K) = (1000, 10) days.
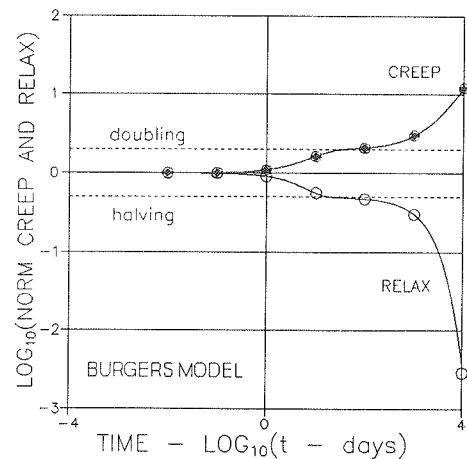
Figure 13.6. Creep and relaxation calculated from "experimental" complex Young's modulus in Figure 13.6.

13.3.1 Approximate analysis

The well-known 'effective modulus method' (E^{EFF}-method) (e.g.144,145) presented in Equation 13.19 for quasi-static stress-strain analysis of viscoelastic materials is a crude approximation of the accurate stress-strain analysis considered

141

in this chapter. The advantage in practice of the E^{EFF}-method is that it is very convenient to use for first stress-strain estimates. It is emphasized, however, that the method when used un-reflected (as it commonly is) may lead to results which are completely wrong. This discrepancy was recognized already in (144). An obvious false prediction is that ϵ becomes 0 whenever σ drops to 0. Obviously the method can not be used in vibration analysis.

$$\varepsilon(t) \approx \frac{\sigma(t)}{E^{EFF}} \quad with \quad E^{EFF} = \frac{1}{C(t)} = \frac{E}{1 + \phi} \qquad \underline{E^{EFF}\text{-}method}$$

where $\phi = \phi(t) = EC(t) - 1$ is the so-called creep-parameter   (13.19)

A general description of the 'accuracy' of the E^{EFF}-method is impossible. It will depend on both type of materials viscosity and type of problem to be solved. However, for the type of problems (analysis of material properties) considered in this monograph we 'risk' to state the following simple quality assessment of the E^{EFF}-method. It is based on results obtained from running a number of evaluation calculations on Burgers, Thomson, Maxwell, and Power-Law viscoelastic materials - and on the author's work on creep of concrete in (146,147):

> Reasonable estimates can be obtained by the E^{EFF}-method when stress varies monotonically, restricted as outlined in Equation 13.20. The better estimates are obtained when the materials considered have creep functions (C) and relaxations functions (R) which are, approximately, each others reciprocals, meaning $R*C > $ approx 0.9.
>
> When $R*C < 0.9$ the E^{EFF}-method can still be used (with stress restricted as just explained). Creep parameters $\phi < 4$, however, are required. Obviously the E^{EFF}-method cannot in general be used to predict a relaxation function. It might be necessary to determine this function numerically from the creep function using the basic Equation 13.2.

$$\sigma_o(1 + \phi)^{-1} < \sigma < \sigma_o(1 + \phi) \qquad \sigma_o = \sigma(t=0)$$
$$or \quad \sigma = k\phi \qquad\qquad k \ is \ a \ constant \qquad (13.20)$$

Similar 'rules' will apply when modified E^{EFF}-methods are used as these are presented in (e.g.148,149).

The E^{EFF}-method applies almost accurately when Power-Law materials are considered with b < 0.3. As previously observed the creep function and the relaxation function for such materials are each others reciprocals.

Approximate inversion method

The effective Young's modulus can be related to the analogy Young's modulus E^A by the following deductions involving Equation 13.4 and the general properties section of Table 13.1.

142

$$\overline{C}(s) = \frac{1}{sE^A(s)} \quad \Rightarrow$$

$$C(\infty) = \lim_{s \to 0} \frac{1}{E^A(s)} \quad ; \quad C(0) = \lim_{s \to \infty} \frac{1}{E^A(s)} \quad \Rightarrow \qquad (13.21)$$

$$C(t) \approx \frac{1}{E^A(\gamma/t)} \quad ; \quad \underline{E^{EFF} = \frac{1}{C(t)} \approx E^A(\gamma/t)}$$

where γ is a so-called inversion parameter for which the order of magnitude can be estimated to be $0.5 < \gamma < 1$ with minimum and maximum applying to 'only reversible creep' and 'only viscous creep' respectively.

Remark: It can easily be shown that Equation 13.21 is a special result of using the following approximate inversion rule developed from Table 13.1,

$$F(t) \approx sF(s) \quad with \quad s = \frac{\gamma}{t} \qquad approximate \ inversion \ rule \qquad (13.22)$$

which can be used directly to develop approximate real solutions from their Laplace transformed counterparts. This procedure (*approximate inversion method*) is demonstrated in the following expression for stress in a Thomson material subjected to a constant strain, $\epsilon = 1$ (laplace transformed $1/s$).

$$\overline{\sigma} = \overline{\epsilon} * \overline{E}^A = \frac{E}{s} \frac{s + 1/\tau_K}{s + m_T/\tau_K} \quad \Rightarrow \quad \sigma(t) \approx E \frac{1 + t/\gamma/\tau_K}{1 + m_T t/\gamma/\tau_K} \qquad (13.23)$$
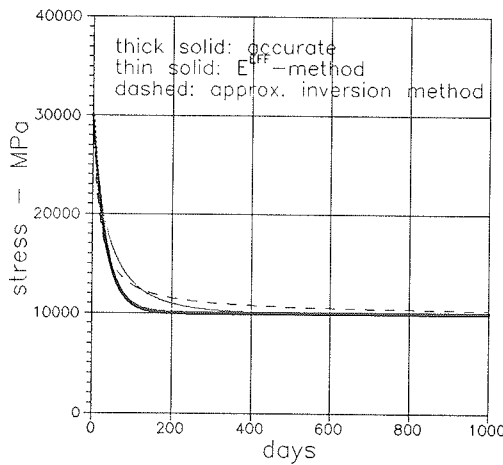
Figure 13.7. Thomson model loaded with constant strain $\epsilon = 1$. $E = 30000$ MPa, $\alpha = 2$, $\tau_K = 100$ days. Approximate inversion with $\gamma = 0.5$.

The results of a stress analysis of a Thomson material using the E^{EFF}-method and the approximate inversion method respectively are compared in Figure 13.7.

Remark: In this monograph the approximate inversion method is considered mainly as an interesting curiosum. Approximate analysis are always made with the E^{EFF}-method unless otherwise indicated.

14. Viscoelastic composite analysis

Creep functions, relaxation functions, internal stresses, and eigenstress/strain phenomenons of composite materials with various geometrical configurations are predicted in this chapter from known viscoelastic properties of the constituent phases.

Basically the composites considered in this chapter are the same as those defined in Chapters 13 and 10: Viscoelastic composite components are considered with constant Poisson's ratios of the order of magnitudes ≈ 0.2. The composite geometry can be sufficiently well described using the 3-parameter shape function descriptions. As previously indicated in Chapters 10 and 13: There are no problems theoretically in generalizing the analysis to more general composites with respect to Poisson's ratios and shape functions. The mathematics, however, will increase to a level which cannot be justified by our present knowledge on geometries and rheological properties of composite phases.

In principles the analytical methods used in this chapter are the same as have been developed previously by the author (109,110) in studies on the rheological behavior of prestressed concrete and on the viscoelasticity of concrete as a function of aggregate content - and in (150) in a study of stiffness and damping of impregnated materials.

In most examples presented the theory is illustrated using composite components which exhibit Power Law creep. The principles, however, are kept general such that composites can be considered with components of any viscoelastic observance. The reason for choosing Power law creep as 'default viscoelastic behavior' in examples is that many viscoelastic materials in practice can be well approximated in this way - and that analytical results obtained can be presented very explicitly. These features have previously been discussed in Section 13.2.2.

14.1 Composite analysis

14.1.1 Accurate analysis

The theoretical basis of the analysis presented in this chapter is the finding in (151,152) that the complex stiffness (E_c) of a composite made of viscoelastic phases (P,S) can be determined by the elastic counterpart composite stiffness (E), replacing phase stiffness (E_P, E_s) with their respective complex counterparts (E_{PC}, E_{sc}).

Keeping in mind the significance of the analogy Young's modulus previously introduced in Section 13.1.1, and re-calling the vibration analogy from Section 13.1.2, this means that the analogy Young's modulus of a composite material (E^A) can be

144

obtained from the elastic counterpart stiffness solution (E), replacing phase stiffness (E_P, E_S) with their respective analogy Young's moduli $(E_P{}^A, E_S{}^A)$.

Having established the basic rheological property (E^A) of the composite material we may proceed just as explained in Chapter 13 with the composite material considered as a homogeneous viscoelastic material. A further conclusion which can be made from (151,152) and the concept presented in this monograph of a analogy Young's modulus, is that composite stress/strain solutions can be established from Laplace transforming the elastic counterpart solutions (Tables 10.3 and 10.4) and replacing (E_P, E_S) with $(E_P{}^A, E_S{}^A)$. A summary of results such obtained from an analysis of composite materials is presented in Tables 14.1 and 14.2. Analogy Young's moduli $(E_P{}^A, E_S{}^A)$ for various homogeneous materials are presented in Section 13.2.

YOUNG'S MODULUS $\Rightarrow$ ANALOGY YOUNG'S MODULUS
$E = E(E_p, E_s) \Rightarrow E^A = E^A(s) = E(E_p^A, E_s^A)$
EXAMPLE $\quad E_P^A = \left[E\dfrac{(\tau s)^b}{\Gamma(1+b) + (\tau s)^b} \right]_P \quad ; \quad E_s^A = \left[E\dfrac{(\tau s)^b}{\Gamma(1+b) + (\tau s)^b} \right]_s$
ANALOGY YOUNG'S MODULUS $\Rightarrow$ COMPLEX YOUNG'S MODULUS
$E^A = E^A(s) = E(E_p^A, E_s^A) \Rightarrow E_c = E^A(i\omega) = E(E_{PC}, E_{SC}) = E_R(\omega) + iE_I(\omega)$
EXAMPLE $\quad E_{PC} = \left[E\dfrac{(i\tau\omega)^b}{\Gamma(1+b) + (i\tau\omega)^b} \right]_P \quad ; \quad E_{SC} = \left[E\dfrac{(i\tau\omega)^b}{\Gamma(1+b) + (i\tau\omega)^b} \right]_s$
COMPLEX YOUNG'S MODULUS $\Rightarrow$ RELAXATION AND CREEP
$R(t) = E - \dfrac{2}{\pi} \displaystyle\int_0^\infty E_I(\omega)\, \dfrac{1 - \cos(\omega t)}{\omega}\, d\omega$
$C(t) = \dfrac{1}{E} + \dfrac{2}{\pi} \displaystyle\int_0^\infty J_I(\omega)\, \dfrac{1 - \cos(\omega t)}{\omega}\, d\omega \quad ; \quad \left[J_I = \dfrac{E_I}{\mid E_C \mid^2} \right]$
OR ANALOGY YOUNG'S MODULUS $\Rightarrow$ RELAXATION AND CREEP
$C(t) = \mathscr{L}^{-1}\left[\dfrac{1}{sE^A} \right] \quad ; \quad R(t) = \mathscr{L}^{-1}\left[\dfrac{E^A}{s} \right]$

Table 14.1. Complex Young's modulus, creep, and relaxation of composite material determined from Young's modulus of such material. Examples are composites made of components exhibiting Power law viscoelasticity. []$_P$ and []$_s$ mean that E, b, and τ in [] are subscripted as indicated.

Remarks: The procedure presented in Table 14.1 of determining the creep and relaxation functions for a composite material from the complex stiffness is very efficient using computers with the capability of handling complex numbers. It is

obvious how the experimental vibration analysis explained in Section 13.1.2 can be used also in the research on composite geometry versus viscoelasticity of composite materials.

With respect to the determination of creep- and relaxation functions we re-call that only one of these functions are needed to predict the other one by the basic Equation 13.2.

In general the determination of internal stress and eigenstrain-stress as expressed in Table 14.2 calls for numerical laplace-inversions. Alternatively, approximate solutions can be found as explained in the following section.

INTERNAL STRESS FROM EXT-LOAD $(e^A = E^A/E_s{}^A;\ n^A = E_p{}^A/E_s{}^A)$	
$\sigma_p(t) = \dfrac{1}{c}\ \mathscr{L}^{-1}\left[\bar{\sigma}\ \dfrac{1/e^A - 1}{1/n^A - 1}\right]$	$\sigma_s(t) = \dfrac{\sigma(t) - c\sigma_p(t)}{1 - c}$
EIGENSTRAIN/STRESS $(K_s{}^A \approx E_s{}^A/1.8)$	
$\lambda(t) = \mathscr{L}^{-1}\left[\bar{\lambda}_s + \overline{\Delta\lambda}\dfrac{1/e^A - 1}{1/n^A - 1}\right]$ *with* $\overline{\Delta\lambda} = \bar{\lambda}_p - \bar{\lambda}_s$	
$\sigma_p(t) = -\mathscr{L}^{-1}\left[\overline{\Delta\lambda}K_s{}^A\dfrac{c(1/n^A - 1) - (1/e^A - 1)}{c(1/n^A - 1)^2}\right]$	$\sigma_s(t) = -\dfrac{c}{1 - c}\sigma_p(t)$

Table 14.2. Internal stress from external load and eigenstrain/stress in composite material determined from analogy Young's modulus of such material.

14.1.2 Approximate analysis

A very simple approximate quasi-static analysis of viscoelastic composites can be obtained from the elastic counterpart analysis explained in Equation 14.1,

$$F \approx F_{ELAST}(P,E_p^{EFF},E_s^{EFF}) \quad where \quad F_{ELAST} = F_{ELAST}(P,E_p,E_s) \tag{14.1}$$

where F_{ELAST} and F are the elastic and viscoelastic solutions respectively to the problem considered. E_p^{EFF} and E_s^{EFF} are the effective Young's moduli explained in Section 13.3.1. Load (stress or strain) is denoted by P. In another formulation the method was first suggested by Ross (144) as an easy way of estimating the stress distribution in a composite structure made of concrete and steel. An example of applying Equation 14.1 in a composite analysis is explained in Equation 14.2. The elastic composite stiffness, E, is converted to the creep function of the counterpart viscoelastic composite.

$$C(t) \approx \frac{1}{E^{EFF}} \quad with \quad E^{EFF} = E(E_p^{EFF},E_s^{EFF}) \quad where \quad E = E(E_p,E_s) \tag{14.2}$$

Remark: The quality of composite solutions obtained by the 'composite E^{EFF}-method' depends on the quality of E_P^{EFF} and E_S^{EFF} considered in Section 13.3.1. The load restrictions explained in this section must hold for each phase also on a 'composite level'. The author's (tentative) experience with respect to the quality of E^{EFF}-estimates is the following after having tested the composite E^{EFF}-method on isotropic composites made of Maxwell materials mixed with elastic spheres, isotropic composites made of two materials exhibiting Power Law creep, and layered composites made of two Maxwell materials:

> Estimates of 'reasonable accuracy' can be obtained for the material properties, creep functions, creep stresses, eigenstress/strain properties. To get a similar level of accuracy for 'estimated' relaxation functions, it might be necessary to determine this function numerically from the creep function using the basic Equation 13.2.

> In general, estimates of reasonable accuracy can be expected in any analysis when composites are considered where both components have Power Law viscoelasticity with b < 1/3.

Approximate inversion method

It is tempting (see Section 13.3.1) to use this method when problem solutions are formulated by their Laplace transformed as they are in Table 14.2: Multiply the Laplace transformed solution with s and then replace s with γ/t. The inversion parameter γ, however, has to be estimated as some composite average of inversion parameters applying to phases P and S. In the author's opinion this feature disqualifies, in practice, the approximate inversion method to be better than the plain E^{EFF}-method. In any case, more research has to be made on this matter.

14.2 Applications

Some examples are presented in this section which illustrate how the analysis of viscoelastic composites just explained in Section 14.1 works on various composites. We emphasize that the accurate method of analysis is always used - unless otherwise indicated.

14.2.1 Porous materials and stiff pore systems

It is of some interest to know how does a very soft phase P (n = 0) and a very stiff phase P (n = ∞) modify the rheology of a composite. The question is immediately answered as presented in Equation 14.3 developed from Equations 10.9, 10.14, and 13.4.

This expression tells that composite creep- and relaxation functions are proportional with the corresponding function of the matrix material (phase S). Examples: Viscosity of a fresh concrete is proportional with the viscosity of fresh cement paste, such that Figure 10.30 can be read with η_∞/η_s as second axis. In a similar way the creep function of asphalt concrete is proportional with the creep function of asphalt (considered as Newton material).

$$\frac{R_o(t)}{R_s(t)} = \frac{C_s(t)}{C_o(t)} = \frac{1 - c}{1 + c/\theta_o} \quad ; \quad \theta_o = \begin{cases} \mu_P & c \le c_P \\ 0 & c > c_P \end{cases}$$

$$\frac{R_\infty(t)}{R_s(t)} = \frac{C_s(t)}{C_\infty(t)} = \frac{1 + \theta_\infty c}{1 - c} \quad ; \quad \theta_\infty = \begin{cases} \dfrac{\mu_P + \mu_s - 1}{\mu_s} & c < c_s \\ \infty & c > c_s \end{cases} \tag{14.3}$$

Equation 14.3 has been used by the author in (78) to predict the rheological behavior of fluids mixed with voids or with very stiff particles. The latter application is of special interest when modern self compacting concretes (SCC) are considered (79).

14.2.2 Particulate composite

A CSA_P composite is considered with viscoelastic components. The questions are, how does this composite creep, relax, and how do stresses develops internally when the composite is loaded externally or by eigenstrains.

The questions asked are solved as explained in Section 14.1: The elastic solutions are presented in Chapter 10, Tables 10.3 and 10.4. The laplace transformed "viscoelastic" answers to the problems formulated are determined from these solutions

replacing the stiffness moduli (E, n) with their viscoelastic counterparts (E^A, n^A) and load with the laplace transformed load. The final solutions are determined by laplace inversion. The analysis is exemplified in Equation 14.4 looking at the phase P stress in a CSA_P composite subjected to an external load.

$$
\begin{aligned}
\sigma_P &= \sigma\frac{(1 + A)n}{A + n} \quad \text{(elastic particle stress)} \quad \Rightarrow \\
\overline{\sigma}_P &= \overline{\sigma}\frac{(1 + A)n^A}{A + n^A} \quad \Rightarrow \quad \sigma_P(t) = \mathcal{L}^{-1}\left[\overline{\sigma}\frac{(1 + A)n^A}{A + n^A}\right]
\end{aligned}
\tag{14.4}
$$

The abbreviations used (and others for further viscoelastic analysis of CSA composites) are explained in Equation 14.5.

$$
\left.
\begin{aligned}
e &= \frac{A + n}{1 + An} \quad ; \quad E = E_s\frac{A + n}{1 + An} \quad \text{with} \quad n = \frac{E_P}{E_s} \\
e^A &= \frac{A + n^A}{1 + An^A} \quad ; \quad E^A = E_s^A\frac{A + n^A}{1 + An^A} \quad \text{with} \quad n^A = \frac{E_P^A}{E_s^A}
\end{aligned}
\right\}
\begin{aligned}
&CSA_P \text{ with} \\
&A = \frac{1 - c}{1 + c}
\end{aligned}
\tag{14.5}
$$

Maxwell-Hooke CSA_P-composite

It is now assumed that the particle phase (P) is elastic and the matrix phase (S) is viscoelastic like a Maxwell material. The analysis proceeds as just explained with material specific analogy stiffness properties and appropriate abbreviations presented in Table 14.3, and with laplace transformation/inversion used as described in Table 13.1. The final set of answers to the questions asked are summarized in Table 14.4.

Maxwell-Hooke CSA_P-material	
Phase properties	$\left.\begin{aligned} E_s^A &= E_s\frac{s}{s + 1/\tau} \quad Maxwell \\ E_P^A &= E_P \quad\quad\quad Hooke \end{aligned}\right\} \quad ; \quad n^A = n\frac{s + 1/\tau}{s}$
Abbreviations appropriate in viscoelastic analysis	$Q_1 = \frac{n}{A + n} \quad ; \quad Q_2 = \frac{An}{1 + An}$
Analogy Young's modulus	$e^A = e\frac{s + Q_1/\tau}{s + Q_2/\tau} \quad ; \quad E^A = E\frac{s}{s + 1/\tau}\frac{s + Q_1/\tau}{s + Q_2/\tau}$

Table 14.3. Auxiliary quantities for viscoelastic analysis of CSA_P-material with Maxwell matrix (phase S) and elastic particles (phase P). The abbreviations, E (composite Young's modulus) and A are explained in Equation 14.5.

PROBLEM	VISCOELASTIC CSA$_P$-SOLUTIONS
Creep function	$C(t) = \dfrac{1}{E}\left[1 + Ae\dfrac{t}{\tau} + \dfrac{A(1-Ae)}{n}\left[1 - \exp\left[-Q_1\dfrac{t}{\tau}\right]\right]\right]$
Relaxation function	$R(t) = E\left[\dfrac{A}{e}\exp\left[-\dfrac{t}{\tau}\right] + \dfrac{n(1-A^2)}{A+n}\exp\left[-Q_2\dfrac{t}{\tau}\right]\right]$
Internal stress caused by constant external load σ	$\sigma_P = \sigma\dfrac{n(1+A)}{A+n}\left[1 + \dfrac{A}{n}\left[1 - \exp\left[-Q_1\dfrac{t}{\tau}\right]\right]\right]$ $\sigma_S = \dfrac{\sigma - c\sigma_P}{1-c}$
Eigenstrain/stress caused by matrix (linear) eigenstrain $\lambda_S = kt$ Max-matrix stress at spheres	$\lambda = kA\left[t + \dfrac{1-A}{n}\tau\left[1 - \exp\left[-Q_1\dfrac{t}{\tau}\right]\right]\right]$ $\rho_P = 3kK_SA\tau\left[1 - \exp\left[-Q_1\dfrac{t}{\tau}\right]\right] \quad ; \quad \rho_S = -\dfrac{c}{1-c}\rho_P$ $\sigma_{S,RAD} = \rho_P \quad ; \quad \sigma_{S,TAN} = -\dfrac{3-A}{4A}\rho_P$
Matrix stress at spheres from const $\Delta\lambda = \lambda_P - \lambda_S$	$\sigma_{S,RAD} = -3K_P\Delta\lambda\dfrac{A}{A+n}\exp\left[-Q_1\dfrac{t}{\tau}\right] \quad ; \quad \sigma_{S,TAN} = -\dfrac{3-A}{4A}\sigma_{S,RAD}$

Table 14.4. *Viscoelastic composite analysis of CSA_P-material. In eigenstrain/stress analysis:* λ *is composite eigenstrain (linear).* (λ_P, λ_S) *and* (ρ_P, ρ_S) *are eigenstrain (linear) and eigenstress (hydrostatic) of phase P and phase S respectively.* $\sigma_{S,RAD}$ *and* $\sigma_{S,TAN}$ *are radial and tangential phase S stress respectively at sphere. Bulk modulus* $K_{S,P} \approx E_{S,P}/1.8$. *The abbreviations, A, E (composite Young's modulus), e, Q1, and Q2, are explained in Table 14.3.*

PROBLEM	CONCRETE SOLUTIONS
Creep function	$C(t) = \dfrac{1}{E}\left[1 + Ae\phi_s + \dfrac{A(1-Ae)}{n}\left(1 - \exp(-Q_1\phi_s)\right)\right]$
Relaxation function	$R(t) = E\left[\dfrac{A}{e}\exp(-\phi_s) + \dfrac{n(1-A^2)}{A+n}\exp(-Q_2\phi_s)\right]$
Internal stress caused by constant external load σ	$\sigma_P = \sigma\dfrac{n(1+A)}{A+n}\left[1 + \dfrac{A}{n}\left(1 - \exp(-Q_1\phi_s)\right)\right]$ $\sigma_S = \dfrac{\sigma - c\sigma_P}{1-c}$
Eigenstrain/stress caused by matrix (linear) eigenstrain $\lambda_S = k\phi_s$ Max-matrix stress at spheres	$\lambda = kA\left[\phi_s + \dfrac{1-A}{n}\left(1 - \exp(-Q_1\phi_s)\right)\right]$ $\rho_P = 3kK_SA\left(1 - \exp(-Q_1\phi_s)\right) \quad ; \quad \rho_S = -\dfrac{c}{1-c}\rho_P$ $\sigma_{S,RAD} = \rho_P \quad ; \quad \sigma_{S,TAN} = -\dfrac{3-A}{4A}\rho_P$
Matrix stress at spheres from const $\Delta\lambda = \lambda_P - \lambda_S$	$\sigma_{S,RAD} = -3K_P\Delta\lambda\dfrac{A}{A+n}\exp(-Q_1\phi_s) \quad ; \quad \sigma_{S,TAN} = -\dfrac{3-A}{4A}\sigma_{S,RAD}$

Table 14.5. *Viscoelastic composite analysis of Concrete. Abbreviation are explained in Table 14.4*

14.2.3 Mature cement concrete

It has previously been discussed that concrete (and cement paste) can be considered non-aging introducing the authors concept of modified time, see Section 13.2.2. This means that the results of Table 14.4 apply for concrete when the Maxwell relaxation time $,\tau,$ is replaced with '1', and time in general $,t,$ is replaced with the modified time $,\phi$.

The results obtained are presented in Table 14.5. The expressions presented in Table 14.6 are of special interest when normal concretes and porous "concretes" are considered.

We emphasize that phase S properties in general (including E_s and ϕ) are the HCP properties presented in Table 13.6.

PROBLEM	SPECIAL CONCRETE SOLUTIONS		
Creep function	$C(t) = \dfrac{1}{E}(1 + \phi) \quad with \quad \phi =$	$\begin{cases} A\dfrac{E}{E_s}\phi_s & when \quad n > 2 \\ \phi_s & when \quad n = 0 \end{cases}$	
Eigenstrain caused by matrix eigenstrain λ_s	$\lambda = \begin{cases} \approx A * \lambda_s & when \quad n > 2 \\ = \lambda_s & when \quad n = 0 \end{cases}$		

Table 14.6. Special solutions for concretes with hard aggregates and very soft aggregates (voids).

The normal concrete results in Table 14.6 comply well with orders of magnitudes observed in (153) that creep strain for concrete relative to creep strain of cement paste varies with $(1 - c)^B$ with B increasing from 1.7 to 2.1 with time under load, and that shrinkage of concrete relative to shrinkage of cement paste varies with $(1 - c)^B$ with B $\approx$ 1.7 observed in (154), B $\approx$ 1.4 in (155), and B $\approx$ 1.2 - 1.7 observed in (156).

Examples

Two examples are now presented on how the results in Table 14.5 can be used in practice to predict creep, relaxation, and eigenstrain/stress in concrete. The concrete considered has a water/cement ratio of W/C = 0.4 and a total aggregate/cement ratio of A/C = 4.33 from which a volume concentration of c = 0.7 is obtained from Table 2.1. The aggregate stiffness is E_P = 55000 Mpa. The rheological cement paste properties used in the analysis are predicted from Table 13.6 with an estimated creep factor of $\phi^* = 1.4$.

Example 1: The concrete is loaded at the age of t_o = 28 days. The creep function and the relaxation function predicted from Table 14.5 are illustrated in Figures 14.1 and 14.2.
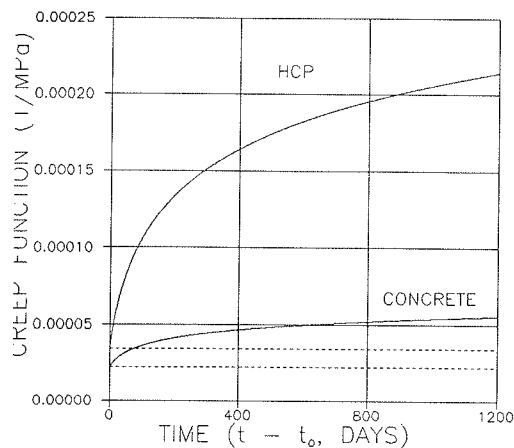
Figure 14.1. Creep function of concrete considered. t_o = 28 days.
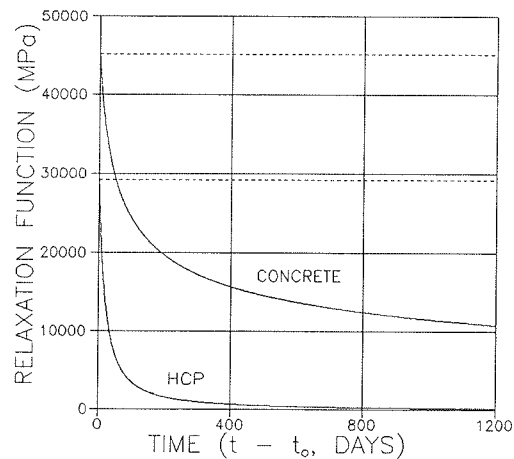
Figure 14.2. Relaxation function of concrete considered. t_o = 28 days.

Example 2: The concrete is exposed to drying from the age of t_o = 28 days. The drying is anticipated to cause a HCP shrinkage corresponding to a shrinkage factor of k = -0.0005 (see Table 13.7) which causes concrete eigenstrain and internal stresses to be predicted by Table 14.5 as shown in Figures 14.3 and 14.4. The dotted data presented in Figures 14.3 and 14.4 are from an experimental study by Nielsen (98) on the influence of shrinkage on aggregate stress in concrete. The concrete (LL3) used by Nielsen is exactly as defined above.
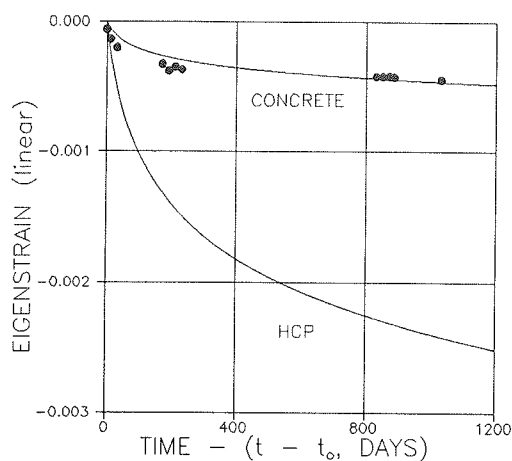
Figure 14.3. Eigenstrain of concrete considered due to drying at RH = 60% from the age of t_o = 28 days.
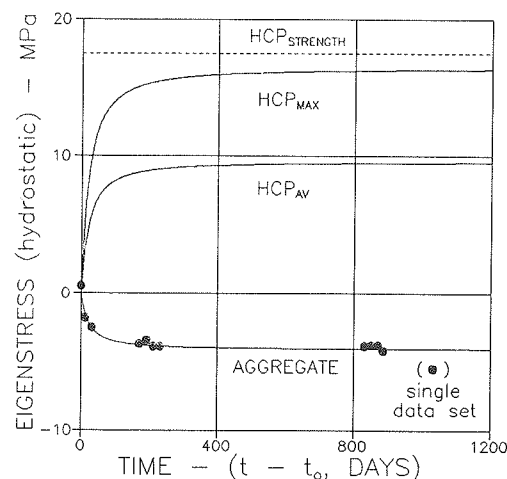
Figure 14.4. Eigenstresses in concrete considered in example 2. t_o = 28 days. Drying at RH = 60%.

152

Nielsen's study in (98): Strain gauges were attached to an artificial steel "stone" constructed to simulate very precisely the stiffness properties of the other coarse aggregates. The data shown in Figures 14.3 and 14.4 are typical discrete averages. The experiments, however, were continuously monitored in age periods 0-60, 200-260, and 860-915 days. A single set of data were monitored at the end of the experiment at 1060 days. Unfortunately no rheological information on cement paste and concrete are reported in (98). There is also no information on shrinkage of paste. The *simultaneous* agreement, however, between experimental and theoretical strain/stress data observed in Figures 14.3 and 14.4 indicates that the creep- and shrinkage factors, assumed in this analysis are probably close to simulate the real creep and shrinkage behavior of the concrete used by Nielsen.

Remark: It is noticed from Figure 14.4 the max HCP stress is threateningly close to the tensile strength of HCP estimated to be one tenth of the compressive strength predicted by Equation 11.10.

A strength mechanism for concrete. The stress solutions at a sphere (phase P) in an infinite continuum (phase S) can be developed from Goodier (50) as presented by the former expression in Equation 14.6. Load at infinity (S) and stresses of interest at the sphere are defined in Figure 14.5 together with coordinates. The corresponding stresses in a CSA$_P$-composite with many spheres are predicted by the SCS method previously introduced (E_s is replaced with E and n with $E_P/E = n/e$). The results are presented in the second expression in Equation 14.6.

$$\sigma_R = S\left(1 + \cos(2\theta)\right)\frac{n}{1 + n} \quad ; \quad \tau = S\sin(2\theta)\frac{n}{1 + n} \quad (single\ sphere)$$

$$\sigma_R = S\left(1 + \cos(2\theta)\right)\frac{n}{e + n} \quad ; \quad \tau = S\sin(2\theta)\frac{n}{e + n} \quad (SCS\ solution) \qquad (14.6)$$

$$e = e(c,n) = \frac{A + n}{1 + An} \quad with \quad A = \frac{1 - c}{1 + c} \quad and \quad n = \frac{E_P}{E_s} \quad (Stiffness)$$

The elastic composite strength expression presented in Equation 14.8 can be predicted from the composite stresses if we assume that the so-called Coulomb's failure condition expressed in Equation 14.7 applies in bond areas between phases.

$$\tau = C + \sigma_R tg(\lambda) \quad ; \quad \begin{cases} C\ is\ cohesion\ in\ bond\ area \\ \lambda\ is\ friction\ angle\ in\ bond\ area \end{cases} \qquad (14.7)$$

$$S_{CR} = \frac{C\cos(\lambda)}{1 - \sin(\lambda)}\frac{n + e}{n} \quad at \quad \theta = \frac{1}{2}\arctan\left[-\frac{1}{\tan(\lambda)}\right] + \frac{\pi}{2} \qquad (14.8)$$

The strength of concrete can be found approximately as follows using the simple E^{EFF}-method with $n = E_P/E_{HCP}$.

$$S_{CR} = \frac{C\cos(\lambda)}{1 - \sin(\lambda)} \frac{n_{EFF} + e_{EFF}}{n_{EFF}} \quad with \quad \begin{bmatrix} n_{EFF} = n(1 + \phi_{HCP}) \\ e_{EFF} = e(c, n_{EFF}) \end{bmatrix} \tag{14.9}$$

Some results of strength prediction by Equation 14.9 are presented in Figure 14.6. A concrete is considered made with $W/C = 0.4$ and a total aggregate concentration ($E_p = 70000$ MPa) of $c = 0.7$. Age at loading is $t_o = 28$ days. A creep factor of $\phi^* = 1.4$ is assumed (Table 13.6). Bond failure is controlled by Coulomb parameters $C = 30$ MPa and $\lambda = 30°$ (producing $\theta = 60°$).
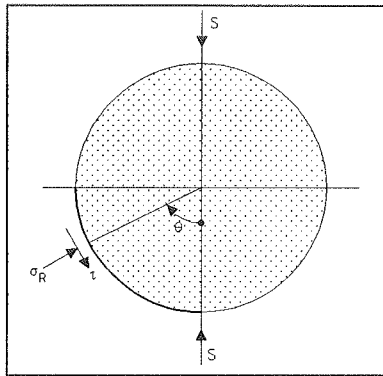
Figure 14.5. The sphere of Goodier's.
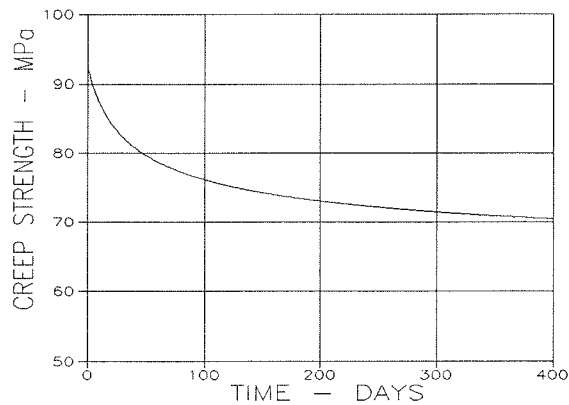
Figure 14.6. Creep strength of concrete. Bond shear failure between coarse aggregate and mortar.

It i noticed that the concrete considered has a threshold strength of approximately 70%. Sustained loads lower than this threshold strength will never cause failure. A similar conclusion was made by Rüsch in his classical experimental work on creep-rupture in concrete (157,158).

14.2.4 Young concrete

It is recalled that the creep parameter presented in Table 13.6 for cement pastes applies for ages $> \approx 3$ weeks. This time limit of validity applies of course also for the concrete results presented in Section 14.2.3.

When Young's modulus of the material considered changes significantly with time the method of introducing modified time cannot be used. More refined models have to be used which reflect the general effect of aging on all sub-elements in the materials stress-strain relation, for example on any p and q appearing in Equation 13.1. A general constitutive model of this kind has recently been developed by the author in (113) which applies for concretes (including HCP) of any composition (water/cement and aggregate/cement ratios), any curing conditions, and for any age of loading greater than about half a day.

The results of a general composite analysis of concrete (creep, relaxation, and eigenstrain/eigenstress/prestress phenomenons) are not presented in this monograph.

154

They can, however, be studied on the software "ComCon" with manuals (159, 160) which can be downloaded from *http://www.byg.dtu.dk/publicering/software_d.htm*. Quite recently (114) the general theory has been adapted for fast FEM analysis of concrete structures.

14.2.5 Influence of geometry on viscoelastic composite behavior

Particulate composite versus grid reinforced composite

Two viscoelastic composites are considered. They are identical except for geometry. One composite is a particle reinforced material like cement concrete. The other composite is a regular frame work reinforced material like the CROSS-material previously defined. The geometries are quantified as follows,

> *Composite A:* DC-DC (TROC) with $(\mu_P^\circ, \mu_S^\circ, c_P)$ = (1,-1,3.33), c = 0.5
>
> *Composite B:* CC-CC (CROSS) with $(\mu_P^\circ, \mu_S^\circ, c_P)$ = (0.75,0.15,1.25), c = 0.5

Both phases are Power Law viscoelastic with the following parameters,

> *Phase S:* E_S = 30000 MPa, τ_S = 15 days, b = 0.3
>
> *Phase P:* E_P = 70000 MPa, τ_P = 10^{10} days, b = 0.3

The complex stiffness of the composites just defined are calculated as shown in Table 14.1. The resulting absolute stiffness and loss-angle (see Equation 13.10) are shown in Figures 14.7 and 14.8. Quantities at the very high and at the very low frequencies are of rather academic interest. In the present context, however, they are needed in order to get a complete picture of the phenomena considered.

Creep and relaxation of the composite are calculated as shown in Table 14.1 from the composite complex Young's moduli just determined in Figures 14.7 and 14.8. The results are presented by solid lines in Figure 14.9. The results shown by dotted lines are calculated by the approximate E^{EFF}-method explained in Section 14.1.2 with elastic solutions from Table 10.3. As expected from Section 14.1.2 accurately determined data and approximately determined data almost coincide. Both creep powers are b < $\approx$0.3.

When the two composites considered are subjected to a constant external load, internal stresses develop as shown in Figure 14.10. The stress state has been determined using the approximate method. As both b < $\approx$0.3 we may expect stresses to be fairly well predicted in this way.

Other examples on composite viscoelastic behavior as influenced by TROC and CROSS geometries are illustrated in Figures 14.11 and 14.12. Again, the two composites considered only differ by their internal geometries.

155
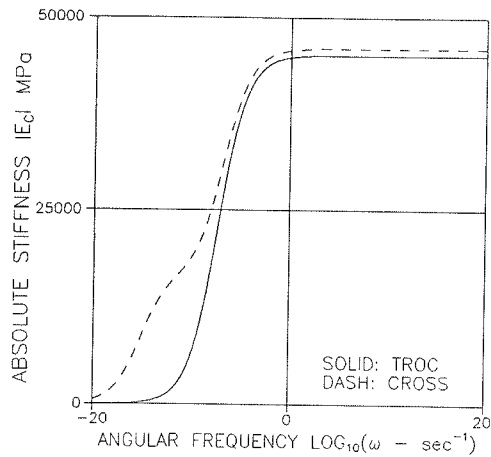
Figure 14.7. *Influence of phase geometry on absolute stiffness of composites described in text. Accurate analysis.*
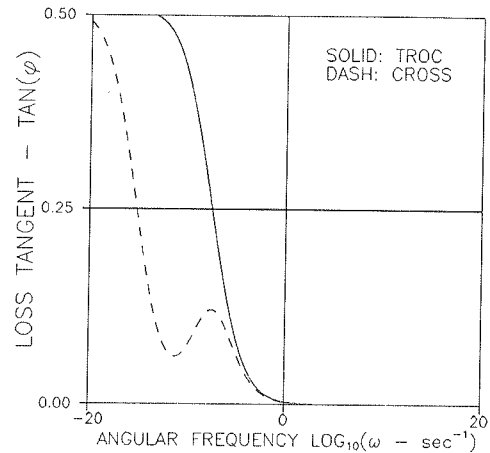
Figure 14.8. *Influence of phase geometry on loss-tangents of composites described in text. Accurate analysis.*
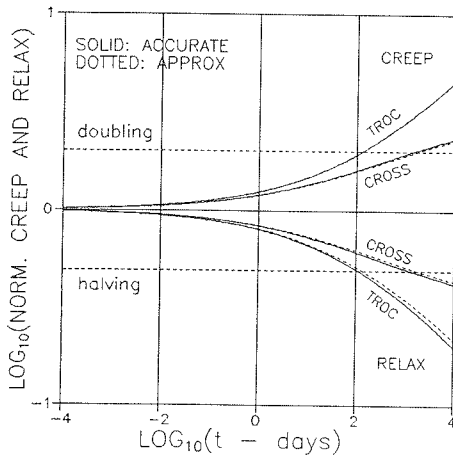
Figure 14.9. *Influence of phase geometry on creep and relaxation for composites defined in text.*
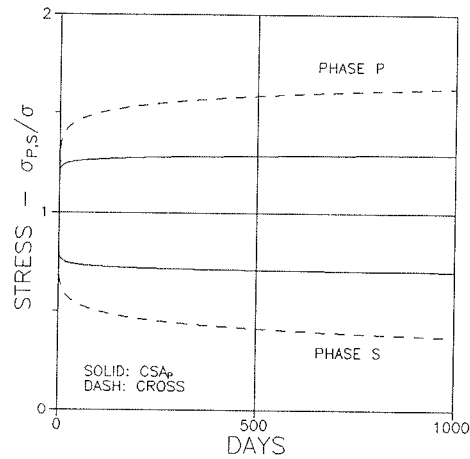
Figure 14.10. *Influence of phase geometry on internal creep stresses in composites described in text.*
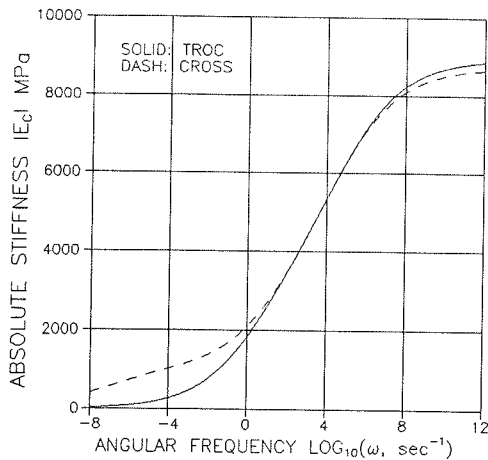
Figure 14.11. $(E_P, E_S) = (5000, 15000)$ *MPa.* $(\tau_P, \tau_S) = (100, 10^{10})$ *days.* $b_P = b_S = 1/4.$ $c = 0.5$
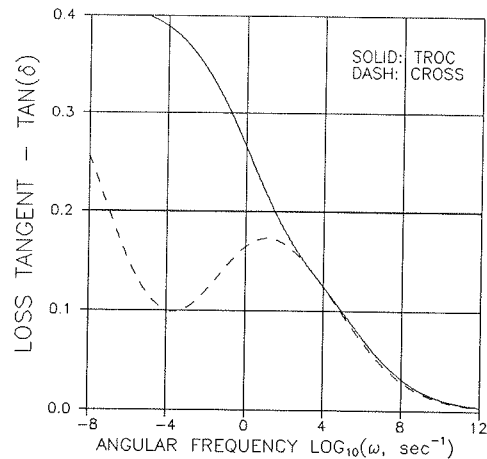
Figure 14.12. $(E_P, E_S) = (5000, 15000)$ *MPa.* $(\tau_P, \tau_S) = (100, 10^{10})$ *days.* $b_P = b_S = 1/4.$ $c = 0.5$

156

Two particulate composites with different particle shapes

Two particulate composites like asphaltic concretes are considered with the following geometrical properties and Power Law viscoelastic phase properties.

Composite A: DC-DC (spheres) with $(\mu_P^\circ, \mu_S^\circ, c_P) = (1, -1, \infty)$, c = 0.7
Composite B: DC-DC (discs, A = 0.0035) with $(\mu_P^\circ, \mu_S^\circ, c_P) = (0.01, -0.01, \infty)$, c = 0.7
Phase S: $E_S = 1000$ MPa, $\tau_S = 100$ days, b = 0.8
Phase P: $E_P = 70000$ MPa, $\tau_P = 10^4$ days, b = 0.25

The complex stiffness of the composites just defined are calculated as shown in Table 14.1. The resulting real stiffness and imaginary stiffness are shown in Figures 14.13 and 14.14.
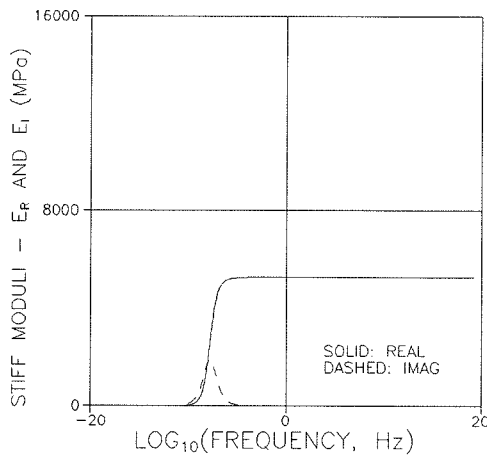
Figure 14.13. Complex Young's modulus of asphaltic concrete with spherical aggregates.
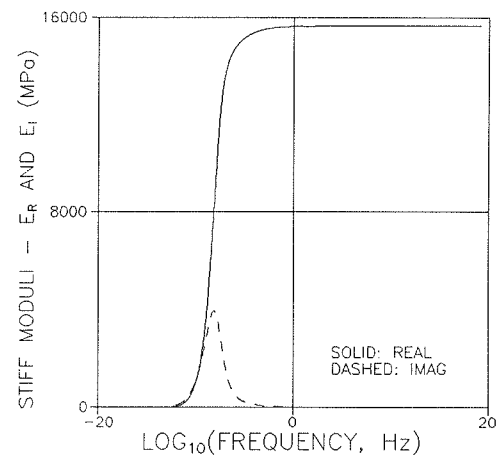
Figure 14.14. Complex Young's modulus of asphaltic concrete with very thin disc shaped aggregates.
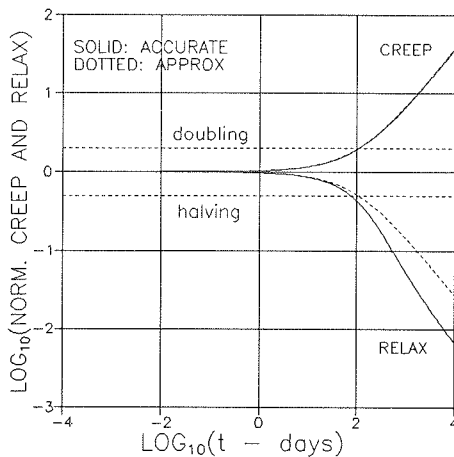
Figure 14.15. Asphaltic concrete with spherical aggregates.
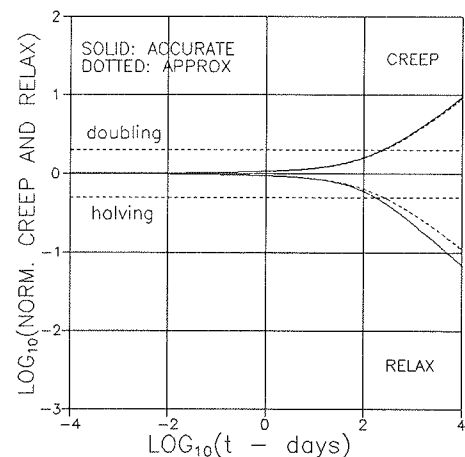
Figure 14.16. Asphaltic concrete with very thin disc shaped aggregates.

157

Subsequently the creep and relaxation functions of the composite are calculated. Table 14.1 is used again, now with the composite complex Young's moduli just determined as in-put data. The results are presented with solid lines in Figures 14.15 and 14.16. The results shown by dotted lines are calculated by the approximate E^{EFF}-method explained in Section 14.1.2 with elastic solutions presented in Table 10.3. As expected, these results cannot in general be considered very reliable as both creep powers b are not $< \approx 0.33$.

14.2.6 Monomer impregnated HCP and porous glass

Experiments on HCP and porous glass being impregnated with a monomer are made by Hastrup in (161). Specific properties considered are composite viscoelasticity versus degree of impregnation (β = volume of impregnant/accessible pore volume). The results of Hastrup's are shown in Figures 14.17 - 14.20.

A more detailed description of the materials used is the following: The impregnant is in situ polymerized methylmethacrylate monomer. The porous glass considered is porous fused silica glass[6] (porosity 33%, accessible for both water and impregnant). The HCP considered is made with W/C = 0.4 (degree of hydration $\approx$ 0.75, porosity 36% and 30%, accessible for water and impregnant respectively).

Detailed materials description

The material properties presented below are from (161) except the HCP data with respect to porosity and the Young's modulus E_s of the solid phase. These data are reproduced from a composite analysis made in (150) of the original HCP data respecting that porosity must relate to voids accessible for the impregnant.

> *Glass:* $E_s = 64300 \; MPa$, *loss* $\tan(\delta_s) = 0.06\%$
> *HCP (solid):* $E_s = 57000 \; MPa$, *loss* $\tan(\delta_s) = 0.27\%$
> *Monomer:* $E_P = 4700 \; MPa$, *loss* $\tan(\delta_P) = 6.16\%$

The geo-parameters ($\mu_P{}^\circ, c_P$) presented are determined from the 'porous data' using the regression method explained in Section 10.3.4. Open (impregnable) pore systems are assumed with $\mu_s{}^\circ = 0$.

> *Porous glass:* CC-CC *with* $(\mu_P{}^\circ, \mu_s{}^\circ, c_P) = (0.35, 0, 1), \; c = 0.33$
> *HCP:*   CC-CC *with* $(\mu_P{}^\circ, \mu_s{}^\circ, c_P) = (0.50, 0, 1), \; c = 0.30$

---

6)   Vycor, Corning Glass Works, Corning, NY

Composite analysis

It is now demonstrated that the results of Hastrup's can be explained by the theories developed in this monograph - more specifically by the 'Complex Young's modulus' expression in Table 14.1.

First, however, we have to re-organize Hastrup's stiffness and loss data for phases P and S in a way he does not present them, namely by their complex stiffness moduli, E_{PC} and E_{SC}. We do that by suggesting that both phases are Power law viscoelastic [7] - and then re-writing Equation 13.13 to obtain Equation 14.10 with Power law creep powers (b) to be determined by calibration with experimental data (it is worthwhile noticing that relaxation times (τ) do not appear in Equation 14.10). The degree of impregnation, ß, is considered in Equation 14.10 by the efficiency factor ß/(2-ß) defined in Section 11.1.2.

$$
\begin{aligned}
E_{PC} &= E_P \frac{1 + Y_P\cos(b_P\pi/2) + iY_P\sin(b_P\pi/2)}{1 + Y_P^2 + 2Y_P\cos(b_P\pi/2)} \frac{\beta}{2 - \beta} \\
E_{SC} &= E_S \frac{1 + Y_S\cos(b_S\pi/2) + iY_S\sin(b_S\pi/2)}{1 + Y_S^2 + 2Y_S\cos(b_S\pi/2)} \qquad \text{with} \\
Y_P &= \frac{\tan\delta_P}{\sin(b_P\pi/2)-\cos(b_P\pi/2)\tan\delta_P} \quad ; \quad Y_S = \frac{\tan\delta_S}{\sin(b_S\pi/2)-\cos(b_S\pi/2)\tan\delta_S}
\end{aligned}
\qquad (14.10)
$$
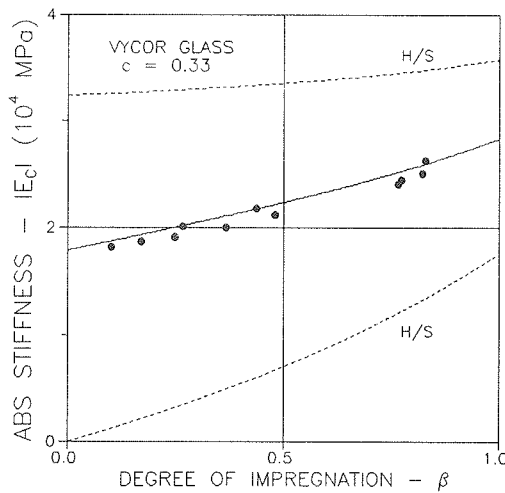
Figure 14.17. Absolute Young's modulus of impregnated porous glass.
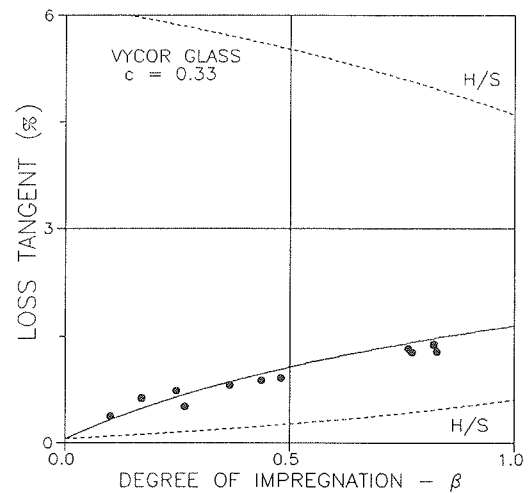
Figure 14.18. Loss tangent of impregnated porous glass.

---

7) At this stage of the analysis this suggestion is a qualified estimate for any of the constituent components. The relevance of the estimates can be justified when looking at the final, overall results of the analysis.

Results and discussion

The solid lines shown in Figures 14.17-14.20 are data predicted by $E_c = E(E_{PC}, E_{SC})$ as explained in Table 14.1. A very satisfactory agreement is demonstrated between experiments and the theory developed in this monograph. This means that the suggestion of phase P and phase S behaving as Power Law viscoelastic materials is justified. For both matrix phases (S) the calibrated creep power is $b_S = 0.25$. The calibrated creep power, $b_P = 1$, indicates that the impregnant behaves like a Maxwell material.
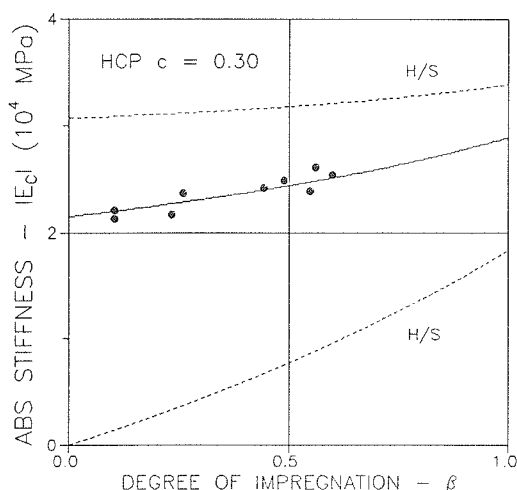
Figure 14.19. Absolute Young's modulus of impregnated Hardened cement paste.
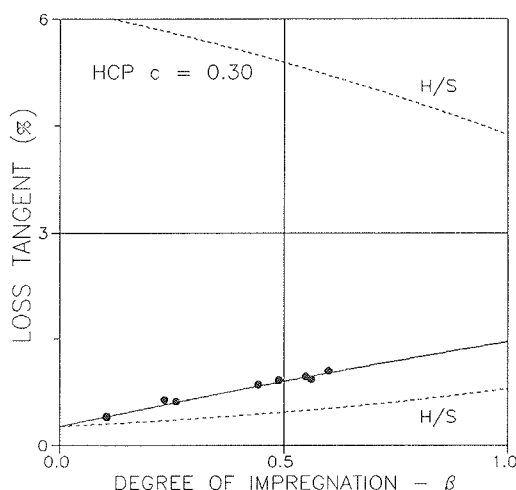
Figure 14.20. Loss tangent of impregnated Hardened Portland cement paste.

14.2.7 Damping of wood

A study on the damping properties of wood has been reported by the author in (162). One purpose of the study was to explain the 'curious' damping results from bending vibration experiments on Hoop Pine, reported by Pentoney (163).

Pentoney's data, shown in Figure 14.21 by dashed lines [8], cannot at all be explained by the Power law creep model normally assumed for wood (see Figure 14.22 from (129)). They can, however (162), if wood is considered as a composite made of very long parallel fibres (P) in an isotropic matrix (S, Lignin mainly) with both phases exhibiting simple Power-law viscoelastic behavior.

The theoretical results shown in Figure 14.21 (solid line) are obtained by the theory presented in this monograph with c = 0.9, (E_P, E_S) = (16000,16000) MPa, $(b_P,$

8) Right graph: Average of 6 domestic woods. Left upper graph: Compression wood. Left lower graph: Normal wood.

b_S) = (0.25, 0.2), and (τ_P, τ_S) = $(10^4, 10^{-10})$ days - and a geo-function of θ ≡ ∞ as suggested in Section 5.3.3 for equal-strain analysis of anisotropic composites.
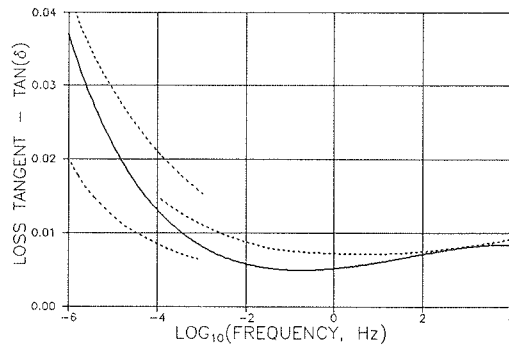
Figure 14.21. Damping of Hoop Pine wood in bending parallel to grain.
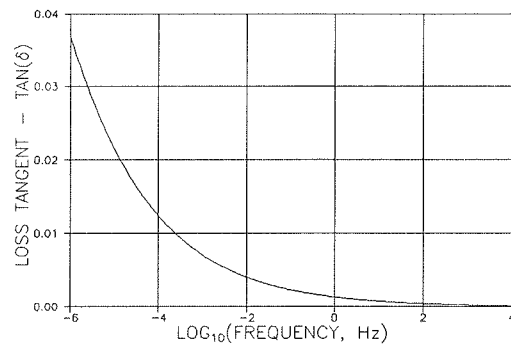
Figure 14.22. Damping of 'normal' wood in bending parallel to grain. (E, τ, b) = (16000 MPa, 10^4 days, 0.25)

Remarks: The damping of 'normal' wood is calculated from assuming that this material is homogeneous with a Power Law creep function as it is measured in static tests (f < approx 0.005 Hz). The main conclusion which can be drawn from the analysis made in (162) is that the rheological behavior of materials at high frequency loading can only be detected by vibration analysis.

A full understanding of the mechanical behavior of a material requires the most complete rheological knowledge one can get on this material. The example considered in this section has shown how vibration experiments may change the traditional modelling of a material from being a homogeneous material to being a micro-composite. In this context we re-call from Sections 13.1.2 and 14.1.1 the great potentials offered by modern experimental vibration analysis.

14.3 Discussion

It has been demonstrated in this chapter how the influence of geometry on the behavior of viscoelastic composites can be determined by relatively simple mathematical means. The power of Table 14.1 to predict composite creep and relaxation from known elastic composite behavior should be emphasized.

The significance of knowing the complex stiffness of the composite is of special interest in this context. This property can be determined theoretically by knowing the geometry (as described in this monograph) of the composite considered - or it can be determined experimentally (without knowing the geometry, as shown by the author in (130)). This means that further research on geometry versus composite behavior can benefit very much from refining the experimental and mathematical techniques used in modern experimental vibration analysis (132).

15. Other physical properties (Conductivity)

Many physical properties are proportionality constants between fluxes and potential gradients (just as Young's modulus is proportionality constant between stress and strain), e.g. thermal and electrical conductivities, and diffusion coefficients. Other physical properties are proportionality constants between inductions and force field strengths, e.g. dielectric constants and magnetic permeabilities. A composite materials analysis with respect to any of these properties will, by analogy, follow the same pattern and produce similar solutions. For example, expressions developed to predict the bulk stiffness of composites can also be used to predict thermal conductivity of composites. Of course appropriate substitutions of notations have to be introduced (including proper transformation of vector field phenomenons (stiffness) to scalar field phenomenons (like thermal conductivity). The existence of an analogy is clearly observed comparing the works on dielectric properties by Hashin (164) and Hashin and Shtrikman (165) on CSA materials with the same authors analysis (3,4) previously referred to on stiffness of such materials.

The bulk stiffness expressions presented in this monograph for composites of arbitrary geometry are generalized by the author (24) to include other physical properties only by introducing $\nu_S = \nu_P = 0$ into the geometry function θ_k, which means $\kappa_S = \kappa_P = 2$ and bulk shape factors determined for $\nu_S = \nu_P = 0$.

Note: The term conductivity is subsequently used as a synonym for any of the scalar field properties previously considered. This means, for example, that the solutions subsequently presented apply to both thermal conductivity and electrical conductivity as well as to dielectricity and magnetic permeability.

15.1 Theory

The results of the analogy presented above are summarized in Equations 15.1 - 15.3. The bounds presented in the latter expression are the exact conductivities for CSA$_P$ and CSA$_S$ composites respectively. They correspond to $\theta = 2$ and $\theta = 2n$ respectively, see Figure 15.1.

$$q = \frac{Q}{Q_S} = \frac{n + \theta[1 + c\,(n - 1)]}{n + \theta - c(n - 1)} \quad ; \quad \left[n = \frac{Q_P}{Q_S} \right] \tag{15.1}$$

$$\theta = \mu_P + n\mu_S + \sqrt{(\mu_P + n\mu_S)^2 + 4n(1 - \mu_P - \mu_S)} \tag{15.2}$$

$$\frac{n + 2[1 + c\ (n - 1)]}{n + 2 - c(n - 1)} \leq q \leq n\frac{3 + 2c\ (n - 1)}{3n - c(n - 1)} \qquad (15.3)$$

valid for $n \geq 1$; reverse signs when $n < 1$

We notice that the left side expression in Equation 15.3 equals the well-known Maxwell relation for electrical and magnetic permeability (108) of particulate composites with spherical particles.
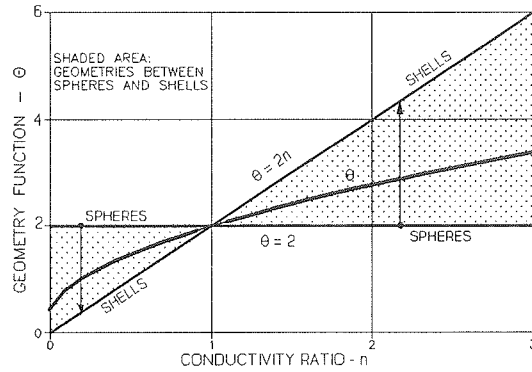
Figure 15.1. Influence of phase P geometry on geometry function.

It is emphasized that composite geometry is considered in conductivity analysis just as in stiffness analysis, meaning that shape functions to introduce into Equation 15.2 are the bulk shape functions determined from Section 7.1 (with $\nu_P = \nu_S = 0$).

15.1.1 Shape functions

The description of these shape functions require that at least 6 geo-parameters are known: Shape factors $(\mu_{Pk}^{\circ}, \mu_{Sk}^{\circ}, \mu_{Pk}^{1}, \mu_{Sk}^{1})$ for $\nu_S = \nu_P = 0$ and critical concentrations (c_P, c_S). For demonstrative purposes it is assumed in the former of the subsequent examples that such geometrical knowledge is actually available.

In general, however, such 'accurate' determination of shape functions cannot be justified in practice. We therefore simplify the conductivity analysis as we have simplified the elastic analysis introducing the 3-parameter descriptions of shape functions developed in Chapter 10. We summarize: The geo-function expressed by Equation 15.2 is kept. The shape functions (μ_P, μ_S), including shape factors $(\mu_P^{\circ}, \mu_S^{\circ})$, however, are determined as explained in Chapter 10.

It is recognized that some accuracy is lost in a conductivity analysis using the simple shape descriptions. However, subsequent examples and previous examples re-considered show that the loss of accuracy is not very significant. In the author's opinion the level of analytical accuracy corresponds rather well to the level of accuracy characterizing the determination of geometrical in-put data.

Remark: In the subsequent text we keep the general way of shape function description - unless otherwise indicated.

163

15.2 Illustrative examples

Results from a conductivity analysis of the DC-CD composite defined in Figure 15.2 are presented in Figure 15.3. The composite considered has previously been subjected to a stiffness analysis in this monograph, see Section 7.2.4, Figure 7.20, and Section 8.1.1, Figure 8.1.
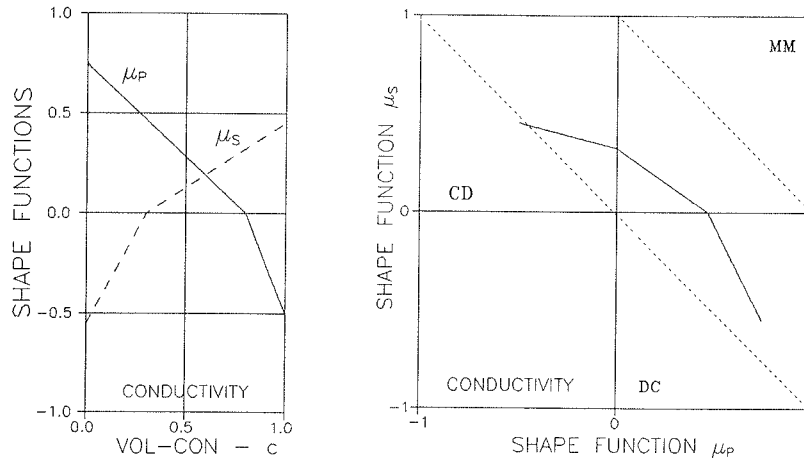
Figure 15.2. Geo-path and shape functions for a DC-CD composite with $(c_P, c_S) = (0.8, 0.3)$. At $c = 0$: P-particles: 80% A = 3 + 20% A = 0.3. At $c = 1$: S-particles 50% A = 5 + 50% A = 0.2.
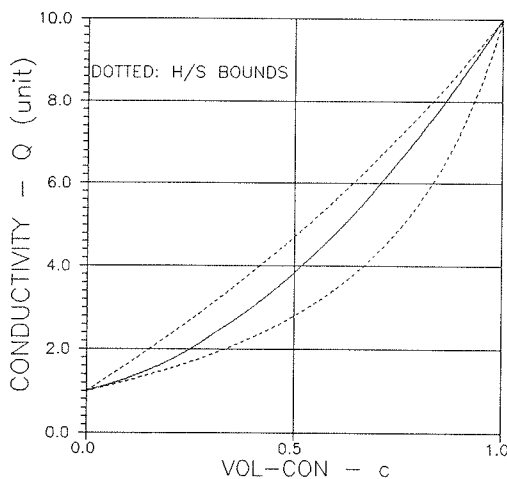
Figure 15.3. Conductivity of composite as defined in Figure 15.3. $(Q_P, Q_S) = (10,1)$, same units.

15.2.1 Porous materials and stiff pore systems

It comes immediately from Equation 15.2 and the analogy previously explained ($\kappa = 2$) that the conductivity of particulate composites with very "soft" (n = 0) particles and very "stiff" particles (n = ∞) can be written as presented in Equation 15.4.

164

$$q_o = \frac{Q_o}{Q_s} = \frac{1 - c}{1 + c/\theta_o} \quad with \quad \theta_o = \begin{cases} 2\mu_P & when \ c < c_P \\ 0 & when \ c > c_P \end{cases}$$

$$q_\infty = \frac{Q_\infty}{Q_s} = \frac{1 + \theta_\infty c}{1 - c} \quad with \quad \theta_\infty = \begin{cases} 2\dfrac{\mu_P + \mu_S - 1}{\mu_S} & when \ c < c_S \\ \infty & when \ c > c_S \end{cases} \quad (15.4)$$

15.2.2 Dilute porous materials and stiff pore systems

The conductivities of dilute systems are obtained introducing $c \rightarrow 0$ into Equation 15.4. The results are presented in Equation 15.5.

$$q_o = 1 - \left[1 + \frac{1}{2\mu_P^o}\right] c \quad ; \quad q_\infty = 1 + \left[1 + 2\frac{\mu_P^o + \mu_S^o - 1}{\mu_S^o}\right] c \quad (15.5)$$

Notes: Special solutions obtained by Equation 15.5 are presented in Equation 15.6. They agree with results obtained in (53,52) for spheres and in (55) for fibres. The disc (crack) result is presented only for the sake of completeness. Cracks have no volume.

Spheres $(A = 1)$:	$q_o = 1 - 1.5c$	; $q_\infty = 1 + 3c$
Fibres $(A = \infty)$:	$q_o = 1 - \dfrac{5}{3}c$	; $q_\infty = 1 + \infty c$ (15.6)
Discs (*crackc*) $(A = 0)$:	$q_o = 1 - \infty c$	; $q_\infty = 1 + \infty c$

15.2.3 Cracked materials (soft and stiff cracks)

The conductivity of materials with cracks (soft cracks, $n = 0$) or stiff "cracks" ($n = \infty$) can be considered by Equation 15.5. We introduce $c = (\pi/6)pAd^3$ where p is crack density (number of cracks per vol-unit), A is aspect ratio of (ellipsoidal) fibre considered (with $A \rightarrow 0$), and d is crack (fiber) diameter. We get

$$q = 1 - h_q pd^3 \quad with \quad h_q = \frac{\pi A}{6}\left[1 + \frac{1}{2\mu_P^o}\right] \quad cracks \ (soft)$$

$$\frac{1}{q} = 1 - h_q pd^3 \quad with \quad h_q = \frac{\pi A}{6}\left[1 + 2\frac{\mu_P^o + \mu_S^o - 1}{\mu_S^o}\right] \quad stiff \ cracks \quad (15.7)$$

The h_q-factors are shown in Figure 15.4 with shape factors determined numerically as explained in Chapter 7. It is noticed that discs practically can be considered to

be cracks for any $A < 0.01$. This means that the influence of discs with $A <$ 0.01 on composite conductivity can be considered as if the discs were real cracks $(A = 0)$.
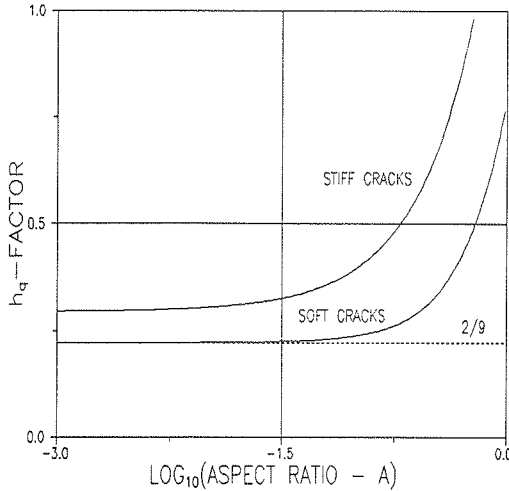
Figure 15.4. h_q factor for conductivity of "cracked" composite.
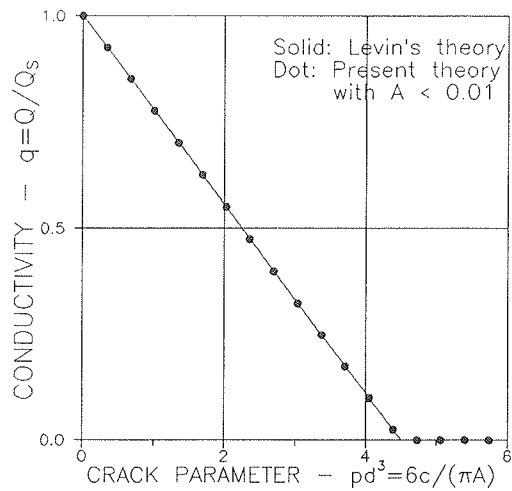
Figure 15.5. Present crack theory versus accurate crack theory (Levin).

The crack results predicted by the present theory are successfully compared in Figure 15.5 with exact results, $q = 1 - (2/9)pd^3$, as they can be obtained from the Levin's bulk modulus analysis (7) considered in Section 9.2 with $\nu_s = 0$.

In a similar way the conductivity of a material with stiff cracks is developed numerically from the latter expression in Equation 15.7. The result is very close to $q = 1 + 0.3pd^3$.

Remark: It has been checked that the results in Figure 15.5 can be predicted accurately also by the SCS-method presented in Appendix C with $(Q_P,Q_s) = (0^+,1)$ and $A < 0.01$. The statement previously made that SCS-solutions can be considered accurate when composites considered are dilute is clearly supported by this observation where very little crack "volume" is involved.

15.2.4 Crumbled foils composite

In a crumbled foils composite, see Section 4.1.4, both phases have continuous flat geometries, meaning that both shape functions $(\mu_P,\mu_s) \equiv 0$. The conductivity of such composites is easily derived from Equation 15.1 with a geo function $\theta = 2\sqrt{n}$ introduced from Equation 15.2.

$$q = \frac{Q}{Q_s} = \frac{n + 2\sqrt{n}\,[1 + c(n - 1)]}{n + 2\sqrt{n} - c(n - 1)} \qquad (15.8)$$

166

15.3 Theory versus experiments

15.3.1 Chloride diffusion in HCP and HCP with Silica fume

The data shown in Figures 15.6 and 15.7 are from a study reported in Bentz et al. (166) on the influence of silica fume on the chloride diffusion in cement based materials. The materials considered were computer-simulated applying a cement paste model which has previously been developed by Bentz in (167). Bentz et al. (166) verify their (model)results comparing them with experimental data reported in (168) and re-evaluated experimental data (W/C = 0.3, c ≈ 0.043) reported in (169). (Leaching systems used in (169) versus un-leaching systems in (166)).

The diffusion coefficients presented in Figures 15.6 and 15.7 are normalized with respect to the chloride diffusion coefficient of free water, $Q_P ≈ 2*10^{-9}$ m²/sec, suggested in (170). Volume concentration of capillary pores (obtained using W/C ranging from 0.2 to 0.7) are denoted by c.

Percolation (model)results presented in (166) show that phase P (capillary pores) starts being continuous at c ≈ 0.2. In the terminology of the present monograph this corresponds to a critical concentration of c_S ≈ 0.2. Adding an estimate of c_P ≈ 0.6 for the other critical concentration (beyond which 0-stiffness of HCP is normally expected) the solid lines presented in Figures 15.6 and 15.7 are predicted by the conductivity analysis presented in this monograph with shape functions as illustrated in Figure 15.8. A_P and A_S denote aspect ratios of phase P at c = 0 (discrete ellipsoidal cap-pores) and of phase S at c = 1 (discrete ellipsoidal solid particles dissolved in a continuous cap-pore system) respectively.
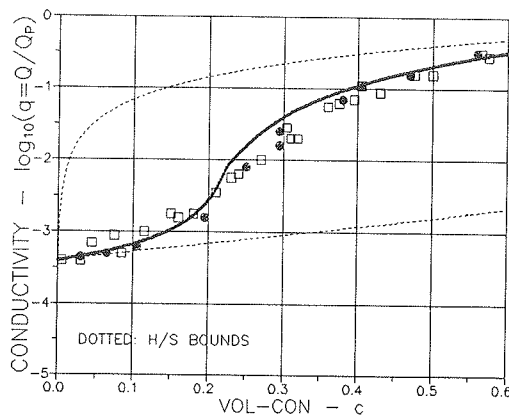
Figure 15.6. (c_P, c_S) = (0.6, 0.225). (Q_P, Q_S) = (1, 0.0004). (A_P, A_S) = (3, 0.3). Silica fume: (□, ■) = (0,3)%.
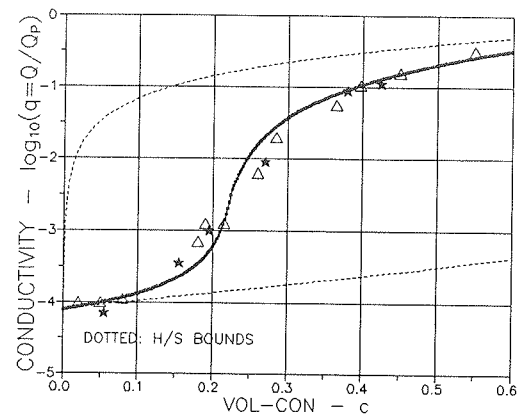
Figure 15.7. (c_P, c_S) = (0.6, 0.225). (Q_P, Q_S) = (1, 0.00008). (A_P, A_S) = (3, 0.3). Silica fume: (△, ✦) = (6, 20)%.

167
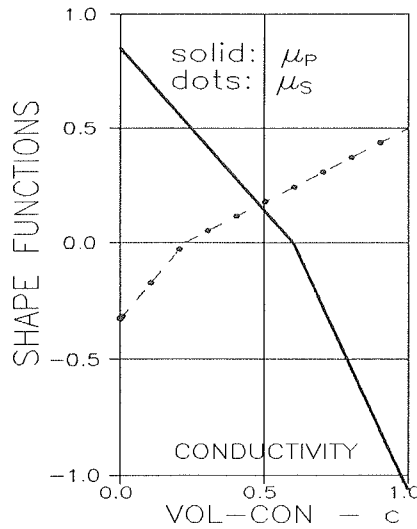
Figure 15.8. Shape functions: (c_P, c_S) = (0.6,0.225), (A_P, A_S) = (3,0.3).

Curiosum: It has been mentioned that the model-results of Bentz et al. (166) were verified by re-evaluated experimental data (W/C = 0.3, c ≈ 0.043) reported by Mejlhede in (169). The data shown in Figure 15.9 are the original chloride diffusion data for leaching systems reported in (169). The following discussion will show that these data can, on their own, be given a microstructural explanation: Apparently the capillary pores of Mejlhede's system are permeable already from c = 0, meaning that c_S ≤ 0. The diffusivities shown in Figure 15.9 with a solid line are predicted with shape functions as presented in Figure 15.10, meaning that the capillary pore system always has a MM-geometry, starting at c = 0 with a pore geometry of long shapes mixed with flat shapes, and ending at c = 1 with a shape of crumbled foils.
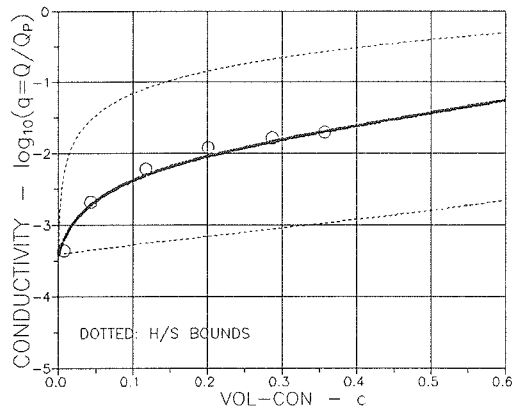
Figure 15.9. (c_P, c_S) = (0.6, <0). (Q_P, Q_S) = (1,0.0004). μ_P^o = 0.3, μ_S ≡ 0. No silica fume.
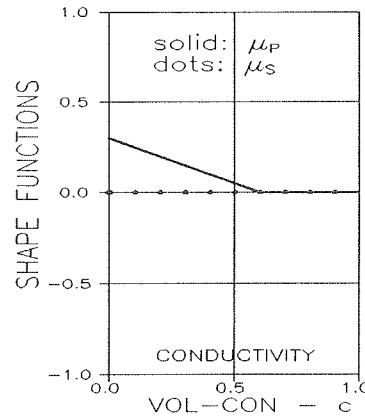
Figure 15.10. Shape functions: (c_P, c_S) = (0.6, <0), μ_P^o = 0.3, μ_S ≡ 0.

Discussion: Apparently two different capillary pore systems are revealed by the studies on leaching systems (169) and on un-leaching systems (166). An explanation is that the pore system changes as the results of leaching. The pore system opens up decreasing the critical concentration c_S and transforming the capillary pore system to be crumbled foils.

It is interesting to notice that the experimental chloride diffusion data obtained by Mejlhede (169) (including HCP with silica fume) under leaching conditions were

168

fitted excellently by Equation 15.8. This expression applies for pores with crumbled foil geometries at any pore concentration. The hypothesis can be made that stiffness (and strength) of HCP reduces as the result of leaching chloride exposure.

Future research on chloride diffusivity of HCP will show that this problem can be solved only by considering also the mechanical behavior of this material: Measured stiffness before, and after chloride exposure.

The theory developed in this monograph for the prediction of conductivity of composite materials is well justified by the results of this section. The justification is even more pronounced by the observation made in (166) that the general trends of chloride diffusivity of leaching HCP systems are in good agreement with experimental data obtained by Christensen (171) with respect to the electrical conductivity of such systems: $W/C = 0.4$ with 0% and 20% silica fumes.

15.3.2 Thermal conductivity of special DC-CD composite

The results presented in Figures 15.11 and 15.12 are from an analysis of the special DC-CD composite defined in Section 9.3. In the example considered phase P is Silicon carbide (SiC) with $Q_P = 135$ Wm^{-1}/°C. Phase S is Carbon (C) with $Q_S = 9.5$ Wm^{-1}/°C. These phase properties are adopted from the FEM-analysis (15,16) previously referred to in Section 9.3.1 of a layered fiber composite.
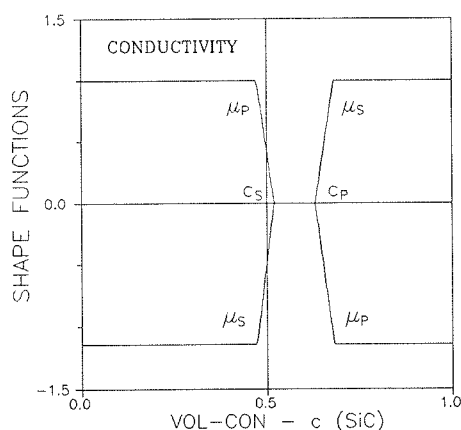
Figure 15.11. Shape functions of isotropic DC-CD composite considered.
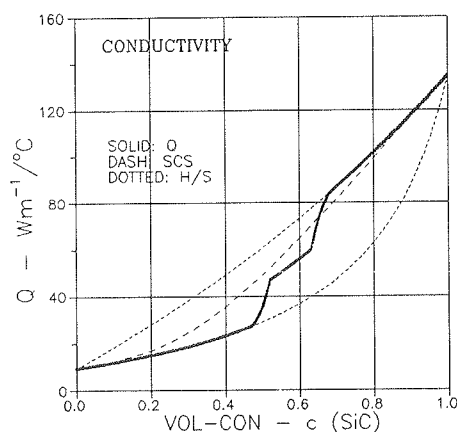
Figure 15.12. Conductivity of isotropic DC-CD composite considered.

Plane-isotropic fiber composite with long parallel fibres

A plane-isotropic version of the composite just considered has been described in Section 9.3.1. The conductivity (perp to fibres) of this composite can be predicted by by Equation 15.9 developed from a plane-isotropic version (24, Appendix C) of the isotropic composite theory presented in this monograph. For the composite
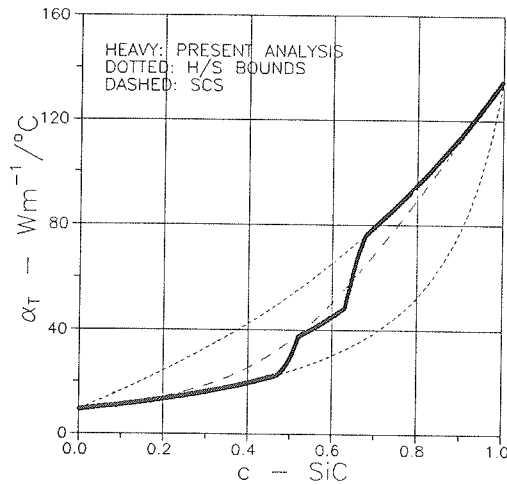
Figure 15.13. *Perp to fibre thermal conductivity of plane-isotropic composite with parallel circular fibres.* (Q_P, Q_S) = *(135,9.5)* $Wm^{-1}/°C$.

presently considered with fibres of circular cross-sections, shape functions can be based on shape factors very close to $(\mu_P°, \mu_S°)$ = $-(\mu_P^1, \mu_S^1)$ = $(1,-1)$.

The results of the analysis are shown in Figure 15.13 which agrees very positively with results (16, Figure 7) deduced from the FEM-analysis (15,16) previously referred to on DC-CD fiber composites.

Remark: In principles, the discussion made in Section 9.3.2 on the description of geometry transitions around c = 0.5 applies also when conductivity predictions are considered.

$$q_T = \frac{Q_T}{Q_S} = \frac{n + \theta[1 + c(n - 1)]}{n + \theta - c(n - 1)} \quad \text{(plane isotropy, perp to fibre)}$$

$$\text{with} \quad \theta = \frac{1}{2}\left[\mu_P + n\mu_S + \sqrt{(\mu_P + n\mu_S)^2 + 4n(1 - \mu_P - \mu_S)}\right] \tag{15.9}$$

$$H/S \text{ bounds: } \theta \equiv 1 \text{ and } \theta \equiv n$$

15.3.3 Electrical conductivity of binary metallic mixtures

(Considered with simple 3-parameter descriptions of shape functions). The experimental data shown in Figure 15.14 are from tests (172) on the electrical conductivity of Cu_2Sb-Sb systems with n = 0.27. The solid line is conductivity theoretically predicted with $(\mu_P°, \mu_S°, c_P)$ = (1,-1, 0.5) - which define the same composite geometry as previously detected in Chapter 12 for the Budiansky's SCS stiffness analysis.

Landauer (52) showed that experimental data from a number of binary metallic mixtures were well fitted by the Bötcher/Landauer expression subsequently presented in Table 15.1. Some data, however were not. An example is shown in Figure 15.15 with experimental data from (173) on Mg_2Pb-Pb systems with n = 8.55. The solid line represents data theoretically predicted with $(\mu_P°, \mu_S°, c_P)$ = (-1,1,0.5).

170

Discussion: Conductivity for a number of binary metallic mixtures can be predicted on the basis of phase-symmetric DC-CD geometries created by compacted spheres - which also apply for the Budiansky's stiffness expression previously considered. It is noticed from Figure 15.14 that the prediction qualities of the present theory and of the Böttcher/Landauer expression are identical.
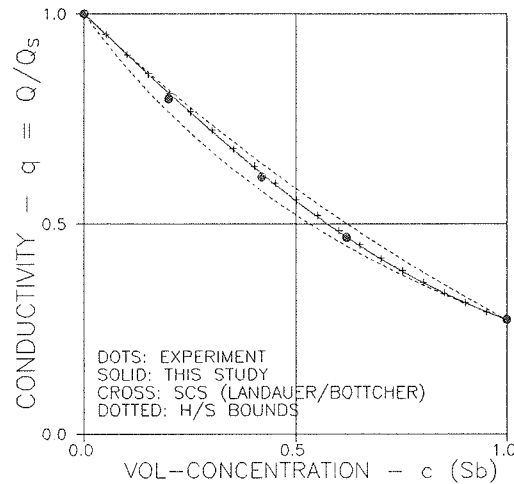
Figure 15.14. Electrical conductivity of Cu₂Sb-Sb. Shape functions defined by $(\mu_P^o, \mu_S^o, c_P) = (1,-1,0.5)$.
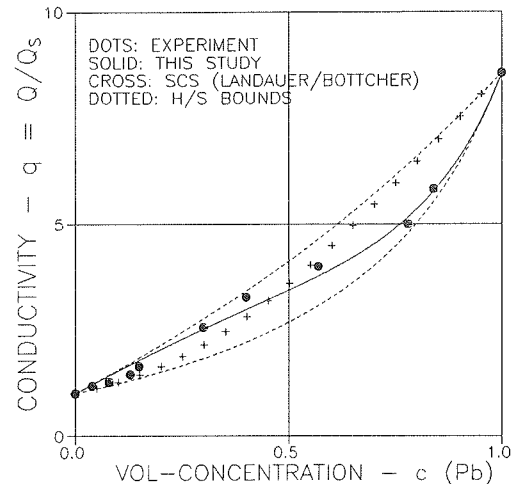
Figure 15.15. Electrical conductivity of Mg₂Pb-Pb. Shape functions defined by $(\mu_P^o, \mu_S^o, c_P) = (-1,1,0.5)$.

Apparently the geometries of the Cu₂Sb-Sb and Mg₂Pb-Pb systems considered in Figure 15.14 and Figure 15.15 respectively vary differently. Figure 15.14 indicates that small amounts of Sb have spherical shapes such as in a CSA_P composite. Figure 15.15 indicates that small amounts of Pb have continuous shapes such as in a CSA_S composite. From a mechanical point of view the latter statement sounds somewhat strange. Apparently the electrical diffusion in a Mg₂Pb-Pb system is a phenomenon which has its own way of using the mechanical composite structure. A first hypothesis to explain this feature might be that certain conductivity phenomenons utilize the surfaces primarily of microstructures. A special future composite study is revealed by these remarks.

Incidentally, the discussion just made tells that the theory developed has no difficulty in handling the opposite geometrical trend CD → DC than what is implicitly assumed as default (DC → CD) in this monograph, see Chapter 2.3.

15.3.4 Thermal conductivity of fire-brick

(Considered with simple 3-parameter descriptions of shape functions). The experimental data in Figure 15.16 are from (174). A thermal conductivity of the

solid $Q_S \approx 0.825$ kcal/mh°C, a shape factor $\mu_P^° \approx 1$, and a critical concentration $c_P \approx 0.82$ have been deduced by regression of experimental data as explained in Equation 15.10. A shape factor of $\mu_S^° = 0$ is estimated observing that fire-bricks normally are impregnable already at low porosities. With these geo-parameters the conductivity of the porous brick are predicted as shown in Figure 15.16.
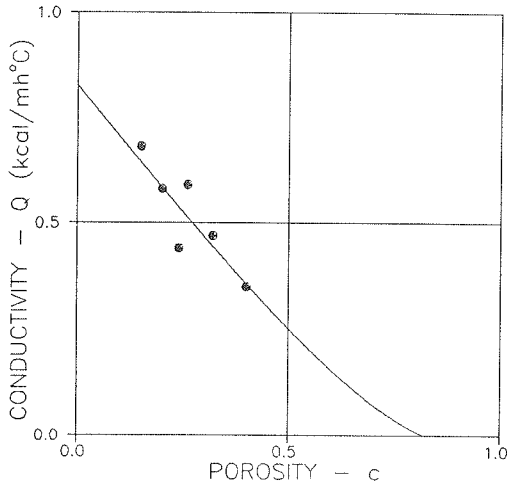
Figure 15.16. Thermal conductivity of fire-brick. Geometry: $(\mu_P^°, \mu_S^°, c_P) = (1, 0, 0.82)$
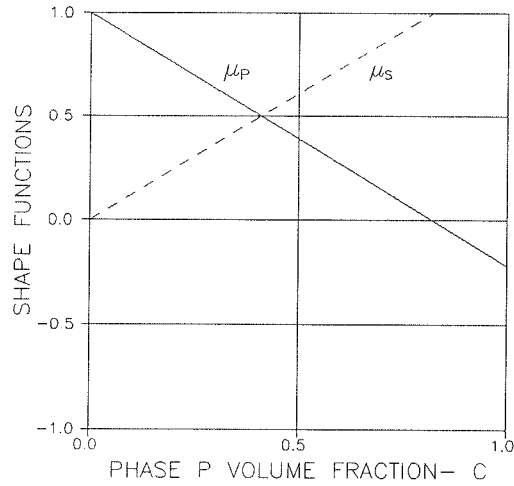
Figure 15.17. Geometry of fire-brick considered. $\mu_P^°, \mu_S^°, c_P = 1, 0, 0.82. Max(\mu_S) = 1.$

Deduction of geo-parameters from experiments

With a 3-parameter descriptions of shape functions the conductivity expression for porous materials, Equation 15.4, can be re-written as shown in the former expression of Equation 15.10. It is subsequently shown, how this expression can be used to derive the shape factor $\mu_P^°$ and the critical concentration c_P from experimental observations. The regression is made optimizing the fit quality (r^2) with respect to the critical concentration.

Remark: Ideally, c_P must agree with c_P determined by a linear regression of data from stiffness tests on the porous material considered, see Equation 10.13.

$$\frac{Q}{Q_S} = \frac{1 - c}{1 + c/[2\mu_P^°(1 - c/c_P)]} \quad \Rightarrow$$

$$Y = Y_o + \alpha X \quad \text{with} \quad X = \frac{c}{1 - c/c_P} \quad \text{and} \quad Y = \frac{1 - c}{Q} \quad \Rightarrow \qquad (15.10)$$

$$Q_S = \frac{1}{Y_o} \quad ; \quad \mu_P^° = \frac{Y_o}{2\alpha} \quad \text{from intersection } (Y_o) \text{ and slope } (\alpha)$$

172

15.4 SCS-estimates

The numerical SCS-method previously referred to in Chapter 3 (with Appendix C) to estimate composite stiffness has also been generalized in this monograph to consider composite conductivity. The results are presented in Appendix C where composites are considered with a larger range of particle shapes than what is considered in analytical SCS-methods presented in the literature:

Electrical conductivity and dielectricity of two-phase materials was studied by Landauer (52) and Böttcher (53) respectively using a SCS-model with spheres as the basic element. Their theoretical results can, after some re-writing, be expressed as shown in Table 15.1, first row. It is interesting to observe that this expression can be obtained from Equation 15.1 introducing $\theta = 2q$ (just as the Budiansky's stiffness expression in Equation 10.7 can be obtained from the stiffness equation in Table 10.3 introducing $\theta = e$).

AUTHOR	BASIC ELEMENT	CONDUCTIVITY - $q = Q/Q_s$
Böttcher (53) Landauer (52)	Sphere (A = 1)	$q = \frac{1}{4}\left[B + \sqrt{B^2 + 8n} \right]$ *with* $B = 2 - 3c - n(1 - 3c)$
Beek (55)	Long fiber (A = ∞)	$q = \frac{1}{2}\left[B + \sqrt{B^2 + 4n[1 + \frac{c}{3}(n - 1)]} \right]$ *with* $B = (1 - n)\left[1 - \frac{5}{3}c\right]$
Bruggeman (54)	Thin disc (A = 0)	$q = n\dfrac{3 + 2c(n - 1)}{3n - c(n - 1)}$

Table 15.1. Some SCS solutions for the conductivity of composite materials. Strict ellipsoidal particles.

Other conductivity expressions were developed for a composite with extremely long fibres by Van Beek (55), and for a composite with extremely thin discs by Bruggeman (54). After some re-writing the results obtained by these authors can be formulated as shown in Table 15.1, second and third row respectively. All three SCS solutions presented in Table 15.1 are illustrated in Figures 15.18 and 15.19 which compare very accurately with the numerical SCS-results obtained in Appendix C.

15.4.1 Examination of SCS-expressions

We re-call that the composite geometries for SCS-solutions are self-defined and unknown, except at small phase P concentrations. To compare the present analysis with results from a SCS-analysis it is of interest to know the underlying geometries. The geometrical reference to be used is the concept of organic geometries applied throughout this monograph. This means that geometries revealed are those for which the present analysis and the SCS-analysis being investigated will predict the same stiffness.
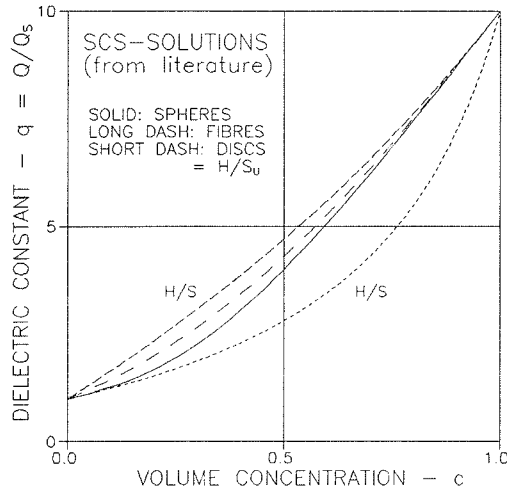
Figure 15.18. Composite dielectricity. Fibres (A=∞), spheres (A=1), discs (H-S upper bound) (A=0). (n = 10).
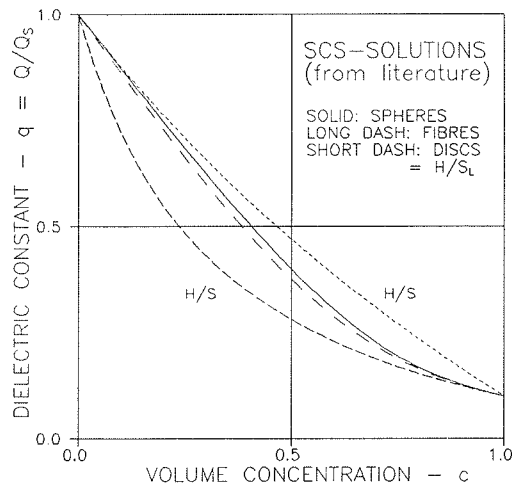
Figure 15.19. Composite dielectricity. Fibres (A=∞), spheres (A=1), discs (H-S lower bound) (A=0). (n = 0.1).

SCS-expressions (and other estimates) suggested for prediction of composite conductivity can be examined with respect to isotropy and geometry just as stiffness expressions have been examined in Chapter 12. The analogy between stiffness and conductivity is considered such that Equations 12.1 and 12.7 become Equations 15.11 and 15.12.

$$\theta = \frac{[n - c(n - 1)]q_{EST} - n}{1 + c(n - 1) - q_{EST}} \quad ; \quad isotropy\ check$$

$$with \quad \begin{cases} 2n \le \theta \le 2 & when\ n \le 1 \\ 2n \ge \theta \ge 2 & when\ n > 1 \end{cases} \tag{15.11}$$

$$\mu_P = \frac{4n_1 n_2(\theta_2 - \theta_1) + \theta_1^2 n_2(2 - \theta_2) - \theta_2^2 n_1(2 - \theta_1)}{4n_1 n_2(\theta_2 - \theta_1) + 2\theta_1 n_2(2 - \theta_2) - 2\theta_2 n_1(2 - \theta_1)}$$

$$\mu_S = \frac{4n_1(1 - \mu_P) - \theta_1(\theta_1 - 2\mu_P)}{2n_1(2 - \theta_1)} \quad ; \quad geometry\ check \tag{15.12}$$

These expressions will be used in this section to reveal the underlying 'hidden' geometries in the SCS-expressions presented in Table 15.1.

15.4.2 Spheres: Böttcher/Landauer
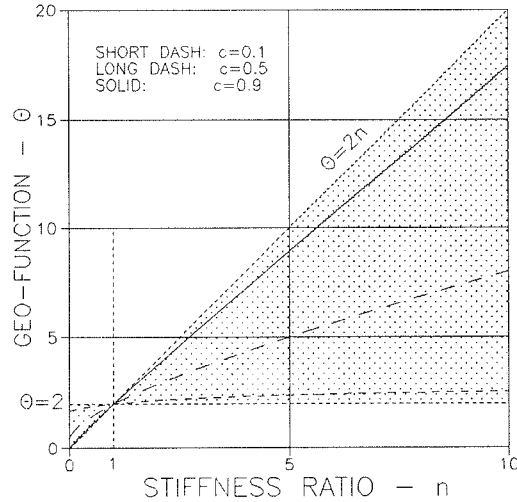
Figure 15.20. Underlying geo-functions in the Böttcher/Landauer analysis.
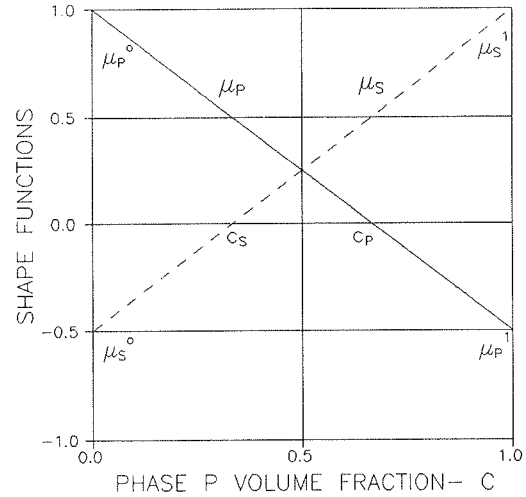
Figure 15.21. Underlying geometry in the Böttcher/Landauer analysis.

The results of a geo-analysis of the Böttcher/Landauer's SCS-solution in Table 15.1 are shown in Figures 15.20 and 15.21. They define a phase-symmetric DC-CD composite geometry with $(\mu_P^\circ, \mu_S^\circ) = (1,-0.5)$ and $c_P = 2/3$. With Figures 7.10 and 10.5 the geometry can be estimated to be the result of compacting powders made of very rugged fibres (many spheres mixed with a few fibres).

Remark: We notice that the shape functions in Figure 15.21 deviate from those revealed in Chapter 12 for the Budiansky's SCS-stiffness analysis which also has a sphere as the basic inclusion. Theoretically, the reason for not getting the same shape functions, is that a conductivity analysis, basically is a bulk modulus analysis released from the restraints of a simultaneous shear modulus analysis.

Practically, however, we should not be disturbed: Whatever shape functions are chosen, conductivities are predicted with equal reliabilities, see Section 15.3.3.

15.4.3 Long fibres: Beek

We re-call from Section 12.1 that we cannot expect a fully consistent geometry revealed from this SCS-solution (A > 4), unless at extreme stiffness ratios (n $\approx$ 0 or ∞). The type of composite, however, is consistently revealed by Equations 15.11 and 15.12 for various stiffness ratios as a MM-CD with $(\mu_P^\circ, \mu_S^\circ) =$

175

(0.75,0.25) and $(\mu_P{}^1,\mu_S{}^1)$ = (-0.5,1). The shape functions in Figure 15.23 are determined with (n_1,n_2) = $(10^{-10},10^{10})$, simulating extreme stiffness ratios.

We may then conclude that the analysis reveals a MM-CD composite geometry with $(\mu_P{}^o,\mu_S{}^o)$ = (0.75,0.25), $(\mu_P{}^1,\mu_S{}^1)$ = (-0.5,1.), and c_P = 0.6. With Figure 10.5 the geometry can be estimated at c = 0 to be agglomerating P-fibreworks, changing to end at c = 1 as a mixture of S-fibres and S-spheres in a continuous phase P. Phase P changes from being continuous to being discrete at c = 0.6.
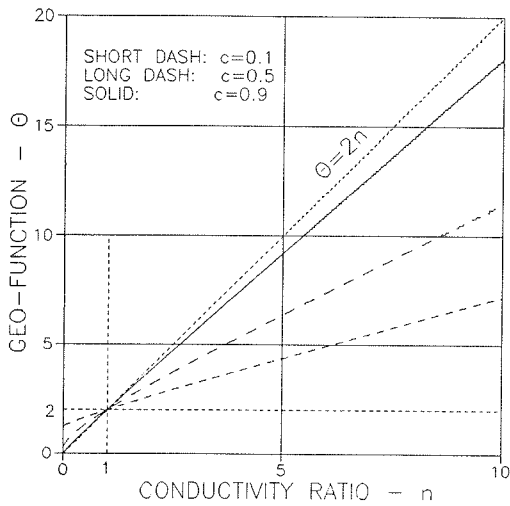
Figure 15.22. Underlying geo-functions in the Beek analysis.
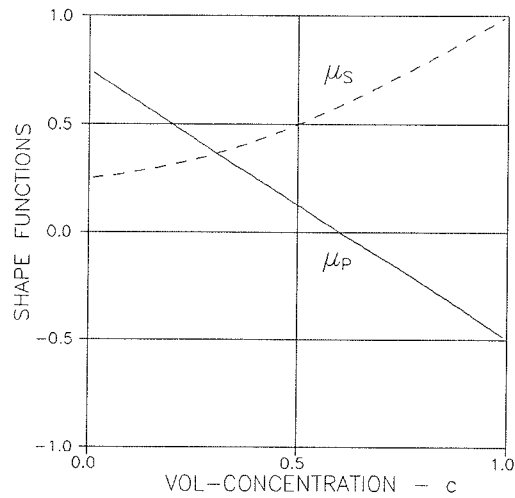
Figure 15.23. Underlying geometry in the Beek analysis.

Remarks: We notice from Figure 15.23 that the 'accurate' shape functions revealed do not comply with the feature discussed in Section 15.1.1 on simple 3-parameter shape descriptions. The following example, however, will demonstrate the statement made in Section 15.1.1 that simple descriptions will only cause insignificant loss of accuracy in conductivity predictions.

Conductivity of MM-CD fibre composite

The Beek-solution, presented in Table 15.1, for the conductivity of composites with very long fibres are considered in Figure 15.24 as experimental data from tests on a MM-CD composite.

An analysis with $(\mu_P{}^o,\mu_S{}^o,c_P)$ = (0.75,0,0.6) produces the conductivities presented with a solid line. The shape functions associated are illustrated in Figure 15.25.

Remark: It is noticed that there are only small differences between the Beek prediction and the prediction made by the analysis of this monograph.
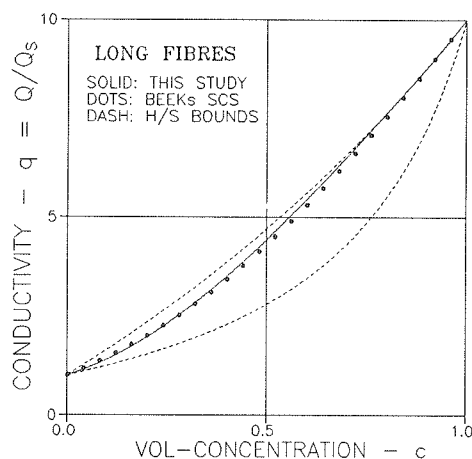
Figure 15.24. Long fibres: Present analysis versus Beek's solution. n = 10.
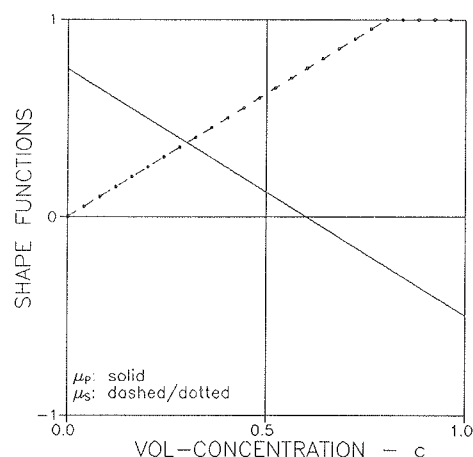
Figure 15.25. Long fibres: Shape functions in present analysis.

15.4.4 Thin discs: Bruggeman

Obviously, see Equation 15.3, a CSA_S geometry is the underlying composite geometry in the SCS-analysis of Bruggeman which is based on strict discs with A « 1. This geometry-observation agrees with numerical SCS results obtained in Appendix C on both stiffness and conductivity of particulate composites with thin discs. It also agrees with conclusions made in analytical studies on particulate composites (e.g. 14) such as made with thin discs.

In the context of the geometrical concept applied in this monograph thin discs act, by agglomeration, as phase P envelopes for phase S particles (CSA_S). From the opposite geometry (CSA_P) the geometry changes through the crumbled foils geometry previously explained in this monograph (e.g. Sections 4.1.4 and 8.1.2), defining the 'half way' phase P geometry between the geometry of a CSA_P and the geometry of a CSA_S.

The conductivity expression for crumbled foils has already been presented in Equation 15.8. Experimental justifications for this expression has been presented in Section 15.3.1.

15.4.5 Summary and discussion

The SCS-estimates of conductivity presented in Table 15.1 are checked with the results summarized in Table 15.2. All estimates are evaluated positively with respect to both isotropy and stability of underlying composite geometries. All estimates are included in the theory presented in this monograph. There are, however, two minor comments to be made:

177

Although the Böttcher/Landauer's estimate on conductivity and the Budiansky's stiffness estimate on stiffness are both based on a spherical particle, they do not reveal exactly the same composite geometry. The theoretical reason for that is explained in Section 15.4.2. The same *type* of geometry (phase-symmetric DC-CD), however, is revealed. Because of that there will bee no significant difference between predictions made with the Bötcher/Landauer' expressions or made with the theory presented in this monograph using the 'Budiansky geometry', an example is presented in Section 15.3.3.

METHOD → ↓ CHECK	Böttcher/Landauer (Spheres)	Beek (Long fibres)	Bruggemann (Thin discs)
Isotropy	+	+	+
Geometry	+	(+)	+

Table 15.2 Summary of check results for conductivity SCS-estimates considered in Table 15.1. Good results are marked +. A positive check on type of geometry is denoted (+).

The second comment to be made concerns the Beek analysis of long fibre composites. Because the particle aspect ratio is very high ($A = \infty$) no fully consistent geometry can be found, as expected from Section 12.1. The *type* of geometry, however, is fully consistent (also as expected).

15.5 Conclusion

A method has been developed in this chapter by which the stiffness theory for composite materials presented in Chapter 8 can be used in the analysis of other physical properties of composites with arbitrary geometry. Examples of properties considered are thermal conductivity, electrical conductivity, dielectric constant, and magnetic permeability.

The method presented is based on a very simple modification of the bulk modulus expression from the general stiffness theory. It is emphasized that the influence of composite geometry on other physical properties considered is the same as on stiffness. The analysis is verified by comparison of predicted results with theoretically and experimentally obtained data - including SCS-estimates (Self-Consistent-Scheme) known from the literature.

A new generalized, numerical SCS-method has been developed (in Appendix C) for estimation of composite conductivity. The method is based on mixtures of ellipsoidal particles of any shapes.

16. Conclusion and final remarks

We re-call from the introductory chapter, 'Overview': The subject dealt with in this monograph is the mechanical and physical behavior of composites as influenced by composite geometry. This subject has a high priority in the general study of composite materials. A better understanding of the behavior of natural composites, improvement of such materials, and design of new materials with prescribed properties are just three examples in modern materials research where more knowledge on geometry versus materials property is absolutely necessary.

The author's contribution in this respect is presented in this monograph: A theory is developed which predicts the influence of variable composite geometry on the mechanical and physical behavior of isotropic composites. Features especially considered are the elastic behavior (including eigenstrain/stress), the viscoelastic behavior, and the conductivity behavior.

16.1 Analysis

The complete analysis presented in this monograph on composite materials is based on the following three step procedure used to determine the influence of composite geometry on the elastic behavior of such materials:

1. Composite geometries are classified. Various types of composites are considered such as particulate composites, laminated composites, and compacted powder composites. A special scheme for composite classification is developed in Chapter 2.
2. Global elastic solutions (master solutions) are developed in Chapters 3 - 6 which are valid for any composite geometry. The influence of specific composite geometries are 'hidden' in so-called geometry functions (θ).
3. Shape functions (μ) are developed in Chapter 7 such that geometry functions can be related to the special composite geometries classified under step 1, meaning $\theta = \theta(\mu)$.

16.1.1 Elastic composite analysis

Elastic composite solutions can now be determined, as summarized in Chapter 8, for any composite, introducing its special geometry functions, $\theta = \theta(\mu)$ developed under step 3, into the global solutions obtained under step 2.

Simplified analysis

Recognizing that elastic and geometrical information are often not very accurate in practice, a simplified version of the elastic theory is presented in Chapter 10.

16.1.2 Viscoelastic and conductivity analysis

Composite solutions for viscoelastic and conductivity problems are developed, in Chapters 14 and 15, from the elastic solutions applying some analogy schemes presented in these chapters.

16.1.3 Inverse analysis (diagnostics, materials design)

Any expression presented in this monograph is consistent with respect to isotropy and geometry assumed. Well-known empirical methods often used in composite analysis are not always consistent in this respect. The composite theory developed is re-organized in Chapters 12 and 15 to become a "test method" with respect to quality control of prediction methods suggested in the field of composite materials. In Chapter 12 is demonstrated that this method can be used in materials design. In Chapter 15 it is used to reveal the underlying geometries in composite solutions obtained by SCS-analysis (Self Consistent Scheme).

16.2 Justification

The very basis of the analysis, namely the elastic part is justified in Chapter 9 comparing the analytical results with experimental and theoretical works made by other authors in the field of composite materials - and with results obtained in the author's own FEM analysis reported in Appendix D.

In any field considered (elasticity, viscoelasticity, conductivity) the theories developed are successfully checked against a number of experimental data and composite theories previously reported in the composite literature.

16.2.1 General SCS analysis

To test some elementary influence of particle shapes on the stiffness and conductivity of particulate composites a generalized SCS-analysis has been developed in Appendix C. It works with mixtures of ellipsoidal particles of arbitrary shapes.

16.3 Applications

In general no special composite materials are thought of. In examples, however, constitutive materials such as cement and wood materials, polymers, ceramics, and metals are used. Among the subjects considered by the theory are the following:

Elasticity: Internal stress/strain states, stiffness, shrinkage and hygro-thermal behavior. Quality control of existing expressions for estimation of stiffness. Porous materials. Image analysis. Stiffness of hardened cement paste (HCP) and concrete. A strength mechanism for concrete.

Viscoelasticity: Creep- and relaxation analysis, complex stiffness moduli and damping. Internal stress/strain state. Experimental vibration analysis. Power-law creep of wood, polymers, and ceramics. Time-modified creep for HCP and concrete. A lifetime mechanism for concrete.

180

Conductivity (Other physical properties): Thermal and electrical conductivities, diffusion coefficients, dielectric constants and magnetic permeabilities. Electrical conductivity of binary metallic structures. Examination of existing SCS-estimates on conductivity. Thermal conductivity of fire-brick. Chloride diffusion in HCP.

17. Notations

The notations most frequently used in this monograph are listed below. A few symbols have been allowed to have two meanings - only, however, where the proper meaning is obvious from the text associated. The list does not include local symbols used only in intermediate results.

Sub/supscripts

P, S	Phase P and phase S respectively
no sub/supscript	Composite material
k, g	Bulk- and deviatoric behavior respectively
$(\text{sub})_o$	Porous material (or state of reference)
$(\text{sup})^o$	Dilute solution
∞	Very stiff inclusions
EFF	Effective quantity used to simplify/approximate analysis

Volume

V	Phase volumes
$c = V_P/(V_S + V_P)$	Volume concentration of phase P
$1 - c$	Volume concentration of phase S
$A = (1-c)/(1+c)$	Volume parameter
c_{PACK}	Void ratio in a packed pile of particles

Geometry

c_P, c_S	Critical concentrations
$c_{SYM} = (c_P + c_S)/2$	Symmetry concentration
μ^o, μ^1	Shape factors
μ	Shape function
θ	Geometry function
A	Fiber aspect ratio (length/diameter)
α	Volume fraction of particles with one shape in a mixture of particles of various shapes
ß	Pore saturation of impregnated phase P
p	Density (number per volume unit) of voids or cracks

Elasticity

E	Young's modulus
K	Bulk modulus
G	Shear modulus
ν	Poisson's ratio
$\kappa = 2(1 - 2\nu)/(1 + \nu)$	Bulk Poisson factor
$\gamma = (7 - 5\nu)/(4 - 5\nu)/2$	Shear Poisson factor

Stiffness ratio - relative stiffness

$n = E_p/E_s$ — Young stiffness ratio

$n_k = K_p/K_s$ — Bulk stiffness ratio

$n_g = G_p/G_s$ — Shear stiffness ratio

$N_k = n_k \kappa_p/\kappa_s = n_g$ — Modified bulk stiffness ratio

$N_g = n_g \gamma_p/\gamma_s$ — Modified shear stiffness ratio

Relative stiffness of composite

$e = E/E_s$ — Relative Young's modulus of composite

$k = K/K_s$ — Relative bulk modulus of composite

$g = G/G_s$ — Relative shear modulus of composite

Viscoelasticity

t — time

T — Oscillation (cyclic) time

ω — $= 2\pi/T$, angular frequency

f — $= \omega/(2\pi)$, traditional frequency, cycles/time unit

$C(t)$ — Creep function

$R(t)$ — Relaxation function

τ — Relaxation time

b — Creep power in Power-Law creep

ϕ,ϕ^* — Creep parameter and creep factor respectively for HCP and concrete

E_c — Complex Young's modulus

E_R — Real Young's modulus

E_I — Imaginary Young's modulus

δ — Loss angle

$\tan(\delta) = E_I/E_R$ — Loss tangent

Stress/strain

σ_{ij} — General stress (i = 1,2,3, j = 1,2,3)

σ_{kk} — Volumetric stress $(\sigma_{11} + \sigma_{22} + \sigma_{33})$

$\sigma_{kk}/3$ — Hydraulic pressure/tension

s_{ij} — Deviatoric stress

ϵ_{ij} — General strain

ϵ_{kk} — Volumetric strain

e_{ij} — Deviatoric strain

Eigenstrain/stress

λ — Eigenstrain (linear)

ρ — Eigenstress (hydrostatic)

183

Abbreviations

CSA	Composites spheres assemblage
CSA_p/CSA_s	CSA with phase P/phase S as kernel
TROC	Special particulate composite
CROSS	Special grid composite
H/S	Hashin-Shtrikman's stiffness/conductivity bounds
P/H	Paul-Hansen's stiffness bounds
W/C	Water/cement ratio by weight
HCP	Hardened cement paste

Literature

1. Paul, B.: "Prediction of elastic constants of multi-phase materials". Trans. of the Metallurgical Soc. of AIME, 218(1960), 36 - 41.

2. Hansen, T.C.: "Creep of concrete: A discussion of some fundamental problems". Bulletin no. 33(1958), Svenska Forskningsinstitutet för Cement och Betong, Tekniska Högskolan, Stockholm".

3. Hashin, Z. and Shtrikman, S.: "Variational approach to the theory of elastic behavior of multi-phase materials". J. Mech. Solids, 11(1963), 127 - 140.

4. Hashin, Z.: "Elastic moduli of heterogeneous materials". J. Appl. Mech., 29 (1962), 143 - 150.

5. Hill, R.: "Elastic properties of reinforced solids: Some theoretical principles". J. Mech. Phys. Solids, 11(1963), 357 - 372.

6. Christoffersen, J.: "Elastic and elastic-plastic composites - a new approach, DCAMM Rep. 61 1973 (Danish Centre for Applied Mathematics and Mechanics, Tech. Univ. Denmark, Copenhagen.

7. Levin, V.M.: "Determination of effective elastic moduli of composite materials", Sov. Phys. - Dokl., 20(1975), 147.

8. G.P. Sendeckyj (ed): "Mechanics of composite materials", Vol. II in "Composite materials" (edited by Broutman, L.J. and R.H. Krock), Academic Press, New York, 1974.

9. Chow, T.S.: "The effect of particle shape on the mechanical properties of filled polymers" (review), Journ. Materials Science, Vol 15(1980), pp 1873 - 1888.

10. Halpin, J.C. and N.J. Pagano. 1970. Stiffness and Expansion Estimates for oriented and random fibrous composites. AFML-TR-69-341.

11. Mori, T., and Tanaka, K.: "Average stress in matrix and average energy of materials with misfitting inclusions", Acta Metallica, 21(1973), 571-574.

12. Benveniste, Y.: "A new approach to the application of Mori-Tanaka's theory in composite materials", Mechanics Mater., 6(1987), 147-157.

13. Budiansky, B.: On the elastic moduli of some heterogeneous materials". J. Mech. Phys. Solids, 13(1965), 223 - 227.

14. Stang, Henrik: "En kompositmaterialeteori og dens anvendelse til beskrivelse af trækpåvirkede cementkompositter" (in danish, "A composite theory and its application to cement based composites subjected to tension"), Thesis, Institute of Structural Mechanics, Tech. Univ. Denmark, 1984.

15. Reiter, T., Dvorak, G.J. and Tvergaard, V.: "Micromechanical models for graded composite materials", J. of the Mechanics and Physics of Solids, 45(1997), 1281-1302.

16. Reiter, T. and Dvorak, G.J.: "Micromechanical models for graded composite materials: II. Thermomechanical loading", J. of the Mechanics and Physics of Solids, 46(1998), 1655-1673.

17. Hale, D.K.: "The physical properties of composite materials" (review paper), Journ. Mat. Sc. Vol 11(1976), pp 2105-2141.

18.   Torquato, S.: "Effective stiffness tensor of composite media: I. Exact series expansions", J. Mech. Phys. Solids, 45(1997), 1421-1448.

19.   *Idem:* "Effective stiffness tensor of composite media: II, Application to isotropic dispersions", J. Mech. Phys. Solids, 46(1998), 1411-1440.

20.   Fagerlund, G.: "Samband mellan porositet och materials mekaniske egenskaper" (in swedish, "Relations between porosity and mechanical properties of materials"), Div. Build. Technology, Tech. Univ. Lund, Sweden, 1971.

21.   Hasselman, D.P.H.: "Relation between effects of porosity on strength and on Young's modulus of elasticity of polycrystalline materials", J. Am. Ceram. Soc., 46((1963), 564 - 565.

22.   Coble, R.L., and Kingery, W.D.: "Effect of porosity on physical properties of sintered alumina", J. Am. Ceram. Soc., 39(1956), 377 - 385.

23.   Nielsen, L. Fuglsang: "Strength and Stiffness of Porous Materials", Journ. Am. Ceramic Soc., 73(1990), 2684 - 89.

24.   *Idem:* "Elastic Properties of Two-Phase Materials", Materials Science and Engineering, 52(1982), 39-62.

25.   Milton, G. W.: "Composites: A myriad of Microstructure Independent Relations", pp. 443-459 in Proc. (eds. T. Tatsumi, E. Watanabe, T. Kambe) of the XIXth Int. Congr. of Theoretical and Applied Mechanics, Kyoto, Japan, 25-31 August 1996, published by Elsevier 1997.

26.   Sigmund, O.: "Materials with prescribed constitutive parameters: An inverse homogenization problem" Int. J. Solids Structures 31(1994), 2313 - 2229.

27.   *Idem:* "Tailoring materials with prescribed elastic properties", Mechanics of Materials 20(1995), 304 - 368.

28.   Milton, G.W. and Cherkaev, A.V.: "Which elasticity tensors are realizable", J. of Engineering Materials and Technology, 117(1995), 483 - 493.

29.   Agarwal, B.D., Panizza, G.A., and Broutman, L.J.: "Micromechanics analysis of porous and filled ceramic composites", Journ. Am. Ceramic Soc., 54(1971), 620-624.

30.   Adams, D.F.: Section D: "Solution techniques" in "Elastoplastic behavior of composites", pp 169-208 in "Mechanics of Composite Materials", Vol.II in "Composite materials" (edited by Broutman, L.J. and R.H. Krock), Academic Press, New York 1974.

31.   Zaitsev, Y.B.: "Crack propagation in a composite material", in "Fracture Mechanics of Concrete", (ed. F.H. Wittmann), Elsevier 1983.

32.   Y.W. Zaitsev and F.H. Wittmann: "Simulation of crack propagation and failure of concrete", Mater. and Struct. 14(1981), 357-365.

33.   Tvergaard, V.: "Fibre debonding and breakage in a whisker-reinforced metal", Mat. Sc. & Eng., A190(1995), 215-222.

34.   Bentz, D.: "Three-Dimensional Computer Simulation of Portland Cement Hydration and Microstructure Development", J. Am. Ceram. Soc., 80(1997), 3-21.

35.   Garboczi, E.J.: "Finite Element and Finite Difference Programs for Computing

the Linear Electric and Elastic Properties of Digital Images of Random Materials", Report NISTIR 6269(1998), National Institute of Standards and Technology (NIST), Gaithersburg, Maryland 20899, USA.

36.   Bentz, D.P., Garboczi, E.J., Jennings, H.M., and Quenard, D.A.: "Multi-Scale Digital-Image-Based Modelling of Cement-Based Materials", MRS Proceedings, ibid(1995), 33-42

37.   Bendsøe, M.P.: "Methods for the optimization of structural topology, shape and material", Springer Verlag, Berlin, 1995, 271 p.

38.   Jacobsen, J.B., Olhoff, N., and Rønholt, E: "Generalized shape optimization of three-dimensional structures using materials with optimum microstructure", Mechanics of Materials, 28(1998), 207 - 225.

39.   Pedersen, P.: "On sensitivity analysis and optimal design of specially orthotropic laminates", Eng. Opt., 11(1987), 305-316.

40.   Nielsen, L. Fuglsang: "On strength of porous material - simple systems and densified systems", Materials and Structures, 31(1998), 651-661.

41.   Ditto: "On the Prediction of Rheological Parameters for Concrete", Nordic Conference on Deformations in Concrete Structures, Copenhagen, march 1980. Proc. DIALOG 1/80(1980), 81, Danish Engineering Academy, Dept. Civ. Eng., Lyngby, Denmark

42.   Powers, T.C.: "Physical properties of cement paste", Proc. Fourth Int. Symp. on the Chemistry of Cement, Washington, D.C.,1960, US Dept. of Commerce, National Bureau of Standards, Monograph 2(1962), no. 43.

43.   Powers, T.C. and T.L. Brownyard: "Studies of the physical properties of hardened cement paste", ACI Journ., Proc. 41(1946-47), 101, 249, 469, 549, 669, 845, 865, 933, 971, (Chicago, Portland Cement Ass., Res. Dept. Bulletin 22(1948))

44.   Nielsen, L. Fuglsang: "Strength developments in hardened cement paste - Examination of some empirical equations", Materials and Structures, 26(1993), 255-260.

45.   Hansen, P. Freiesleben: "Hærdeteknologi-1, Portland cement" og "Hærdeteknologi-2, Dekrementmetoden", Bkf-centralen, 1978.

46.   Hammerslev, J.M. in Proc. Cambridge Phil. Soc., 53(1957), 642.

47.   Stauffer, D. and Aharony, A.: "Introduction to percolation theory", 2nd ed., Taqylor and Francis, London, 1992.

48.   Nielsen, L. Fuglsang: "Stiffness and other physical properties of composites as related to phase geometry and connectivity - Part I: Methods of analysis", 3rd Symposium on Building Physics in the Nordic Countries, Copenhagen, Sept. 13.-15. 1993. Proceedings Vol. 2 (Bjarne Saxhof, editor) Thermal Insulation Laboratory, Technical University Denmark, 1993, pp 725 - 734.

49.   Bentz, D.P.: Modelling cement microstructure: "Pixels, particles, and property prediction", Materials and Structures, vol. 32(1999), 187-195.

50.   Goodier, J.N.: "Concentration of Stress around Spherical and Cylindrical Inclusions and Flaws", J. Appl. Mech., 55(1933), 39

51.   Dewey, J.M.: "The elastic constants of materials loaded with non-rigid fillers", J. Appl. Phys., 18(1947), 578.

52.   Landauer, R.: "The electric resistance of binary metallic mixtures", J. Appl. Phys. 23(1952), 779.

53.   Böttcher, C.J.F.: "The dielectric constant of crystalline powders", Rec. Trav. Pays-Bas, 64(1945), 47.

54.   Bruggeman, D.A.G.: "The calculation of various physical constants of heterogeneous substances, I: The dielectric constants and conductivities of mixtures composed of isotropic substances", Ann. Phys. Lpz., 24(1935), 636.

55.   Van Beek, L.K.H.: "Progress in dielectrics", Vol. 7, 69 - 114, Heywood, London, 1967.

56.   Christensen, R.M. and Lo, K.H.: "Solutions for the effective shear properties in three phase sphere and cylinder models", J. Mech. Phys. Solids, 27(1979), 315.

57.   Sokolnikoff, J.S.: " Mathematical theory of elasticity", McGraw-Hill, New York, 2nd edn., 1956.

58.   Eshelby, J.D.: "The determination of the elastic field of an ellipsoidal inclusion, and related problems", Proc. R. Soc. London, Ser.A, 241(1957), 376-396.

59.   Grabovsky, Y., Milton, G.W.: "Exact relations for composites: Towards a complete solution", Documenta Mathematica, Extra Volume ICM III(1998), 623-632

60.   Grabovsky, Y., Milton, G.W., and Sage, D.S.: "Exact relations for effective tensors of composites: Necessary conditions and sufficient conditions", Report November (1998), Department of Mathematics, University of Utah, Salt Lake City, USA.

61.   Nielsen, L. Fuglsang: "Shrinkage, Swelling, and Stiffness of Composites - Strain and Stress caused by Hygro-thermal action and Solidification or Freezing of Liquid Impregnant", Bygningsstatiske Meddelelser, 62(1991), 47-78.

62.   Idem: "Mechanics of composite material subjected to eigenstress - With special reference to frost resistance of porous brittle material", Danish Building Research Institute, SBI-Bulletin 96(1993).

63.   Nielsen, L. Fuglsang: "Drying of wood, Part I: Stresses caused by drying", ".., Part II: Damage free drying", Bygningsstatiske Meddelelser, 57(1986), p. 73-115.

64.   Idem: "Interne Spannungen sowie Schwind- und Temperaturdeformationen des Betons", Cement and Concrete Research, 4(1974), 31 - 44.

65.   Pickett, G.: "Effect of aggregate on shrinkage of concrete", Journ. Am. Concrte Inst., 52(1956), 581.

66.   Hansen, T.C. and Nielsen, K.E.C.: "Effect of aggregate properties on concrete shrinkage", Journ. Am. Concrete Inst., 62(1965), 783.

67.   Xi, Yunping and Jennings, H.M.: "Shrinkage of cement paste and concrete modelled by a multiscale effective homogeneous theory", Materials and Structures, 30(1997), 329-339.

68.   Sendeckyi, G.P.: "Elastic behavior of composites", pp 46-83 in "Mechanics of

Composite Materials", Vol.II in "Composite materials" (edited by Broutman, L.J. and R.H. Krock), Academic Press, New York 1974.

69.   Nielsen, L. Fuglsang: "Pore size distribution and shrinkage of porous materials", Report 316(1994), Building Materials Lab., Techn. University of Denmark.

70.   Bentz, P.B.: "Modelling drying shrinkage in reconstructed porous materials: Application to porous Vycor glass", Modelling Simul. Mater. Sci. Eng. 6(1998), 211-236.

71.   *Idem:* "On the Effect of Defective Phase Contact on the Mechanical Behavior of Particulate Composites like Concrete", Cement and Concrete Research, 12(1982), 685.

72.   Budiansky, B. and R.J. O'Connell: "Elastic moduli of a cracked solid", Int. J. Solids Struct., 12(1976), 81-97.

73.   Davis, W.E.A.: "The dielectric constants of axially isotropic composite materials", J.Phys.D. 7(1974), 1016-1029.

74.   Powers, T. C.: "Fundamental aspects of the shrinkage of concrete" (in german), Die Bauwirtschaft, 15(1961), 344-49.

75.   Helmuth, R.A. and D.H. Turk: "Elastic moduli of hardened Portland cement and Tricalcium silicate pastes: Effects of porosity", pp. 135-144 in Symposium on structure of Portland cement and concrete. Highw. Res. Bd., Spec. Rept., No. 90, 1966.

76.   Murray et al: "The hot pressing of ceramics", in W.D. Kingery: Ceramic Fabrication Processes, J. Wiley & Sons, New York, 1958.

77.   Spriggs, R. M., Brissette, L. A., and Vasilos, T.: "Effect of porosity on elastic and shear moduli of polycrystalline magnesium oxide". J. Am. Ceram. Soc., 45(1962), 400.

78.   Nielsen, L. Fuglsang: "Rheology of extreme composites", In "Papers in Structural Engineering and Materials - A Centenary Celebration", 179-187, Dept. of Struct. and Materials, Tech. Univ. Denmark, 2000.

79.   *Idem:* Rheology of some extreme liquid composites - such as fresh self-compacting concretes. Nordic Concrete Research, 2(2001), no 7.

80.   Wu, T.T.: "The effect of inclusion shape on the elastic moduli of a two-phase material", Int. J. Solids Structures, 2(1966), 1

81.   Ollivier, J.P. and Massat, M.: Permeability and microstructure of concrete: A review of modelling", Cem. and Concr. Res., 22(1992), 503-514.

82.   Hansen, E. dePlace and Schmidt, L.: "Sammenhæng mellem porøsitet og elasticitetsmodul, samt porøsitet og styrke for teglsten", (in danish, Stiffness and strength of bricks as related to porosity), A students report in Material mechanics (Course 6110), Spring 1988, Build. Mat. Lab., Techn. Univ. Denmark.

83.   Knudsen, F. P.: "Effect of porosity on Young's modulus of Alumina", J. Am. Ceram. Soc., 45(1962), 94-95.

84.   Konow, Thorborg von: "Restaurering och reparation med puts- och murbruk" (in swedish: Restoration and repair with lime mortars), dr. thesis, Åbo Akademi University Press, Åbo, Finland, 1997.

85.   Nielsen, Anders: "Porous materials - structure and properties", in "Selected research

studies from Scandinavia", pp 94-103, Report TVBM-3078(1997), Lund Institute of Technology, Div. Building Materials, Lund, Sweden.

86. *Idem:* "Ny viden om kalk og kalkmørtler" (in danish: New knowledge on lime and lime mortars), MAT-NYT 2(1998), Danish Society of Materials Testing and Research, Copenhagen, Denmark.

87. Madsen, D.H., Jeppesen, M.J., and Weidemann, H.C.: "Porestørrelsesfordeling i kalkmørtel" (in danish, Pore size distribution in lime mortar). A students report, course 59409, spring 1998, Dept. Struct. Eng. and Materials, (supervisors: Nielsen.A. and Nielsen, L.F.).

88. Hansen, T. C.: "Influence of aggregate and voids on modulus of elasticity of concrete, cement mortar, and cement paste", Proc. Am. Concr. Inst., 62(1965), 193-216.

89. J.J. Beaudoin and R.F. Feldman: "A study of mechanical properties of autoclaved Calcium silicate systems", Cem. Concr. Res., 5(1975), 103-118.

90. R.F. Feldman and J.J. Beaudoin: Studies of composites made by impregnation of porous bodies. I. Sulphur impregnant in Portland cement systems", Cem. Concr. Res., 7(1977), 19-30.

91. Clark, S.P.: "Handbook og physical constants", rev. ed; Memoir 97, The geological Society of America, Inc., New York, 1966.

92. Larsen, E.S. and Nielsen, C.B.: "Decay of bricks due to salt". Materials and Structures, 23(1990), 16 - 25.

93. Ashby, M. F.: "Materials data", Cambridge Univ. Eng, Dept., 1981.

94. Ishai, O.: "Influence of sand concentration on deformations of mortar beams under low stresses", ACI Journ., Proceedings 58(1961), 611-622.

95. Palmus, L.: "Letklinkerbetons mekaniske egenskaber" (in danish, Mechanical properties of light clinker concrete), M.Sc. thesis, Spring 1996, Dept. Struct. Engineering and Materials, Tech. Univ. Denmark.

96. Hansen, T.C.: "Creep and stress relaxation of concrete", Proc. 31(1960), Swedish Cement and Concrete Res. Ins., Tech. Univ. of Stockholm, Sweden.

97. *Idem:* "Influence of aggregate and voids on modulus of elasticity of concrete, cement, and cement paste", J. Am. Concr. Inst., Proc. 62(1965), 193.

98. Nielsen, K.E.C.: "Aggregate stresses in concrete", Thesis, Proc. 41(1971), Swedish Cement and Concrete Res. Inst., Tech. Univ. Stockholm, Sweden.

99. Tada, H., Paris, P.C., and Irwin, G.C.: "The Stress Analysis of Cracks Handbook", Del Research Corp., Hellertown, Pa, 1973.

100. Spange, H. and Pedersen, E.S.: "Early age properties of selected concrete", in "High Performance Concrete - The Contractors Technology, HETEK", Report 59(1997), Ministry of Transport, Road Directorate, Denmark.

101. Bentz, D.P.: Modelling cement microstructure: Pixels, particles, and property prediction", Materials and Structures, Vol. 32(1999, 187-195.

102. Lokhorst, S.J. and van Breugel, K.: "Simulation of the effect of geometrical changes

of the microstructure on the deformational behavior of hardening concrete", Cement and Concrete Res., vol. 27(1997), 1465 - 1479.

103. Hirsch, T.J.: "Modulus of elasticity of concrete affected by elastic moduli of ce ment paste matrix and aggregate", Proc. Am. Concrete Inst., 59(1962), 427.

104. Dougill, J.W.: "Modulus of elasticity of concrete affected by elastic moduli of cement paste matrix and aggregate, Discussion of paper by T.J. Hirsch", Proc. Am. Concrete Inst., 59(1962), 1363.

105. Popocics, S. and Erdey, M.: "Estimation of the modulus of elasticity of concrete-like composite materials", Mat. and Struct. 3(16)(1970), 253-260.

106. Counto, U. J.: "The effect of the elastic modulus of the aggregate on the elastic modulus, creep, and creep recovery of concrete", Mag. Concrete Res., 16(1964), 129.

107. Tanacan, L. and Ersoy, H. Y.: "Mechanical properties of fired clay-perlite as composite material", Journ. Materials in Civil Engineering, February 2000, 55-59.

108. Maxwell, J.C.: Treatise on electricity and magnetism, 1(1873), 365.

109. Nielsen, L. Fuglsang: "Effects of Creep in Uncracked Composite Structures of Steel and Concrete", Bygningsstatiske Meddelelser, 38(1967), 65.

110. Idem: "Rheologishe Eigenschaften für isotrope linear-viscoelastische Komposit-materialien", Cement and Concrete Research, 3(1973), 751 - 766.

111. Idem: "New Methods in Practical creep Analysis of Concrete", Seventh Int. Congr. on Rheology, Gothenburg, Sweden 1976. Proc. Chalmers Univ. of Technology, Gothenburg (1976), 98.

112. Idem: "Creep of Concrete under a Multi-Axial State of Stress", Fifth Int. Congr. on Rheology, Kyoto, Japan 1968, Proc. Vol. II, 527, University of Tokyo Press 1970.

113. Nielsen, L. Fuglsang: "Composite analysis of concrete - Creep, relaxation, and eigenstrain/stress", in "High Performance Concrete - The Contractors Technology, HETEK", Report 112(1997), Ministry of Transport, Road Directorate, Denmark.

114. Nielsen, L. Fuglsang: "Time-dependent behavior of concrete - a basic algorithm for FEM-analysis", Bygningsstatiske Meddelelser, 70(1999).

115. Flügge, W.: "Viscoelasticity", Blaisdell Publ. Comp., London 1967

116. Lee, E.H.: "Stress analysis in viscoelastic bodies". Quarterly of Appl. Mathematics, 13(1955), 183.

117. Carslaw, H.S. and J.C. Jaeger: "Operational methods in applied mathematics". Dower, New York, 1963.

118. Erdelyi, A. (ed): "Tables of integral transforms, Bateman Manuscript Project, Vol 1, McGraw-Hill, New York, 1954.

119. Murray, R.S.: Mathematical handbook, Schaum's Outline Series, McGraw-Hill, Inc., New York, 1968 (31th printing 1993).

120. Bellman, R.E., R.E. Kalaba, and J. Lockett: "Numerical Inversion of the laplace transforms" Am. Elsevier Publ. Comp., New York, 1966.

121. Garbow, B.S., Giunta, G., Lyness, J.N., and Murli, A.: "Software for the

191

implementation of Week's method for the inverse Laplace transformation problem", ACM Trans. Math. Soft., 14(1988), 163-170.

122. *Idem:* "Algorithm 662. A Fortran software package for the numerical inversion of the Laplace transform based on Week's method", ACM Trans. Math. Soft., 14(1988), 171-176.

123. McHenry, D.: "A new aspect of creep in concrete and its application to design", ASTM Proc., 43(1943), pp 1069-1084.

124. Alfrey, T.: "Non-Homogeneous Stresses in Viscoelastic Media". Qu. Appl. Math. 2(1944), 113.

125. Nowacki, W.: "Dynamics of elastic systems", Chapman & Hall Ltd, London 1963.

126. Ditlevsen, O.: "Stiffness replacement principle in linear visco-elastic structures", personally communicated research note, Dept. Struct. Eng. and Mat., Tech. Univ. Denmark, 16.05.1996.

127. Nowick, A.S., and Berry, B.S.: "Anelastic relaxation in crystalline solids", Academic Press, New York, 1972.

128. Schwarzl, F.R.: "Numerical calculation of stress relaxation modulus from dynamic data for linear viscoelastic materials", Rheologica Acta, 14(1975), pp 581-590.

129. Nielsen, L. Fuglsang: "Power Law Creep as Related to Relaxation, Elasticity, Damping, Rheological Spectra and Creep Recovery - With Special Reference to Wood", Conference of Int. Union of Forestry Research Organizations (IUFRO), Xalapa, Mexico, December 1984. Proc., Build. Mat. Lab., Techn. Univ. Denmark 1985, 181 - 204.

130. *Idem:* "Material properties determined by vibration analysis", Materialenyt 1(1995), 4-46, Danish Society for Materials Testing and Research (DSM).

131. *Idem:* "Improved method for complex modulus estimation", Application Note, 1996, Brüel & Kjær A/S, Denmark, (co-authors, N.J. Wismer and S. Gade).

132. *Idem:* "Further developments in material properties determined by vibration analysis" (co-authors, L.V. Andreasen and M. Seifert), Materialenyt, 3(1996), Danish Society for Materials Testing and Research (DSM).

133. *Idem:* "An improved method for estimating the dynamic properties of materials", Sound & Vibration, Instrumentation reference issue, february 2000, 20-24, (co-authors, N.J. Wismer and S. Gade).

134. Døssing, O.: "Structural testing, Part I: Mechanical mobility measurement and Structural testing" and "Part II: Modal analysis and simulation", Brüel & Kjær, Nærum, Denmark, 1988.

135. Andreasen, L. and Seifert, M.: "Materialeprøvning med Svingningsudstyr", M.Sc. thesis, Build. Mat. Lab., Tec. Univ. Denmark, 1995.

136. Nielsen, A.: "Rheology of building materials", thesis, Statens Institut för Byggnadsforskning, Stockholm, Document D6(1972).

137. *Idem,* 'Lifetime and residual strength of wood subjected to static and variable load', Holz als Roh- u. Werkstoff, 58(2000), 81-90 and 141-152.

138. Dischinger, F.: "Untersuchungen über die Knicksicherheit, die elastische Verformung und das Kriechen des Betons bei Bogenbrücken", Bauingenieur 1937, 487-520, 539-552, 595-621.

139. *Idem:* "Elastische und plastische Verformungen der Eisenbetontragwerke und insbesondere der Bogenbrückken", Bauingenieur 1939, 53-63, 286-294, 426-437, 563-572.

140. Nielsen, L. Fuglsang: "Kriechen und Relaxations des Betons", Beton- und Stahlbetonbau, 11(1970), 272-275.

141. *Idem:* "On the Prediction of Creep Functions for Concrete", in "Fundamental Research on Creep and Shrinkage of Concrete" (ed. F. Wittmann), Martinus Nijhoff Publishers, The Hague 1982, 279 - 289.

142. Nielsen, L. Fuglsang: "On the applicability of modified Dischinger equations", Cement & Concrete Res., 7(1977), 159-160.

143. CEB-FIP: "Model code for concrete structures", Comité Euro-International du Béton, Paris, 1978.

144. Ross, A.D.: "Creep of concrete under variable stress". ACI journ., Proc. 54(1958), 739 - 758.

145. Illston, J.M., Dinwoodie, J.M., and Smith, A.A.: "Concrete, Timber, and Metals - the nature and behavior of structural materials", Van Nostrand Reinhold Company, New York, 1979. (Chapter 10 on "Response of Concrete to Stress")

146. Nielsen, L. Fuglsang: "Constitutive equations for concrete", Bygningsstatiske Meddelelser, 45(1974), 65.

147. *Idem:* "The improved Dischinger method as related to other methods and practical applicability", pp 169 - 191 in "Design for Creep and Shrinkage in Concrete Structures", Special Publication SP-76(1982), American Concrete Institute.

148. Trost, H.: "Auswirkungen des Superpositionsprinzips auf Kriech- und Relaxationsprobleme bei Beton und Spannbeton", Beton- und Stahlbetonbau 62(1962), 230-238, 261-269.

149. Bazant, Z.P.: Prediction of Concrete Creep Effects using Age-Adjusted Effective Modulus Method", ACI-Journal, 69(1972), 212-217.

150. Nielsen, L. Fuglsang: "Elasticity and Damping of Porous Materials and Impregnated Materials", Journ. Am. Ceramic Soc., 67(1984), 93 - 98.

151. Hashin, Z.: "Viscoelastic behavior of heterogeneous media", J. Appl. Mech. (Transaction of the ASME), 1965, 630-636.

152. Hashin, Z.: "Complex moduli of viscoelastic composites", Int. J. Solids Struct., 6(1970), 539-52 and 6(1970),797-807.

153. Neville, A.M.: "Creep of concrete as a function of its cement paste content", Mag. Concr. Res., 16(1964), 21.

154. Pickett, G.: "Effect of aggregate on shrinkage of concrete and a hypothesis concerning shrinkage", Proc. Am. Concrete Inst., 52(1956), 581.

155. Markestad, A. and Maage, M.: "Building Materials, Vol II", (norwegian, Byg-ningsmateriallære II), textbook, TAPIR, Trondheim, Norway, 1978.

156. L'Hermite, R.G.: "Volume changes of concrete", Chemistry of Cement, 4th Int. Symp., Washington, 1960, p. 659.

157. Rüsch, H.: "Physikalishe Fragen der Betonprüfung". Zement-Kalk-Gips 12 (1954), 27-39.

158. *Idem:* "Researches towards a general flexural theory for structural concrete, Proceedings of the ACI, 1957, 1.

159. Nielsen, L. Fuglsang: "ComCon (version 1.0) - Software for Composite analysis of concrete (Creep, relaxation, eigenstrain/stress, loss of prestress): Underlying theory and documentation", http://www.byg.dtu.dk/publicering/software_d.htm, Report I-21, Dept. Struct. Eng. and Materials, Tech. Univ. Denmark, 1999.

160. Mullit, Paw: "ComCon (version 1.0) - Software for Composite analysis of concrete (Creep, relaxation, eigenstrain/stress, loss of prestress): User Manual", http://www.byg. dtu.dk/publicering/software_d.htm, Report I-22, Dept. Struct. Eng. and Materials, Tech. Univ. Denmark, 1999.

161. Hastrup, K.: "Polymerimpregnering af porøse materialer" (in danish, Polymer impregnation of porous materials), Thesis, Build. Mat. Lab., Tech. Univ. Denmark, Tech. report 42(1976).

162. Nielsen, L. Fuglsang: "Power-Law creep of wood - composite and dynamic aspects", Conference of Int. Union of Forestry Research Organizations (IUFRO), Bordeaux - France, 17.- 21. august, 1992. Proc., Build. Mat. Lab., Tech. Univ. Denmark, 1993, pp 25-33.

163. Pentoney, R.E.: "Time-dependent mechanical properties of wood", Int. conf. on "The mechanical behavior of wood", held at the Univ. of California, Berkeley, California, USA, Aug. 27 - Sept. 1, 1962. Proc. (ed. A.P. Schniewind), University Extension, Univ. of California. Northern Area, USA 1963.

164. Hashin, Z.: "Assessment of Self Consistent Scheme approximation: Conductivity of particulate composites", J. Compos. Mater. Vol 2(1968), 284.

165. Hashin, Z. and Shtrikman, S.: "A variational approach to the theory of the effective magnetic permeability of multiphase materials", J. Appl. Phys. 33(1962), 3125.

166. Bentz, D.P., Jensen, O.M., Coats, A.M., and Glasser, F.P.: "Influence of Silica Fume on diffusivity in cement-based Materials. Part I: Experimental and computer modelling studies on cement pastes", Submitted to Cement and Concrete Research 1999.

167. Bentz, D.P.: "Three-dimensional computer simulation of cement hydration and microstructure development", J. Am. Ceram. Soc., 80(1997), 3-21.

168. Delagrave, A, Marchand, J., and Pigeon, M.: "Influence of microstructure on the tritiated water diffusivity of mortars", Adv. Cem. Based Materials, 7(1998), 60-65.

169. Mejlhede Jensen, O.: Chloride ingress in cement paste and mortar measured by Electron Probe Micro Analysis", Report R51(1999), Dept. Struct. Eng. and Materials, Tech. Univ. Denmark.

170.   Mills, R. and Lobo, V.M.M.: "Self-diffusion in electrolyte solutions", Elsevier, Amsterdam, (1989), 317.

171.   Christensen, B.: " Microstructural studies of hydrating portland cement-based materials using impedance spectroscopy", Ph.D. thesis, Northwestern University (1993).

172.   Stephens, E. and Evans, E. J.: "The Hall effect and other properties of copper-antimony series of alloys", Phil. Mag. 7(1929), 161.

173.   Stephanow, N. J.: "Electrical conductivity of alloys", Z. anorg. u. allgem. Chem. 78(1912), 1.

174.   Corson, P. B.: "Correlation functions for predicting properties of heterogeneous materials, IV: Effective thermal conductivity of two-phase solids", J. Appl. Phys. (USA) 45(1974), 3180.

COMPOSITE MATERIALS

Mechanical and physical behavior as influenced by phase geometry

Appendix section

LAUGE FUGLSANG NIELSEN

Introduction

Various aspects of the main text are considered in this appendix section. Most appendixes are auxiliary 'tools' for presenting the ideas developed in the main text of this monograph. Two appendixes, however, can be read as separate papers: Appendix C where a new numerical SCS analysis is developed - and Appendix D where a complete FEM-analysis of composite materials is reported. Notations used in this appendix section are the same as used in the main section of the monograph.

Content

Appendix A - Elasticity

Isotropy

Stiffness of an isotropic elastic material is defined by the bulk modulus K and the shear modulus G. Young's modulus E, and the Poisson's ratio (ν) together with two ν-parameters (κ and γ) are related to K and G as follows.

$$
\begin{aligned}
E &= \frac{9KG}{3K + G} &;\quad \nu &= \frac{3K - 2G}{2(3K + G)} \\
G &= \frac{E}{2(1 + \nu)} &;\quad K &= \frac{E}{3(1 - 2\nu)} \\
\kappa &= \frac{2(1 - 2\nu)}{1 + \nu} &;\quad \gamma &= \frac{7 - 5\nu}{2(4 - 5\nu)}
\end{aligned}
\tag{A1}
$$

Composite aspects

In composite theory it is very often appropriate to relate composite elastic moduli (K, G, E, ν) to elastic moduli (K_s, G_s, E_s, ν_s) of an isotropic reference material S. Dimensionless versions of E and ν are then presented as follows with k = K/K_s, g = G/G_s, and e = E/E_s

$$
e = \frac{3kg}{2(1 + \nu_s)k + (1 - 2\nu_s)g} \quad ; \quad \nu = \frac{(1 + \nu_s)k - (1 - 2\nu_s)g}{2(1 + \nu_s)k + (1 - 2\nu_s)g}
\tag{A2}
$$

Stress-strain

The stress tensor σ_{ij} and the strain tensor ϵ_{ij} are related as follows (ex 1) when an isotropic elastic material is considered with stiffness properties from Equation A1.

$$
\begin{aligned}
\varepsilon_{ij} &= \frac{1 + \nu}{E}\left[\sigma_{ij} - \delta_{ij}\frac{\nu}{1 + \nu}\sigma_{kk}\right] \\
\sigma_{ij} &= \frac{E}{1 + \nu}\left[\varepsilon_{ij} + \delta_{ij}\frac{\nu}{1 - 2\nu}\varepsilon_{kk}\right]
\end{aligned}
\qquad i,j = 1,2,3
$$

$$
\text{with Kronecker's delta} \qquad \delta_{ij} = \begin{cases} 1 & \text{if } i = j \\ 0 & \text{if } i \neq j \end{cases}
\tag{A3}
$$

Volumetric stress and strain are denoted by $\sigma_{kk} = \sigma_{11} + \sigma_{22} + \sigma_{33}$ and $\epsilon_{kk} = \epsilon_{11} + \epsilon_{22} + \epsilon_{33}$ respectively. The stress strain relation can also be written as follows in two expressions - one relating volumetric strain to volumetric stress - and another one relating deviatoric strain (e_{ij}) to deviatoric stress (s_{ij}).

$$
\varepsilon_{kk} = \frac{\sigma_{kk}}{3K} \quad with \quad
\begin{cases}
\varepsilon_{kk} = \varepsilon_{11} + \varepsilon_{22} + \varepsilon_{33} & volumetric\ strain \\
\sigma_{kk} = \sigma_{11} + \sigma_{22} + \sigma_{33} & volumetric\ stress
\end{cases}
$$

$$
e_{ij} = \frac{s_{ij}}{2G} \quad with \quad
\begin{cases}
e_{ij} = \varepsilon_{ij} - \delta_{ij}\varepsilon_{kk}/3 & deviatoric\ strain \\
s_{ij} = \sigma_{ij} - \delta_{ij}\sigma_{kk}/3 & deviatoric\ stress
\end{cases}
\tag{A4}
$$

Cubic elasticity

Stiffness of a cubic elastic material is defined by the cubic bulk modulus K_c, the cubic shear modulus G_c, and the cubic Young's modulus E_c or the cubic Poisson's

Figure A1. Coordinate system used in FEM-analysis.

ratio ν_c. The constitutive equation of a cubical elastic material can be expressed as shown in Equation A5 using the coordinate system defined in Figure A1 with stress-strain planes coinciding with planes of elastic symmetry (and materials symmetry).

Qubic material models are considered in Appendix D of this monograph. The stiffness parameters for these materials can be determined performing the two 'FEM-experiments' outlined in Equations A6 and A7. The cubic Young's modulus, the cubic Poisson's ratio, and the cubic bulk modulus are obtained from the "axial experiment" explained in Equation A6. The cubic shear modulus is obtained from the "shear experiment" explained in Equation A7.

$$
\begin{bmatrix}
\varepsilon_x \\
\varepsilon_y \\
\varepsilon_z \\
\varepsilon_{xy} \\
\varepsilon_{xz} \\
\varepsilon_{yz}
\end{bmatrix}
=
\begin{bmatrix}
1/E_c & -\nu_c/E_c & -\nu_c/E_c & 0 & 0 & 0 \\
-\nu_c/E_c & 1/E_c & -\nu_c/E_c & 0 & 0 & 0 \\
-\nu_c/E_c & -\nu_c/E_c & 1/E_c & 0 & 0 & 0 \\
0 & 0 & 0 & 1/2G_c & 0 & 0 \\
0 & 0 & 0 & 0 & 1/2G_c & 0 \\
0 & 0 & 0 & 0 & 0 & 1/2G_c
\end{bmatrix}
*
\begin{bmatrix}
\sigma_x \\
\sigma_y \\
\sigma_z \\
\sigma_{xy} \\
\sigma_{xz} \\
\sigma_{yz}
\end{bmatrix}
\tag{A5}
$$

Conditions: $\varepsilon_x = \varepsilon_y = \varepsilon_{xy} = \varepsilon_{xz} = \varepsilon_{yz} = 0$

Load ⇒ response: $\varepsilon_z \Rightarrow \sigma_x \ (= \sigma_y)$

Results: $E_c = \dfrac{\sigma_z^2 - 2\sigma_x^2 + \sigma_x\sigma_z}{\varepsilon_z(\sigma_x + \sigma_z)}$; $\nu_c = \dfrac{\sigma_x}{\sigma_x + \sigma_z} \Rightarrow$ (A6)

$K_c = \dfrac{E_c}{3(1 - 2\nu_c)}$

Conditions: $\varepsilon_x = \varepsilon_y = \varepsilon_z = \varepsilon_{xz} = \varepsilon_{yz} = 0$

Load ⇒ response: $\varepsilon_{XY} \Rightarrow \sigma_{XY}$

Result: $G_c = \dfrac{\sigma_{xy}}{2\varepsilon_{xy}}$ (A7)

Poly-cubic elasticity

Isotropic mixtures of parts from a cubic material behave elastically, just as an isotropic mixture of cubic crystals. Equation A8 expresses the exact bulk modulus for such mixtures (2).

$$K = K_c = \frac{E_c}{3(1 - 2\nu_c)} \qquad (A8)$$

No corresponding exact poly-cubic shear modulus solution has yet been found. However, it has been shown (3) that the true value is bounded between two solutions derived in (4,5). Some re-writing of these boundary values imply

$$\left[\frac{1}{G_c} + \frac{2}{5}\left(\frac{2(1 + \nu_c)}{E_c} - \frac{1}{G_c} \right) \right]^{-1} \leq G \leq G_c + \frac{2}{5}\left(\frac{E_c}{2(1 + \nu_c)} - G_c \right) \quad (A9)$$

The lower bound (5) is based on an assumption which is tantamount to assuming that the state of stress is identical from crystal to crystal. Correspondingly the upper bound (4) assumes identical states of strain. If the crystals were isotropic then Equation A9 predicts $G = G_c$. Improved bounds for poly-crystals have been given by Hashin and Shtrikman (6). For the present work, however, the bounds in Equation A9 suffice. The upper and lower bounds are sufficiently close to justify simple mean value approximations.

Composite aspects

When isotropic mixtures of cubic composite elements are considered it is very often appropriate to relate composite cubic elastic moduli (K_c, G_c, E_c, ν_c) to the elastic moduli (K_s, G_s, E_s, ν_s) of an isotropic reference material S. Normalized versions of Equations A8 and A9 with respect to phase S are presented as follows with relative coefficients of cubical elasticity $k_c = K_c/K_s$, $g_c = G_c/G_s$, and $e_c = E_c/E_s$,

$$k = k_c = e_c \frac{1 - 2\nu_s}{1 - 2\nu_c} \qquad \Rightarrow \qquad \nu_c = \frac{1}{2}\left[1 - \frac{e_c}{k_c}(1 - 2\nu_s)\right]$$

$$\left[\frac{1}{g_c} + \frac{2}{5}\left[\frac{1 + \nu_c}{1 + \nu_s}\frac{1}{e_c} - \frac{1}{g_c}\right]\right]^{-1} \leq g \leq g_c + \frac{2}{5}\left[\frac{1 + \nu_s}{1 + \nu_c}e_c - g_c\right] \qquad (A10)$$

which can also be expressed as follows with ν_c introduced

$$\frac{1}{g} \leq \frac{3}{5g_c} + \frac{1}{5(1 + \nu_s)}\left[\frac{3}{e_c} - \frac{1 - 2\nu_s}{k_c}\right]$$

$$g \leq \frac{3g_c}{5} + \frac{4(1 + \nu_s)}{5}\left[\frac{3}{e_c} - \frac{1 - 2\nu_s}{k_c}\right]^{-1} \qquad (A11)$$

Appendix B - Dilute particulate composites

The main purpose of this appendix is to show how average particle stresses in an isotropic dilute particulate composites can be evaluated numerically. The particles are cylindrical with lengths l and cross-sections d*d (aspect ratios A = l/d). The isotropic composite is thought to be an isotropic mixture of parts from a cubic composite with similar particles, see Figures B1.

It is emphasized that whenever cubic behavior is considered the stress coordinate system referred to is the system defined in Figure B2 where coordinate planes coincide with planes of elastic symmetry.
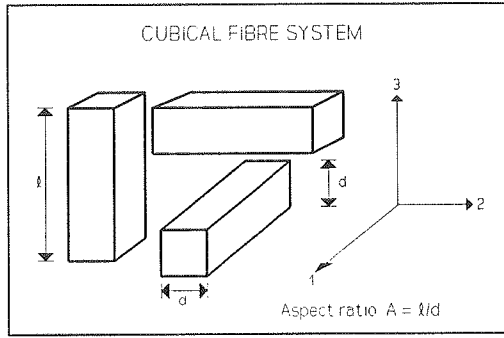
Figure B1. *Isotropic fibre composite is an isotropic mixture of parts from this cubic model.*
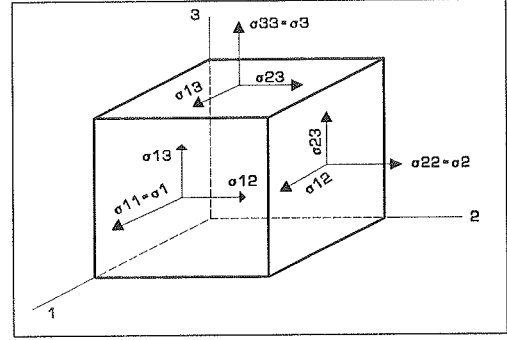
Figure B2. *Coordinate system with coordinate planes coinciding with planes of elastic symmetry.*

Cubic stiffness, shape parameters, and stress

The composite stiffness expressions presented in Section 3.1 (in main text of monograph) can be written as follows applying for the dilute cubic composite just described in Figure B1.

$$
\frac{1}{k^c} = 1 + \left[1 + \frac{1}{p_k^c} \right] c \quad with \quad \frac{1}{p_k^c} = \frac{1 - n_k}{n_k} \frac{\sigma_{Pkk}^{oC}}{\sigma_{kk}} - 1
$$

$$
\frac{1}{g^c} = 1 + \left[1 + \frac{1}{p_g^c} \right] c \quad with \quad \frac{1}{p_g^c} = \frac{1 - n_g}{n_g} \frac{S_{Pij}^{oC}}{S_{ij}} - 1
$$

$$
\frac{1}{e^c} = 1 + \left[1 + \frac{1}{p_e^c} \right] c \quad with \quad \frac{1}{p_e^c} = \frac{1 - n}{n} \frac{S_{Pii}^{oC}}{\sigma_{ii}} - 1 \quad with
$$

$$
S_{Pii}^{oC} = \frac{1 + \nu_p - n(1 + \nu_s)}{1 - n} \sigma_{Pii}^{oC} - \frac{\nu_p - n\nu_s}{1 - n} \sigma_{Pkk}^{oC} \quad ; \quad and \quad n = \frac{E_p}{E_s}
$$

$(ii=11,22,33)$

(B1)

205

Cubical stiffness are denoted by $k^c = K^c/K_s$, $g^c = G^c/G_s$, and $e^c = E^c/E_s$ with supscript C denoting cubical behavior. Cubical shape coefficients are defined by p^c which can be determined numerically if the appropriate stress components are known.

Particle stress

For the cubic composite defined in Figure B1 we can determine these stresses in the following way: The particles are thought of as orthogonal "triple" particles with very large distances between single particles. The average particle stresses for these triple particles can be determined by means of Equation B2 after having solved the stress problems described in Figures B3, B4, and B5 by the Eshelby's classical analysis (7) of the stress field at an ellipsoidal particle in an infinite homogeneous matrix.

Remark: The computer program developed by the author to translate the basic theoretical results of Eshelby to numerical quantities has kindly been cross-checked by Henrik Stang (8) using an algorithm developed for his own work on composite materials (9).
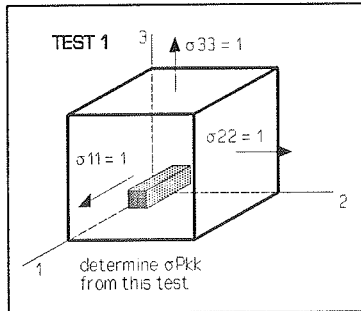
Figure B3. Stress analysis for cubic bulk behavior.
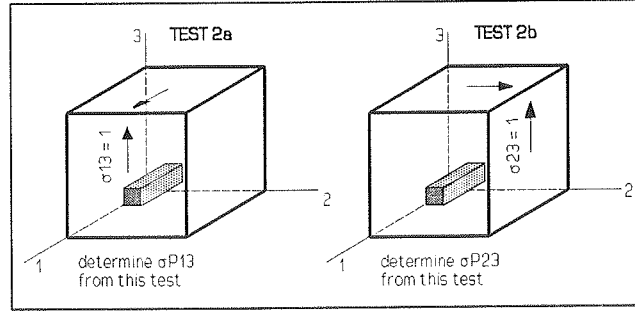
Figure B4. Stress analysis for cubic shear behavior.
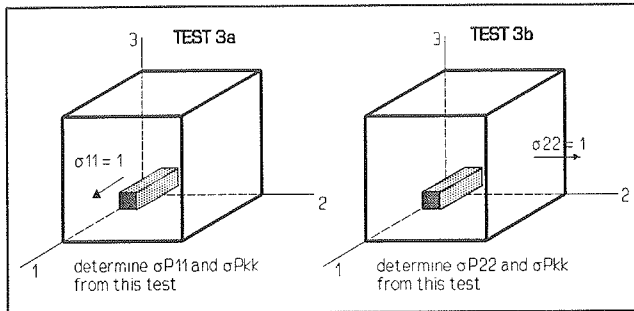
Figure B5. Stress analysis for cubic uni-axial behavior.

206

$$\frac{\sigma_{Pkk}^{oC}}{\sigma_{kk}} = \frac{\sigma_{Pkk}^{o}}{\sigma_{kk}} \qquad \text{from TEST I} \quad (bulk)$$

$$\frac{S_{Pij}^{oC}}{S_{ij}} = \frac{1}{3}\left[2\frac{\sigma_{P13}^{o}}{\sigma_{13}} + \frac{\sigma_{P23}^{o}}{\sigma_{23}}\right] \qquad \text{from TEST II} \quad (shear) \qquad\qquad (B2)$$

$$\frac{S_{Pii}^{oC}}{\sigma_{ii}} = \frac{1}{3}\left[\frac{S_{P11}^{o}}{\sigma_{11}} + 2\frac{S_{P22}^{o}}{\sigma_{22}}\right] \qquad \text{from TEST III} \quad (Young) \quad (ii=11,22,33)$$

Now, cubic stiffness can be determined by Equation B1 calculating the cubic shape parameters, p_k^c, p_g^c, and p_e^c as indicated with stress components calculated from Equation B2.

Isotropic stiffness, shape coefficients, and stress

The isotropic counterpart to Equation B1 is

$$\frac{1}{k} = 1 + \left[1 + \frac{1}{p_k}\right]c \quad ; \quad \frac{1}{g} = 1 + \left[1 + \frac{1}{p_g}\right]c \qquad\qquad (B3)$$

where the isotropic shape coefficients, p_k and p_g, are related to their cubic counterparts presented in Equation B4. This expression is obtained from the poly-cubic (isotropic) stiffness bound solutions presented in Equations A10 and A11 (Appendix A) introducing cubic stiffness from Equation B1 and observing that the g-bounds for dilute poly-cubic materials coincide. This observation means that Equations B4 and B3 are exact.

$$\frac{1}{p_k} = \frac{1}{p_k^c} \quad ; \quad \frac{1}{p_g} = \frac{3}{5p_g^c} + \frac{1}{5(1 + \nu_S)}\left[\frac{3}{p_e^c} - \frac{1 - 2\nu_S}{p_k^c}\right] \qquad\qquad (B4)$$

Particle stress

By means of Equation 3.8 accurate particle stresses in isotropic dilute composites can now be derived from Equation B3 as shown in Equation B5.

$$\frac{\sigma_{Pkk}^{o}}{\sigma_{kk}} = \left[1 + \frac{1}{p_k}\right]\frac{n_k}{1 - n_k} = f_k(E_P, E_S, \nu_P, \nu_S)$$

$$\frac{S_{Pij}^{o}}{S_{ij}} = \left[1 + \frac{1}{p_g}\right]\frac{n_g}{1 - n_g} = f_g(E_P, E_S, \nu_P, \nu_S) \qquad\qquad (B5)$$

Remark: We emphasize that the stress functions, f, in Equation B5 and anywhere in this monograph implicitly also carry the argument A (aspect ratio) - including the stress functions of Goodier's in Equation 3.9 where A = 1 (sphere).

Approximate description of shape factors

Uni-shaped particles

The somewhat cumbersome accurate determination of shape factors represented by Equation 7.6 for uni-shaped particles can be acurately approximated as follows for Poisson's ratios $0 < \nu_S < 0.5$.

$$\mu^o_{Pj} = \overline{m}_{jo} \;\; ; \;\; \mu^o_{Sj} = -\overline{m}_{j\infty}\frac{1 - \overline{m}_{jo}}{1 - \overline{m}_{j\infty}} \;\; (= -X^2_o \;\; at \;\; \mu^o_{Pj} = 1) \;\; ; \;\; (j = k,g) \qquad (B6)$$

$$A \leq 1: \;\; \overline{m}_{j\infty} = \frac{3A}{A^2 + A + 1} \;\; ; \;\; \overline{m}_{jo} = \frac{3A^Z}{A^{2Z} + A^Z + 1} \;\; ; \;\; (j = k,g)$$

$$A > 1: \;\; \overline{m}_{j\infty} = \frac{3A^Z}{A^{2Z} + A^Z + 1} \;\; ; \;\; \overline{m}_{jo} = \frac{3X^2_o(1 - \overline{m}_{j\infty}) + \overline{m}_{j\infty}}{4X^2_o(1 - \overline{m}_{j\infty}) + \overline{m}_{j\infty}} \qquad (B7)$$

$$Power \;\; Z = X + (X_o - X)A^{-3\log(A)}$$

$$Bulk \;\; (k) \;\; \begin{cases} X_o = 0.84 + 0.21\kappa_S - 0.05\kappa^2_S \\ X = 1.3(0.73 + 0.38\kappa_S - 0.11\kappa^2_S) \end{cases}$$

$$Shear \;\; (g) \;\; \begin{cases} X_o = 1.78 - 1.88\gamma_S + 1.10\gamma^2_S \\ X = 0.6 + 0.4\gamma_S \end{cases} \qquad (B8)$$

Remark: Accurately determined shape factors are normally used in this monograph. Approximate shape factors are used only if explicitly noticed as in the simplified theory presented in Chapter 10 where the shear version of the above approximation is used with $\nu_S = 0.2$. The very simple expressions obtained in this way can be seen in Table 10.1.

Multi-shaped particles

The shape factor determination for multi-shaped particles proceeds as explained in Section 7.1. It can, however, also proceed using the following easy approximation.

$$\mu_j^o \simeq \left[\sum_{i=1}^{\infty} \frac{\alpha_i}{\mu_{j,i}^o} \right]^{-1} \quad ; \quad j = P,S \quad ; \quad \sum_{i=1}^{\infty} \alpha_i = 1 \qquad (B9)$$

where α_i is volume fraction of joining aspect ratio A_i

The difference between the results of the two methods is small enough to suggest Equation B9 to be used as a 'next best' way of determining shape factors for particulate composites with multi-shaped particles.

Appendix C - SCS-Analysis

Stiffness

As previously mentioned in Chapter 3 exact composite stiffness can be predicted by Equation 3.6 if exact stress solutions are known (at any concentration c) for one of the constituent phases. Stiffness estimates, however, can be made on considerably less stress information using the so-called Self Consistency Scheme (SCS) introduced in Section 3.3: The stress of a phase P element at any concentration in a composite can be estimated from the low concentration stress solution (c = 0) for phase P replacing the properties of phase S in that solution with the isotropic properties of the composite. This statement is formalized in Equation C1 with stress functions, f_k and f_g. In the present study these functions, are as determined numerically in Equation B5 (Appendix) B for ellipsoidal particles.

$$
\begin{array}{ll}
\textit{Single particle } c \ll 1 & \textit{SCS-estimates: } c \textit{ in general} \\[1em]
\left.\begin{array}{l}
\dfrac{\sigma^o_{Pkk}}{\sigma_{kk}} = f_k = f_k(E_P, E_S, \nu_P, \nu_S) \\[1.5em]
\dfrac{S^o_{Pij}}{S_{ij}} = f_g = f_g(E_P, E_S, \nu_P, \nu_S)
\end{array}\right\} \Rightarrow &
\left[\begin{array}{l}
\dfrac{\sigma_{Pkk}}{\sigma_{kk}} = f_k(E_P, E, \nu_P, \nu) \\[1.5em]
\dfrac{S_{Pij}}{S_{ij}} = f_g(E_P, E, \nu_P, \nu)
\end{array}\right.
\end{array} \qquad (C1)
$$

With known stress functions composite stiffness is now predicted implicitly by Equation 3.6 introducing the SCS-estimates of phase P stresses. The results of this procedure are summarized in Equation C2. The two stiffness expressions are coupled by the third expression shown relating stiffness to Poisson's ratio. Relations between elastic moduli are reproduced from Equation A1 in Appendix A.

$$
\begin{array}{l}
Y_k = \dfrac{K_P}{K} - \dfrac{K_P}{K_S} + c\left[\dfrac{K_P}{K_S} - 1\right] f_k(E_P, E, \nu_P, \nu) = 0 \; ; \; E = 3K(1 - 2\nu) \\[2em]
Y_g = \dfrac{G_P}{G} - \dfrac{G_P}{G_S} + c\left[\dfrac{G_P}{G_S} - 1\right] f_g(E_P, E, \nu_P, \nu) = 0 \; ; \; E = 2G(1 + \nu) \\[2em]
\nu = \dfrac{3K - 2G}{2(3K + G)}
\end{array} \qquad (C2)
$$

As previously mentioned in Chapter 3 the SCS method was first applied for stiffness prediction of particulate composites with spherical particles (10). The solution could be given an analytical form because of the very simple Goodier/Dewey stress functions presented in Equation 3.9. In this appendix the SCS-method various particle shapes can be considered because shape dependent stress

functions can be introduced from Appendix B where such functions are developed as part of the main study presented in this monograph.

In general Equation C2 has to be solved numerically. From known f_k and f_g functions calculation starts at c $\approx$ 0 with estimating the Poisson's ratio $\nu \approx \nu_S$ of the composite. Then K and G are determined by the former two expressions in Equation C2 (letting K and G grow between their limits, K_S-K_P and G_S-G_P, respectively). Then a new Poisson's ratio is calculated from K and G, and the analysis is repeated with a better estimate of the Poisson's ratio. Calculation stops when a satisfactory agreement is obtained between estimated and calculated Poisson's ratios. Then the analysis proceeds with next volume concentration c.
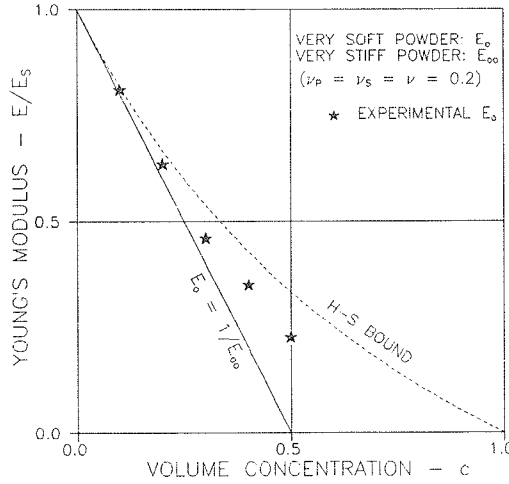
Figure C1. Composite with very soft and very stiff spherical powders.

It is obvious that SCS-solutions are accurate at low phase P concentrations if f_k and f_g are accurately known. The approximate nature, however, of stiffness estimates by SCS at higher phase P concentrations must be emphasized. The geometry considered in this region is somewhat self-defining. This feature is clearly observed from the subsequent section where results from a SCS-analysis are compared with experimental results.

Spherical particles

It has previously been indicated that the present analysis, Equation C2, reduces to become the Budiansky's analysis (10) when particulate composites with spherical particles are considered. For this particular the expressions decouple when $\nu_P = \nu_S = 0.2$, meaning that the following results can be calculated immediately.

$$e = k = g = 0.5\left[D + \sqrt{D^2 + 4n}\,\right] \quad ; \quad (\nu \equiv 0.2)$$

$$with \quad D = (1 - n)(1 - 2c) \quad ; \quad (n = n_k = n_g) \tag{C3}$$

Equation C3 (Figure C1) predicts zero stiffness of porous materials (n = 0) and infinite stiffness of stiff pore systems (n = ∞) for c > 0.5. Obviously the geometrical model of the composite considered is that of a phase symmetric DC-CD powder composite with agglomerating spherical phase P elements which create a fully continuous phase P at c = 0.5 dissolving phase S into discrete elements which approach spherical particles at c = 1. The concentration area of geometry transition is extremely narrow. Thus both critical concentrations c_P and c_s are 0.5.

The experimental stiffness shown in Figure C1 are from tests on porous sintered aluminum reported in (11). Obviously the pore geometry of material used in these tests does not comply with the pore system "described" by the Budiansky analysis. No better predictions, however, can be obtained by the SCS-method. This feature is demonstrated in the following section where the SCS-analysis is applied to particulate composites with particles of non-spherical shapes: Any shape different from spherical causes predicted stiffness of porous materials to be lower than the Budiansky solution.

Various particle shapes and cracks

A number of examples of the present SCS-analysis applied to materials reinforced with fibres of aspect ratios (particle length/diameter) A > 1, spheres with A = 1, and discs and plates with A < 1 are presented in Figures C2 - C5. The H/S bounds referred to are calculated from the general expressions presented in Chapter 5.
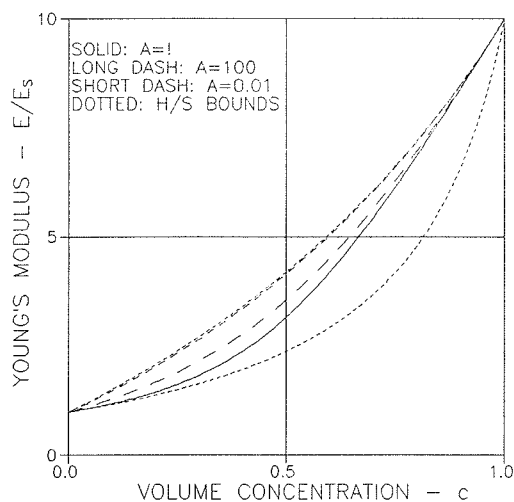
Figure C2. Composites with discs (A = 0.01), compacts (A = 1), and fibres (A = 100). $(E_P, E_S) = (10,1)$, $(v_P = v_S = 0.2$.
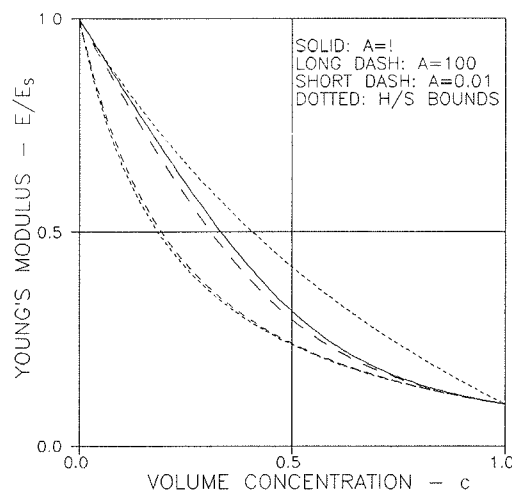
Figure C3. Composites with discs (A = 0.01), compacts (A = 1), and fibres (A = 100). $(E_P, E_S) = (0.1,1)$, $v_P = v_S = 0.2$.

212

It is noticed from Figures C2 and C3 that any deviation from spherical shapes of particles will increase composite stiffness from that predicted by the Budiansky solution (spheres, A = 1) when n > 1. Any deviation from spherical shapes will decrease composite stiffness from that predicted by the Budiansky solution when n < 1. The most efficient influence on stiffness of particle shape is observed when particles are plates and discs (A < 1).

It is, at the same time observed that stiffness of a composite made with very thin discs (A « 1) approaches the H/S upper bound when n > 1, and the H/S lower bound when n < 1. These observations agree with statements made in analytical studies on particulate materials (ex 9) made with very thin discs.
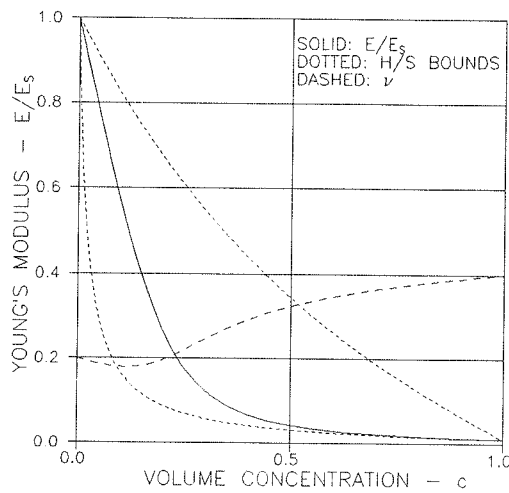
Figure C4. Composite with plate particles (A = 0.1), $(E_p, E_s) = (0.01, 1)$, $(\nu_p, \nu_s) = (0.4, 0.2)$.
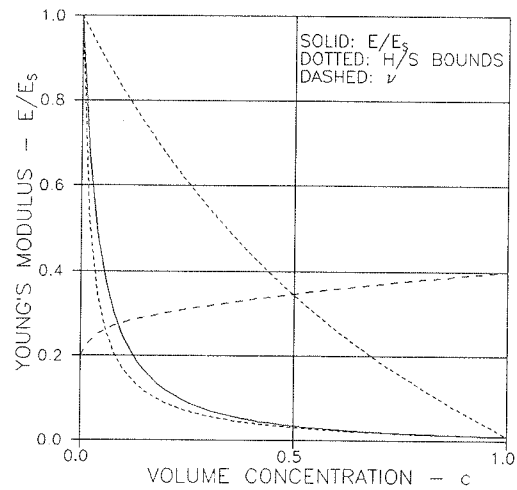
Figure C5. Composite as in Figure C4. Plate particles, however is a mixture of 50% A = 0.1 + 50% A = 0.001.

Cracks: The stiffness of cracked materials can also be considered by the SCS-method presented. The results coincide perfectly with results obtained in Section 9.2.1 from the general composite theory developed in this monograph - and also with results otherwise determined in the composite literature.

Multi-shaped particles

When particulate composites are considered with multi-shaped particles Equations C1 and C2 are used with averaged stress functions expressed as follows, see Section 7.1.1. An example of stiffness prediction for such materials is presented in Figure C5.

$$<f_k> = \sum_{i=1}^{\infty} \alpha_i f_{k,i} \quad ; \quad <f_g> = \sum_{i=1}^{\infty} \alpha_i f_{g,i} \quad ; \quad \sum_{i=1}^{\infty} \alpha_i = 1 \qquad (C4)$$

213

Other physical properties

Other physical properties (conductivities) such as thermal and electrical conductivities, diffusion coefficients, dielectric constants, and magnetic permeabilities can be determined from stiffness analysis by an analogy explained in Chapter 15. In the present SCS context this analogy can be formulated from Equation C2 as shown in Equation C5 where Q_S, $Q_P = nQ_S$, and Q are the physical properties of phase S, phase P, and composite respectively. Ratio of conductivity is introduced as $n = Q_P/Q_S$.

$$Y = \frac{Q_P}{Q} - \frac{Q_P}{Q_S} + c\left[\frac{Q_P}{Q_S} - 1\right] f_k(3Q_P, 3Q, 0, 0) = 0 \qquad (C5)$$

The point of departure in developing Equation C5 from the analogy just mentioned is the former expression in Equation C1 with $f_k = f_k(E_P, E_S, \nu_P, \nu_S) = f_k(3Q_P, 3Q_S, 0, 0)$ with $(Q_P, Q_S) = (K_P, K_S)$ and $(\nu_P, \nu_S) = (0,0)$.

In principles, the conductivity Equation C5 can solved numerically just as the stiffness were solved in Equation C2.

Spherical particles

When particulate composites with spherical particles are considered the stress functions f_k and f_g in Equation C5 are introduced by the Goodier/Dewey expressions in Equation 3.9. Then the following conductivity expression can be developed immediately,

$$q = \frac{1}{4}\left[B + \sqrt{B^2 + 8n}\right] \quad with \quad B = 2 - 3c - n(1 - 3c) \qquad (C6)$$

which was first developed by Böttcher and Landauer in their analysis (12,13) of spherical powder composites.

Particles of various shapes and cracks

Some examples are presented in Figures C6 - C8 on composite conductivity determined by Equation C5. The bounds shown are calculated by Equation 15.3.

Similar comments can be made on composite conductivities determined by SCS-analysis as were previously made on composite stiffness determined by SCS: For conductivity ratios, n > 1, it is noticed from Figure C6 that any deviation from

spherical shapes of particles in a particulate composite will increase composite conductivity relative to that determined for spherical particles. For conductivity ratios, n < 1, it is noticed from Figure C7 that any deviation from spherical shapes will decrease composite conductivity from that determined for spherical particles.

In general, the most efficient influence on composite conductivity of particle shape is observed when particles are plates and discs (A < 1).
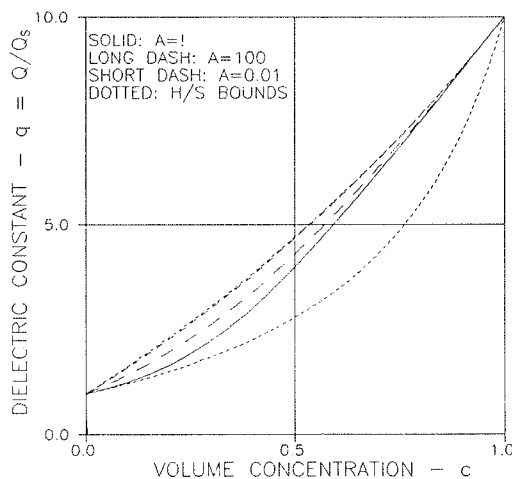
Figure C6. *Conductivity of particulate composite with particles of various aspect ratios,* $(Q_P, Q_S) = (10,1)$.
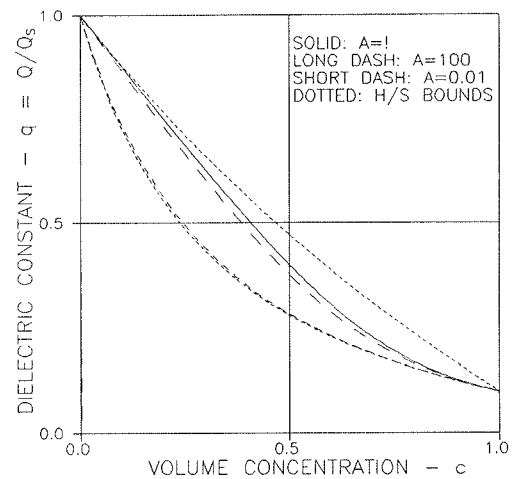
Figure C7. *Conductivity of particulate composite with particles of various aspect ratios,* $(Q_P, Q_S) = (0.1,1)$.

Figures C6 and C7 also indicate that the conductivity of a composite made with very thin discs (A « 1) approaches the H/S upper bound when n = $Q_P/Q_S > 1$, and the H/S lower bound when n < 1.
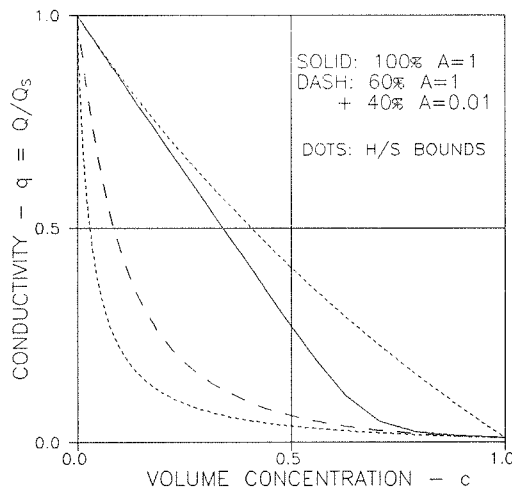
Figure C8. *Conductivity of a composite: 1) with spheres and 2) with a mixture of spheres and discs.* $(Q_P, Q_S) = (0.01,1)$.

composite literature.

Cracks: The conductivity of cracked materials can also be considered by the SCS-method presented. The results coincide perfectly with results obtained in Section 15.1.4 from the general composite theory developed in this monograph - and also with results otherwise determined in the

Multi-shaped particles

When particulate composites are considered with multi-shaped particles Equation C5 is used with an averaged "stress function" just as in a stiffness analysis. An example is shown in Figure C8.

Appendix D - FEM-analysis

Introduction

Parts of the FEM-analysis reported in Chapter 9 has been reported in (14, 15). A full report on the analysis is made in this appendix with references made to the original research reports (16,17,18,19,20,21,22). The FEM-method used is STRUDL (23).

Preliminaries

Composite models used in the FEM-analysis presented are models which can be made by a tight stacking of equally sized congruent *composite elements*. A number of composite elements form so-called *basic-cells* (such as cubic cells) which repeat themselves into a macro model of the material considered. A *test volume* for FEM-analysis is volume large enough to represent the macro model with respect to specific material property considered in analysis. Test volumes can be small as they are in the present study (smaller than the volume of a basic cell) when they are carefully selected with respect to loading and materials symmetry.

Cubical elasticity

The material models presented have cubic basic cells which means that cubical elasticity (E_c, ν_c, and G_c) of the macro model (material model) can be determined by the following "theoretical FEM-experiments", see Appendix A, cubical elasticity. Only two experiments are needed. The cubic Young's modulus and the cubic Poisson's ratio are obtained from the "axial experiment" explained in Equation D1. The cubic shear modulus is obtained from the "shear experiment" explained in Equation D2. The results of the axial experiment can be checked by the "control experiment" explained in Equation D3 from which the (E_c,ν_c)-dependent cubic bulk modulus K_c can be obtained.

$$
\begin{array}{ll}
\textit{AXIAL EXPERIMENT} & \\[1ex]
\textit{Conditions:} & \varepsilon_x = \varepsilon_y = \varepsilon_{xy} = \varepsilon_{xz} = \varepsilon_{yz} = 0 \\[1ex]
\textit{Load:} & \varepsilon_z = 10^{-4} \\[1ex]
\textit{Responses:} & \sigma_x \,(= \sigma_y) \\[1ex]
\textit{Results:} & E_c = \dfrac{\sigma_z^2 - 2\sigma_x^2 + \sigma_x\sigma_z}{\varepsilon_z(\sigma_x + \sigma_z)} \quad ; \quad \nu_c = \dfrac{\sigma_x}{\sigma_x + \sigma_z}
\end{array}
\tag{D1}
$$

SHEAR EXPERIMENT

Conditions: $\varepsilon_x = \varepsilon_y = \varepsilon_z = \varepsilon_{xz} = \varepsilon_{yz} = 0$

Load: $\varepsilon_{XY} = 10^{-4}$ (D2)

Responses: σ_{XY}

Results: $G_c = \dfrac{\sigma_{xy}}{2\varepsilon_{xy}}$

Control experiment

Conditions: $\varepsilon_{xz} = \varepsilon_{xy} = \varepsilon_{xz} = \varepsilon_{yz} = 0$

Load: $\varepsilon_X = \varepsilon_Y = \varepsilon_Z = 10^{-4}$ (D3)

Responses: $\sigma_Z \ (= \sigma_X = \sigma_Y)$

Results: $K_c = \dfrac{\sigma_z}{3\varepsilon_z} \quad \left[= \dfrac{E_c}{3(1 - 2\nu_c)} \right]$

Isotropy

Isotropic material models can be thought of as isotropic mixtures of parts from cubic model sources. These sources may have different sizes of composite elements which allows for size graduation in the total composite. Isotropic stiffness is converted from cubic stiffness by Equations D4 and D5 reproduced from Appendix A, poly-cubic elasticity. The isotropic bulk modulus is calculated exact. The isotropic shear modulus is given by upper and lower g-bound solutions. In the present analysis the bounds are sufficiently close to justify a simple mean value approximation.

$$K = K_c = \frac{E_c}{3(1 - 2\nu_c)}$$ (D4)

$$\left[\frac{1}{G_c} + \frac{2}{5} \left[\frac{2(1 + \nu_c)}{E_c} - \frac{1}{G_c} \right] \right]^{-1} \leq G \leq G_c + \frac{2}{5} \left[\frac{E_c}{2(1 + \nu_c)} - G_c \right]$$ (D5)

Composite models and analysis

Particulate composite (DC-DC)

The so-called TROC-composite outlined in Figures D1 and D2 is considered. It is a tight composition of identical composite elements each of which has the shape of a TRuncated OCtahedron with edges of equal lengths. The composite element is reinforced by a centrally placed particle the shape and orientation of which are similar to the composite element itself.
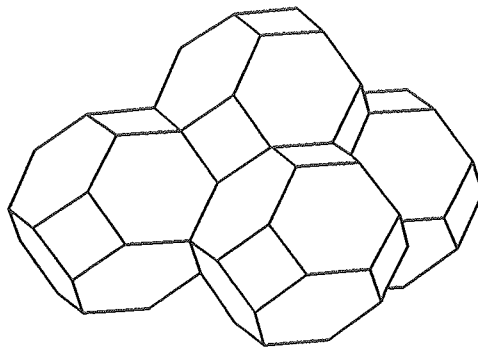
Figure D1. Stacked TROC-elements. Distance between square faces of element is 1.
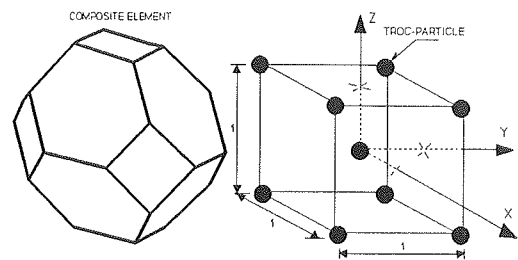
Figure D2. TROC-composite: Composite element and basic cell. Length unit 1 is heigth of composite element.

Test volume and FEM-division

Due to symmetry and antimetry with respect to both materials model and the FEM-setup, subsequently explained, a test volume of only 1/16 of the basic cell is used in the stiffness analysis of TROC-composites. The test volume and basic cell are shown in Figure D3. Another illustration of the test volume is shown in Figure D4 with coordinate system and symbols introduced which define the FEM-division subsequently used.

With θ and θ' as points of affinity the test volume is divided into 2 times 13 layers affine to the surfaces C'B'EABDD' and CBEA'B'D'D respectively, see Figure D5. Thickness of layers can be chosen arbitrarily. By taking the factors of affinity as independent variables this feature gives us the possibility of choosing an arbitrary volume concentration of particles (defined as the area inside a layer).

Every layer is then subdivided into finite elements as shown in Figure D6. The elements used are isoparametric and of the types IPLS and TRIP defined in (23), see Figure D7. The total amount of finite elements in the basis element is 738 with 948 sets of joint coordinates. The supporting joints in planes AA'θ'C and

219

A'C'θ' are modified by infinitely stiff bars to pick up reaction forces on the test volume. The version of the finite element program applied, STRUDL (23), is unable to give reactions directly from finite element joints.
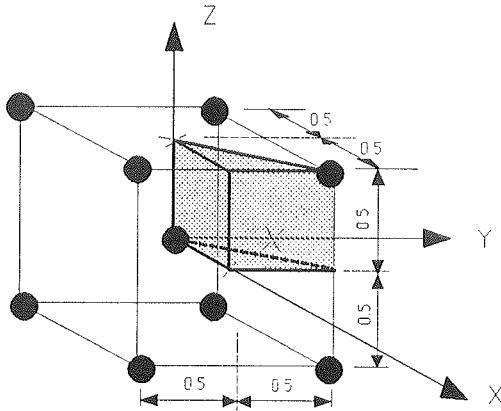
Figure D3. *Basic cell and test volume for FEM-analysis of TROC-composite*
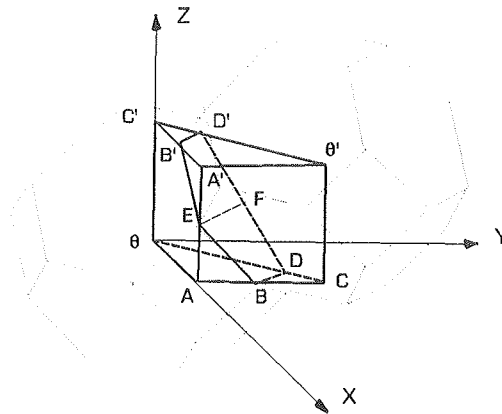
Figure D4. *Test volume for FEM-analysis of TROC-composite.*
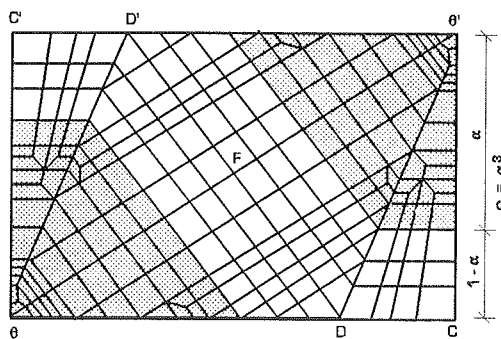
Figure D5. *FEM-division of test volume in X = Y. Shaded areas are TROC-particles. Arbitrarily chosen phase P concentration c. (As illustrated c ≈ 0.34).*
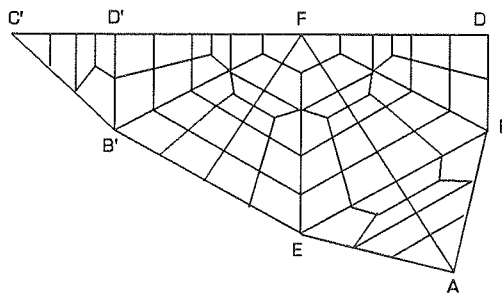
Figure D6. *Principle of FEM-division of test volume. Unfolded surface of TROC-element.*
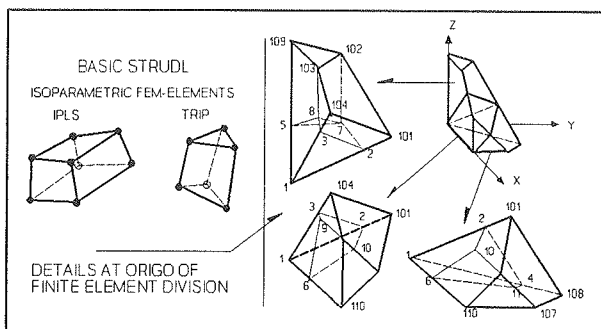
Figure D7. *FEM-elements used and some combinations.*

220

A detailed description of the finite element division is given in (16). This reference also describes a program which is developed to generate automatically the 1255 sets of joint coordinates needed when changing the particle concentration (factors of affinity).

FEM-setup

The following set-ups are designed to execute the experiments outlined in E-quations D1-D3. The average strain is joint movement divided by associated length (0.5) of test volume, see Figure D3. The average stress is sum of bar forces divided by associated surface area of test volume.

AXIAL EXPERIMENT

Conditions: All joints in faces of test volume are smoothly supported against infinitely stiff parallel walls.

Load: Joints in face $A\theta C$ are moved $0.5*10^{-4}$ in Z-direction.

Response: Sum of Z-forces picked up from bars in face $A'C'\theta'$

SHEAR EXPERIMENT

Conditions: All joints in faces of test volume except $A\theta C'A'$ and $AA'\theta'C$ are smoothly supported against infinitely stiff parallel walls. The joints in face $A\theta C'A'$ can move freely only in Y-direction. Joints in $AA'\theta'C$ can move freely only in X-direction.

Load: All joints in face $A\theta C'A'$ are moved $0.5*10^{-4}$ in X-direction.

Response: Sum of Y-forces picked up from bars in face $AA'\theta'C$

CONTROL EXPERIMENT (spot checks only)

Conditions: As in axial experiment.

Load: Joints in face $A\theta C$ are moved $0.5*10^{-4}$ in Z-direction. Face $AA'\theta'C$ is moved $-0.5*10^{-4}$ in X-direction.

Response: Sum of Z-forces picked up from bars in face $A'C'\theta'$

FEM-results

A number of FEM-experiments have been made varying the stiffness parameters and the volume concentrations (see Figure D5) of the TROC-model. The variables are summarized as follows:

Variables: $c = 0.22 - 0.86$, $\nu_s = 0 - 0.4$, $\nu_p = 0 - 0.4$, $n = 0 - 10^5$

The raw data obtained from the axial experiment (σ_X, σ_Y) and the shear experiment (σ_{XY}) are presented in Table D1. Cubic stiffness parameters derived from these

data by Equations D2 and D3 are presented in Table D2. Isotropic stiffness parameters derived from Equations D4 and D5 are presented in Table D3.

n	c	E_s	ν_s	ν_s	σ_x	σ_z	σ_{xy}
.0	.216	8.e5	.2	.2	14.71278	55.06929	43.23578
.0	.343	8.e5	.2	.2	11.68733	40.53782	32.33229
.0	.512	8.e5	.2	.2	8.29173	25.76719	20.28353
.0	.729	8.e5	.0	.2	2.19976	11.43127	10.40773
.0	.729	8.e5	.2	.2	4.35933	12.12563	8.88100
.0	.729	8.e5	.4	.2	7.97351	14.75839	7.93490
.0	.8574	8.e5	.0	.2	1.22059	5.55475	4.76655
.0	.8574	8.e5	.2	.2	2.21903	5.84648	4.02942
.0	.8574	8.e5	.4	.2	3.78670	6.93173	3.55923
1/14	.729	2.e5	.4	.0	2.02856	5.30578	3.56397
.1	.512	2.e5	.2	.2	2.46370	8.63511	6.71724
1/3	.512	2.e5	.2	.2	3.36936	13.00879	9.92820
1/3	.729	2.e5	.2	.2	2.64806	10.24968	7.79571
1.	.5	6.e5	.2	.2	16.68391	66.73593	50.05188
3.	.216	2.e5	.2	.2	6.95928	27.63501	20.93380
3.	.512	2.e5	.2	.2	9.49556	37.53126	28.90596
3.	.729	2.e5	.2	.2	12.03125	47.74705	36.73804
10.	.512	2.e5	.2	.2	13.90655	54.83788	44.99459
10.	.729	2.e5	.2	.2	22.24486	89.02735	73.71604
35/3	.729	2.e5	.2	.4	39.03639	105.92799	73.82064
100.	.512	2.e5	.2	.2	17.21308	68.72851	60.51260
100.	.729	2.e5	.2	.2	33.13180	138.70803	128.49007
1.e5	.729	2.e5	.0	.2	21.06033	145.07626	144.18834
1.e5	.729	2.e5	.2	.2	35.15577	147.93230	140.50922
1.e5	.729	2.e5	.4	.2	107.13340	237.20075	197.75796

Table D1. Reaction stresses (kp/cm^2) in experiments on plain TROC-composite. Axial σ_X and σ_Y. Shear: σ_{XY}.

n	c	ν_s	ν_P	E_{CUB}/E_s	ν_{CUB}	G_{CUB}/G_s
.00000	.21600	.20000	.20000	.61082	.21084	.64854
.00000	.34300	.20000	.20000	.44134	.22379	.48498
.00000	.51200	.20000	.20000	.27162	.24345	.30425
.00000	.72900	.00000	.20000	.13402	.16138	.13010
.00000	.72900	.20000	.20000	.12275	.26444	.13321
.00000	.72900	.40000	.20000	.11456	.35076	.13886
.00000	.85740	.00000	.20000	.06394	.18015	.05958
.00000	.85740	.20000	.20000	.05782	.27513	.06044
.00000	.85740	.40000	.20000	.05320	.35329	.06229
.07143	.72900	.40000	.00000	.20918	.27658	.24948
.10000	.51200	.20000	.20000	.37707	.22198	.40303
.33330	.51200	.20000	.20000	.58112	.20572	.59569
.33330	.72900	.20000	.20000	.45812	.20531	.46774
1.00000	.50000	.20000	.20000	1.00104	.20000	1.00104
3.00000	.21600	.20000	.20000	1.24175	.20117	1.25603
3.00000	.51200	.20000	.20000	1.68483	.20192	1.73436
3.00000	.72900	.20000	.20000	2.14521	.20126	2.20428
10.00000	.51200	.20000	.20000	2.46057	.20229	2.69968
10.00000	.72900	.20000	.20000	4.00666	.19991	4.42296
11.66700	.72900	.20000	.40000	4.24522	.26928	4.42924
100.00000	.51200	.20000	.20000	3.09167	.20029	3.63076
100.00000	.72900	.20000	.20000	6.29660	.19281	7.70940
100000.00000	.72900	.00000	.20000	6.98684	.12677	7.20942
100000.00000	.72900	.20000	.20000	6.72157	.19202	8.43055
100000.00000	.72900	.40000	.20000	8.52677	.31113	13.84306

Table D2. Cubic stiffness of plain TROC-composite.

222

n	c	ν_s	ν_p	G/G_s	K/K_s	E/E_s	ν
.00000	.21600	.20000	.20000	.63054 .63126	.63371 -	.63117 .63175	.20120 .20093
.00000	.34300	.20000	.20000	.46265 .46409	.47934	.46590 .46707	.20842 .20768
.00000	.51200	.20000	.20000	.28588 .28740	.31763	.29171 .29298	.22448 .22328
.00000	.72900	.00000	.20000	.12379 .12422	.19788	.14144 .14181	.14262 .14168
.00000	.72900	.20000	.20000	.12598 .12653	.15633	.13107 .13154	.24848 .24757
.00000	.72900	.40000	.20000	.13004 .13081	.07676	.12429 .12495	.33808 .33723
.00000	.85740	.00000	.20000	.05730 .05742	.09995	.06680 .06691	.16584 .16258
.00000	.85740	.20000	.20000	.05788 .05803	.07713	.06092 .06105	.26307 .26254
.00000	.85740	.40000	.20000	.05917 .05939	.03626	.05678 .05697	.34343 .34291
.07143	.72900	.40000	.00000	.24104 .24145	.09363	.21814 .21846	.26701 .26668
.10000	.51200	.20000	.20000	.38926 .38993	.40688	.39266 .39321	.21048 .21008
.33330	.51200	.20000	.20000	.58864 .58876	.59243	.58939 .58949	.20154 .20149
.33330	.72900	.20000	.20000	.46301 .46308	.46637	.46368 .46374	.20173 .20170
1.00000	.50000	.20000	.20000	1.00104 1.00104	1.00104	1.00104 1.00104	.20000 .20000
3.00000	.21600	.20000	.20000	1.24979 1.24983	1.24661	1.24915 1.24919	.19939 .19938
3.00000	.51200	.20000	.20000	1.71309 1.71347	1.69567	1.70958 1.70988	.19754 .19749
3.00000	.72900	.20000	.20000	2.17933 2.17975	2.15429	2.17428 2.17461	.19722 .19717
10.00000	.51200	.20000	.20000	2.59657 2.60216	2.47953	2.57229 2.57667	.18878 .18825
10.00000	.72900	.20000	.20000	4.24660 4.25656	4.00551	4.19609 4.20386	.18573 .18514
11.66700	.72900	.20000	.40000	4.25302 4.26294	5.52002	4.45765 4.46637	.25774 .25726
100.00000	.51200	.20000	.20000	3.39367 3.41482	3.09464	3.32933 3.34559	.17725 .17567
100.00000	.72900	.20000	.20000	7.09358 7.15947	6.14915	6.88218 6.93169	.16424 .16182
100000.00000	.72900	.00000	.20000	6.76900 6.80597	9.35985	7.45705 7.48692	.10165 .10005
100000.00000	.72900	.20000	.20000	7.67556 7.76497	6.54732	7.41984 7.48650	.16002 .15697
100000.00000	.72900	.40000	.20000	11.45786 11.94772	4.51468	10.39236 10.76603	.26981 .26153

Table D3. Poly-cubic stiffness bounds for plain TROC-composite.

223

Defective particulate composite

Particulate composites with defective phase contact are considered in a FEM-analysis just as the TROC-material. A thin layer of "voids" (or zones of missing phase contact), however, is spread over the surface of the particle phase covering several fractions of the total surface. The degree of missing phase contact is defined by Equation D6 where S denotes particle surface.

$$\chi = S_{inactive}/S_{total} \quad \textit{degree of missing phase contact}$$
$$c_a = \chi c[(1 + \Delta)^3 - 1] \quad \textit{associated void volume} \tag{D6}$$

Each zone of missing phase contact may be covered by a void of uniform thickness Δ (relative to mean radius vector of particle) which is related to void concentration c_a (relative to composite volume) and χ as given in Equation D6.

Remark: The zones of missing contact are introduced into FEM-analysis by simple joint-cutting and by finite elements of no stiffness. Sufficient openings are assumed between opposite zone faces such that load does not produce closure effects.

FEM-setup and results

The FEM models used have an area of missing phase contact centrally placed on each of the 6-edge faces (N = 8) or on each of the 4-edge faces (N = 6) of the TROC-particle. A number of FEM-experiments have been made varying the stiffness parameters, the volume concentrations (see Figure D5) and degree (α) of missing phase contact. The variables are summarized as follows:

$$\textit{Variables:} \quad c = 0.25, \nu_s = \nu_p = 0.2, n = 0.1\text{-}10, \chi = 22\%\text{-}78\%, c_a = 0\text{-}6\%$$
$$c = 0.42, \nu_s = \nu_p = 0.2: n = 1\text{-}10 \text{ with } \chi = 42\% \text{ and } c_a = 4.1\%$$

The raw data obtained from the axial experiment (σ_X, σ_Y) and the shear experiment (σ_{XY}) are presented in Table D4. Cubic stiffness parameters derived from these data by Equations D2 and D3 are presented in Table D5. Isotropic stiffness parameters derived from Equations D4 and D5 are presented in Table D6.

Defects as cracks

$\chi = 78$ % corresponds to no contact at all between matrix and 6-edge faces of particle. $\chi = 0.224$ corresponds to no contact at all between matrix and 4-edge faces of particle.

224

The defective areas including voids corespond to short hollow cylindrical fibres the characteristics of which can be calculated by Equation D7. H is height of composite element, h is corresponding height of inclusion. N = 8 for number of 6-edge faces per TROC-particle. N = 4 for number of 4-edge faces per TROC-particel.

Fibre diameter: d (diameter of void)
Fibre aspect ratio: A = l/d (l is length of fibre = thickness of void)
Crack density: p (number of cracks per volume unit)
Crack parameter: pd^3 (easily calculated by (16))

$$d = h * \sqrt{\frac{3\chi}{8\pi}\left(1 + 2\sqrt{3}\right)} \quad where \quad h = H * \sqrt[3]{c} \quad (crack\ diameter)$$

$$p = \frac{2Nc}{h^3} \quad (crack\ density) \quad \Rightarrow \quad pd^3 = 2N * c * \left[\frac{3\chi}{8\pi}\left(1 + 2\sqrt{3}\right)\right]^{3/2} \quad (D7)$$

$$A = \frac{4\chi c}{\pi pd^3}\left[(1 + A)^3 - 1\right] \quad\quad (aspect\ ratio)$$

A cracked homogeneous material

A 'defective particulate composite' with a stiffness ratio of n = 1 is of special interest because this composite is, in fact, a cracked homogeneous material. One such material with cracks placed on the 8-edge faces of fictitious TROC-particles is defined in Equation D8. The crack characteristics (pd^3,A) are calculated by Equation D7 with geometrical information introduced from Table D6. The (cracked) materials stiffness associated (E/E_s) is also shown in Equation D8.

$$(c, N, \chi, \Delta) = (0.25, 8, 0.3128, 0) \quad \Rightarrow \quad \begin{cases} pd^3 = 0.272 \\ A = 0 \\ E/E_s = 0.96 \end{cases}$$

$$(c, N, \chi, \Delta) = (0.25, 8, 0.3128, 0.1111) \quad \Rightarrow \quad \begin{cases} pd^3 = 0.272 \\ A = 0.136 \\ E/E_s = 0.92 \end{cases} \quad (D8)$$

$$(c, N, \chi, \Delta) = (0.422, 8, 0.497, 0.067) \quad \Rightarrow \quad \begin{cases} pd^3 = 0.92 \\ A = 0.0623 \\ E/E_s = 0.82 \end{cases}$$

n	c	E_s	χ	N	Δ	c_A	σ_x	σ_z	σ_{xy}
0.1	0.25	3.e5	0.0	8.	0.0	0.0	5.64187	21.4337	16.6075
0.1	0.25	3.e5	0.3128	8.	0.0	0.0	5.52754	21.0901	16.4699
0.1	0.25	3.e5	0.3128	8.	0.1111	0.0252	5.30531	20.3145	15.7044
0.1	0.25	3.e5	0.7760	8.	0.0	0.0	5.31115	20.2065	15.8471
0.1	0.25	3.e5	0.7760	8.	0.1111	0.0596	4.78016	18.0350	13.9938
1.0	0.25	3.e5	0.3128	8.	0.0	0.0	7.63060	31.7567	24.1558
1.0	0.25	3.e5	0.3128	8.	0.1111	0.0252	7.47874	30.5322	23.1879
2.3333	0.25	3.e5	0.2240	6.	0.1111	0.0232	9.07449	37.0004	28.4921
2.3333	0.25	3.e5	0.3128	8.	0.0	0.0	9.13265	38.5681	29.4133
2.3333	0.25	3.e5	0.3128	8.	0.1111	0.0252	8.91010	37.0617	28.1979
2.3333	0.25	3.e5	0.7760	8.	0.0	0.0	6.43111	31.9672	24.7755
2.3333	0.25	3.e5	0.7760	8.	0.0317	0.0170	6.47292	30.8845	23.9469
2.3333	0.25	3.e5	0.7760	8.	0.1111	0.0596	6.47904	29.4582	22.6830
10.	0.25	3.e5	0.0	8.	0.0	0.0	12.9076	50.7740	39.5445
10.	0.25	3.e5	0.3128	8.	0.0	0.0	11.2129	47.9405	37.4999
10.	0.25	3.e5	0.3128	8.	0.1111	0.0252	10.7837	46.0183	35.7760
10.	0.25	3.e5	0.7760	8.	0.0	0.0	6.93955	38.9623	30.7241
10.	0.25	3.e5	0.7760	8.	0.1111	0.0596	7.15779	35.4200	27.2428
1.	0.422	3.e5	0.497	8.	0.067	0.041	6.37132	26.7849	20.6577
10.	0.422	3.e5	0.497	8.	0.067	0.041	11.1205	53.4810	41.3576

Table D4. *Reaction stresses (kp/cm^2) in experiments on defective TROC-composite. Axial σ_X and σ_Y. Shear: σ_{XY}.*

n	c	χ	Δ	c_A	E_{CUB}/E_S	ν_{CUB}	G_{CUB}/G_S
.100000	.25000	.00000	.00000	.00000	.63608	.20837	.66430
.100000	.25000	.31280	.00000	.00000	.62648	.20766	.65880
.100000	.25000	.31280	.11110	.02520	.60391	.20708	.62818
.100000	.25000	.77600	.00000	.00000	.59985	.20814	.63388
.100000	.25000	.77600	.11110	.05960	.53440	.20952	.55975
1.000000	.25000	.31280	.00000	.00000	.96000	.19373	.96623
1.000000	.25000	.31280	.11110	.02520	.91964	.19675	.92752
2.333300	.25000	.22400	.11110	.02320	1.11420	.19695	1.13968
2.333300	.25000	.31280	.00000	.00000	1.16904	.19146	1.17653
2.333300	.25000	.31280	.11110	.02520	1.12026	.19382	1.12792
2.333300	.25000	.77600	.00000	.00000	.99377	.16748	.99102
2.333300	.25000	.77600	.03170	.01700	.95471	.17327	.95788
2.333300	.25000	.77600	.11110	.05960	.90407	.18029	.90732
10.000000	.25000	.00000	.00000	.00000	1.51805	.20269	1.58178
10.000000	.25000	.31280	.00000	.00000	1.45632	.18956	1.50000
10.000000	.25000	.31280	.11110	.02520	1.39746	.18985	1.43104
10.000000	.25000	.77600	.00000	.00000	1.22880	.15118	1.22896
10.000000	.25000	.77600	.11110	.05960	1.10045	.16811	1.08971
1.000000	.42200	.49700	.06700	.04100	.81121	.19216	.82631
10.000000	.42200	.49700	.06700	.04100	1.65508	.17214	1.65430

Table D5. *Cubic stiffness of defective TROC-composite.*

n	c	χ	Δ	c_A	G/G_s	K/K_s	E/E_s	ν
.100000	.25000	.00000	.00000	.00000	.65085	.65435	.65155	.20128
					.65125		.65187	.20114
.100000	.25000	.31280	.00000	.00000	.64378	.64290	.64361	.19967
					.64428		.64400	.19949
.100000	.25000	.31280	.11110	.02520	.61675	.61850	.61710	.20068
					.61705		.61734	.20056
.100000	.25000	.77600	.00000	.00000	.61809	.61658	.61778	.19941
					.61866		.61824	.19919
.100000	.25000	.77600	.11110	.05960	.54754	.55191	.54841	.20190
					.54793		.54872	.20173
1.000000	.25000	.31280	.00000	.00000	.96576	.94036	.96057	.19355
					.96576		.96057	.19355
1.000000	.25000	.31280	.11110	.02520	.92536	.90979	.92220	.19591
					.92537		.92221	.19591
2.333300	.25000	.22400	.11110	.02320	1.13052	1.10299	1.12490	.19404
					1.13063		1.12499	.19402
2.333300	.25000	.31280	.00000	.00000	1.17689	1.13667	1.16862	.19157
					1.17689		1.16862	.19157
2.333300	.25000	.31280	.11110	.02520	1.12717	1.09764	1.12114	.19358
					1.12718		1.12114	.19358
2.333300	.25000	.77600	.00000	.00000	1.00297	.89659	.97972	.17218
					1.00319		.97989	.17213
2.333300	.25000	.77600	.03170	.01700	.96523	.87661	.94610	.17622
					.96531		.94616	.17620
2.333300	.25000	.77600	.11110	.05960	.91202	.84833	.89853	.18225
					.91206		.89856	.18224
10.000000	.25000	.00000	.00000	.00000	1.55423	1.53178	1.54969	.19649
					1.55493		1.55025	.19638
10.000000	.25000	.31280	.00000	.00000	1.48748	1.40733	1.47073	.18648
					1.48764		1.47085	.18646
10.000000	.25000	.31280	.11110	.02520	1.42230	1.35171	1.40760	.18760
					1.42238		1.40766	.18758
10.000000	.25000	.77600	.00000	.00000	1.24923	1.05683	1.20534	.15784
					1.24974		1.20572	.15773
10.000000	.25000	.77600	.11110	.05960	1.10566	.99471	1.08154	.17381
					1.10602		1.08181	.17373
1.000000	.42200	.49700	.06700	.04100	.82237	.79055	.81581	.19042
					.82240		.81583	.19041
10.000000	.42200	.49700	.06700	.04100	1.67012	1.51444	1.63648	.17583
					1.67035		1.63665	.17579

Table D6. Poly-cubic stiffness bounds for defective TROC-composite.

Pearls on a string composite (CC-CC)

The FEM-analysis of a TROC-material is also used in an analysis of composites where particles have grown together changing phase P from being discrete to being continuous like pearls on a string - or in other words, from being a *closed "pore" system* to being an *open "pore" system*.

FEM-setup and results

FEM-setup is as explained in Figures D1 - D7. The "pearls on a string" geometry of phase P is obtained by interconnecting the TROC-particles between the 6-edge faces of the TROC-particles. Cylindrical tunnels are formed by letting the finite elements between particles, see Figure D5, take the properties of the particles. The volume fraction of phase P TROC-particles relative to total phase P volume (both TROC and tunnels) is denoted by α.

A number of FEM-experiments have been made on Pearls on a string composites defined as follows:

Variables: $c = 0.36$, $\alpha = 60\%$, $\nu_s = \nu_p = 0.2$: $n = 0$ - 10
      $c = 0.45$, $\alpha = 76\%$, $\nu_s = \nu_p = 0.2$: $n = 0$ and 100
      $c = 0.67$, $\alpha = 76\%$, $\nu_s = \nu_p = 0.2$: $n = 0$ - 100

The raw data obtained from the axial experiment (σ_x, σ_y) and the shear experiment (σ_{xy}) are presented in Table D7. Cubic stiffness parameters derived from these data by Equations D2 and D3 are presented in Table D8. Isotropic stiffness parameters derived from Equations D4 and D5 are presented in Table D9.

228

n	c	$\alpha(\%)$	E_s	ν_s	ν_s	σ_x	σ_z	σ_{xy}
0.	.36	60.	8.e5	.2	.2	8.34233	36.98560	24.36056
.333333	.36	60.	2.e5	.2	.2	3.78127	15.24916	11.37820
3.	.36	60.	2.e5	.2	.2	8.49105	32.80770	25.30464
10.	.36	60.	2.e5	.2	.2	16.42488	51.60347	45.69911
1.e-5	.451	76.	2.e5	.2	.2	1.729845	7.21862	4.77155
100.	.451	76.	2.e5	.2	.2	124.22087	286.63932	321.55018
1.e-5	.674	76.	2.e5	.2	.2	0.65792	3.43617	1.46436
.333333	.674	76.	2.e5	.2	.2	2.66456	10.89348	7.99115
3.	.674	76.	2.e5	.2	.2	11.67492	46.63378	35.29817
10.	.674	76.	2.e5	.2	.2	28.42779	107.75521	86.38002
100.	.674	76.	2.e5	.2	.2	229.42133	770.07510	679.22262

Table D7. Reaction stresses (kp/cm²) in experiments on Pearls on a String TROC-composite. Axial σ_x and σ_y. Shear: σ_{xy}.

n	c	$\alpha(\%)$	ν_s	ν_p	E_{CUB}/E_s	ν_{CUB}	G_{CUB}/G_s
.00000	.36000	60.	.20000	.20000	.42394	.18404	.36541
.33333	.36000	60.	.20000	.20000	.68733	.19870	.68269
3.00000	.36000	60.	.20000	.20000	1.46581	.20560	1.51828
10.00000	.36000	60.	.20000	.20000	2.18361	.24144	2.74195
.00001	.45100	76.	.20000	.20000	.32749	.19331	.28629
100.00000	.45100	76.	.20000	.20000	10.57623	.30234	19.29301
.00001	.67400	76.	.20000	.20000	.16124	.16070	.08786
.33333	.67400	76.	.20000	.20000	.49231	.19653	.47947
3.00000	.67400	76.	.20000	.20000	2.09793	.20023	2.11789
10.00000	.67400	76.	.20000	.20000	4.79434	.20875	5.18280
100.00000	.67400	76.	.20000	.20000	33.23769	.22954	40.75335

Table D8. Cubic stiffness of Pearls on a String TROC-composite.

n	$c(\alpha\%)$	ν_s	ν_p	G/G_s	K/K_s	E/E_s		ν
.00000	.360(60)	.20000	.20000	.38865	.40253	.39135		.20833
				.39110		.39334		.20685
.33333	.360(60)	.20000	.20000	.68483	.68435	.68474		.19983
				.68484		.68475		.19983
3.00000	.360(60)	.20000	.20000	1.49400	1.49369	1.49394		.19995
				1.49457		1.49439		.19986
10.00000	.360(60)	.20000	.20000	2.44899	2.53360	2.46546		.20807
				2.48945		2.49816		.20420
.00001	.451(76)	.20000	.20000	.30208	.32035	.30557		.21384
				.30351		.30673		.21275
100.00000	.451(76)	.20000	.20000	13.86086	16.05243	14.24996		.23369
				15.47385		15.58620		.20871
.00001	.674(76)	.20000	.20000	.10836	.14256	.11382		.26048
				.11939		.12341		.24031
.33333	.674(76)	.20000	.20000	.48508	.48668	.48540		.20079
				.48518		.48548		.20074
3.00000	.674(76)	.20000	.20000	2.10970	2.09951	2.10765		.19884
				2.10975		2.10769		.19883
10.00000	.674(76)	.20000	.20000	5.00482	4.93832	4.99138		.19678
				5.01354		4.99831		.19636
100.00000	.674(76)	.20000	.20000	36.96384	36.86753	36.94454		.19937
				37.42770		37.31431		.19636

Table D9. Poly-cubic stiffness bounds for Pearls on a String TROC-composite.

Grid composite (CC-CC)

The so-called CROSS-composite shown in Figure D8 is considered. It is a phase symmetric cubic frame work of phase P embedded in a complementary cubic frame work of phase S. The composite element and the basic cell of a CROSS-composite are shown in Figure D9.
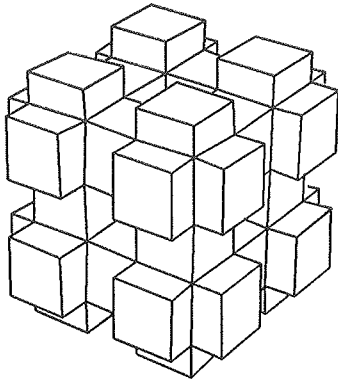
Figure D8. CROSS-com-pos-ite
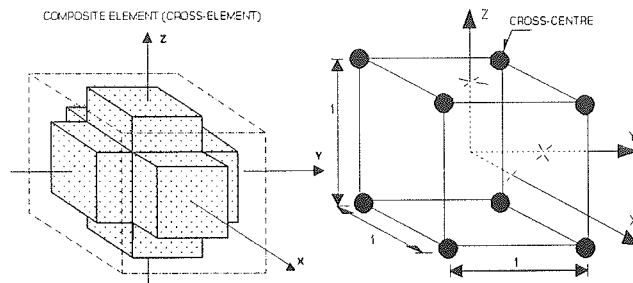
Figure D9. Composite element and basic cell for CROSS-composite. Both heights are 1.
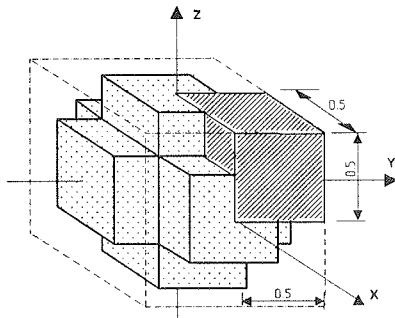
Figure D10. Shaded box is test volume for FEM-analysis. Length unit 1 is heigth of composite element.
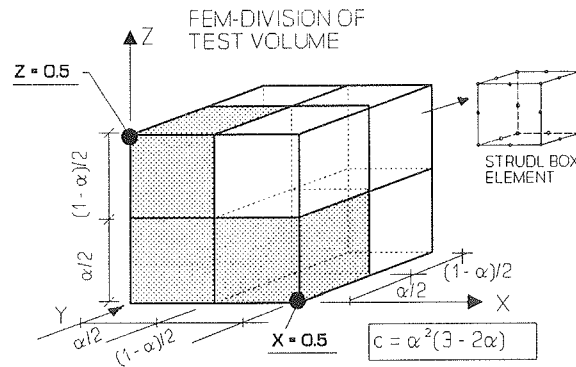
Figure D11. FEM-structure of test volume. Size of FEM-elements and phase P concentration (c) is regulated by $0 \le \alpha \le 1$ as indicated.

Test volume and FEM-division

Due to symmetry and antimetry with respect to both materials model and the FEM-setup, subsequently explained, a test volume of only 1/64 of the basic cell is used in the stiffness analysis of CROSS-composites. The composite element, basic cell and test volume are shown in Figures D9 and D10.

The very simple FEM-structure of the test volume shown in Figure D11 is made possible combining the cubic regularity of the composite element with very

230

refined STRUDL box type elements, see Figure D11, defined in (23). It is indicated in Figure D11 how volume concentrations (c) can be chosen arbitrarily in analysis.

The supporting joints in planes X = 1/2 and Z = 1/2 are modified by infinitely stiff bars to pick up reaction forces on the test volume. The version of the finite element program applied, STRUDL (23), is unable to give reactions directly from finite element joints.

FEM-setup

The following set-ups are designed to execute the experiments outlined in Equations D1-D3. The average strain is joint movement divided by associated length (0.5) of test volume, see Figure D10. The average stress is sum of bar forces divided by associated surface area (0.25) of test volume, see Figure 10 again.

AXIAL EXPERIMENT
Conditions: All joints in faces of test volume are smoothly supported against infinitely stiff parallel walls.
Load: Joints in face Z = 0 are moved $0.5*10^{-4}$ in Z-direction.
Response: Sum of Z-forces picked up from bars in face Z = 1/2.

SHEAR EXPERIMENT
Conditions: All joints in planes Z = 0 and Z = 1/2 are smoothly supported against infinitely stiff parallel walls. The joints in planes Y = 0 and Y = 1/2 can move freely only in Y-direction. Joints in X = 0 and X = 1/2 can move freely only in X-direction.
Load: All joints in plane Y = 0 are moved $0.5*10^{-4}$ in X-direction. All joints in X = 0 are moved $0.5*10^{-4}$ in Y-direction
Response: Sum of Y-forces picked up from bars in plane X = 1/2

CONTROL EXPERIMENT (spot checks only)
Conditions: As in axial experiment.
Load: Joints in plane Z = 0 are moved $0.5*10^{-4}$ in Z-direction. Joints in plane X = 0 are moved $0.5*10^{-4}$ in X-direction. Joints in plane Y = 0 are moved $0.5*10^{-4}$ in Y-direction.
Response: Sum of Z-forces picked up from bars in plane Z = 1/2 (= sum of X-forces picked up from bars in plane X = 1/2).

FEM-results

A number of FEM-experiments have been made varying the stiffness parameters and the volume concentrations, c, of the CROSS-model. The variables are summarized as follows:

Variables: c = 0.25 - 0.75, ν_P = ν_S = 0.2, n = 0 - 10³

The raw data obtained from the axial experiment (σ_X,σ_Y) and the shear experiment (σ_{XY}) are presented in Table D10. Cubic stiffness parameters derived from these data by Equations D2 and D3 are presented in Table D11. Isotropic stiffness parameters derived from Equations D4 and D5 are presented in Table D12.

n	c	E_S	ν_S	ν_S	σ_x	σ_z	σ_{xy}
5.e-6	.2522	2.e5	.2	.2	2.34360	12.2310	7.56482
.01	.2522	2.e5	.2	.2	2.42376	12.4551	7.79996
.1	.2522	2.e5	.2	.2	3.04553	14.1795	9.56759
.333333	.2522	2.e5	.2	.2	4.11096	17.2564	12.5175
3.	.2522	2.e5	.2	.2	7.10379	30.3116	21.5464
10.	.2522	2.e5	.2	.2	9.18508	49.9761	27.8779
100.	.2522	2.e5	.2	.2	27.1192	275.502	67.9144
1000.	.2522	2.e5	.2	.2	203.517	2515.67	443.012
0.	.5	2.e5	.2	.2	.830440	6.23841	2.45587
.001	.5	2.e5	.2	.2	.839332	6.26705	2.48726
.01	.5	2.e5	.2	.2	.918772	6.52110	2.76339
.1	.5	2.e5	.2	.2	1.64688	8.78233	5.11944
.333333	.5	2.e5	.2	.2	3.08359	13.3206	9.39984
1.	.5	2.e5	.2	.2	5.55480	22.2220	16.6656
10.	.5	2.e5	.2	.2	16.4687	87.8232	51.1945
0.	.7478	2.e5	.2	.2	.195981	2.48889	.416377
.01	.7478	2.e5	.2	.2	.271191	2.75504	.679140
.1	.7478	2.e5	.2	.2	.918508	4.99762	2.78779
1000.	.7478	2.e5	.2	.2	2351.29	12252.7	7588.46

Table D10. Reaction stresses (kp/cm²) in experiments on CROSS-composite. Axial σ_X and σ_Y. Shear: σ_{XY}.

n	c	ν_S	ν_P	E_{CUB}/E_S	ν_{CUB}	G_{CUB}/G_S
5.e-6	.25220	.20000	.20000	.57386	.16080	.45389
.01000	.25220	.20000	.20000	.58327	.16290	.46800
.10000	.25220	.20000	.20000	.65513	.17681	.57406
.33333	.25220	.20000	.20000	.78373	.19239	.75105
3.00000	.25220	.20000	.20000	1.38071	.18986	1.29278
10.00000	.25220	.20000	.20000	2.35620	.15526	1.67267
100.00000	.25220	.20000	.20000	13.53207	.08961	4.07486
1000.00000	.25220	.20000	.20000	124.26030	.07484	26.58072
.00000	.50000	.20000	.20000	.30216	.11748	.14735
.00100	.50000	.20000	.20000	.30344	.11811	.14924
.01000	.50000	.20000	.20000	.31471	.12349	.16580
.10000	.50000	.20000	.20000	.41311	.15791	.30717
.33333	.50000	.20000	.20000	.60807	.18798	.56399
1.00000	.50000	.20000	.20000	1.00002	.19997	.99994
10.00000	.50000	.20000	.20000	4.13110	.15791	3.07167
.00000	.74780	.20000	.20000	.12301	.07299	.02498
.01000	.74780	.20000	.20000	.13532	.08961	.04075
.10000	.74780	.20000	.20000	.23562	.15525	.16727
1000.00000	.74780	.20000	.20000	574.77850	.16100	455.30760

Table D11. Cubic stiffness of CROSS-composite.

n	c	ν_s	ν_p	G/G_s	K/K_s	E/E_s	ν
5.e-6	.25220	.20000	.20000	.50096	.50755	.50226	.20312
				.50963	-	.50921	.19901
.01000	.25220	.20000	.20000	.51371	.51908	.51477	.20249
				.52155	-	.52105	.19886
.10000	.25220	.20000	.20000	.60829	.60812	.60825	.19993
				.61165	-	.61094	.19861
.33333	.25220	.20000	.20000	.76568	.76435	.76541	.19958
				.76612	-	.76577	.19944
3.00000	.25220	.20000	.20000	1.33089	1.33558	1.33183	.20084
				1.33266	-	1.33324	.20052
10.00000	.25220	.20000	.20000	1.91519	2.05039	1.94078	.21604
				1.98256	-	1.99579	.20799
100.00000	.25220	.20000	.20000	5.74434	9.89221	6.27016	.30985
				8.40611	-	8.66650	.23717
1000.00000	.25220	.20000	.20000	39.28336	87.68112	44.15820	.34891
				71.44010	-	74.18846	.24616
.00000	.50000	.20000	.20000	.18851	.23698	.19655	.25117
				.21820	-	.22172	.21932
.00100	.50000	.20000	.20000	.19052	.23837	.19849	.25019
				.21981	-	.22328	.21899
.01000	.50000	.20000	.20000	.20796	.25076	.21531	.24242
				.23394	-	.23712	.21632
.10000	.50000	.20000	.20000	.34630	.36228	.34939	.21068
				.35555	-	.35688	.20448
.33333	.50000	.20000	.20000	.58306	.58463	.58338	.20064
				.58408	-	.58419	.20023
1.00000	.50000	.20000	.20000	.99998	.99992	1.00002	.19999
				.99998	-	1.00002	.19999
10.00000	.50000	.20000	.20000	3.46304	3.62282	3.49386	.21068
				3.55551	-	3.56877	.20448
.00000	.74780	.20000	.20000	.03714	.08643	.04192	.35448
				.07002	-	.07278	.24736
.01000	.74780	.20000	.20000	.05744	.09892	.06270	.30985
				.08406	-	.08667	.23717
.10000	.74780	.20000	.20000	.19152	.20504	.19408	.21604
				.19826	-	.19958	.20799
1000.00000	.74780	.20000	.20000	502.23610	508.65840	503.50760	.20304
				510.81840	-	510.38490	.19898

Table D12. Poly-cubic stiffness bounds for CROSS-composite.

On the accuracy of analysis

Approximately every second cubic bulk $K_c = E_c/(1 - 2\nu_c)$ obtained from axial experiments are checked by the control experiment explained in Equation D3. The results agree within the first five significant digits. The isotropic Young's modulus for n = 1 and $\nu_p = \nu_s = 0.2$ is calculated with an accuracy < 1 ‰. It is concluded from these observations that the FEM-partitioning used in the analysis is appropriate in general, and that numerical errors are very modest at moderate stiffness ratios.

In general no accurate error analysis can be made on the stiffness moduli predicted by FEM-analysis. Some valuable estimates on accuracy, however, can be

made at $\nu_P = \nu_S = 0.2$ from Equation D9 which is an adapted compilation of expressions presented in Equations 10.3 and 12.1 in the main text.

$$\theta_{FEM} = \frac{[n - c(n - 1)]e_{FEM} - n}{1 + c(n - 1) - e_{FEM}} \qquad \begin{bmatrix} n < \theta_{FEM} < 1 & at\ n < 1 \\ 1 < \theta_{FEM} < n & at\ n > 1 \end{bmatrix}$$

$$e_{FEM}(n,c) = \frac{1}{e_{FEM}(1/n,c)} \qquad (CSA_P) \qquad\qquad\qquad (D9)$$

$$e_{FEM}(n,c) = n * e_{FEM}(1/n,1-c) \qquad (Phase-symmetry)$$

- The former expression checks that no FEM results violate the H/S bounds. A high accuracy of the FEM-analysis is indicated by a continuous and smooth development of $\theta_{FEM}(c)$ at increasing stiffness ratios, n. Particulate composites will have $\theta_{FEM}(c)$ close to 1. Phase-symmetric composites will have $\theta_{FEM}(c)$ closer to $\sqrt{n}$.
- The second expression can be used to check the accuracy of the FEM-analysis of the TROC material assuming that this material behaves as a CSP_P composite
- The latter expression can be used to check the FEM-analysis of the CROSS material because this material is in fact phase-symmetric.

The TROC FEM-results (with $\nu_P = \nu_S = 0.2$) have been checked by the former expression in Equation D9. No violations of the H/S bounds were found (Figures D12 and D13). It was observed that $\theta_{FEM}(c)$ keeps very much to ≈ 1, meaning that the material tested behaves approximately as a CSA_P composite (Figure D14). An accuracy of about 1% is then calculated by the second expression in Equation D9.
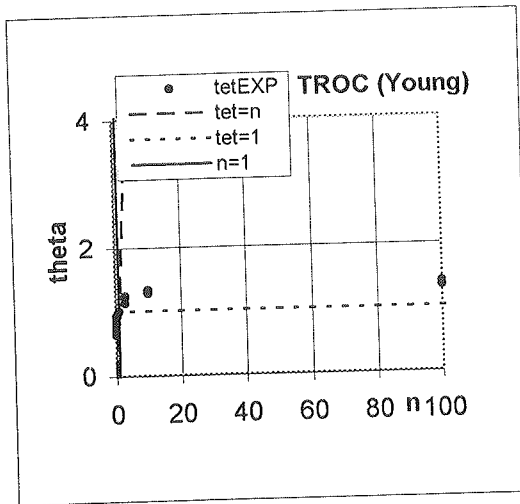

Figure D12. TROC-composite with $\nu_P = \nu_S = 0.2$: θ-test on FEM-data obtained to determine Young's modulus.
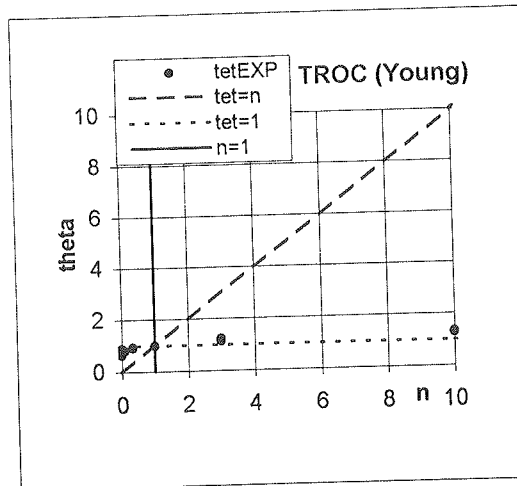
Figure D13. TROC-composite with $\nu_P = \nu_S = 0.2$: θ-test on FEM-data obtained to determine Young's modulus.

234

Also for the CROSS FEM-results (with $\nu_P = \nu_S = 0.2$), no violations of the H/S bounds were found (Figures D15 and D16). The phase-symmetric geometry is confirmed which means that an accuracy of « 1 % is calculated by the latter term in Equation D9.

Conclusion: From the above discussion is stated that only very modest errors are attached to the stiffness properties determined in this monograph by FEM-analysis.
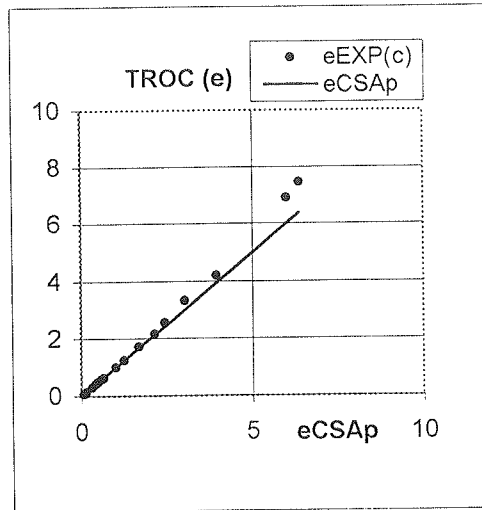

Figure D14. TROC-composite with $\nu_P = \nu_S = 0.2$: *FEM-Young's modulus compared with Young's modulus of CSA$_P$ composite.*
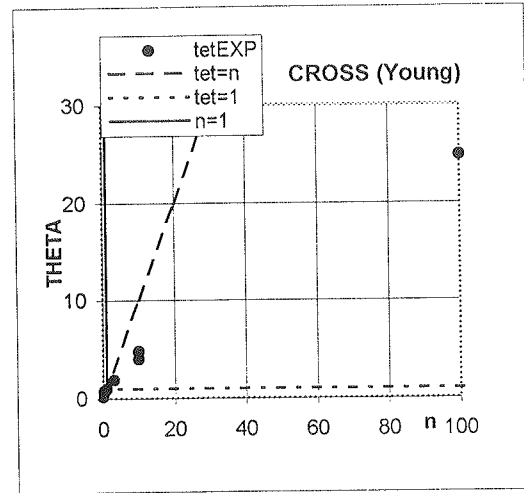

Figure D15. CROSS-composite with $\nu_P = \nu_S = 0.2$: *θ-test on FEM-data obtained to determine Young's modulus.*
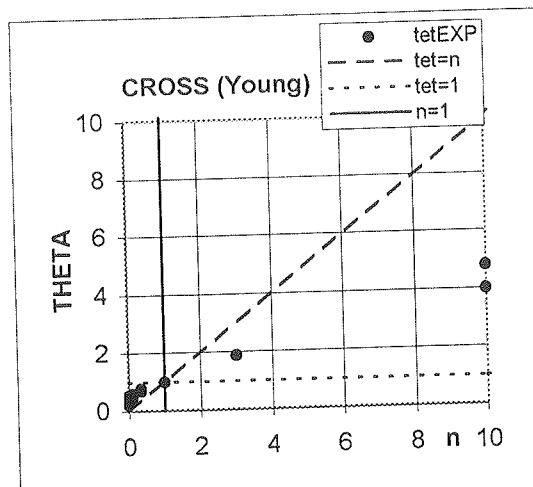
False data

Figure D16. CROSS-composite with $\nu_P = \nu_S = 0.2$: *θ-test on FEM-data obtained to determine Young's modulus.*

The following rule has been used to exclude false data (mistakes in tests or data treatment): If a description can be made which fits very well a large number of familiar data with only a few data as clear exceptions - then these data can be considered false. Only one false data set was found in this FEM-analysis, namely shear modulus g of the TROC-composite at $(n, \nu_S, \nu_P, c) = (10^5, 0.4, 0.2, 0.73)$. The reason for exclusion is obvious from Figure 9.5 in Chapter 9.

Appendix E - Complex shape functions

When composites are considered where shape function values are known better than just at c = 0, c_P, c_S, and 1 a more detailed description may be justified, for example as outlined in Table E1 and Figure E1.

MORE DETAILED SHAPE FUNCTIONS	
$\mu_P = \mu_P^o$ $\mu_S = \mu_S^o$	$0 \leq c < c_{SS}$
$\mu_P = \mu_P^o(c_S - c)/(c_S - c_{SS}) + \mu_{PS}(c - c_{SS})/(c_S - c_{SS})$ $\mu_S = \mu_S^o(c_S - c)/(c_S - c_{SS})$	$c_{SS} \leq c < c_S$
$\mu_P = \mu_{PS}(c_P - c)/(c_P - c_S)$ $\mu_S = \mu_{SP}(c - c_S)/(c_P - c_S)$	$c_S \leq c < c_P$
$\mu_P = \mu_P^1(c - c_P)/(c_{PP} - c_P)$ $\mu_S = \mu_{SP}(c_{PP} - c)/(c_{PP} - c_P) + \mu_S^1(c - c_P)/(c_{PP} - c_P)$	$c_P \leq c < c_{PP}$
$\mu_P = \mu_P^1$ $\mu_S = \mu_S^1$	$c_{PP} \leq c < 1$

Table E1. Special shape functions. The symbols used are explained in Figure E1. Shape factors $\mu_P^o, \mu_S^o, \mu_P^1, \mu_P^1$ are as determined from Section 7.1.
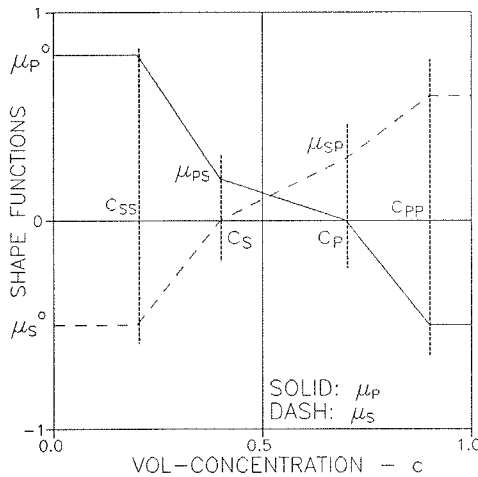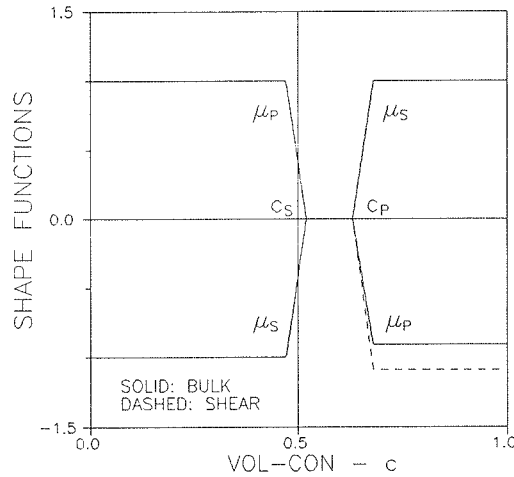

Figure E1. More detailed shape functions.

Figure E2. Detailed shape functions for special DC-CD composite defined in the main text. $(v_P, v_S) = (0.3, 0.2)$.

Example: Special DC-CD composite

A special fabrication technique has been developed such that the following DC-CD composite can be produced: Up to a concentration of c = 0.47 the geometry is that of discrete phase P spheres in a continuous phase S. From a concentration

236

of c = 0.68 the geometry is that of discrete phase S spheres in a continuous phase P. The agglomeration of P-spheres starts creating continuous phase P elements at c = 0.52. "De-agglomeration" of phase S into discrete spheres starts at c = 0.63. A skeletal microstructure defines the composite geometry in the transition area c = 0.52 - 0.63 where there is no clearly defined matrix and reinforcement phase.

These observations are enough to suggest a special shape function description defined by $(\mu_{PS}, \mu_{SP}) = (0,0)$ and $(c_{SS}, c_S, c_P, c_{PP}) = (0.47, 0.52, 0.63, 0.68)$. An example with $(\nu_P, \nu_S) = (0.3, 0.2)$ is presented in Figure E2.

Appendix F - General viscoelastic models

It can be shown (e.g. 2) that general mechanical models for viscoelastic materials can be established in two ways as illustrated in Table E1. One general model is a Maxwell model connected in series with a chain of several Kelvin models in series. E denotes momentary stiffness, E_{REV} denotes delayed stiffness and τ denotes relaxation time. The number of Kelvin elements can be finite (N) with creep functions consequently described as shown in Equation F1 - or it can be infinite in which case creep functions can be expressed as shown in Table F1 with continuously distributed Kelvin relaxation times considered by the so-called retardation spectrum, $L = L(\tau)$.

RETARDATION SPECTRUM L(τ)	RELAXATION SPECTRUM H(τ)
$L(\tau)$ with $\displaystyle\int_0^\infty \frac{L(\tau)}{\tau}d\tau = \frac{1}{E_{REV}}$	$H(\tau)$ with $\displaystyle\int_0^\infty \frac{H(\tau)}{\tau}d\tau = E - E_{REL}$

CREEP FUNCTION C(t)	RELAXATION FUNCTION R(t)
$\displaystyle\frac{1}{E} + \frac{t}{\eta} + \int_0^\infty \frac{L(\tau)}{\tau}\left[1 - EXP\left(-\frac{t}{\tau}\right)\right]d\tau$	$\displaystyle E_{REL} + \int_0^\infty \frac{H(\tau)}{\tau}EXP\left(-\frac{t}{\tau}\right)d\tau$

ANALOGY YOUNG'S MODULUS E^A(s)	
$\displaystyle\left[\frac{1}{E} + \frac{1}{\eta s} + \int_0^\infty \frac{L(\tau)}{\tau(1 + \tau s)}d\tau\right]^{-1} =$	$\displaystyle = E_{REL} + \int_0^\infty \frac{s\,H(\tau)}{1 + \tau s}d\tau$

Table F1. Complex viscoelastic models with spectra and analogy Young's moduli. Reproduced from (24).

The other general model is a Hooke model connected in parallel with a chain of several Maxwell models in parallel. E denotes momentary stiffness, E_{REL} denotes relaxed (final) stiffness and τ denotes relaxation time. The number of Maxwell elements can be finite (N) with relaxation functions consequently described as shown in Equation F1 - or it can be infinite in which case relaxation functions can

be expressed as shown in Table F1 with continuously distributed Maxwell relaxation times considered by the so-called relaxation spectrum, H = H(τ).

$$C(t) = \frac{1}{E} + \frac{t}{\eta} + \sum_{n=1}^{N} \frac{1}{E_n}\left[1 - EXP\left(-\frac{t}{\tau_n}\right)\right] \quad ; \quad Kelvin \ chain$$

$$R(t) = E_{REL} + \sum_{n=1}^{N} E_n \exp\left(-\frac{t}{\tau_n}\right) \quad ; \quad Maxwell \ chain$$

(F1)

The *Power Law model* introduced in Section 13.2.2 is a model which can only be explained by a composition of an infinite number of elementary mechanical elements. The spectra associated are presented in Table F2 reproduced from (25).

POWER LAW CREEP	
RETARDATION SPECTRUM L(τ)	**RELAXATION SPECTRUM H(τ)**
$\dfrac{Z(\tau)\sin(b\pi)}{\pi E}$	$\dfrac{E}{\pi} \dfrac{Z(\tau)\sin(b\pi)}{1 + Z(\tau)^2 + 2Z(\tau)\cos(b\pi)}$

Table F2. Power law creep. $Z(x) = \Gamma(1+b)(x/\tau_o)^b$ where Γ means gamma function. Reproduced from (25).

Remark: It is emphasized that the two spectra are not independent. They relate to each other as indicated by the two alternate expressions in Table F1 for the analogy Young's modulus. It is also emphasized that the results in Equation F1 can be predicted from Table F1 with discrete rheological spectra (retardation, relaxation). Most often the analysis of complex viscoelastic materials can only be made numerically. In this context should be mentioned that useful information on couplings between rheological characteristics of materials can be found in (fx 2,26,27,25).

Appendix G - Re-interpretation of flat and long shapes

We re-call from introductory remarks to Chapter 7 that the quantification of geometries made in this chapter is based very much on the cylindrical inclusions model. It is obvious that this model, strictly speaking, does not comply with the continuous description of geometry changes considered in this monograph. It shows, however, that this discrepancy is effectively compensated for by the geo-function, θ, introduced in Section 4.1.

This feature is illustrated in this appendix by comparing the 'dilute' phase P stresses obtained by the method presented in this monograph with the accurate stresses for strict fibres numerically developed in Appendix B. The former stresses are determined from Equation G1 reproduced from Section 4.3 with a particle P concentration of c = 0.

$$
\frac{\sigma^o_{Pkk}}{\sigma_{kk}} = n_k \frac{1 + \theta^o_k}{n_k + \theta^o_k} \quad and \quad \frac{S^o_{Pij}}{S_{ij}} = n_g \frac{1 + \theta^o_g}{n_g + \theta^o_g} \quad with
$$

$$
\theta^o_k = \frac{\kappa_s}{2}\left[\mu^o_{Pk} + N_k\mu^o_{Sk} + \sqrt{(\mu^o_{Pk} + N_k\mu^o_{Sk})^2 + 4N_k(1 - \mu^o_{Pk} - \mu^o_{Sk})}\right]
$$

$$
\theta^o_g = \frac{\gamma_s}{2}\left[\mu^o_{Pg} + N_g\mu^o_{Sg} + \sqrt{(\mu^o_{Pg} + N_g\mu^o_{Sg})^2 + 4N_g(1 - \mu^o_{Pg} - \mu^o_{Sg})}\right]
$$

(G1)

Remark: From a descriptive point of view, we introduce the term 'particles, preparing to become continuous' as a re-interpretation of strict cylindrical inclusions when discussing the role of particles in the history of a continuous geometry changes.

Flat shapes

Some results of comparing stresses in organic particles and in strict particles are shown in Figures G1-G6. We notice that CSA_s-shells ($\mu_{Pk}^o = -1$) have the same phase P stress as can be determined accurately for strict thin discs. This feature is consistent with the following observations:

From (9) can be deduced that the bulk modulus of a particulate composite with randomly distributed thin strict discs equals the bulk modulus (a H/S bound solution) which is predicted by the present theory for a CSA_s-composite. This means that the volumetric particle stresses, at identical volume concentrations (including c $\approx$ 0) are the same in thin strict discs and in spherical shells as these are defined in this monograph.
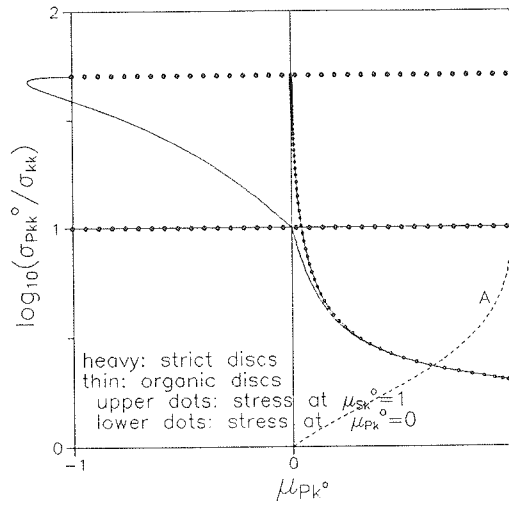
Figure G1. (n, v_P, v_S) = $(100, 0.2, 0.2)$.
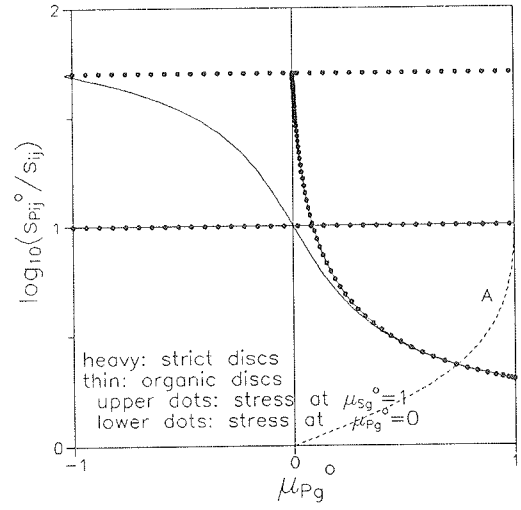Aspect ratio is indicated by A (0-1).

Figure G2. (n, v_P, v_S) = $(100, 0.2, 0.2)$.
Aspect rtion is indicated by A (0-1).

From Figures G7 and G8 is observed that accurate stress in strict discs become increasingly well predicted by the present method when very high stiffness ratios or very low stiffness ratios are approached. At such stiffness ratios this means that there will be no difference between accurately determined stiffness for particulate composites with strict discs, and stiffness determined by the present method assuming organic discs. This statement follows from Equation 3.6: If stress is accurate, then stiffness is accurate - and vice versa. Of course the observations just made are closely related to the procedure applied in Chapter 7 of letting n approach zero and infinity when shape factors are determined.
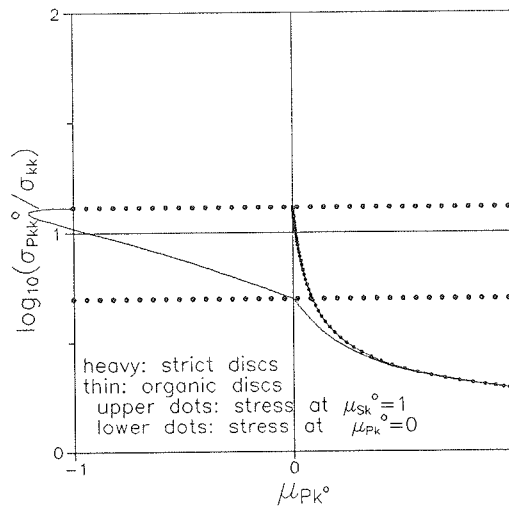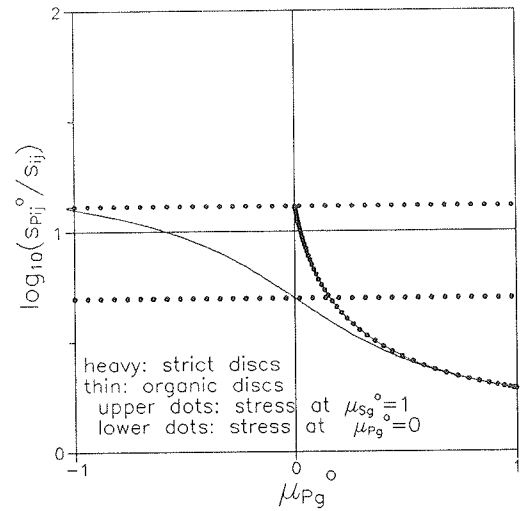

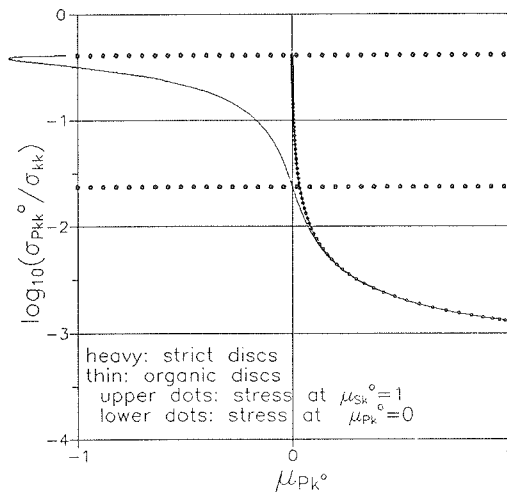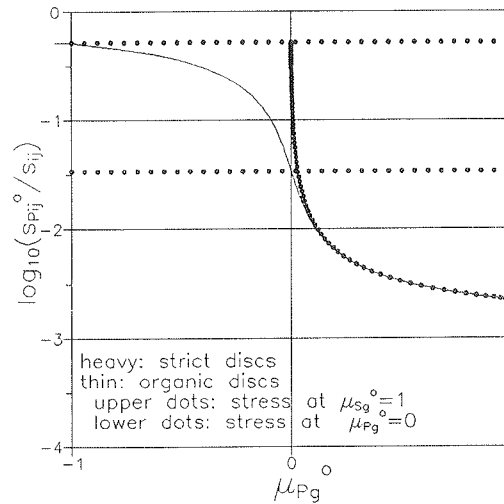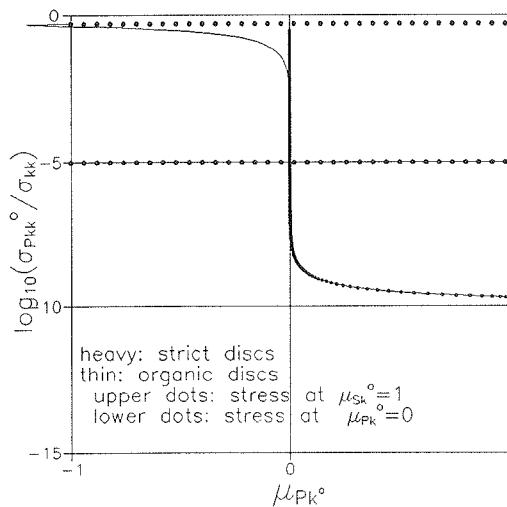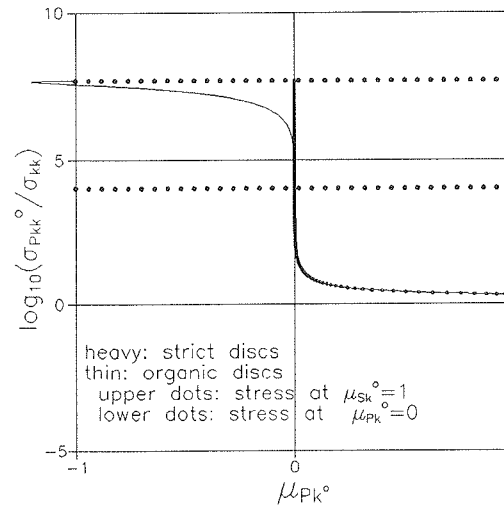**Figure G3.** (n, v_P, v_S) = $(25, 0.2, 0.2)$

Figure G4. (n, v_P, v_S) = $(25, 0.2, 0.2)$

Figure G5. $(n, \nu_P, \nu_S) = (0.001, 0.1, 0.3)$

Figure G6. $(n, \nu_P, \nu_S) = (0.001, 0.1, 0.3)$

Figure G7. $(n, \nu_P, \nu_S) = (1.e{-}10, 0.2, 0.2)$.

Figure G8. $(n, \nu_P, \nu_S) = (1.e8, 0.2, 0.2)$.

Re-interpretation of flat shapes

Looking at Figures G1 - G6 it seems appropriate to introduce the following re-interpretation of flat shapes: For moderate stiffness ratios aspect ratios have the traditional (strict) meanings when $A > \approx 1/4$. For lower aspect ratios flat shapes have to be re-interpreted as has previously been indicated: Shapes are agglomerating discs preparing to become a continuous laminate (crumbled sheets/foils).

For extreme stiffness ratios, composite stresses in strict disc reinforced composites keep very close to those calculated by the present method (with organic discs).

Crumbled foil: A flat organic shape of special interest is the crumbled foil defined in Section 4.1.4. In the present context we consider a crumbled foil to be the

result of the agglomeration of many thin discs (A = 0). The dilute version of the geo-function for such geometry becomes as shown in Equation G2, consistent with Equation 4.10c. Dilute phase P stresses are as presented in Equation G3.

$$\theta_k^o = \kappa_S \sqrt{N_k} \quad ; \quad \theta_g^o = \gamma_S \sqrt{N_g} \quad for \ \mu_{Pkg}^o = \mu_{Skg}^o = 0 \quad ; \quad Crumbled \ disc \qquad (G2)$$

$$\frac{\sigma_{Pkk}^o}{\sigma_{kk}} = \frac{S_{Pij}^o}{S_{ij}} = \sqrt{n} \quad (\nu_S = 0.2) \qquad (G3)$$

Long shapes

An analysis of dilute composites with fibres has been made with results similar to the disc results. A joint conclusion is presented just below.

Conclusion

In the present work organic particles are considered by the strict cylinder model in the following way: Long shapes (A > 4) define fibre particles preparing to serve as an enveloping matrix phase. Flat shapes (A < 1/4) define disc particles preparing to serve as an enveloping matrix phase. For intermediate particle shapes ($\approx$ 1/4 < A < $\approx$ 4) no reinterpretations of particles have to be introduced.

The rate of 'preparing to become continuous' is such that the results of an analysis of a composite with organic particles approach the results of a counterpart analysis of a composite with strict particles - when extreme stiffness ratios are approached (n → 0 or n → ∞).

Thus, a composite analysis based on strict cylindrical particles and a composie analysis based on organic particles will produce similar results when the following combinations of aspect ratio (A) - stiffness-ratio (n) are held:

-      Moderate aspect ratios ($\approx$ 1/4 < A < $\approx$ 4) at any stiffness ratio.
-      Any aspect ratio at extreme stiffness ratios (n → 0 and n → ∞).

We notice that "preparing to become continuous" shapes are probably more relevant in practice than strict shapes. It is very likely that interference between long and thin particles will form these particles to appear organically.

243

Literature in Appendix section

1.   Sokolnikoff, J.S.: "Mathematical theory of elasticity", McGraw-Hill, New York, 2nd edn., 1956.

2.   Nowick, A.S., and Berry, B.S.: "Anelastic relaxation in crystalline solids", Academic Press, New York, 1972.

3.   Hill, R.: "Elastic behaviour of crystalline aggregate", Proc. Phys. Soc. (London), A65(1952), nr 389, 349.

4.   Voigt, W.: "Lehrbuch der Krystallphysik", Teubner, Leipzig, 1910 (reprinted, Teubner, Stuttgart, 1966).

5.   Reuss, A.: "Berechnung der fliessgrenze von Mischkristallen auf Grund der Plastizitätsbedingung für Einkristalle", Ztschr. f. angew. Math. u. Mech., 9(1929), 49.

6.   Hashin, Z. and Shtrikman, S.: "A variational approach to the theory of the elastic behavior of polycrystals", Mech. Phys. Solids, 10(1962), 343.

7.   Eshelby, J.D.: "The determination of the elastic field of an ellipsoidal inclusion, and related problems", Proc. R. Soc. London, Ser.A, 241(1957), 376-396.

8.   Stang, Henrik: Personal communication, Dept. Struct. Eng. and Mat., Tech. Univ., Denmark, april 1997.

9.   *Idem:* "En kompositmaterialeteori og dens anvendelse til beskrivelse af trækpåvirkede cementkompositter" (in danish, "A composite theory and its application to cement based composites subjected to tension"), Thesis, Institute of Structural Mechanics, Tech. Univ. Denmark, 1984.

10.   Budiansky, B.: On the elastic moduli of some heterogeneous materials". J. Mech. Phys. Solids, 13(1965), 223 - 227.

11.   Coble, R.L., and Kingery, W.D.: "Effect of porosity on physical properties of sintered alumina", J. Am. Ceram. Soc., 39(1956), 377 - 385.

12.   Böttcher, C.J.F.: "The dielectric constant of crystalline powders", Rec. Trav. Pays-Bas, 64(1945), 47.

13.   Landauer, R.: "The electric resistance of binary metallic mixtures", J. Appl. Phys. 23(1952), 779.

14.   Nielsen, L. Fuglsang: "Elastic Properties of Two-Phase Materials", Materials Science and Engineering, 52(1982), 39-62.

15.   *Idem:* "On the Effect of Defective Phase Contact on the Mechanical Behavior of Particulate Composites like Concrete", Cement and Concrete Research, 12(1982), 685.

16.   *Idem:* "The TROC-material - definition and topology", Build. Mat. Lab., Tech. Univ. Denmark, Tech. rep. 32(1974), 31 pp., (Application report on StvF-project 516-3571.B370).

17.   *Idem:* "Partikel-armerede materialers elastiske egenskaber". Progress report 1975(feb) on StvF-project 516-3571.B370, 24 sider.

18.   *Idem:* "Partikel-armerede materialers elastiske egenskaber I: Perfekt fasekontakt",

Build. Mat. Lab., tech. rep. 41(1976), 25 sider. (Progress report on StvF-projects 516-3571.B-370 and 516-3748.B-415).

19.   *Idem:* "Partikel-armerede materialers elastiske egenskaber II: Defekt fasekontakt", Build. Mat. Lab., Tech. Univ. Denmark, tech. rep. 46(1976), 16 pp., (Progress report on StvF-projects 516-3571.B-370 og 516-3748.B-415).

20.   *Idem:* "Fase-symmetriske tokomponentmaterialer". Application report mar(1976), 7 pp, StvF 516-6572.B-508.

21.   *Idem:* "Elastic properties of isotropic particle-reinforced and phase-symmetric materials". Build. Mat. Lab., Tech. Univ. Denmark, tech. rep. 54(1977), 37 pp, (Progress report on StvF-project 516-6572.B-508).

22.   *Idem:* "FEM-resultater for nogle kompositmaterialer". Build. Mat. Lab., Tecg. Univ. Denmark, Documentation report sep(1981), 14 pp.

23.   ICES STRUDL-II, "The structural design language", Engineering user's manuals, 1(1968), 1st ed., and 2(1971), 2nd ed., Dept. Civ. Eng., Massachusetts Institute of Technology.

24.   Nielsen, L. Fuglsang: "Materialemekanik II - Rheologi, Brud, Kompositmaterialer og Levetid", (in danish, Material mechanics II - Rheology, Damage, Composites, and Fatigue), Textbook (TR-189), Build. Mat, Lab., Techn. Univ. Denmark, 1988.

25.   *Idem:* "Power Law Creep as Related to Relaxation, Elasticity, Damping, Rheological Spectra and Creep Recovery - With Special Reference to Wood", Conference of Int. Union of Forestry Research Organizations (IUFRO), Xalapa, Mexico, December 1984. Proc., Build. Mat. Lab., Techn. Univ. Denmark 1985, 181 - 204.

26.   Leaderman, H.: "Viscoelastic phenomena in amorphous high polymeric systems", Chapter 1 in Eirich, F. (ed): "Rheology", Vol. II, Academic Press Inc., New York, 1958.

27.   Schwarzl, F.R.: "Numerical calculation of stress relaxation modulus from dynamic data for linear viscoelastic materials", Rheologica Acta, 14(1975), pp 581-590.